Surface Modified Superparamagnetic Iron Oxide Nanoparticles for Long-Term Stem Cell Tracking

UNIVERSITY OF LIVERPOOL

Thesis submitted in accordance with the requirements of the University of Liverpool for the degree of
Doctor in Philosophy
by

Anita K. Peacock

April 2016

PAGE LEFT INTENTIONALLY BLANK

CONTENTS

Acknowledgements II
Declaration III
Abstract IV
Abbreviations V

1 CHAPTER 1 - An Introduction to Stem Cell Labelling 1

List of Figures 2
List of Tables 2
List of Schemes 3
I. Prelude 3
1.1 Stem Cells in Regenerative Medicine 4
1.1.2 Safety Issues 6
1.1.2.1 Current Labelling Technologies 7
1.1.2.2 Imaging Methods 9
1.1.2.3 Commonly used Materials 9
1.1.3 Summary of Nanoparticle Qualities Required for Long Term Stem Cell Tracking 11
1.2 Superparamagnetic Nanoparticles as Stem Cell Labelling Agents 11
1.2.1 Magnetic Resonance Imaging (MRI) Technique 11
1.2.2 MRI Contrast Agents 14
1.2.3 Iron Oxides 14
1.2.4 Synthesis of Superparamagnetic Iron Oxide Nanoparticles (SPIONs) 16
1.3 SPION Surface Functionalisation 19
1.3.1 Stabilisation Methods 19
1.3.2 Coating Strategies 21
1.2.2.1 Co-ordinating End Groups 22
1.2.2.2 Ligand Exchange 23
1.2.2.3 Grafting-to *vs* Grafting-from 24
1.4 Coating Materials for Biocompatible SPIONs 26
1.4.1 Organic Coatings 28
1.4.1.1 Polymer Synthesis 29
1.5 Targets and Layout of Thesis 33
1.6 References 33

2 CHAPTER 2 - Experimental **43**

List of Figures 44
List of Tables 45
List of Schemes 45
2.1 Materials 45
2.2 Characterisation Techniques 46
2.2.1 Dynamic Light Scattering (DLS) 46
2.2.1.1 DLS Technique Used 46
2.2.2 Powder X-Ray Diffraction (PXRD) 47
2.2.2.1 Wavelength Selection 47
2.2.3 Transmission Electron Microscopy (TEM) 48
2.2.3.1 Conventional Transmission Electron Microscopy (TEM) theory 48
2.2.4 Fourier-Transform Infrared (FT-IR) Spectroscopy 49
2.2.5 Thermogravimetric Analysis (TGA) 50
2.2.6 Gel Permeation Chromatography (GPC) 50
2.2.6.1 GPC Theory 50
2.2.7 Nuclear Magnetic Resonance (NMR) 52
2.2.8 Micromass LCT Mass Spectroscopy (MS) 52
2.2.9 Inductively Coupled Plasma Optical Emission Spectrometry (ICP-OES) 53
2.2.10 Elemental Analysis 53
2.2.11 Electrophoretic Mobility 53
2.2.12 Differential Scanning Calorimetry (DSC) 54
2.2.13 UV-Vis Spectroscopy 54
2.2.14 Magnetic Resonance Imaging (MRI) 54
2.2.15 Superconducting Quantum Interference Device (SQUID) 55
2.2.15.1 Magnetic Core Characterisation 55
2.2.16 Atomic and Magnetic Force Microscopy (AFM) 56
2.2.17 Cell Tracking Velocimetry (CTV) 56
2.2.18 Photothermal Microscopy 59
2.3 Protocols and Assays Used Throughout the Thesis 61
2.3.1 Colorimetric Iron Quantification Assay 61
2.3.1.1 Stability of SPIONs in a Model of Lysosomal Environment 61
2.3.1.2 Protocol for Iron Measurement in SPION samples 62
2.3.2 In Vitro Studies 63
2.3.2.1 Cytotoxicity/Cell Viability Assay 63
2.3.2.2 Cell Uptake 64
2.4 Synthetic Material Used Throughout the Thesis 64
2.4.1 Synthesis of Monodisperse Oleic Acid Coated Magnetite SPIONs (Fe_3O_4) by Thermal Decomposition Reaction 64
2.4.1.1 Preparation of Iron(III) Oleate Complex 64

		2.4.1.2 Thermal Decomposition of Iron(III) Oleate to Synthesise Monodisperse Oleic Acid Coated Iron Oxide Nanoparticles (OA-SPIONs)	65
	2.4.2	Ligand Exchange Reaction of OA-SPIONs with (3-amino) propyltrimethoxysilane (APTMS) to form Amino Silane Coated SPIONS (A-SPIONs).	66
2.5	Chapter 3 Experimental Procedures		67
	2.5.1	Synthesis of N-succinimidyl-2-bromoisobutyrate Initiator for ATRP	67
	2.5.2	Atom Transfer Radical Polymerisation (ATRP) of 2-methacryloylethyl phosphorylcholine (MPC) using N-succinimidyl-2-bromoisobutyrate (NSBriB) Initiator	68
	2.5.3	Amidation reaction of N-succinimidyl functional polymers with A-SPIONs	71
2.6	Chapter 4 Experimental Procedures		72
	2.6.1	Synthesis of pH 2 Stable Maghemite SPIONs (γFe_2O_3) by Co-precipitation Reaction	72
	2.6.2	Removal of Oleic Acid from the Surface of OA-SPIONs (Fe_3O_4) to form pH 8 Water Dispersible SPIONs with a Bare Surface	73
	2.6.3	Pre-treatment of pH 2 Water Dispersible Maghemite (γFe_2O_3) Nanoparticles to make them pH 8 Water Dispersible in Preparation for Silica Coating	73
	2.6.4	Synthesis of Silica Coated Maghemite (γFe_2O_3) or Magnetite (Fe_3O_4) Nanoparticles using Sol-gel Stöber method	74
2.7	Chapter 5 Experimental Procedures		75
	2.7.1	Sonochemical Synthesis of Core/Shell Iron oxide/Gold Nanoparticles using A-SPIONs.	75
	2.7.2	Synthesis of Disulphide ATRP Initator bis[2-(2'-bromoisobutyryloxy) ethyl] disulfide (BriBOEDS)	76
	2.7.3	ATRP of MPC using Disulphide Initator bis[2-(2'-bromoisobutyryloxy) ethyl] Disulfide (BriBOEDS)	76
	2.7.4	Coating Au-SPIONs with pMPC	76
	2.7.5	Sonochemical Synthesis of A-SPIONs with Thin Gold Shell	77
	2.7.6	Reaction of A-SPIONs with Auric Chloride Solution	78
2.8	References		78

CHAPTER 3 –
3 Preparation of poly(2-methacryloyloxyethyl phosphorylcholine) Functionalised SPIONs for Stem Cell Labelling **81**

82
List of Figures 85
List of Tables 85
List of Schemes 85
3.1 Introduction 90
3.2 Results and Discussion 90
3.2.1 Preparation of Oleic Acid Coated SPIONs (OA-SPIONs) 91
3.2.2 Preparation of Amino Silane Functionalised SPIONs (A-SPIONs) 94
3.2.2.1 Quantification of Amine Groups Reacted to the SPION Surface 99
3.2.3 Preparation of N-Succinimidyl Functional poly[2-(methacryroyloxy)ethylphosphorylcholine] (NS-pMPC) Homopolymers by Atom Transfer Radical Polymerisation (ATRP) 103
3.2.4 Amidation Reaction of *NS*-pMPC Homopolymers with A-SPIONs 109
3.3 Poly[2-(methacryroyloxy)ethylphosphorylcholine]-Coated Iron Oxide Nanoparticles (pMPC-SPIONs): Synthesis, Colloidal Stability and Evaluation for Stem Cell Labelling. 109
3.3.1 Preparation of pMPC-SPIONs 109
3.3.2 Nanoparticle Characterisation 111
3.3.3 Polymer Coverage Calculations 118
3.3.4 Cytotoxicity 123
3.3.5 Stability studies 124
3.3.5.1 Colloidal Stability 124
3.3.5.2 Chemical Stability 126
3.3.6 Magnetic Measurements 127
3.3.6.1 Magnetisation Saturation (M_s) Measurements 127
3.3.6.2 Magnetic Resonance Imaging (MRI) 130
3.4 Conclusion 131
3.5 References 132

CHAPTER 4 - Synthesis of Silica Coated SPIONs:
4 The Development of SPIONs Stable to the Conditions of the Lysosomal Environment **137**

List of Figures 138
List of Tables 140

4.1 Introduction 140
4.2 Results and Discussion 145
4.2.1 Synthesis and Characterisation of Magnetite Fe_3O_4 SPIONs 146
4.2.2 Synthesis and Characterisation of Maghemite γFe_2O_3 SPIONs 147
4.2.3 Preparation of pH 8 Water Dispersible SPIONs from OA-SPIONs 149
4.2.4 Preparation of pH 8 Water Dispersible SPIONs from pH 2 Water Dispersible SPIONs 152
4.2.5 Synthesis of Silica Coated SPIONs (γFe_2O_3 and Fe_3O_4) by the sol-gel Stöber process 153
4.2.5.1 Preliminary Experiments 153
4.2.5.2 Characterisation of silica coated γ Fe_2O_3 SPIONs 154
4.2.5.3 Synthesis and Characterisation of Silica Coated Fe_3O_4 SPIONs 161
4.2.5.4 Properties of Silica Coated SPIONs (γFe_2O_3 and Fe_3O_4) 165
4.2.5.5 Magnetic Measurements 167
4.3 Conclusion 169
4.4 References 170

CHAPTER 5 - Synthesis of Gold Coated SPIONs:
5 The Development of SPIONs Stable to the Conditions of a Lysosomal Environment 173

List of Figures 174
List of Tables 176
List of Schemes 177
5.1 Introduction 177
5.2 Results and Discussion: First Generation Gold Coated SPIONs (Au-SPIONs) 180
5.2.1 Synthesis and Characterisation of OA-SPIONs 180
5.2.2 Synthesis and Characterisation of A-SPIONs 180
5.2.3 Sonochemical Synthesis and Characterisation of Au-SPIONs 183
5.2.3.1 First Generation Au-SPIONs: Cytotoxicity 191
5.2.3.2 First Generation Au-SPIONs: Chemical Stability 192
5.2.3.3 First Generation Au-SPIONs: Magnetisation Saturation (M_s) Measurements 193
5.2.3.4 First Generation Au-SPIONs: Relaxivity Measurements 194
5.2.4 Outlook: First Generation Au-SPIONs 194
5.3 Results and Discussion: Second generation Au-SPIONs 196
5.3.1 Synthesis and Characterisation of OA-SPIONs 197
5.3.2 Synthesis and Characterisation of A-SPIONs 197
5.3.3 Sonochemical Synthesis and Characterisation of Au-SPIONs 197

5.3.3.1 Second Generation Au-SPIONs: Cytotoxicity 200
5.3.3.2 Second Generation Au-SPIONs: Chemical Stability 206
5.3.3.3 Second Generation Au-SPIONs: Magnetisation Saturation (M_s) Measurements 208
5.3.3.4 Second Generation Au-SPIONs: Relaxivity Measurements 213
5.3.3.5 Second Generation Au-SPIONs: Elemental Mapping Measurements 216
5.4 Conclusions 218
5.5 References 220

6 CHAPTER 6 - Stem Cell Labelling Studies 223

List of Figures 224
List of Tables 227
6.1 Introduction 227
6.2 Results and Discussion 230
6.2.1 Molday Ion Contrast Agents 230
6.2.2 Stem Cell Labelling Studies using poly[2-(methacryroyloxy)ethylphosphorylcholine] (pMPC) Coated SPIONs 231
6.2.2.1 Stem Cell Retention of $pMPC_{29}$-SPIONs 239
6.2.3 Conclusions: pMPC coated SPIONs 243
6.2.4 Stem Cell Labelling Studies using Silica Coated γFe_2O_3 and Fe_3O_4 SPIONs 244
6.2.5 Conclusions: Silica Coated γFe_2O_3 and Fe_3O_4 SPIONs 248
6.2.6 Stem Cell Labelling Studies using Au-SPIONs 249
6.2.6.1 First Generation Au-SPIONs 250
6.2.6.2 Second Generation Au-SPIONs 251
6.2.6 Conclusions: Au-SPIONs 257
6.4 Conclusions: Overall 258
6.5 References 259

7 CHAPTER 7 - Conclusions and Outlook 261

List of Figures 262
List of Tables 262
7.1 Conclusions 262
7.1.1 Chapter 3 262
7.1.2 Chapter 4 263
7.1.3 Chapter 5 264
7.1.4 Chapter 6 266

7.1.5 Overall Conclusions 268
7.2 Future Outlook – Can Long-Term Stem Cell Labelling be Achieved? 271
7.3 Future Work 273
7.4 References 273
Appendix A **275**
Appendix B **288**

Dedication

For my late grandfather William (Billy) Sothern

Acknowledgements

Firstly, I would first like to thank my supervisors Professor Matthew Rosseinsky and Professor Dave Adams for giving me the opportunity to work on such an interesting project and field of science. I have thoroughly relished the challenges of this project and scope of the work involved. In addition, I acknowledge and thank them and the other senior members involved in this research grant, Dr Jonathan Weaver, Dr Raphaël Lévy, Dr Patricia Murray and Professor Steve Williams for their invaluable guidance and academic training. I also gratefully thank the EPSRC for the financial support I have received and the Centre for Materials Discovery at the University of Liverpool for training and access to a wide range of state of the art scientific equipment.

This thesis would not be possible without the help from my colleagues who have worked with me during this collaboration project: Dr Solène Cauët, Dr Arthur Taylor, Dr Lara Bogart, Dr Erol Hasan, Dr Cristina Olariu and Dr Michael Barrow. I would like to acknowledge and thank my colleagues who have helped with testing and analytical measurements: Dr Pavel Borisov and Dr Pranab Mandal for SQUID measurements, Dr Sean Higgins for GPC and DSC measurements, Dr Tobias Heil for STEM related measurements, Ms Alison Beckett for TEM assistance, Ms Karen Davies for MRI measurements, Mr George Miller for ICP measurements and Dr Natasha Flack for AFM measurements.

To the past and present members I have come to know at the University of Liverpool Department of Chemistry, thank you for your friendship and intriguing scientific discussions. I wish you all the best of luck for the future. To my close friends Lisa, Debra, Becky and Mya, thank you for helping me to relax and sometimes take my mind away from science.

Special thanks to my partner, my mother and father, my sisters and other family members for their unconditional love and support.

Declaration

I hereby certify that this dissertation constitutes my own product, where the language of others is set forth, quotation marks so indicate, and that the work carried out by collaborators Dr Solène Cauët for polymer synthesis and characterisation, Dr Arthur Taylor for stem cell labelling, cytotoxicity experiments and cell imaging, Dr Lara Bogart for photothermal microscopy, cell tracking velocimetry and magnetic characterisation and interpretation and Dr Tobias Heil for high resolution transmission electron microscopy is acknowledged as appropriate throughout this thesis.

I declare that this thesis describes original work that has not previously been presented for the award of any other degree of any institution.

Signed,

Anita Peacock

Abstract

Thesis “Surface Modified Superparamagnetic Iron Oxide Nanoparticles for Long-Term Stem Cell Tracking”

In the initial stages of this project, the aim was to develop polymer coated superparamagnetic iron oxide nanoparticles (SPIONs) which would be stable in physiological buffer solutions at 37 °C (body temperature) for cell labelling experiments. Well-defined end functional hydrophilic poly(2-methacryloyloxyethyl phosphorylcholine) (pMPC) homopolymers were prepared by atom transfer radical polymerisation (ATRP) and used to couple onto the surface of functionalised SPIONs using an end grafting-to approach. pMPC was chosen due to its well-known biocompatibility. The pMPC coated SPIONs were investigated as a potential T_2 magnetic resonance image (MRI) contrast agent through biocompatibility and colloidal stability screening prior to biological studies of the polymer coated SPIONs with stem cells. In the later stages of this project, silica and gold nanoparticle (NP) surface coatings were individually investigated for their chemical stability and protection of the SPION core to acidic conditions mimicking those found in the lysosome of the stem cell. This was carried out in order to develop and screen a coating that would enable long term stem cell tracking. Again, the nanomaterials prepared were assessed for biocompatibility and their magnetic properties were measured prior to stem cell labelling studies. In the final chapter, the nanomaterials prepared throughout this Thesis were subjected to stem cell labelling and the retention of the nanomaterials inside stem cells was investigated.

Abbreviations

AFM	Atomic force microscope
APTMS	(3-amino)propyltrimethoxysilane
A-SPIONs	Amino silane coated SPIONs
ATRP	Atom transfer radical polymerisation
Au-SPIONs	Gold SPIONs
bipy	2,2-bipyridine
BriB	2-bromoisobutyrylbromide
BriBOEDS	Bis[2-(2'-bromoisobutyryloxy)ethyl]disulfide
BzBriB	Benzyl-2-bromoisobutyrate
CCK-8	Cell counting kit 8
CTA	Chain transfer agent
CTV	Cell tracking velocimetry
CuCl	Copper chloride
DAPI	4',6-diamidino-2-phenylindole
DCM	dichloromethane
DIW	Deionised water
DLS	Dynamic light scattering
DMAP	4-(dimethylamino)pyridine
DMEM	Dubeccos modified eagle medium
DMF	Dimethylformamide
DMSO	Dimethyl sulfoxide
DP_n	Degree of polymerisation
DSC	Differential scanning calorimetry
DRI	Differential refractive index
EDC	1-ethyl-3-(3-dimethylaminopropyl)carbodiimide
EDX	Energy dispersive X-ray
EELS	Electron energy loss spectroscopy
FBS	Fetal bovine serum
fcc	Face-centred cubic
FDA	Food and Drug Administration
γFe_2O_3	Maghemite
Fe_3O_4	Magnetite
FT-IR	Fourier transform infrared
FWHM	Full width half maximum
GPC	Gel permeation chromatography
GVHD	Graft-versus-host disease
HAADF	High angle annular dark field
HR-TEM	High resolution transmission electron microscopy
ICP-OES	Inductively coupled plasma optical emission spectrometry
IV	Intrinsic viscosity
KSC	Kidney murine stem cells
LALS	Low angle light scattering
LCST	Lower critical solution temperature
MICB	Molday Ion Coumarin Blue

MIEG	Molday Ion EverGreen
MIRB	Molday Ion Rhodamine B
M_n	Number average molecular weight
M_p	Peak molecular weight
mPEG	Methoxy PEG
MPC	2-(methacryloyloxy)ethyl choline phosphate
MR	Magnetic resonance
MRI	Magnetic resonance imaging
M_s	Magnetisation saturation
MSC	Mesenchymal stem cells
MW	Molecular weight
M_w	Weight average molecular weight
NHS	N-hydroxysuccinimide
NMP	Nitroxide-mediated polymerisation
NMR	Nuclear magnetic resonance
NP	Nanoparticle
NS-pMPC	N-succinimidyl pMPC
NSBriB	N-succinimidyl-2-bromoisobutyrate
OA	Oleic acid
OA-SPIONs	Oleic acid coated SPIONs
PBS	Phosphate buffered saline
PEG	Polyethylene glycol
PEG-COOH	PEG(monomethyl ether)succinic acid ester
PEGMA	Polyethylene glycol methacrylate
PEO	Polyethylene oxide
PRE	Persistent radical effect
pMPC	Poly (2-methyacryloyloxyethyl phosphorylcholine)
PTA	Phosphotungstic acid
pXRD	Powder X-ray diffraction
QD	Quantum dot
R_1	$1/T_1$ Relaxivity
R_2	$1/T_2$ Relaxivity
RAFT	Reversible addition−fragmentation chain-transfer
RALS	Right angle light scattering
R_h	Hydrodynamic radius
R_s	Solvodynamic radius
RI	Refractive index
ROS	Reactive oxygen species
SiO_2	Silica
SiO_2-SPIONS	Silica coated SPIONs
SPIONS	Superparamagnetic iron oxide nanoparticles
S-pMPC	Thiol functional pMPC
SPR	Surface plasmon resonance
SQUID	Superconducting quantum interference device
SS-2pMPC	Bifunctional disulphide pMPC
STEM	Scanning transmission electron microscopy

T_1	Longitudinal relaxation time
T_2	Transverse relaxation time
TCEP	Tris(2-carboxyethyl)phosphine
TD-GPC	Triple detection gel permeation chromatography
TEA	Tetraethylamine
TEM	Transmission electron microscopy
TEOS	Tetraethyl orthosilicate
TGA	Thermal gravimetric analysis
THF	Tetrahydrofuran
UCST	Upper critical solution temperature
UV-Vis	UV-Visible

List of Symbols

B	Magnetic field
Đ	Dispersity
D_m	Magnetic SPION core diameter
D_t	Total SPION core diameter
f_c	Coating weight fraction
L_{exp}	Expected number of ligands
L_{pred}	Predicated number of ligands
m_{Fe}	Mass of iron per stem cell
M_{sb}	Saturation magnetisation of bulk material
M_{sp}	Saturation magnetisation of SPIONs
η	Viscosity
N_m	Number of magnetic NPs
r_{cell}	Radius of the stem cell
r_m	Radius of the magnetic NP
υ_m	Magnetic velocity
ζ	Zeta potential

1

An Introduction to Stem Cell Labelling

List of Figures

Figure 1.1. Differentiation of stem cells into specialised cells.[10] 5
Figure 1.2. Potential uses of stem cells in regenerative medicine.[11] 5
Figure 1.3. Schematic diagram showing nanoparticle internalisation *via* endocytosis. Here, degradation of NPs due to acidic conditions found in the late endosome and lysosome can occur.[22] 7
Figure 1.4. Direction of hydrogen nuclei in water molecules precesses A) randomly (normal conditions) and B) aligned under the presences of B_0 (externally applied magnetic field). C) Showing the direction of B_0 on a patient when placed into the hospital MRI machine.[44] 12
Figure 1.5. Magnetic resonance theory. A) hydrogen nuclei precessing about the external magnetic field axis $B_{0.}$ B) schematic shows how RF pulses decrease longitudinal magnetisation M_z to form transverse magnetisation M_{xy}. Nuclear spins then return back to equilibrium M_z through relaxation.[44] 13
Figure 1.6. Images show A) a simplified structure of magnetite and B) the octahedral and tetrahedral sites.[57] 15
Figure 1.7. Mechanisms of stabilisation of colloids.[91] 19
Figure 1.8. Nanoparticle coating strategies.[96] 22
Figure 1.9. Arrangements of amino silanes on the surface of a nanoparticle. Image taken from reference.[108] 24
Figure 1.10. Molecular structures for a selection of hydrophilic polymers commonly used as SPION surface coatings. 28
Figure 1.11. A generic structure of a thiocarbonylthio RAFT CTA where Z and R perform different functions. 30

List of Tables

Table 1.1. Summary of synthetic methods used for the preparation of SPIONs. 16
Table 1.2. A summary of reaction conditions and properties obtained from the most commonly used iron oxide wet chemical synthesis methods.[92] 20

List of Schemes

Scheme 1.1. Hydrothermal reduction for the synthesis of SPIONs by liquid-solid-solution (LSS) phase transfer.[90] 18

Scheme 1.2. Examples of co-ordinating groups for the attachment of ligands to iron oxide NP surface. [98] 23

Scheme 1.3. End grafted polymer coating methods showing A) grafting-from and B) grafting-to approaches.[112] 25

Scheme 1.4. Examples of direct nanoparticle conjugation chemistries.[117,96] 27

Scheme 1.5. A generic RAFT mechanism showing M as the monomer and X as the initiator. [116] 30

Scheme 1.6. An outline of functionalisation routes for polymers prepared *via* RAFT. Showing (i) RAFT polymerisation with a vinyl monomer and (ii) copolymerisation. Functionalisation can be carried out on the (iii) R-group; (iv) Z-group; (v) polymer chain and (vi) thiocarbonylthio group. Showing X as a hydrogen or methyl group.[116] 31

Scheme 1.7. Scheme for the mechanism of ATRP: (A) initiation; (B) equilibrium; (C) propagation. Where P_n is polymer, R is the initiator, M is monomer, X is halide (Cl or Br) and L(s) is ligand(s).[185, 186] 32

I. Prelude

Stem cell therapy is a rapidly emerging field of regenerative medicine which has demonstrated cell renewal and 'healing' properties through the interaction of stem cells with damaged tissues/organs. Stem cell therapy can potentially heal a vast range of damaged tissues/organs in patients with a disability/physical impairment.[1-5] To progress stem cell therapy further and encourage its use in medical practices, the behaviour and mechanisms of how stem cells work and their interaction with damaged tissues/organs after administration *in vivo* needs to be fully understood. To achieve this, technology needs to be developed to provide the capability to track stem cells over a long period of time (typically up to the life time of the cell). Stem cell tracking is also crucial in terms of health and safety because if cells migrate to other organs and/or tissues besides the targeted tissue/organ, serious health problems for the patient could occur.

The technology proposed in the EPSRC grant for this PhD project is to track and image stem cells long term *via* magnetic resonance imaging (MRI). MRI is a non-invasive imaging technique that is capable of imaging stem cells labelled with an MRI contrast agent *in vivo*.[6] Superparamagnetic iron oxide nanoparticles (SPIONs) are the MRI contrast agent of choice for this project primarily due to known low cytotoxicity of iron oxide, its biodegradability and use as a nutrient for the body. The nanoscale dimensions of SPIONs allow easy introduction and uptake into a stem cell and hence allow for cell labelling and tracking capabilities.[7]

There are many challenges in this project since SPIONs readily biodegrade within a period of days/weeks when subjected to conditions inside the stem cell.[8] To ensure SPIONs remain stable for a long period of time, nanoparticle surface coatings are developed in this PhD project and their stability to conditions mimicking those found inside the stem cell is investigated. Their interactions and up take with stem cells are also studied.

To address the challenges in the project, interdisciplinary collaboration was set up between physical scientists and stem cell biologists. The most suitable SPION surface coatings were screened using imaging techniques developed by the biophysicists in this project (photothermal imaging and cell tracking velocimetry (CTV)) by assessing stem cell uptake and retention time of SPIONs.

1.1 Stem Cells in Regenerative Medicine

Stem cells are unspecialised cells which have the ability to differentiate into any specialised cell type within the body such as a heart cell, nerve cell, or a skin cell, **Figure 1.1**.[1, 2] Stem cells unique properties make them a key feature of the rapidly emerging field of regenerative medicine. Regenerative therapy is an area of translational medicine which uses tissue engineering and molecular biology techniques for the renewal, replacement, repair or regeneration of damaged or diseased cells/tissue with new cells/tissue in order to achieve the restoration of normal tissue function. Stem cells can regenerate old cells with new cells through self-renewal (cell division and replication by mitosis), and cell potency (the ability to differentiate into a specialised cell type)[9] which thus provides the ability to repair and heal damaged tissue. Such examples for the potential use of stem cells for

regenerative therapy include the repair of damaged spinal cord tissue or damaged retinal tissue to allow patients suffering from paralysis or blindness to regain mobility or eye sight respectively.[3-5] There are many other possible medical applications where stem cell therapy could also be beneficial, **Figure 1.2**.

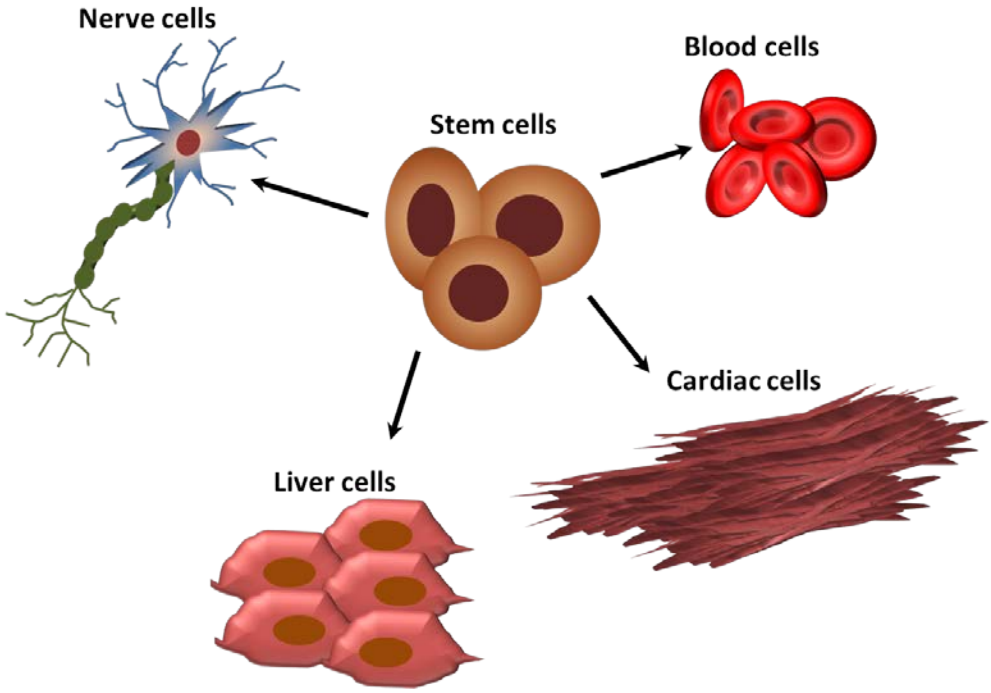

Figure 1.1. Differentiation of stem cells into specialised cells.[10]

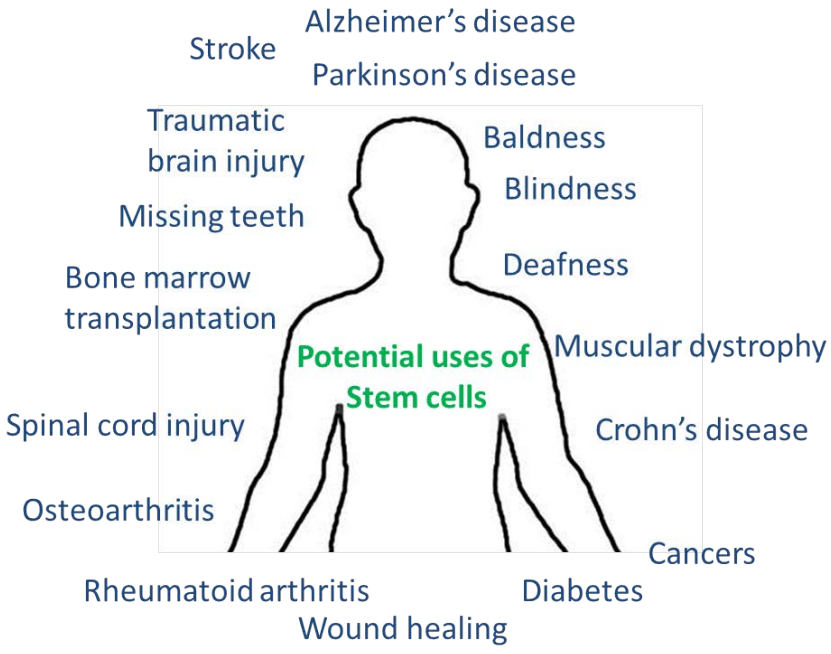

Figure 1.2. Potential uses of stem cells in regenerative medicine.[11]

1.1.2 Safety Issues

To research and fully understand the cell biology and benefits of stem cells for regenerative therapy, stem cells need to be cultured as a single cellular type (pure) and be sourced in large numbers. There are two main sources where pure animal stem cells are abundant: i) embryonic stem cells, typically sourced from inner cell mass of blastocysts[12, 13] and ii) adult stem cells, found in bone marrow, adipose tissues and blood (e.g. umbilical cord blood).[14-16] Although sources of stem cells can be cultured in large numbers and defined as "pure", the next major hurdle is the need to fully understand the behaviour of stem cells after administration into organisms *in vivo*. In addition, from a health and safety point of view, it is necessary to ensure stem cells only target the specific tissues/organs in the body where they are needed and do not migrate to neighbouring organs/tissues of differing specialised cell types since serious health problems can occur. The health issues arise mainly because there are different types of stem cell transplant which pose risks to the patient which include: whether stem cells originate from the patient (autologous), if the stem cells come from a matched related or unrelated donor (allogenic) and finally if the stem cells come from an identical twin or triplet (syngeneic). Such risks therefore include: infection from the donor which can lead to death, failure of stem cells grafting to the target tissue/organ area which could lead to infection and death and contamination of stem cells from the donor to the recipient such as cancer cells. A major risk can be that the stem cells from the donor see the recipient's body as foreign (graft-versus-host disease (GVHD)) and therefore attack organs thus increasing the chance of an infection. Acute GVHD can occur 10 to 90 days after transplant whereas chronic GVHD can occur from 100 to 400 days after stem cell transplant so the ability to monitor stem cells past 400 days would be advantageous. Long-term risks from transplantation could lead to organ damage and abnormal growth of tissues which can lead to a variety of issues for the patient.[17] Technological advancements therefore need to be developed so that stem cells can be tracked using imaging techniques after stem cells have been administered *in vivo*. By doing so, we can understand the fate, distribution and behaviour/function of stem cells in the body. The knowledge gained from this research will enable the field of stem cell therapy to progress further and allow routine use in medicine.

1.1.2.1 Current Labelling Technologies

At present, there are two main methods for labelling and tracking stem cells. The first method is through gene modification of stem cells using fluorescent proteins which can be detected by optical microscopy. The main concern and limitation of fluorescent imaging by optical microscopy is the limited tissue penetration (no more than a few cm) which prevents non-invasive imaging of stem cells in the body. In addition, there is concerns over using foreign genes which may change the overall function and behaviour of the stem cells.[18, 19] The other method to track and image stem cells *in vivo* is through the use of nanoparticles (NP) which have interesting optical and imaging properties. Due to their nanoscale dimensions, NPs can be easily internalised into cells *in vitro via* endocytosis, **Figure 1.3**.[20, 21]

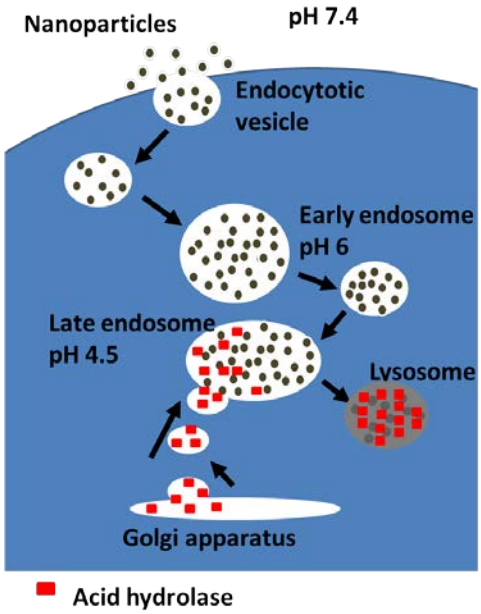

Figure 1.3. Schematic diagram showing nanoparticle internalisation *via* endocytosis. Here, degradation of NPs due to acidic conditions found in the late endosome and lysosome can occur.[22]

Endocytosis is a process by which a cell uptakes nutrients. The endosome forms through invagination of the cell membrane to form a vesicle which contains nutrients for the cell which are then released into the cytoplasm. Endocytosis or pinocytosis (cell drinking) is the uptake of fluid for the cell which allows for non-specific internalisation of NPs.[22] Internalisation of NPs into the endosome can also occur through receptor-mediated uptake whereby a transfection agent present on the surface of the NP can induce endosome formation once NPs come in contact with the

surface of the cell membrane and increase the rate of NP cell uptake.[23] Transfection agents typically consist of positively charged polypeptides. The attraction and adsorption of NPs coated with positively charged polypeptides to the cell membrane has been demonstrated and has thus prevented internalisation into the cell.[24] The use of transfection agents onto NP surfaces have also shown cytotoxic effects with cells.[8, 25] During the endocytosis process, acid hydrolase enzymes produced by the golgi apparatus are gradually introduced into the endosome. The endosome develops into a late endosome and eventually a lysosome containing a pH 4.5 acidic environment.[8] The acidic conditions inside the endosome/lysosome can dissolve inorganic NPs over a period of days/weeks and thus cause toxic effects to the cell. In addition, the intensity of the signal used for imaging purposes can also be removed or damaged which in terms of the goal for this project, to achieve long term tracking of stem cells, is a major obstacle. Careful consideration must therefore be made when selecting the NP material and surface coating used for eventual biodegradation and low cytotoxicity.

For example, iron oxide nanoparticles are generally regarded as having low cytotoxicity since iron is a requirement for life but if too much free Fe ions are present within a cell, iron can become potentially toxic. Based on Fenton and Haber-Weiss chemistry, catalytic amounts of iron lead to the formation of the hydroxyl OH• radical.[26] A hydroxyl radical is a powerful oxidising agent which can cause oxidative stress and cellular damage. Cells can regulate free iron ions through iron homeostasis using iron storage proteins, iron importers/exporters and regulators.[27, 28]

A strategy to provide chemical stability *via* the surface coating must also be developed in order to achieve long term stem cell tracking. The intracellular fate of NPs after endocytosis is not clear for all NPs, and not a great deal of reports in this area, since there are many NP surface coatings with different surface chemistry and functionality that can have different interactions and thus lead down different pathways after endocytosis. The general consensus is that after endocytosis and reaching the lysosome, intracellular NPs eventually become exocytosed out of the stem cell or escape out of the endosome into the cytoplasm of the cell through endosomal escape.[29-31]

To successfully label cells with NPs, NPs are required to be colloidally stable in bioactive media at 37 °C during cell uptake for 24 to 48 hours in order to achieve efficient labelling. The timescale required to monitor and fully understand the stem cell behaviour of an administered stem cell therapy depends on the lifetime of the targeted cells/tissue. In addition, stem cells need to be monitored in term of health and safety if they start to migrate to other organs nearby and thus cause any potential serious health problems to the patient. The lifetime of human cells vary from days (small intestine epithelium) to the entire life span of the patient (brain cells).

With respect to this Ph.D project, kidney murine stem cells (KSCs) and mesenchymal stem cells (MSCs) are of focus here. To develop contrast agents that are stable in a patient's body and provide long-term tracking would mean contrast agents would need to be stable based on the life time of the stem cell after administration and the time it would take the labelled stem cells to graft to the target tissue and specialise. If administered stem cells migrate to neighbouring organs/tissue, then for health and safety purposes, the contrast agent would need to be stable until the stem cells eventually grafts onto the host tissue and specialise. The location of migrated stem cells could then be monitored. A problem to this is that the administered stem cells may not decide to differentiate or only partially differentiate once in contact with the desired tissue to repair. Stem cells could develop into cancers or teratomas by continuing to proliferate. It may then just be best to say that the stability of contrast agents would require a life-span long enough to locate areas where stem cells have grafted to so that the areas could be monitored long term.

1.1.2.2 Imaging Methods

There are various nanomaterials which have interesting optical and imaging properties required for stem cell labelling with the selected nanomaterial of choice for this project being superparamagnetic iron oxide NPs (SPIONs).

1.1.2.3 Commonly used Materials

Gold Nanoparticles

At present, gold NPs are the most commonly used inorganic nanomaterials in biomedicine.[32, 33] It is widely accepted that using gold NPs as a way to track and

monitor stem cells for long term in clinical trials is promising.[34] Gold NPs have a strong vibrant colour due to their surface plasmon resonance (SPR) absorption at a specific wavelength in the UV-Visible spectrum which can be visualised using optical microscopy.[35] The SPR absorbance wavelength can be fine-tuned by varying the size and shape of the gold NPs. Gold NPs can also be used for multimodal imaging since they can be visualised by photothermal microscopy and optoacoustic imaging.[36] Advantages of gold NPs include excellent biocompatibility as they exhibit very low or non-cytotoxicity towards a broad range of biological cells and easy surface functionalisation as ligands can be easily co-ordinated to the NP surface *via* Au-thiol coupling chemistry.[37] The principal limitations to the use of gold NPs *in vivo* imaging of stem cells focus on limited penetration depth due to low signal intensity from the SPR for imaging or tracking cells *in vivo*.

Quantum Dots

Quantum dots (QDs) are light-emitting semiconductor nanocrystals typically containing cadmium (such as CdS, CdSe, CdTe) with diameters ranging typically between 2 to 10 nm. QDs possess a stable, bright/intense and long fluorescence lifespan which is accounted for by their high Stokes shift.[38] QDs come in a range of excitation wavelengths with narrow emission bandwidths. They have high resistance to photobleaching, high extinction coefficient and fluorescent quantum yields.[39] Their long fluorescent lifespan means that they outlive any biological sample with auto-fluorescence.[40] QDs fluorescent colours can be adjusted depending on overall NP diameter.[41] Smaller QDs emit light in the blue region, whereas larger ones emit light in the red region of the visible light spectrum. With regards to imaging cells *in vivo*, it is preferable to use QDs with excitation and emission wavelengths in the infrared region which achieve a greater penetration depth.[42] The main disadvantage of QDs is that they are generally cytotoxic due the release of cadmium ions from the core. Cytotoxicity has been reduced by coating the core with another semiconductor material that possesses a wider bandgap (such as ZnS) to create a core/shell composite NP.[43] The coating thus improves biocompatibility, slightly increases the size and improves their quantum yield to give a brighter fluorescence. These nanomaterials are likely to be the most extensively used nanomaterials to image biological samples at the cellular and tissue level however due to limitations of

optical intensity and poor imaging penetration depth *in vivo* tracking of cells is limited to small animals such as rodents.[18,19]

1.1.3 Summary of Nanoparticle Qualities Required for Long Term Stem Cell Tracking

To summarise the NP qualities required for long term stem cell tracking *in vivo*, the NPs need to either 1) possess excellent signal intensity to allow for deep imaging penetration or 2) be imaged using an non-invasive imaging technique which would allow NP imaging penetration *in vivo*. The NP must eventually be biodegradable past the required tracking time frame so the core needs to consist of a material which has low or no cytotoxicity. The NP must also have a surface coating which is also eventually biodegradable, biocompatible, has low or non-cytotoxicity with cells and is readily up taken into stem cells *via* the endosome. The surface coating must be colloidally stable in bio-active media at 37 °C for cell labelling experiments which require 24 to 48 hours for efficient labelling. The surface coating must also protect the core during the required cell tracking time period from degradation inside the cell.

1.2 Superparamagnetic Nanoparticles as Stem Cell Labelling Agents

Superparamagnetic NPs can be used as contrast agents for imaging by magnetic resonance imaging (MRI). Superparamagnetism is a property of small ferromagnetic NPs in which they become magnetic only under the presence of a strong externally applied magnetic field such as that used for MRI. Once SPIONs are removed from the strong external magnetic field, they cease to be magnetic and thus their magnetic moment returns to random orientation *via* Brownian motion and magnetisation to zero.

1.2.1 Magnetic Resonance Imaging (MRI) Technique

A magnetic resonance (MR) image is produced by converting relaxation times of hydrogen nuclei in a specimen containing water and/or fat molecules to a black and white contrasting image. Since humans are made up of 70 % of water, this technique can be used as a non-invasive imaging method in medical practices to investigate

and visualise the anatomy of organisms. MRI theory is based on the same principles as nuclear magnetic resonance (NMR) spectroscopy.[6]

Under normal conditions, the spin rotation orientation of hydrogen nuclei in water molecules precesses randomly; **Figure 1.4A**. **Figure 1.4B** and **Figure 1.5** shows that in MRI, the spin orientation of hydrogen nuclei will precess and align with (parallel, low energy state, spin 'up') or against (anti-parallel, high energy state, spin 'down') the direction (z-axis) of the external magnetic field applied, $\boldsymbol{B_0}$. **Figure 1.4C** shows the direction of $\boldsymbol{B_0}$ on a patient when placed into the hospital MRI machine. In the bulk, according to the Boltzmann distribution, nuclear spins from hydrogen nuclei occupy slightly more low energy states than high energy states. The sum of all the spins leads to a net magnetisation vector, ***M***.

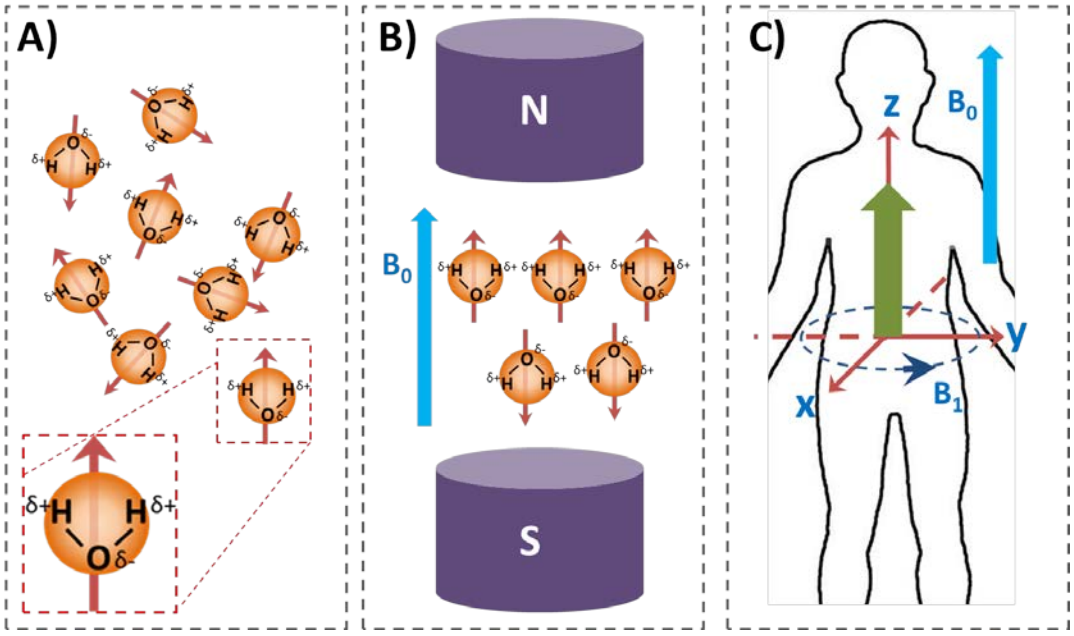

Figure 1.4. Direction of hydrogen nuclei in water molecules precesses A) randomly (normal conditions) and B) aligned under the presences of B_0 (externally applied magnetic field). C) Showing the direction of B_0 on a patient when placed into the hospital MRI machine.[44]

A rapidly changing magnetic field ($\boldsymbol{B_1}$) perpendicular to $\boldsymbol{B_0}$ is additionally applied which is generated by radio frequency (RF) pulses (hydrogen nuclei under the presence of a strong/weak magnetic field have a corresponding high/low resonant RF respectively – this is known as resonance). The RF generated field $\boldsymbol{B_1}$ at a specific resonant frequency allows hydrogen nuclei under the presence of corresponding magnetic field strength with low energy state to absorb electromagnetic radiation

energy. The absorption of energy changes the energy state of the hydrogen nuclei by exciting it from low to high energy state and thus causing the spin rotation orientation of hydrogen nuclei to change and precess perpendicular to $\boldsymbol{B_0}$ in the direction of the x-/y-axis, **Figure 1.5B**. The nuclear spin rotation of hydrogen nuclei in the x-/y- axes causes the production of current. After the RF pulses have stopped, the $\boldsymbol{B_1}$ field ceases to exist therefore allowing the nuclear spin rotation of hydrogen nuclei to precess back to their low energy state and realign in the direction of $\boldsymbol{B_0}$ (z-axis) during which the production of current reduces and allows the nuclear spins to interact with the surrounding environment during precession. This interaction process is known as relaxation. The time taken for the disappearance of current produced is measured and is known as the relaxation time. Relaxation times taken from a sample are measured and used to produce a magnetic resonance image.[6, 45]

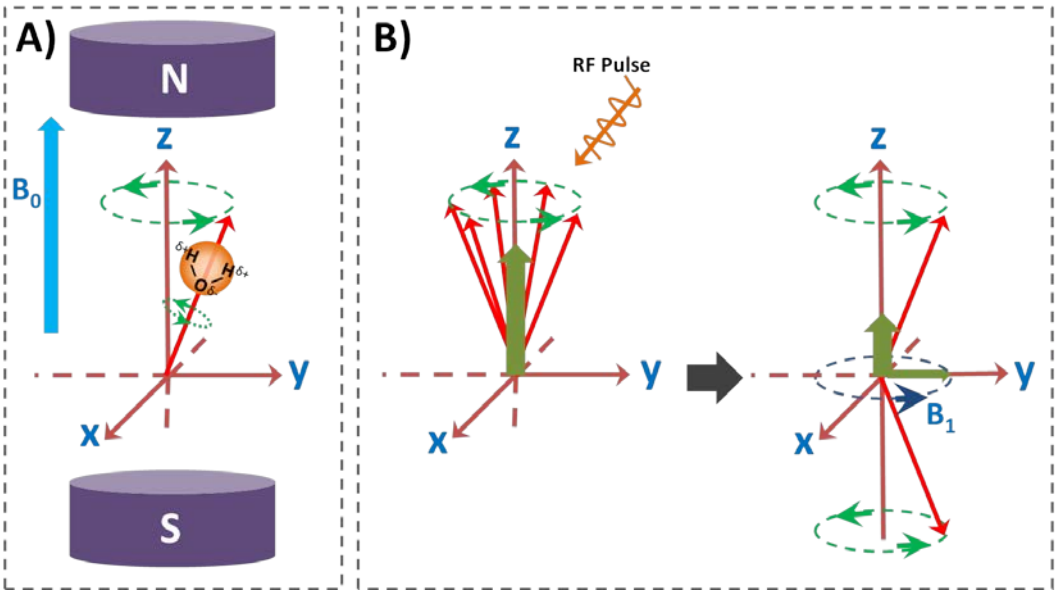

Figure 1.5. Magnetic resonance theory. A) hydrogen nuclei precessing about the external magnetic field axis B_0. B) schematic shows how RF pulses decrease longitudinal magnetisation M_z to form transverse magnetisation M_{xy}. Nuclear spins then return back to equilibrium M_z through relaxation.[44]

Relaxation can be measured in two different ways: longitudinal (spin-lattice) relaxation time, $\boldsymbol{T_1}$ and transverse (spin-spin) relaxation time, $\boldsymbol{T_2}$. Superparamagnetic nanoparticles act as magnetic dipole moments ($\boldsymbol{\mu}$) and generate a localised magnetic field when under the presence of an applied external magnetic field ($\boldsymbol{B_0}$). This localised magnetic field perturbs the nuclear magnetic spin relaxation process of hydrogen nuclei present in water molecules contained within the cell which leads to

a shortening of the relaxation time (either T_1 or T_2) and an enhanced contrast in the MR image. Water molecules diffuse to the outer sphere of cell labelled induced magnetic dipole moments (superparamagnetic nanoparticles), thus allowing for tracking capabilities by MRI.[7]

1.2.2 MRI Contrast Agents

Superparamagnetic NPs are typically composed of gadolinium (Gd), manganese (Mn) or iron oxide, although other compositions do exist.[46] Gd and Mn based superparamagnetic nanomaterials are positive T_1 contrast agents which produce an enhanced whitened area in a T_1 weighted MR image since they cause a reduction of the T_1 relaxation time, thus an increased signal intensity on a T_1 weighted MR image is observed. Iron oxide NPs are negative T_2 contrast agents which produce an enhanced, darkened area of a T_2 weighted MR image since they cause a reduction of the T_2 relaxation time, thus an increased signal intensity on T_2 weighted MR images is observed.[47] The degree of T_1 or T_2 contrast is measured by relaxivity, R_1 or R_2 respectively which is calculated by $R_1=1/T_1$ or $R_2=1/T_2$. The relaxivity coefficient of a contrast agent is represented at 1 mM of the metallic magnetic atom which is calculated from the construction of a calibration curve where higher relaxivity values result in greater contrast.[44]

To achieve maximum R_2 value, control of NP magnetism must be carried out when synthesising NPs. Since R_2 is strongly related to the magnetic moment μ, synthesising nanoparticles with the maximum μ possible is important. The magnetic moment, μ, of a NP is dependent on size, the magneto-crystalline phase and composition.[48]

Despite Gd and Mn based contrast agents possessing excellent contrast in T_1 weighted MR images, they are unsuitable for long term tracking *in vivo* due to having a short lifespan and concerns over safety caused by toxicity and stability issues.[46]

1.2.3 Iron Oxides

SPIONs are generally known to be biocompatible, have low cytotoxicity, are biodegradable and recyclable by cells and have received approval from the Food and

Drug Administration (FDA) for clinical use in humans as an MRI contrast agent (e.g. Feraheme® (also known as ferumoxytol)).[49, 50] The disadvantage for the use of SPIONs is their negative dark contrast can be confused with low level MR signal such as bone or vasculature.[51] Feridex I.V. is a clinically approved injectable aqueous colloidal solution of dextran coated SPIONs (120 nm to 180 nm). During the administration of the infusion in human clinical trials, 2.5 % of patients experienced severe pain which led interruption or discontinuation of its use.[17, 52]

At a critical domain size up to 30 nm,[53] iron oxide NPs are superparamagnetic. Two main iron oxides used as SPIONs for MR imaging are maghemite (γFe_2O_3) and magnetite (Fe_3O_4). The saturation magnetisation, $\boldsymbol{M_s}$, values of magnetite and maghemite in bulk form can reach up to 92 emu g^{-1} Fe_3O_4 and 73.5 emu g^{-1} γFe_2O_3 respectively.[54] As size decreases, the $\boldsymbol{M_s}$ values also decrease; this is also contributed from surface effects.[55] Magnetite, Fe_3O_4, has a cubic inverse spinel structure with a mixed (Fe^{2+} and Fe^{3+}) iron oxide content where Fe ions occupy interstitial tetrahedral, ***t***, and octahedral, ***o***, sites with oxygen forming face-centred cubic (fcc) closed packing (**Figure 1.6**).[56]

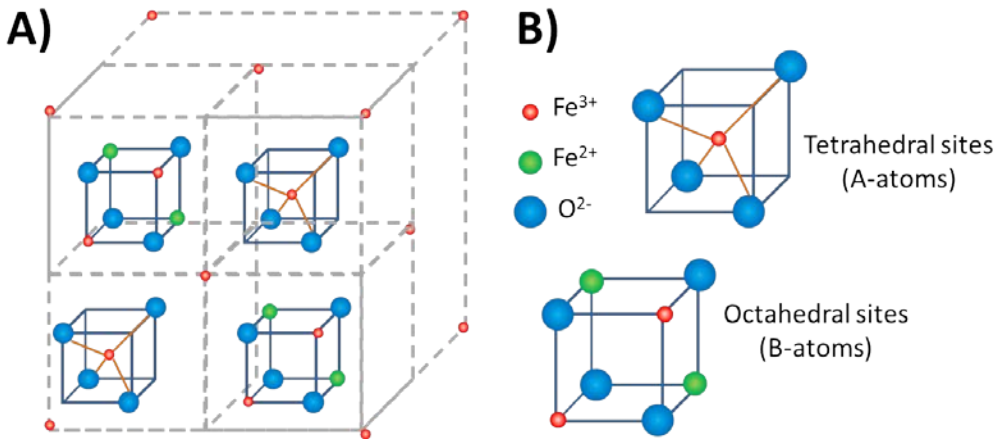

Figure 1.6. Images show A) a simplified structure of magnetite and B) the octahedral and tetrahedral sites.[57]

The formula for magnetite is written as $Fe^{3+}{}_A[Fe^{3+}Fe^{2+}]_BO_4$ or $[Fe^{3+}{}_8]_t\,[Fe^{3+}Fe^{2+}{}_8]_o\,O_{32}$ which oxidises to $[Fe^{3+}{}_8]_t\,[Fe^{3+}{}_{5,33\square 2,67}\,Fe^{3+}{}_8]_o\,O_{32}$ for maghemite (where □ is vacancy). Due to large surface area and quantum size effects, magnetic properties are dramatically changed and thus each NP can be considered as a single domain.

This allows magnetic NPs to exhibit quantum tunnelling and superparamagnetic phenomena.[58, 59]

1.2.4 Synthesis of Superparamagnetic Iron Oxide Nanoparticles (SPIONs)

There are many synthetic methods for the synthesis of SPIONs. The main synthetic routes for the preparation of Fe_3O_4 NPs are defined by physical, wet chemical or microbial synthetic routes which are summarised in **Table 1.1.**[60]

Table 1.1. Summary of synthetic methods used for the preparation of SPIONs.

Synthetic Route	Preparation Method(s)	Comments
Physical	Electron beam lithography[61, 62], gas-phase deposition[63]	Difficult to achieve control of particle size down to the nanoscale.
Wet Chemical	Co-precipitation[64, 65], oxidation[66, 67], hydrothermal[68, 69], thermal decomposition[70, 71], sol-gel[72, 73], sonochemical decomposition[74, 75], aerosol/vapour phase[76, 77], super critical fluid[78, 79], micellisation[80, 81], flow injection[82], electrochemical[83, 84].	Properties vary depending on chemical reaction and the parameters/conditions used. **Table 1.2** summaries a selection of most commonly used methods.
Microbial	Iron oxidising bacteria[85, 86],	Efficient, simple and versatile. Good control over nanoparticle geometry.

Wet chemical synthetic routes are highly practised. Co-precipitation is a technique most commonly used for the preparation of SPIONs because of quick reaction time, low reaction temperature, high yield and simplicity of protocol. Here, aqueous salt solutions of Fe^{2+} and Fe^{3+} (1:2 molar ratio) are mixed together and added to a base (typically NaOH or NH_4OH) under high speed mixing or vortex to yield either magnetite (Fe_3O_4) or maghemite (γFe_2O_3) according to **Equations (1.1) and (1.2).**[87] A disadvantage to this approach is that it is difficult to control the shape of the NPs

synthesised and to achieve a very narrow size distribution.[79,80] Control of size, shape and iron oxide type can be improved though reverse micellisation/mini-emulsion and by varying the Fe^{2+} and Fe^{3+} molar ratio, pH and ionic strength of the solutions and the type of salts used (e.g. chlorides, nitrates, sulphates).[88]

$$Fe^{2+} + 2Fe^{3+} + 8OH^{-} \rightarrow Fe_3O_4 + 4H_2O \qquad \textbf{(1.1)}$$

$$Fe_3O_4 + 2H^{+} \rightarrow \gamma Fe_2O_3 + Fe^{2+} + H_2O \qquad \textbf{(1.2)}$$

Thermal decomposition is a technique that provides excellent control over size and shape. The size distribution of NPs obtained is typically very narrow and often monodisperse.[70] The reaction involves the decomposition and nucleation of an iron (III) complex precursor which is carried out at temperatures between 100 and 320 °C in the presence of a high-boiling point organic solvent containing surface capping agents. Sun *et al.*[71] reported the thermal decomposition of iron (III) acetylacetonate ($Fe(acac)_3$) in the presence of oleic acid and hexadeylamine for the nucleation of iron oxide nanoparticles. A large scale synthesis of magnetic iron oxide nanocrystals by thermal decomposition has been reported by Hyeon and co-workers.[70] They have shown that batches of monodisperse oleic acid coated iron oxide NPs with yields up to 40 g can be synthesised. This was achieved through a two-step procedure whereby iron (III) oleate precursor is prepared and then the thermal decomposition of iron (III) oleate in the presence of oleic acid in 1-octadecene at 320 °C for 1 hour is carried out. The proposed mechanism for the synthesis procedure is that nucleation begins at 200 to 240 °C which is caused by the dissociation of an oleate ligand from the iron (III) oleate precursor through CO_2 elimination. The remaining two oleate ligands dissociate around 300 °C where major growth occurs.

Hydrothermal synthesis is an interesting synthetic approach since a variety of different nanocrystals can be formed through a liquid-solid-solution (LSS) process, **Scheme 1.1**.[89] The mechanism of the hydrothermal reduction synthesis procedure is based at the liquid solid interface during general phase transfer and separation. Each layer is added to an autoclave tube in the order of solid, then liquid and then solution phase. The mechanism for this approach starts by the synthesis of the iron precursor which is formed through phase transfer *via* ion exchange at the solid/solution interface.

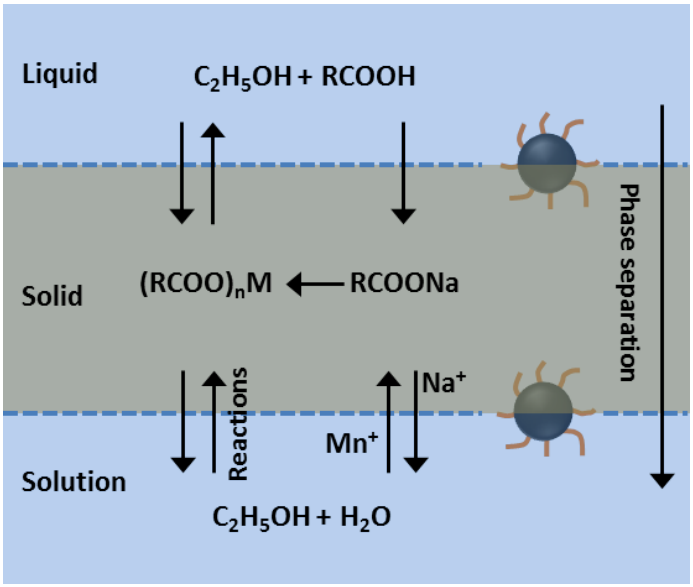

Scheme 1.1. Hydrothermal reduction for the synthesis of SPIONs by liquid-solid-solution (LSS) phase transfer.[90]

Wang *et al.*[90] prepared SPIONs by hydrothermal reduction from iron(III) linoleate which was prepared by sodium linoleate and iron salt solution. An operating temperature of 160 °C, ethanol was used for the liquid/solid or solution/solid interface to reduce Fe^{3+} ions and thus spontaneously initiate the nucleation of iron oxide NPs. As NPs grew, fatty acids present in the liquid phase such as linoleic acid acted as capping agents and adsorbed onto the iron oxide NP surface through the co-ordination of the carbonyl moiety which acted as a foot with the long chain alkyl arranged toward the solvent to provide an overall hydrophobic surface. Once NPs reached a specific density and size, a process of phase-separation and precipitation of NPs occurred. This process was not only driven by the instability of NPs through their density but also by the incompatibility of NPs with the hydrophobic/hydrophilic environment interface. The iron oxide NPs reported by Wang *et al.*[90] had a number average diameter of 9.1 ± 0.8 nm by transmission electron microscopy (TEM). The reaction was run for 10 hours using a Fe^{2+}:Fe^{3+} molar ratio of 1:2. A direct comparison of the synthetic techniques described is shown in **Table 1.2**. The synthetic methods listed in **Table 1.2** require surface capping ligands which are typically added during the reaction. In the case of the co-precipitation method, surface capping ligands can be added after the reaction. To summarise, co-precipitation is frequently the method of choice due to simplicity. However, poor control over shape, size and distribution deems this approach unsuitable for the

design of well-defined contrast agents. Thermal decomposition is a preferred technique if requiring control over shape, size and distribution to produce well defined NPs. In addition, high yield batches of SPIONs obtained from this synthetic route support its suitability as the SPION synthesis method for this project. The protocol can however be complicated due to efforts to maintain constant heating rate and control at high heating temperature. Hydrothermal reduction is an interesting simplistic method to achieve well defined SPIONs but requires improvement in the protocol to obtain higher yield SPION batches.

1.3 SPION Surface Functionalisation

SPIONs need to be dispersible in aqueous solution and physiological buffer if they are to be suitable for cell labelling experiments since NPs interact with themselves and/or biological molecules which cause them to rapidly aggregate and precipitate out of solution.

1.3.1 Stabilisation Methods

A colloidal suspension of NPs in solution can be achieved by various stabilisation mechanisms, **Figure 1.7**.

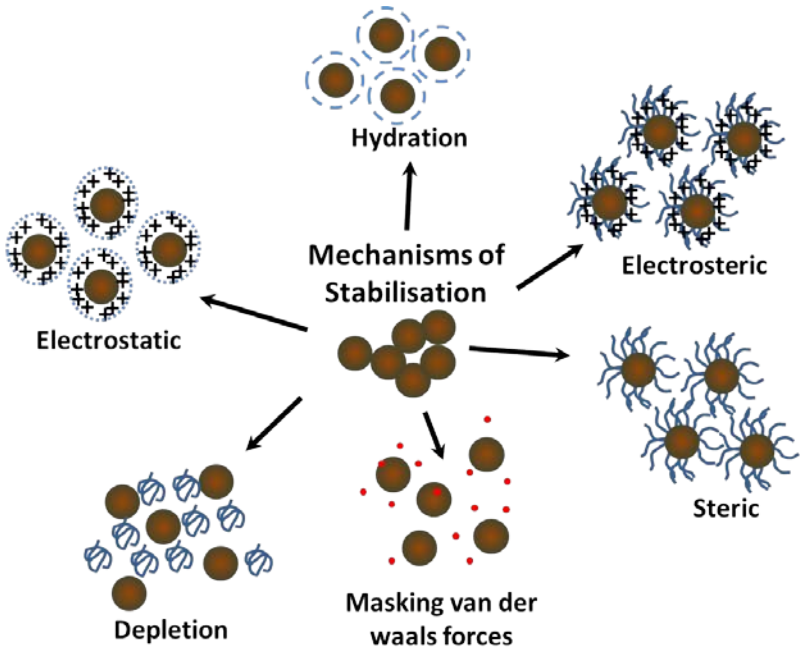

Figure 1.7. Mechanisms of stabilisation of colloids.[91]

Table 1.2. A summary of reaction conditions and properties obtained from the most commonly used iron oxide wet chemical synthesis methods.[92]

Synthetic Method	Reaction Temperature (°C)	Reaction Time	Solvent	Size Distribution	Shape Control	Yield	Procedure
Co-precipitation	Up to 90	Minutes	Water	Reasonably Narrow	Not good	High	Very simple
Thermal Decomposition	100 – 320	Hours to days	Organic	Very narrow	Very good	High	Complicated
Hydrothermal	220	Hours to days	Aqueous	Very narrow	Very good	Medium	Simple

The most commonly used methods are steric stabilisation and electrostatic stabilisation. Steric stabilisation involves using non-ionic polymer coupled to the NP surface which can create space between NPs. Electrostatic stabilisation involves using small ionic molecules which are coupled or co-ordinated to the NP which provide space between NPs through the repulsion of similar surface charge. Electrosteric stabilisation is another method which combines both steric and electrostatic mechanisms using charged steric polymers to create space between NPs. Other stabilisation mechanisms create space between NPs by hydration forces, masking van-der waals forces and depletion which uses unbound polymer.

1.3.2 Coating Strategies

Steric stabilisation of NPs in solution can be achieved by various surface coating methods. These include coating NPs *in situ* during the SPION synthesis procedure or through post synthesis methods, which involve micellisation (using phospholipids or amphiphilic polymers), end grafting or adsorption, **Figure 1.8**. Micellisation involves the use of amphiphilic polymers or phospholipids which contain hydrophobic and hydrophilic sections.[93] During the micellisation reaction, amphiphilic polymers self-assemble so that the hydrophobic section of the polymer chain is facing the hydrophobic capping ligands on the NP surface and that the hydrophilic section is facing towards the outer peripheral of the NP in the direction of the solvent. Through this assembly, amphiphilic polymers create a micelle around either each NP or a cluster of hydrophobic NPs. The conditions of the coating reaction must be optimal and the amphiphilic polymers must have the optimal polymer chain length or branching of each section if coating of individual NPs is to occur. This is typically very difficult to do. The most likely outcome from the coating procedure is the formation and coating of a cluster of NPs rather than coating individual NPs.[94, 95] Micellisation involving phospholipids also self-assemble in a similar fashion to amphiphilic polymers by arranging themselves based on the hydrophilic phosphate ‘head’ group and two hydrophobic fatty acid ‘tail’ groups. The phospholipids arrange so that the hydrophilic head groups both face the aqueous solvent and hydrophilic NP surface. By doing this, they form a phospholipid bilayer because of the two layers of phospholipids required to stabilise the NP in solution.

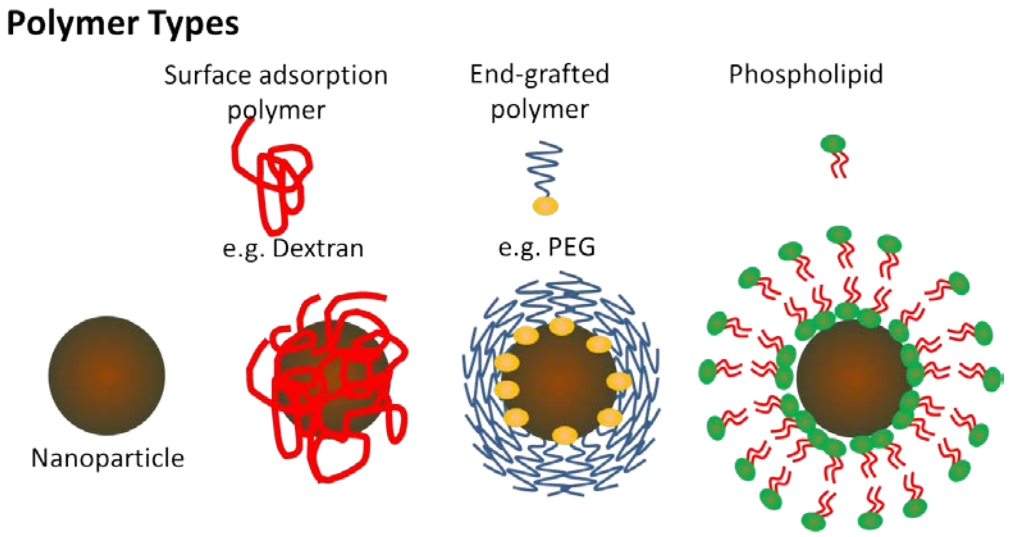

Figure 1.8. Nanoparticle coating strategies.[96]

For the *in situ* coating method, a biocompatible polymer is used as a surface capping ligand during the synthesis reaction. This coating method is beneficial for reducing the number of steps required to prepare NPs for cell labelling experiments.

1.2.2.1 Co-ordinating End Groups

The end grafting coating method involves the use of polymers which are covalently attached to the NP surface through the co-ordination of a bi- or tri-dentate functional group present at the polymer chain end. There are a variety of functional groups that will co-ordinate to the SPION surface which have been highlighted in **Scheme 1.2**. Covalently bound polymers are a preferred choice for this project since they provide stability for long-term storage and colloidal stability in aqueous media.[97, 98] The most commonly used functional groups that will co-ordinate to the SPION surface are silane, catechol, carboxylic acid and phosphonic acid.[98]

Carboxylic acid functional ligands, such as oleic acid or citric acid, and phosphonic acid functional ligands have a bi-dentate co-ordination with iron oxide. These ligands have been known to become easily detached from the surface under moderate conditions, such as temperature increase and changes to pH.[98] The catechol bi-dentate functional moiety, as represented by dopamine in **Scheme 1.2.** Examples of co-ordinating groups for the attachment of ligands to iron oxide NP surface. [98]

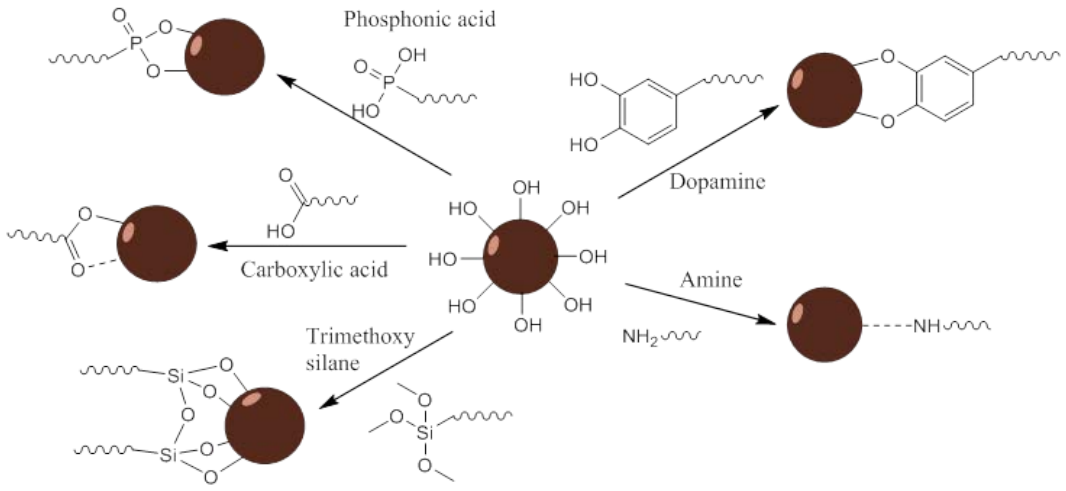

Scheme 1.2. Examples of co-ordinating groups for the attachment of ligands to iron oxide NP surface.[98]

has a strong affinity for the surface of iron oxide.[99] However, catechol has been reported to detach from iron oxide surfaces under low pH conditions through hydrolysis.[98] The instability issues of these functional ligands thus prove they are inadequate for the development of SPION coatings for long-term tracking. Silane functional ligands however, such as tetraethyl orthosilicate or alkoxy functional silanes, have a bi- or tri-dentate footprint depending on conformation and self-polymerisation. The Si-O-Fe bond is one of the strongest bonds that can be used to covalently bind ligands to the SPION surface.[98] The addition of the formation a thin biocompatible silica layer adds to the stability of the functional ligand to the surface of the SPION.[100]

1.2.2.2 Ligand Exchange

Thermal decomposition methods for the synthesis of SPIONs use lipophilic molecules as surfactants, which in turn, produce hydrophobic nanoparticles which dissolve in non-polar solvents. This means that the nanoparticles possess poor water solubility and bad compatibility with aqueous media which is highly unfavourable for use in biomedical applications.

To provide SPIONs with a hydrophilic surface, ligand removal/addition and ligand exchange reactions have been investigated.[101] Ligand removal/addition involves a two-step procedure whereby in the first step, lipophilic ligands from the nanoparticle surface are removed (typically under basic conditions and sonication). In the second

step, hydrophilic ligands such as hydrophilic polymers or small molecules can be attached.[102] For an alternative method, a direct one step ligand exchange reaction of the lipophilic ligands with hydrophilic ligands can occur.[103, 104] DePalma *et al.*[105] demonstrated direct ligand exchange of oleic acid coated nanoparticles with 3-aminotrimethoxysilane (APTMS) ligands in order to provide covalent attachment by two or more bonds from the silane ligand. In addition to this, the ligand also provided an amino functionality as an anchor for polymer attachment further on.[106] Alkoxysilanes show promise as a way of obtaining stable surface functionalisation of nanoparticle surfaces. However, alkoxysilanes are moisture sensitive and can self-polymerise if experimental conditions are not kept under anhydrous conditions.[107] The presence of excess APTMS can lead to the formation of multilayers around the surface of the nanoparticle as demonstrated in **Figure 1.9**.

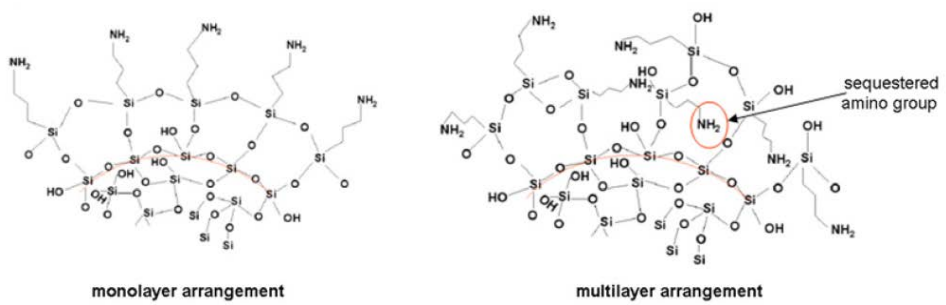

Figure 1.9. Arrangements of amino silanes on the surface of a nanoparticle. Image taken from reference.[108]

The condensation and polymerisation of the silane ligand and its attachment to the surface can become uncontrolled if the conditions of the reaction are not pursued thus causing fusion and aggregation of NPs.[109-111]

1.2.2.3 Grafting-to *vs* Grafting-from

End grafted polymer coatings can be achieved by either grafting-from or grafting-to approaches.[112] The grafting-from method firstly requires firm attachment of low molecular weight initiators to the NP surface. Monomer(s) is/are then added to the NP dispersion. Under the conditions for the polymerisation technique, polymer chains are grown from the NP surface at the initiating sites *in situ* as depicted in **Scheme 1.3A**. The advantage of this approach is that polymers are densely packed on the NP surface. However, the disadvantage is that broader molecular weight distribution is often found when compared to polymers prepared in solution.[113]

Therefore, difficulties are found when attempting to calculate polymer coverage. The second approach by the grafting-to method involves preparing the polymer prior to coating. The polymer chain possesses a reactive functional group at the chain end (or sometimes throughout the polymer chain) or a functional group that will readily co-ordinate with the iron oxide NP surface, **Scheme 1.3B**.[114, 115]

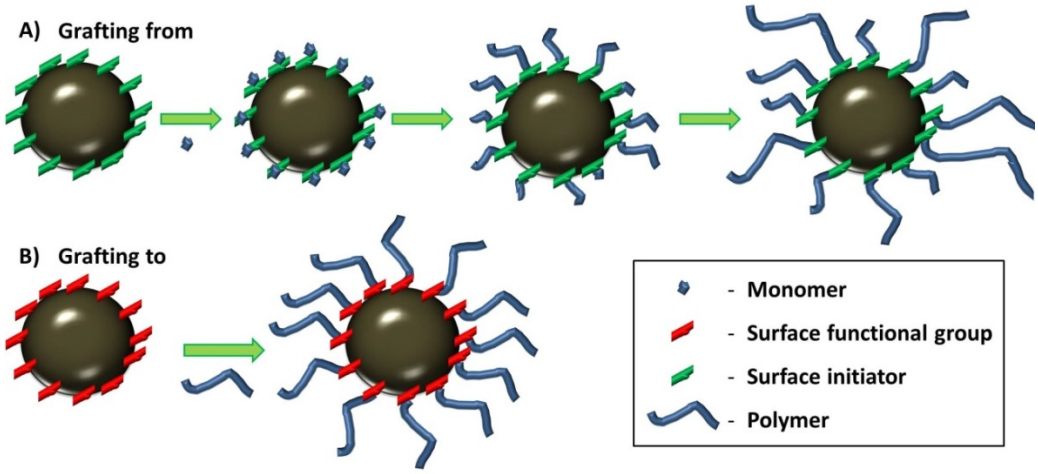

Scheme 1.3. End grafted polymer coating methods showing A) grafting-from and B) grafting-to approaches.[112]

Using a ligand containing a reactive functional group at the chain end, small surface functional ligands will need to be firmly bound to the NP surface in order for the polymer chain end to react and conjugate to the NP surface. Advantages of this method are that well-defined polymers with known chain length and molecular weight which have previously been prepared and characterised can be used which allows for control over the polymer shell thickness. Polymer coverage calculations can be carried out which can provides information of the packing density of the surface with polymer dispersants. The ability to calculate polymer coverage is also beneficial for providing an insight to what the colloidal stability behaviour of the polymer coated NPs in aqueous media could be. A disadvantage is that the packing density is typically much lower than that for the grafting-from method. This is due to issues related to steric hindrance of the length and branching of polymer chains to which they are competing for conjugation to the NP surface. [116] There are many conjugation chemistries that have been explored for the end grafting attachment of polymers to functionalised NP surfaces. These are summarised in **Scheme 1.4**.[96, 117]

Amine functionalised NP surfaces provide a suitable handle for conjugation with a variety of moieties such as anhydride, *N*-succinimidyl activated ester, epoxide and isothiocyanate which all (apart from isothiocyanate) form a stable linkage. Amine functionalised NPs are dispersible in alcohols.[110] This is advantageous since hydrophilic polymers that have solubility in alcohol can therefore be used during the coating procedure prior to transfer of the NPs into water or bio-active media.

1.4 Coating Materials for Biocompatible SPIONs

The nature of NP surface coatings is very important with regards to influencing NP cell uptake and interactions with cells. The selection of coating material is therefore a crucial aspect of this project. There are various materials that can be used to coat NPs. These fall under three main categories: organic, inorganic or hybrid (consisting of both organic and inorganic) coating forms. Organic coatings are classed under natural or synthetic polymers. Natural polymers consist in the form of polymeric macromolecules which include polysaccharides (dextran[118, 119], cellulose[120, 121], chitosan[122-124], alginate[125, 126]), proteins (gelatin[127-129], serum albumin[130, 131]), peptides[132] (polylysine[133, 134]) and lipids (oleic acid[70, 71], oleylamine[135], phospholipid[136, 137]). Synthetic polymers classed as hydrophilic include polyethylene glycol (PEG)[138-140], polyacrylic acid (PAA)[141, 142], polyvinylalcohol (PVA)[143, 144], polyethylenimine (PEI)[145, 146] and polyvinylpyrrolidone (PVP).[147, 148] Synthetic hydrophobic polymers include polystyrene[149, 150], poly(n-butyl methacrylate) (PnBMA).[149]

Amphiphilic polymers consist of a hydrophilic and hydrophobic block from either natural or synthetic classes.[151, 152] For inorganic coatings, these include silica[153, 154], titanium dioxide[155], metallic (gold[156-158], silver[158], platinum[159], palladium[159]) and carbon[160, 161] (graphene[162, 163]). **Figure 1.10** shows the molecular structures for a selection of hydrophilic polymers commonly used as NP surface coatings for bio-applications.

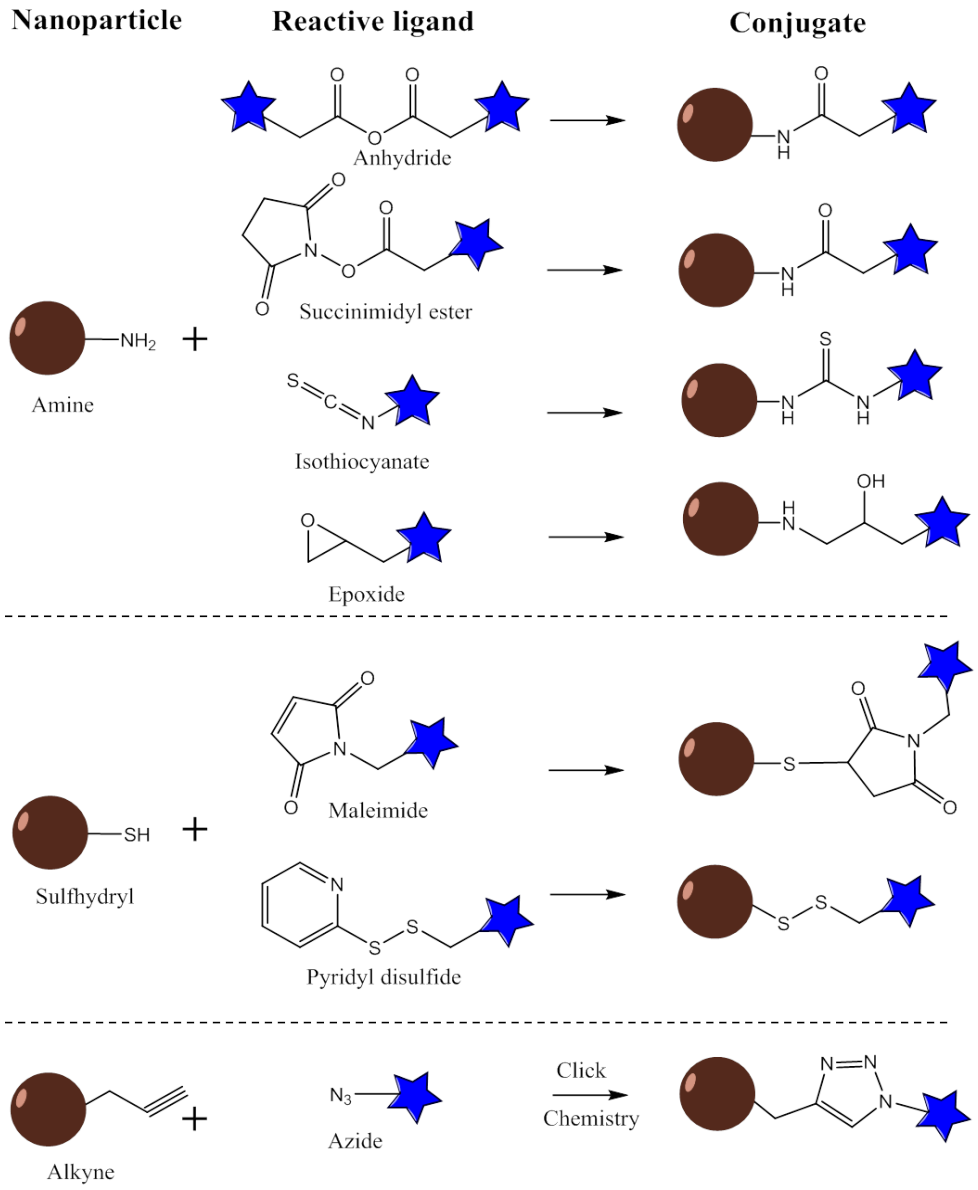

Scheme 1.4. Examples of direct nanoparticle conjugation chemistries.[117,96]

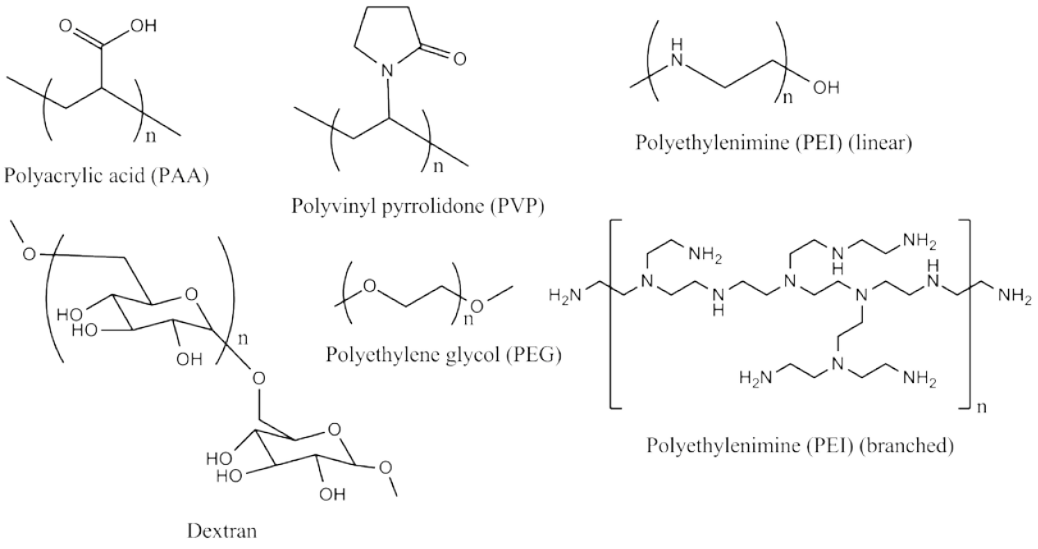

Figure 1.10. Molecular structures for a selection of hydrophilic polymers commonly used as SPION surface coatings.

1.4.1 Organic Coatings

Not only do polymeric surface coatings limit interactions between NPs through steric stabilisation but they provide options for conjugation with small molecules such as targeting ligands or drugs due to the presence of functional groups which act as chemical handle along the polymer chain.

Hydrophilic polymers as surface NP coatings have been heavily researched with polyethylene glycol (PEG) and dextran polymers used most commonly as SPION surface coatings for contrast agents.[7, 164] Polyethylene glycol (PEG) has proven to be a polymer that has provided excellent colloidal stability in aqueous and bio-active media. PEG coatings provide NPs with non-specific uptake which reduces undesired interactions with proteins.[138-140] Interestingly, despite the benefits of PEG as an appropriate coating, the development of preclinical contrast agent Clariscan^{TM} which consisted of low molecular weight PEG coated iron oxide nanoparticles was stopped due to safety concerns[52] in addition anti-PEG antibodies have been found which supports its limitation as a coating for long-term labelling use.[165]

Dextran, a polysaccharide, has shown excellent biocompatibility as a NP surface coating.[77,78] Molday and Mackenzie[166] first reported the *in situ* coating of iron oxide nanoparticles synthesised by co-precipitation with dextran 40 KDa. They oxidised dextran with periodate in order to create hydroxyl groups which would allow for

binding with amino acid groups of proteins. The size of dextran chains provides optimal polar interactions with the iron oxide surface of the NP. Since many hydrogen bonds along the polymer chain can form with the NP surface, thus providing very high binding stability when compared with only one or two hydrogen bonds from an end grafted polymer.[167] Epichlorhydrin[168, 169] can further cross-link dextran around the SPION core since dextran can become detached if diluted or heated to 120 °C.[170, 171]

1.4.1.1 Polymer Synthesis

Controlled free-radical polymerisation methods have been of much interest in the development of novel polymeric surface coatings for SPIONs.[172, 173] This technique provides the ability to control the architecture of the polymer chains which has thus created much interest in the development of polymeric surface coatings for nanotechnology, in particular for biological applications.[174-176]

Controlled free-radical polymerisation is a form of chain-growth (addition) polymerisation from which chain transfer and chain terminations are predominately reduced.[177-179] The rate of chain initiation is fast compared with the rate of chain propagation. Therefore, the number of kinetic-chain carriers is essentially constant throughout the polymerisation to give polymer chains growing at a constant rate and chain length (low dispersity (Đ)). Advantages of this technique include pre-determined molar mass and control over end groups.[180]

There are a number of controlled free radical polymerisation methods available. The most popular methods used include reversible addition-fragmentation chain transfer (RAFT), atom transfer radical polymerisation (ATRP) and nitroxide-mediated polymerisation (NMP) which occur *via* one of the two basic mechanisms: i) the persistent radical effect (PRE) - NMP and ATRP and ii) degenerative transfer – RAFT. These controlled free radical polymerisation systems are based on propagating radicals being reversibly deactivated (alternating between active and dormant states) where in NMP the dormant state is a polymeric alkoxyamine, in ATRP the dormant state is a polymeric alkyl halide and for RAFT the dormant state is a polymer chain with a RAFT end-group.[181]

i) Reversible Addition-Fragmentation chain Transfer (RAFT) Polymerisation

RAFT is a controlled free radical polymerisation technique which uses a thiocarbonylthio compound as a chain transfer agent (CTA). The thiocarbonylthio CTA undergoes a reversible chain-transfer process whereby radical addition through the stabilisation of the Z-group and re-initiation of the R-group (**Figure 1.11** and **Scheme 1.5**) is carried out.

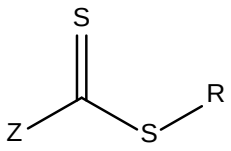

Figure 1.11. A generic structure of a thiocarbonylthio RAFT CTA where Z and R perform different functions.

The continuous reversible deactivation of growing polymer chains allows the CTA to control the polymerisation. As one chain becomes dormant, another polymeric radical is generated for further propagation. Through this exchange, the polymerisation is mediated. The Z group controls the ease at which the radical species adds to the C=S bond and the R group is used as a good homolytic leaving group which allows new polymer chains to initiate.[116]

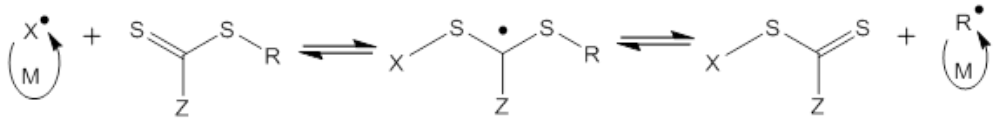

Scheme 1.5. A generic RAFT mechanism showing M as the monomer and X as the initiator. [116]

RAFT is an attractive controlled free radical polymerisation technique because the technique provides the ability to use mild conditions and a wide range of monomers. In addition, functionalisation of the CTA and polymer can be carried out in numerous ways in order to provide polymers with a range of functionality options, **Scheme 1.6**.[116]

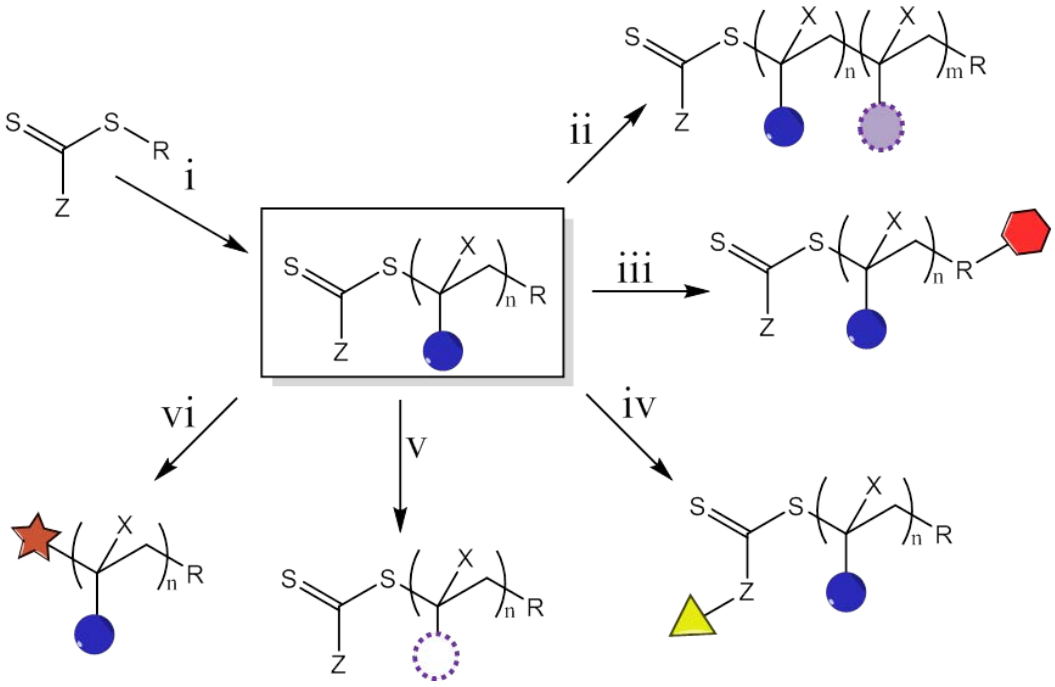

Scheme 1.6. An outline of functionalisation routes for polymers prepared *via* RAFT. Showing (i) RAFT polymerisation with a vinyl monomer and (ii) copolymerisation. Functionalisation can be carried out on the (iii) R-group; (iv) Z-group; (v) polymer chain and (vi) thiocarbonylthio group. Showing X as a hydrogen or methyl group.[116]

ii) Atom Transfer Radical Polymerisation (ATRP)

Another controlled free-radical polymerisation technique is atom transfer radical polymerisation (ATRP) which is a widely used method for the synthesis of well-defined polymers.[182] ATRP involves the use of a metal catalyst complex to activate a free radical species from the initiator. This free radical species allows for the addition of one or a few subunits (monomers) at a time onto a growing polymer chain. This controlled, synthetic process can be shut down or re-started at will by controlling the amount of monomer present in the reaction and by controlling the oxidation state of the metal catalyst complex.[183] An ATRP reaction consists of the following components: a monomer (M), an initiator (R-X), a catalyst (a metal halide (Mt) usually copper based), a ligand and solvent.[184] An ATRP reaction must be carried out in a clean, oxygen free environment (to prevent oxidation of the metal catalyst).

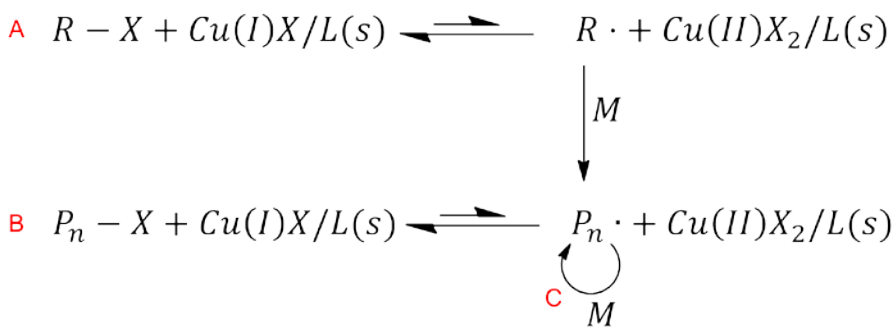

Scheme 1.7. Scheme for the mechanism of ATRP: (A) initiation; (B) equilibrium; (C) propagation. Where P_n is polymer, R is the initiator, M is monomer, X is halide (Cl or Br) and L(s) is ligand(s).[185, 186]

The ATRP mechanism[171,172], **Scheme 1.7**, shows a transition metal compound (Cu(I)X|L(s) used in this example) acting as a halogen atom carrier in a reversible redox reaction. A continuous shift of the metal atom (Cu) between the two different oxidation states (Cu(I) to Cu(II)) leads to the formation of free radicals (R· or P_n·), which can then react with an alkene monomer (M) forming the propagating macro radicals (P_n·).

The propagating step consists of a series of monomer additions to the radicals through halogen exchange. The polymeric halides (P_n-X) are the dormant form of the propagating radicals. This is another way of keeping the concentration of active centres low, suppressing possible termination reactions.

The lower oxidation state metal complex (Cu(I)X|L(s)) reacts with the ATRP initiator (R-X) to yield a radical (R·) and the corresponding higher oxidation state metal complex (Cu(II)X_2|L(s)) can transfer the halogen atom (X) back to the radical (P·), re-generating the alkyl halide (P-X) and the lower oxidation state metal complex (Cu(I)X|L(s)). The radicals (R·) can then react with the monomer (M) to initiate the polymerisation process (P_n·).

The last step of ATRP yields the halogen-terminated polymeric dormant state (P_n-X) which can be reactivated to the polymeric radical (P_n·) *via* a reaction with the higher oxidation state metal complex (Cu(II)X_2|L(s)). If the deactivation process is efficient and all propagating radicals on all polymer chains are restarted within a short period by appropriate selection of the alkyl halide initiator (R-X), the resulting polymer will be characterised by a narrow molecular weight distribution.[187, 188]

1.5 Targets and Layout of Thesis

The aim of this project is to develop a coating that will protect SPIONs from degradation to conditions found in the endosome/lysosome of a stem cell in order to achieve long-term stem cell tracking using MRI. The suitability of the coating developed will be assessed by its ability to allow the SPION to retain its magnetic properties (T_2 relaxivity and M_s) in addition to providing colloidal stability in aqueous and bioactive medium. The coating needs to be hydrophilic, have low or non-cytotoxicity and be biocompatible with stem cells. The coatings investigated will be covalently attached to the SPION surface to ensure long term stability and will be thin enough to maintain overall nanoscale dimension of the SPION for stem cell up-take *via* endocytosis. Most importantly, the coating developed must not affect the overall function of the stem cell.

In Chapter 3, oleic acid coated SPIONs are synthesised and surface functionalisation is carried out using amino functionalised silane. The attachment of polymer to the amine functionalised SPION surface is carried out and the properties and suitability of the coating is investigated for stem cell labelling. In Chapter 4 and 5, silica and gold inorganic coatings are investigated respectively. The synthesis of the inorganic coatings to the SPION surface is carried out and the properties and suitability as a coating for long term stem cell labelling is investigated. In Chapter 6, a summary of the biological cell uptake and retention studies of the coated SPIONs prepared in Chapters 3 to 5 are investigated to determine the most suitable coating for long term stem cell tracking.

1.6 References

1. G. Chamberlain, J. Fox, B. Ashton, *et al.*, *Stem Cells*, 2007, **25**, 2739-2749.
2. H. Wang, F. Cao, A. De, *et al.*, *Stem Cells*, 2009, **27**, 1548-1558.
3. S. Temple, *Nature*, 2001, **414**, 112-117.
4. M. Y. Macias, M. B. Syring, M. A. Pizzi, *et al.*, *Exp. Neurol.*, 2006, **201**, 335-348.
5. B. E. Uygun, N. Sharma and M. Yarmush, *Crit. Rev. Biomed. Eng.*, 2009, **37**, 355-375.

6. B. Doan, S. Meme and J. Beloeil, *The Chemistry of Contrast Agents in Medical Magnetic Resonance Imaging*, John Wiley & Sons Ltd, 2013, 1-23.
7. E. Bull, S. Y. Madani, R. Sheth, *et al.*, *Int. J. Nanomed.*, 2014, **9**, 1641-1653.
8. S. T. Stern, P. P. Adiseshaiah and R. M. Crist, *Part. Fibre Toxicol.*, 2012, **9**, 20.
9. C. Melton and R. Blelloch, *Adv. Exp. Med. Biol.*, 2010, **695**, 105-117.
10. http://www.stemcellclinic.com/main-en/klinika/kletochnaya-terapiya/?lang=en
11. http://www.stemcelltreatments.in/contact_us
12. M. Amit, M. K. Carpenter, M. S. Inokuma, *et al.*, *Dev. Biol.*, 2000, **227**, 271-278.
13. J. Yu, M. A. Vodyanik, K. Smuga-Otto, *et al.*, *Science* 2007, **318**, 1917-1920.
14. S. Kern, H. Eichler, J. Stoeve, *et al.*, *Stem Cells*, 2006, **24**, 1294-1301.
15. T. Reya, S. J. Morrison, M. F. Clarke, *et al.*, *Nature*, 2001, **414**, 105-111.
16. J. Yuehua, B. N. Jahagirdar, R. L. Reinhardt, *et al.*, *Nature*, 2007, **447**, 880-880.
17. www.cancer.org/acs/groups/cid/documents/webcontent/003215-pdf.pdf
18. M. Chalfie, Y. Tu, G. Euskirchen, *et al.*, *Science* 1994, **263**, 802-805.
19. H. S. Liu, M. S. Jan, C. K. Chou, *et al.*, *Biochem. Biophys. Res. Commun.*, 1999, **260**, 712-717.
20. L. Ferreira, J. M. Karp, L. Nobre, *et al.*, *Cell Stem Cell*, 2008, **3**, 136-146.
21. A. Solanki, J. D. Kim and K. B. Lee, *Nanomedicine*, 2008, **3**, 567-578.
22. B. Alberts, A. Johnson, J. Lewis, *et al.*, *Molecular Biology of the Cell*, Garland Science, New York, 4th edn., 2002.
23. C. Lalande, S. Miraux, S. M. Derkaoui, *et al.*, *Eur. Cells Mater.*, 2011, **21**, 341-354.
24. K. Montet-Abou, X. Montet, R. Weissleder, *et al.*, *Mol. Imaging* 2007, **6**, 1-9.
25. T. H. Kim, J. K. Kim, W. Shim, *et al.*, *Magn. Reson. Imaging*, 2010, **28**, 1004-1013.
26. C. C. Winterbourn, *Toxicol. Lett.*, 1995, **82–83**, 969-974.
27. G. Papanikolaou and K. Pantopoulos, *Toxicol. Appl.Pharmacol.*, 2005, **202**, 199-211.

28. W. Breuer, M. Shvartsman and Z. I. Cabantchik, *Int. J. Biochem. Cell Biol.*, 2008, **40**, 350-354.
29. N. Oh and J. Park, *Int. J. Nanomed.*, 2014, **9**, 51-63.
30. S. Salatin, S. Maleki Dizaj and A. Yari Khosroushahi, *Cell Biol. Int.*, 2015, **39**, 881-890.
31. C. Schweiger, P. Gil, W. Parak, *et al.*, *J. Con. Rel.*, 2010, **148**, e67-e68.
32. L. Dykman and N. Khlebtsov, *Chem. Soc. Rev.*, 2012, **41**, 2256-2282.
33. A. Liu and B. Ye, *Clin. Lab.*, 2013, **59**, 23-36.
34. R. A. Farrer, F. L. Butterfield, V. W. Chen, *et al.*, *Nano Lett.*, 2005, **5**, 1139-1142.
35. Z. Shuwen, Y. Ken-Tye, I. Roy, *et al.*, *Plasmonics*, 2011, **6**, 491-506.
36. A. Taylor, K. M. Wilson, P. Murray, *et al.*, *Chem. Soc. Rev.*, 2012, **41**, 2707-2717.
37. P. D. Jadzinsky, G. Calero, C. J. Ackerson, *et al.*, *Science* 2007, **318**, 430-433.
38. F. Xuening, J. Guozhi and W. Jun, *Chalcogenide Lett.*, 2010, **7**, 83-87.
39. I. L. Medintz, H. T. Uyeda, E. R. Goldman, *et al.*, *Nat Mater*, 2005, **4**, 435-446.
40. J. Drbohlavova, V. Adam, R. Kizek, *et al.*, *Int. J. Mol. Sci.*, 2009, **10**, 656-673.
41. T. Torchynska and Y. Vorobiev, *Advanced Biomedical Engineering*, InTech, 2011, ch. 9.
42. E. H. Sargent, *Adv. Mater.*, 2005, **17**, 515-522.
43. A. M. Derfus, W. C. W. Chan and S. N. Bhatia, *Nano Lett.*, 2004, **4**, 11-18.
44. G. B. Chavhan, *MRI Made Easy*, Anshan Ltd, UK, 2007.
45. N. Lee and T. Hyeon, *Chem. Soc. Rev.*, 2012, **41**, 2575-2589.
46. H. B. Na, I. C. Song and T. Hyeon, *Adv. Mater.*, 2009, **21**, 2133-2148.
47. R. C. Semelka and T. K. Helmberger, *Radiology*, 2001, **218**, 27-38.
48. Y. Jun, J. Lee and J. Cheon, *Angew. Chem. Int. Ed.*, 2008, **47**, 5122-5135.
49. B. J. McCullough, O. Kolokythas, J. H. Maki, *et al.*, *J. Magn. Reson. Imaging*, 2013, **37**, 1476-1479.
50. http://dailymed.nlm.nih.gov/dailymed/drugInfo.cfm?setid=32b0e320-a739-11dc-a704-0002a5d5c51b
51. J. W. Bulte and D. L. Kraitchman, *NMR Biomed.*, 2004, **17**, 484-499.

52. Y. X. Wang, *Quant. Imaging Med. Surg.*, 2011, **1**, 35-40.
53. R. Qiao, C. Yang and M. Gao, *J. Mater. Chem.*, 2009, **19**, 6274-6293.
54. D. Maity, D. C. Agrawal, D. Maity, *et al.*, *J. Magn. Magn. Mater.*, 2007, **308**, 46-55.
55. U. S. Rochelle M. Cornell, *The Iron Oxides: Structure, Properties, Reactions, Occurrences and Uses*, John Wiley & Sons, 2006.
56. E. Lima, A. L. Brandl, A. D. Arelaro, *et al.*, *J. Appl. Phys.*, 2006, **99**, 083908-083908-083910.
57. A. Abedini, A. R. Daud, M. A. Abdul Hamid, *et al.*, *PLoS One*, 2014, **9**, e90055.
58. G. F. Goya, T. S. Berquó, F. C. Fonseca, *et al.*, *J. Appl. Phys.*, 2003, **94**, 3520-3528.
59. S. Pal, P. Dutta, N. Shah, *et al.*, *IEEE Trans. Magn.*, 2007, **43**, 3091-3093.
60. B. H. Ong and N. K. Devaraj, *Advanced Structured Materials*, Springer-Verlag, Berlin Heidelberg, 2010, vol. 5, 375-393.
61. J. G. King, W. Williams, C. D. W. Wilkinson, *et al.*, *Geophys. Res. Lett.*, 1996, **23**, 2847-2850.
62. S. A. Rishton, Y. Lu, R. A. Altman, *et al.*, *Microelectron. Eng.*, 1997, **35**, 249-252.
63. S. Mathur, S. Barth, U. Werner, *et al.*, *Adv. Mater.*, 2008, **20**, 1550-1554.
64. R. Massart, *IEEE Trans. Magn.*, 1981, **17**, 1247-1248.
65. J.-H. Wu, S. P. Ko, H.-L. Liu, *et al.*, *Mater. Lett.*, 2007, **61**, 3124-3129.
66. Y. Amemiya, A. Arakaki, S. S. Staniland, *et al.*, *Biomaterials*, 2007, **28**, 5381-5389.
67. F. Vereda, B. Rodríguez-González, J. de Vicente, *et al.*, *J. Colloid Interface Sci.*, 2008, **318**, 520-524.
68. Y. B. Khollam, S. R. Dhage, H. S. Potdar, *et al.*, *Mater. Lett.*, 2002, **56**, 571-577.
69. F. Chen, Q. Gao, G. Hong, *et al.*, *J. Magn. Magn. Mater.*, 2008, **320**, 1775-1780.
70. J. Park, K. An, Y. Hwang, *et al.*, *Nat Mater*, 2004, **3**, 891-895.
71. S. Sun, H. Zeng, D. B. Robinson, *et al.*, *J. Am. Chem. Soc.*, 2004, **126**, 273-279.

72. G. M. da Costa, E. De Grave, P. M. A. de Bakker, *et al.*, *J. Solid State Chem.*, 1994, **113**, 405-412.
73. H. Itoh and T. Sugimoto, *J. Colloid Interface Sci.*, 2003, **265**, 283-295.
74. N. Enomoto, J.-i. Akagi and Z.-e. Nakagawa, *Ultrason. Sonochem.*, 1996, **3**, S97-S103.
75. F. Dang, N. Enomoto, J. Hojo, *et al.*, *Ultrason. Sonochem.*, 2009, **16**, 649-654.
76. T. González-Carreño, M. P. Morales, M. Gracia, *et al.*, *Mater. Lett.*, 1993, **18**, 151-155.
77. R. Strobel and S. E. Pratsinis, *Adv. Powder Technol.*, 2009, **20**, 190-194.
78. C. A. Eckert, B. L. Knutson and P. G. Debenedetti, *Nature*, 1996, **383**, 313-318.
79. U. T. Lam, R. Mammucari, K. Suzuki, *et al.*, *Ind. Eng. Chem. Res.*, 2008, **47**, 599-614.
80. M. Breulmann, H. Cölfen, H.-P. Hentze, *et al.*, *Adv. Mater.*, 1998, **10**, 237-241.
81. M. Abu Bakar and W. L. Tan, *J. Magn. Magn. Mater.*, 2007, **314**, 1-6.
82. G. Salazar-Alvarez, M. Muhammed and A. A. Zagorodni, *Chem. Eng. Sci.*, 2006, **61**, 4625-4633.
83. L. Cabrera, S. Gutierrez, N. Menendez, *et al.*, *Electrochim. Acta*, 2008, **53**, 3436-3441.
84. R. F. C. Marques, C. Garcia, P. Lecante, *et al.*, *J. Magn. Magn. Mater.*, 2008, **320**, 2311-2315.
85. K. B. Narayanan and N. Sakthivel, *Adv. Colloid Interface Sci.*, 2010, **156**, 1-13.
86. J. W. Moon, C. J. Rawn, A. J. Rondinone, *et al.*, *J. Ind. Microbiol. Biotechnol.*, 2010, **37**, 1023-1031.
87. U. Schwertmann and R. M. Cornell, *Iron Oxides in the Laboratory*, Wiley-VCH Verlag GmbH, 2007, 135-140.
88. J.-P. Jolivet, S. Cassaignon, C. Corinne, *et al.*, *J. Sol-Gel Sci. Technol.*, 2008, **46**, 299-305.
89. A. S. Teja and P.-Y. Koh, *Prog. Cryst. Growth Charact. Mater.*, 2009, **55**, 22-45.
90. X. Wang, J. Zhuang, Q. Peng, *et al.*, *Nature*, 2005, **437**, 121-124.

91. *Encyclopedia of Colloid and Interface Science*, ed. T. Tadros, Springer-Verlag, Berlin Heidelberg, 2013, 83-210.
92. A. H. Lu, E. L. Salabas and F. Schüth, *Angew. Chem. Int. Ed.*, 2007, **46**, 1222-1244.
93. K. Letchford and H. Burt, *Eur. J. Pharm. Biopharm.*, 2007, **65**, 259-269.
94. J. A. Dagata, N. Farkas, C. L. Dennis, *et al.*, *Nanotechnology*, 2008, **19**, 305101.
95. M. De Cuyper and M. Joniau, *Eur. Biophys. J.*, 1988, **15**, 311-319.
96. O. Veiseh, J. W. Gunn and M. Zhang, *Adv. Drug Deliver. Rev.*, 2010, **62**, 284-304.
97. C. Fang, N. Bhattarai, C. Sun, *et al.*, *Small*, 2009, **5**, 1637-1641.
98. C. Boyer, M. R. Whittaker, V. Bulmus, *et al.*, *NPG Asia Mater.* , 2010, **2**, 23-30.
99. E. Amstad, T. Gillich, I. Bilecka, *et al.*, *Nano Lett.*, 2009, **9**, 4042-4048.
100. A. K. Gupta and M. Gupta, *Biomaterials*, 2005, **26**, 3995-4021.
101. R. A. Sperling and W. J. Parak, *Philos. Trans. R. Soc. London, Ser. A*, 2010, **368**, 1333-1383.
102. N. Kohler, G. E. Fryxell and M. Zhang, *J. Am. Chem. Soc.*, 2004, **126**, 7206-7211.
103. B. Zargar, H. Parham and A. Hatamie, *Chemosphere*, 2009, **76**, 554-557.
104. Y. Zhang, N. Kohler and M. Q. Zhang, *Biomaterials*, 2002, **23**, 1553-1561.
105. R. De Palma, S. Peeters, M. J. Van Bael, *et al.*, *Chem. Mater.*, 2007, **19**, 1821-1831.
106. B. Arkles, *Chemtech*, 1977, **7**, 766-778.
107. G. T. Hermanson, *Bioconjugate Techniques (Second Edition)*, Academic Press, New York, 2008, 562-581.
108. M. van de Waterbeemd, T. Sen, S. Biagini, *et al.*, *Micro & Nano Letters*, 2010, **5**, 282.
109. A. v. Blaaderen and A. Vrij, *J. Colloid Interface Sci.*, 1993, **156**, 1-18.
110. T. Sen and I. J. Bruce, *Sci. Rep.*, 2012, **2**.
111. D. Rother, T. Sen, D. East, *et al.*, *Nanomedicine*, 2011, **6**, 281-300.
112. S. Minko, *Polymer Surfaces and Interfaces*, ed. M. Stamm, Springer Berlin Heidelberg, 2008, ch. 11, 215-234.

113. R. Barbey, L. Lavanant, D. Paripovic, *et al.*, *Chem. Rev.*, 2009, **109**, 5437-5527.
114. D. S. Achilleos and M. Vamvakaki, *Materials*, 2010, **3**, 1981-2026.
115. B. Zdyrko and I. Luzinov, *Macromol. Rapid Commun.*, 2011, **32**, 859-869.
116. J. Moraes, K. Ohno, T. Maschmeyer, *et al.*, *Chem. Commun.*, 2013, **49**, 9077-9088.
117. G. T. Hermanson, *Bioconjugate Techniques*, Academic Press, San Diego, 1996, 137-166.
118. V. Sreeja and P. A. Joy, *Int. J. Nanotechnol.*, 2011, **8**, 907-915.
119. R. Y. Hong, B. Feng, L. L. Chen, *et al.*, *Biochem. Eng. J.*, 2008, **42**, 290-300.
120. L. C. Fidale, M. Nikolajski, T. Rudolph, *et al.*, *J. Colloid Interface Sci.*, 2013, **390**, 25-33.
121. X. Yu, S. Tong, M. Ge, *et al.*, *J. Mater. Chem. A*, 2013, **1**, 959-965.
122. Z. Stephen, O. Veiseh and M. Zhang, *Adv. Polym. Sci.*, 2011, **243**, 163-184.
123. S. F. Shi, J. F. Jia, X. K. Guo, *et al.*, *Int. J. Nanomed.*, 2012, **7**, 5593-5602.
124. D. Dorniani, M. Z. Hussein, A. U. Kura, *et al.*, *Int. J. Mol. Sci.*, 2013, **14**, 23639-23653.
125. H. L. Ma, X. R. Qi, Y. Maitani, *et al.*, *Int. J. Pharm.*, 2007, **333**, 177-186.
126. H. L. Ma, Y. F. Xu, X. R. Qi, *et al.*, *Int. J. Pharm.*, 2008, **354**, 217-226.
127. Z. Cheng, Y. Dai, X. Kang, *et al.*, *Biomaterials*, 2014, **35**, 6359-6368.
128. B. Gaihre, M. S. Khil, D. R. Lee, *et al.*, *Int. J. Pharm.*, 2009, **365**, 180-189.
129. B. Gaihre, Y. Hee Lee, M. S. Khil, *et al.*, *J. Microencapsulation*, 2011, **28**, 240-247.
130. Z. Li, L. Qiang, S. Zhong, *et al.*, *Colloids Surf., A*, 2013, **436**, 1145-1151.
131. Y. Liang, L. Zhang, W. Li, *et al.*, *Colloid Polym. Sci.*, 2007, **285**, 1193-1199.
132. G. Marcelo, A. Muñoz-Bonilla, J. Rodríguez-Hernández, *et al.*, *Polym. Chem.*, 2013, **4**, 558-567.
133. M. Babic, D. Horák, M. Trchová, *et al.*, *Bioconjugate Chem.*, 2008, **19**, 740-750.
134. X. Wang, F. Wei, A. Liu, *et al.*, *Biomaterials*, 2012, **33**, 3719-3732.
135. S. Yu and G. M. Chow, *J. Nanosci. Nanotechnol.*, 2006, **6**, 2135-2140.
136. S. Tong, S. Hou, B. Ren, *et al.*, *Nano Lett.*, 2011, **11**, 3720-3726.
137. M. de Cuyper and M. Joniau, *Biotechnol. Appl. Biochem.*, 1992, **16**, 201-210.

138. E. K. Larsen, T. Nielsen, T. Wittenborn, *et al.*, *ACS Nano*, 2009, **3**, 1947-1951.
139. J. F. Lutz, S. Stiller, A. Hoth, *et al.*, *Biomacromolecules*, 2006, **7**, 3132-3138.
140. F. Hu, K. G. Neoh, L. Cen, *et al.*, *Biomacromolecules*, 2006, **7**, 809-816.
141. A. Vetter, A. Reinisch, D. Strunk, *et al.*, *J. Drug Targeting*, 2011, **19**, 562-572.
142. B. Cao, P. Qiu and C. Mao, *Microsc. Res. Tech.*, 2013, **76**, 936-941.
143. S. Y. Kim, B. Ramaraj and K. R. Yoon, *Surf. Interface Anal.*, 2012, **44**, 1238-1242.
144. M. Mahmoudi, A. Simchi, M. Imani, *et al.*, *J. Phys. Chem. B*, 2008, **112**, 14470-14481.
145. W. Lu, M. Ling, M. Jia, *et al.*, *Mol. Med. Rep.*, 2014, **9**, 1080-1084.
146. A. Masotti, A. Pitta, G. Ortaggi, *et al.*, *Magn. Reson. Mater. Phys., Biol. Med.*, 2009, **22**, 77-87.
147. A. M. Reddy, B. K. Kwak, H. J. Shim, *et al.*, *Contrast Media Mol. Imaging*, 2009, **4**, 118-126.
148. H. Huang, Q. Xie, M. Kang, *et al.*, *Nanotechnology*, 2009, **20**, 365101.
149. S. Douadi-Masrouki, B. Frka-Petesic, M. Save, *et al.*, *Polymer*, 2010, **51**, 4673-4685.
150. I. Garcia, A. Tercjak, N. E. Zafeiropoulos, *et al.*, *J. Polym. Sci., Part A: Polym. Chem.*, 2007, **45**, 4744-4750.
151. D. Kim, M. K. Yu, T. S. Lee, *et al.*, *Nanotechnology*, 2011, **22**, 155101.
152. H. Bao, Z. Chen, L. Kang, *et al.*, *Mater. Lett.*, 2006, **60**, 2167-2170.
153. R. Alwi, S. Telenkov, A. Mandelis, *et al.*, *Biomed. Opt. Express*, 2012, **3**, 2500-2509.
154. S. Santra, R. Tapec, N. Theodoropoulou, *et al.*, *Langmuir*, 2001, **17**, 2900-2906.
155. M. Abbas, B. P. Rao, V. Reddy, *et al.*, *Ceram. Int.*, 2014, **40**, 11177-11186.
156. C. S. Bell, S. S. Yu and T. D. Giorgio, *Small*, 2011, **7**, 1158-1162.
157. C. Hoskins, Y. Min, M. Gueorguieva, *et al.*, *J Nanobiotechnol*, 2012, **10**, 1-12.
158. M. Mandal, S. Kundu, S. K. Ghosh, *et al.*, *J. Colloid Interface Sci.*, 2005, **286**, 187-194.
159. Q. He, J. Liu and R. Hu, *Nanosci. Nanotechnol. Lett.*, 2013, **5**, 995-1001.

160. H. Heidari and H. Razmi, *Talanta*, 2012, **99**, 13-21.
161. H. Bae, T. Ahmad, I. Rhee, *et al.*, *Nanoscale Res. Lett.*, 2012, **7**, 44.
162. M. Sarno, C. Cirillo and P. Ciambelli, *Chem. Eng. J.*, 2014, **246**, 27-38.
163. R. G. Mendes, A. Bachmatiuk, A. A. El-Gendy, *et al.*, *J. Phys. Chem. C*, 2012, **116**, 23749-23756.
164. S. Laurent, D. Forge, M. Port, *et al.*, *Chem. Rev.*, 2008, **108**, 2064-2110.
165. R. P. Garay, R. El-Gewely, J. K. Armstrong, *et al.*, *Expert Opin. Drug Deliv.*, 2012, **9**, 1319-1323.
166. R. S. Molday and D. Mackenzie, *J. Immunol. Meth.*, 1982, **52**, 353-367.
167. P. Tartaj, M. P. Morales, S. Veintemillas-Verdaguer, *et al.*, *Handbook of Magnetic Materials*, ed. K. H. J. Buschow, Elsevier, 2006, vol. 16, ch. 5, 403-482.
168. H. Holthoff, A. Schmitt, A. Fernández-Barbero, *et al.*, *J. Colloid Interface Sci.*, 1997, **192**, 463-470.
169. C. Fournier, M. Leonard, I. Le Coq-Leonard, *et al.*, *Langmuir*, 1995, **11**, 2344-2347.
170. V. Cabuil, *Curr. Opin. Colloid Interface Sci.*, 2000, **5**, 44-48.
171. M. Carmen Bautista, O. Bomati-Miguel, M. del Puerto Morales, *et al.*, *J. Magn. Magn. Mater.*, 2005, **293**, 20-27.
172. K. Ohno, C. Mori, T. Akashi, *et al.*, *Biomacromolecules*, 2013, **14**, 3453-3462.
173. Q. L. Fan, K. G. Neoh, E. T. Kang, *et al.*, *Biomaterials*, 2007, **28**, 5426-5436.
174. K. Matyjaszewski and N. V. Tsarevsky, *Nat Chem*, 2009, **1**, 276-288.
175. P. Król and P. Chmielarz, *Prog. Org. Coat.*, 2014, **77**, 913-948.
176. J. K. Oh, D. J. Siegwart, H. Lee, *et al.*, *J. Am. Chem. Soc.*, 2007, **129**, 5939-5945.
177. W. A. Braunecker and K. Matyjaszewski, *Prog. Polym. Sci.*, 2007, **32**, 93-146.
178. P. B. Zetterlund, Y. Kagawa and M. Okubo, *Chem. Rev.*, 2008, **108**, 3747-3794.
179. M. F. Cunningham, *Prog. Polym. Sci.*, 2008, **33**, 365-398.
180. N. Tsarevsky, P. McCarthy, W. Jakubowski, *et al.*, *NSTI Nanotech*, 2008, **2**, 665-668.

181. http://www.sigmaaldrich.com/content/dam/sigma-aldrich/docs/SAJ/Brochure/1/controlled-radical-polymerization-guide.pdf
182. W. He, H. Jiang, L. Zhang, *et al.*, *Polym. Chem.*, 2013, **4**, 2919-2938.
183. J.-S. Wang and K. Matyjaszewski, *Macromolecules*, 1995, **28**, 7901-7910.
184. T. E. Patten and K. Matyjaszewski, *Adv Mater*, 1998, **10**, 901-+.
185. http://en.wikipedia.org/wiki/Atom-transfer_radical-polymerization#mediaviewer/File:ATRP_general.png
186. http://www.cmu.edu/maty/chem/fundamentals-atrp/
187. N. Hadjichristidis, S. Pispas and G. Floudas, *Block Copolymers: Synthetic Strategies, Physical Properties, and Applications*, John Wiley & Sons, Inc., Hoboken, USA, 2002, ch. 3.
188. W. A. Braunecker and K. Matyjaszewski, *Prog. Polym. Sci.*, 2007, **32**, 93-146.

2

Experimental

List of Figures

Figure 2.1. Schematic diagram of a TEM.[5] 49
Figure 2.2. GPC size separation and detection process.[6, 7] 51
Figure 2.3. (a) Front view of the NdFeB magnet and channel in which cells are suspended in for magnetic characterisation (b) variation of magnetic field and field gradient within the pole pieces and indicating the magnetic pole pieces that give rise to the spatially varying magnetic field gradient and (c) simplified schematic of the magnetophoresis equipment used to measure magnetic velocity of cells. 57
Figure 2.4. Cell tracking velocimetry (CTV) showing A) the fluorescent sensitive camera, B) the microscope, C) the magnet. Top right zoomed image of the magnet shows the hole where the glass capillary is placed and bottom right images show the front end of the magnet with cover slip removed to so the gap between the two fixed rare earth magnets can be seen. 58
Figure 2.5. Series of fluorescence images of cell nuclei using DAPI taken from (a) unlabelled cells and (b) labelled cells. For each example, three cells are highlighted to indicate the direction of motion. 58
Figure 2.6. Schematic representations for the setup of the photothermal imaging equipment as taken from reference[14] for the measurement of "(A) fluorescence and (B) photothermal imaging of SPIONs in cells. In (B), the heating laser (green) is modulated by an acousto-optical modulator at a frequency of 530.5 kHz; the green laser is blocked before the photodiode, which measures the signal of the probe (red) beam only. A lock-in amplifier is used to extract the magnitude of the signal at the beatnote frequency, which is digitised to yield the photothermal signal. The system is based upon a modified Zeiss Axiovert 200 inverted microscope equipped with a microscope cage incubator"..... 60
Figure 2.7. ^{1}H and ^{13}C NMR of *N*-succinimidyl-2-bromoisobutyrate (NSBriB) initator for ATRP. 68

List of Tables

Table 2.1. Summary of polymers synthesised by ATRP (to be used for amidation coupling reaction) and their respective reaction parameters. Where *NS* refers to the *N*-succinimidyl functional initiator used. 70

List of Schemes

Scheme 1. Synthesis of iron(III) oleate complex 65
Scheme 2. Synthesis of monodisperse iron oxide nanocrystals 65
Scheme 3. Ligand exchange reaction for the synthesis of amino silane coated SPIONs. 66
Scheme 4. Synthesis of *N*-succinimidyl-2-bromoisobutyrate (NSBriB) initator. 67
Scheme 5. ATRP of MPC using *N*-succinimidyl-2-bromoisobutyrate (NSBriB) initiator. 69
Scheme 6. Amidation reaction of *NS*-polymer with A-SPIONs. 71
Scheme 7. Synthesis of silica coated SPION by sol-gel Stöber method. 74
Scheme 8. Synthesis of gold coated amino silane SPIONs. 75
Scheme 9. Synthesis of Bis[2-(2'-bromoisobutyryloxy) ethyl] disulfide (BriBOEDS) ATRP initiator. 76
Scheme 10. Stabilisation of Au-SPIONs with thiol functionalised-pMPC polymer. 77

2.1 Materials

Sodium oleate (>97 %) was purchased from TCI. Gold (III) acetate (99.9 % metals basis) was purchased from Alfa Aesar. Toluene was pre-dried and purified *via* the solvent purification system Pure Solv MD-6 and stored over 3Å activated molecular sieves. All other reagents and solvents were obtained from Sigma-Aldrich and used without further purification unless stated. All aqueous solutions were prepared with ultrapure water from a Milli-Q system (Millipore, resistivity 18.2 MΩcm at 25 °C).

2.2 Characterisation Techniques

2.2.1 Dynamic Light Scattering (DLS)

Dynamic light scattering (DLS) was carried out using a Viscotek 802-100 Dynamic Light Scattering Analyser with 60 mW power class 3B laser with wavelength of 830 nm. The target intensity attenuation was set to 300 k counts and each measurement was collected from data gathered over a 4 second reading. At least 25 experiments of 5 runs each were recorded per sample measurement. Samples were run at 20 °C in the appropriate solvent. The refractive index of the solvent was imputed into the software prior to measurement. Measurements were processed using Malvern OmniSIZE software 3.0.

2.2.1.1 DLS Technique Used

The instrument used to carry out DLS measurements was set up whereby scattered light from a sample in the dispersion medium in the cuvette is detected at a right angle to the laser pathway. The measured data from the intensity of scattered light from a sample is shown as a correlation curve which holds information regarding the diffusion of particles in the solvent. The diffusion coefficient (D) can be calculated by fitting the correlation curve (or correlation function) to an exponential function. Using D, the hydrodynamic radius (R_h) can be calculated by using a variation of the Stokes-Einstein equation. If the sample population is monodisperse, a smooth single exponential decay function is observed. If the sample is polydisperse, the curve is a sum of exponential decays.

The DLS measurements are reported in terms of hydrodynamic radius (R_h) or solvodynamic radius (R_s) whereby the data is reported by three different distribution types: Intensity, Mass and Number. The fundamental outcome from the measurement is found as an intensity distribution. The intensity distribution shows the relative intensity of light scattered by particles of each size fraction. The intensity distribution can however be somewhat misleading, since particles suspended in liquid undergo random Brownian motion which is related to temperature, solvent viscosity and particle size. The smaller the particle, the faster the Brownian motion. The larger the particle, the slower the Brownian motion. Because of this, the

intensity of light scattered from larger particles is greater than that of smaller particles Thus, the presence of a small number of aggregates or larger particles in the sample can dominate the intensity distribution. The intensity distribution can therefore be useful as a sensitive measurement for detecting larger species in the sample. Assuming there is no error in the intensity distribution, the particles in the sample are spherical, homogeneous and the optical properties are known, the data from the intensity distribution can be used and converted using Mie Theory to a mass or volume distribution weighted by their relative mass/volume of the particle size fraction rather than based on their scattering (intensity). Furthermore, the intensity distribution can also be converted using Mie Theory to a number distribution based on the relative number of particles in the given size fraction.[1, 2]

2.2.2 Powder X-Ray Diffraction (PXRD)

Powder X-ray diffraction (PXRD) was carried out using a Panalytical X'pert Pro multipurpose diffractometer with Co Kα1 radiation (λ = 1.789010 Å). PXRD was used to determine the composition of nanoparticles (NPs) synthesised and to measure their average crystal size using the Scherrer equation, **Equation (1)**.

$$\tau = \frac{K\lambda}{\beta cos\theta} \qquad \textbf{(1)}$$

Where τ is the mean crystal size in nanometres (nm), β is the line broadening at half the maximum intensity (FWHM), K is the shape factor (K = 0.9 for particles of unknown size), λ is the x-ray wavelength of the cobalt source (Co, λ = 1.789010 Å) and θ is the Bragg diffraction angle. β and θ are converted into radians and λ is converted to nanometres. PXRD patterns were assigned using reference patterns obtained from the JCPDS database.

2.2.2.1 Wavelength Selection

Atoms of a particular element can absorb incident X-rays and fluoresce X-rays at a different wavelength. Fluorescence can lead to an increase in background signal and absorption of X-rays can decrease the diffracted signal thus causing inaccuracies to the measurements required to calculate crystal size using the Scherrer equation. The

most problematic combination is with a copper anode radiation source to measure Fe and Co which fluoresce the most. For this reason, a different wavelength of radiation was used to measure iron oxide nanocrystal sizes by PXRD. In this case a cobalt anode radiation source was used to increase the diffracted beam signal.[3]

2.2.3 Transmission Electron Microscopy (TEM)

Transmission electron microscopy (TEM) images were collected using a FEI 120kV Tecnai G2 Spirit BioTWIN TEM operating at an accelerating voltage of 100 kV. NP samples were dispersed and allowed to dry onto 200 mesh hexagonal copper grids with a carbon sputter coated Formvar or Piloform substrate. For staining of polymer coating, a 3 % solution of phosphotungstic acid (PTA) was used. Measurements of NP sizes were carried out using ImageJ software. For imaging NPs within stem cells, stem cells were grown and labelled in 3.5 cm dishes followed by fixation with 4 % formaldehyde/2.5 % glutaraldehyde. For viewing organelles within stem cells, stem cells were stained using 5 % uranyl acetate and 2 % lead citrate. Post fixation of cells was carried out by dehydration and embedding in epoxy resin. Thin (70 nm) sections were then taken and imaged over 200 mesh hexagonal copper grids with a Formvar substrate.

High resolution-TEM (HR-TEM), scanning-TEM (STEM) and high angle annular dark field electron energy loss spectroscopy (HAADF-EELS) measurements were carried out by Dr. Tobias Heil, Nanoinvestigation Centre, University of Liverpool.

2.2.3.1 Conventional Transmission Electron Microscopy (TEM) theory

TEM is a technique used to image the morphology of specimens on the nanoscale. Because electrons have a much lower wavelength than light, resolution is increased significantly due to strong interactions of electrons with atoms by elastic and inelastic scattering.[4] In TEM, electrons are produced by thermionic or field electron emission through the connection of an emission source such as tungsten filament or lanthanum hexaboride (LaB_6) cathode to a high voltage source (voltages 60-120 kV). Electrons are condensed and focused down a column held under vacuum using

electromagnetic lenses to produce an electron beam of uniform current density which irradiates a sample on the grid.

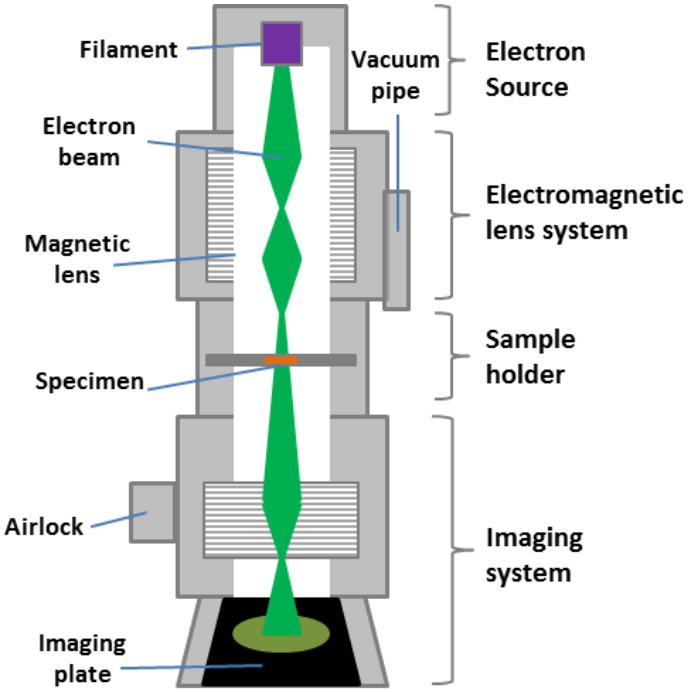

Figure 2.1. Schematic diagram of a TEM.[5]

The electron intensity distribution behind the sample grid is imaged using a lens system onto a phosphor fluorescent screen to create a "shadow image" which is then recorded by a charge-coupled device (CCD) camera. **Figure 2.1** shows a schematic of the components found within a conventional TEM instrument. The sample must be thin enough (< 200 nm) to visualise the specimen. For cellular and polymeric material which has very low electron density, imaging can be improved by increasing the contrast using a stain containing electron-absorbing heavy metals such as phosphotungstic acid, uranyl acetate etc.[5]

2.2.4 Fourier-Transform Infrared (FT-IR) Spectroscopy

Fourier-transform infrared (FT-IR) spectroscopy was carried out using a Bruker Tensor 27 plate reading FT-IR. Samples were prepared with KBr to form a pellet for single sample analysis. For each sample, a background was taken and subtracted from the accumulation of 20 scan measurements in the region from 650 to 4000 cm^{-1} with a resolution of 4 cm^{-1}.

2.2.5 Thermogravimetric Analysis (TGA)

Thermogravimetric analysis (TGA) was carried out using a TA Instruments Q5000IR TGA under air atmosphere at 100 mL/min. For samples not containing polymer, a 5-10 mg sample was heated to 120 °C at 10 °C/min and kept at 120 °C for 20 min to remove all adsorbed solvent. The sample was then heated to 600 °C at 10 °C/min and kept at 600 °C for 20 min. For samples containing polymer, a 5-10 mg sample was heated to 120 °C at 20 °C/min and kept at 120 °C for 20 min to remove all adsorbed solvent. The sample was then heated to 1000 °C at 20 °C/min and kept at 1000 °C for 40 min. The weight loss was calculated by using the weight measured between the maximum boiling point temperature of the solvent used with the material (toluene 120 °C, ethanol 80 °C) and the final TGA temperature. The residual solvent weight loss was used to scale the weight loss of the organic and inorganic content without the presence of residual solvent.

2.2.6 Gel Permeation Chromatography (GPC)

Gel permeation chromatography (GPC) was carried out using a Malvern Viscotek GPCmax 2001 triple-detection GPC system in either 10 % methanol in deionised water eluent at 50 °C or 1 x PBS pH 7.4 eluent at 50 °C. using polyethylene oxide (PEO) narrow and calibration standards. The columns used were two GMPW-XL18/19 plus guard using a flow rate of 1 ml/min. Measurements were performed by Dr. Sean Higgins at the University of Liverpool, Department of Chemistry.

2.2.6.1 GPC Theory

Gel permeation chromatography, a type of size exclusion chromatography (SEC), which is a technique used to sort polymers according to size in solution/hydrodynamic diameter. A solution containing polymers is passed through a column containing porous beaded packing material. The beads have a variety of pore sizes. Smaller MW polymers are retained for longer periods of time in small pores compared with larger MW polymers which are either retained for less time by the larger pores or are not retained at all and simply pass around the beads through the column. Due to this, separation of polymer molecules by size or MW occurs. Elution of polymers through the column occurs in the order of highest molecular weight first

and polymers with decreasing MW following after. **Figure 2.2** shows the separation process of polymers by size/hydrodynamic diameter. This technique is primarily used to obtain information on the molecular weight distribution (also known as the dispersity (Đ)) in addition to the determination of the number average molecular weight M_n and the weight average molecular weight M_w.

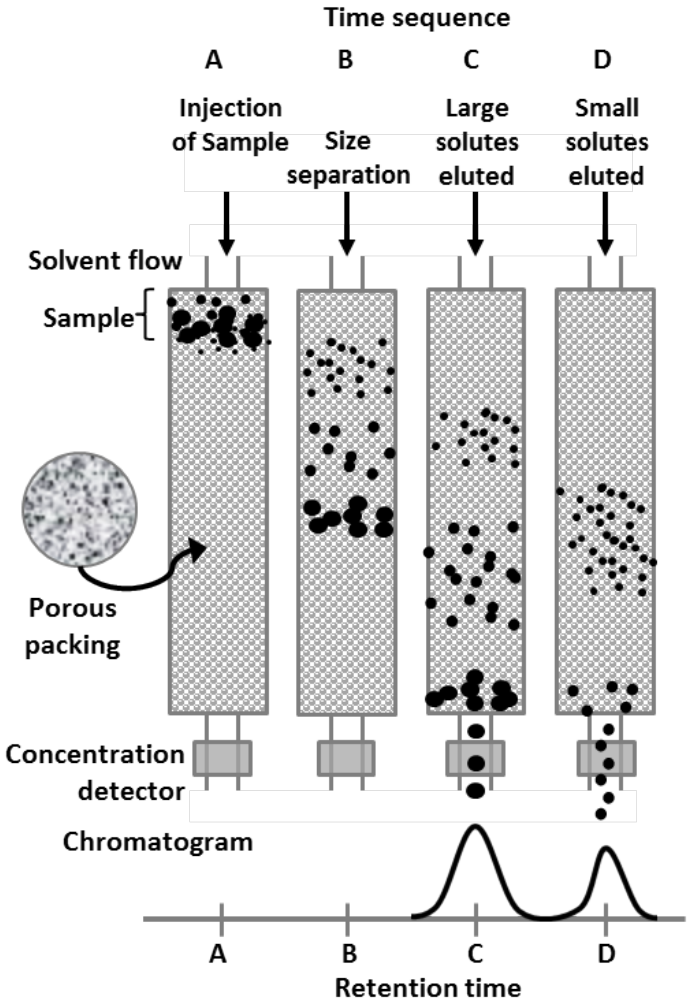

Figure 2.2. GPC size separation and detection process.[6, 7]

Before this information can be obtained for a polymer sample, experimental conditions including column and eluent choice, temperature, pH etc. need to be considered for a proper separation of the sample. To determine the M_w and M_n, polymer standards are required to calibrate the retention volume/time to polymer molecular weight/size. There are two types of calibration methods that can be carried out. The first is conventional calibration whereby a series of up to 12 polymers of known MW are used. This method requires use of only one detector (refractive index

(RI) or UV) to create a calibration curve using their peak positions along the retention volume axis.

Conventional calibration is often used on polymer samples where the polymer concentration in the sample is unknown - such as kinetic samples or polymers that are highly hydroscopic. The drawback of this approach is that the polymer standards used are often not an exact representative of the sample being measured (structure, type and their behaviour in the eluent conditions *i.e.* methacrylate polymers *vs.* linear PEO), so the MW data obtained is therefore only relative. In addition, no structural information of the polymer sample can be obtained from this method especially if analysing branched polymers.

The other main calibration method is based on a polymer narrow standard of known Đ, M_n, M_w, intrinsic viscosity (IV) and concentration with the use of three detection methods known as triple detection GPC, using low angle light scattering (LALS), right angle light scattering (RALS), RI or viscometer. Information obtained from triple detection GPC is considered more sensitive to the detection of structure and true MW of the polymer sample since at least four detection methods are used rather than only one detection method which is used for the conventional calibration method.[6, 7,8]

2.2.7 Nuclear Magnetic Resonance (NMR)

^{1}H and ^{13}C Nuclear Magnetic Resonance (NMR) was carried out using a Bruker Avance 400 MHz spectrometer. Chemical shifts were measured in parts per million (ppm) relative to residual protic solvent. Polymer samples for NMR analysis were prepared in either deuterated methanol (CD_3OD) or deuterated DMSO (DMSO-d6). NMR samples of small molecule initiators were prepared in deuterated chloroform ($CDCl_3$).

2.2.8 Micromass LCT Mass Spectroscopy (MS)

Micromass LCT mass spectroscopy was used to confirm the composition of initiators synthesised for ATRP reactions. Measurements were performed by the Analytical Services at the University of Liverpool, Department of Chemistry.

2.2.9 Inductively Coupled Plasma Optical Emission Spectrometry (ICP-OES)

Quantification of iron in samples containing gold

A known aliquot (100 to 200 µL) of NP dispersion was added to a 10 mL volumetric flask made of perfluoroalkoxy copolymer (Corning, Sigma-Aldrich). 5 mL of fresh aqua regia was added and the sample was left to digest for > 48 h. The volume was then made up to 10 mL with deionised water.

Quantification of iron oxide in samples analysed by SQUID

After SQUID measurement, the gelatine capsule containing a dry sample was placed into a 10 mL volumetric flask made of perfluoroalkoxy copolymer (Corning, Sigma-Aldrich). 5 mL of fresh aqua regia was added and the sample was left to digest for > 48 h. The volume was then made up to 10 mL with deionised water. A control blank containing an empty gelatine capsule digested in aqua regia solution was also analysed alongside the samples.

Quantification of iron in polymer coated SPION samples (not containing gold)

A known aliquot (100 to 200 µL) of NP dispersion was added to a 10 mL volumetric flask made of perfluoroalkoxy copolymer (Corning, Sigma-Aldrich). The volume in the flask was made up to 10 mL with 5 M HCl solution and left to digest > 24 h.

2.2.10 Elemental Analysis

The carbon, hydrogen and nitrogen content of samples were analyzed with a Thermo EA1112 Flash CHNS-O Analyzer. The measurement taken for the elemental content (%) was an average of four measurements. Measurements were performed by the Analytical Services at the University of Liverpool, Department of Chemistry.

2.2.11 Electrophoretic Mobility

Electrophoretic Mobility (ζ-Potential) measurements of SPION samples dispersed in deionised water or buffer solutions were measured using a Malvern Zetasizer Nano ZS equipped with a helium laser 633 nm wavelength at 25 °C. A 1 mL aliquot of

sample was used for measurement. The ζ-Potential values were obtained using the Henry equation by measuring the velocity of particles using Laser Doppler Velocimetry (LDV) during electrophoresis. The ζ-Potential values reported were taken from 3 independent measurements; for each measurement, 50 repeat runs were taken.

2.2.12 Differential Scanning Calorimetry (DSC)

Differential Scanning Calorimetry using a TA Instruments Q2000 DSC was used to measure the lower critical solution temperature (LCST) of polymer sample in solution. Polymer sample in solution (1 % w/v) was prepared in PBS solution with pH 7.4. Closed aluminium sample pan contained 100 µL of the polymer solution and reference pan containing 100 µL of the PBS solution were prepared. The samples were heated from 20 °C to 80 °C at a rate of 1 °C/min under nitrogen gas. Measurements were performed by Dr. Sean Higgins, Centre for Materials Discovery, University of Liverpool.

2.2.13 UV-Vis Spectroscopy

For colloidal stability studies, UV-Vis Spectroscopy was carried out on a Thermo 2000c Nanodrop UV-Vis spectrophotometer. The absorbance of SPIONs dispersed in PBS pH 7.4 was measured in a polypropylene cuvette with a path length of 1 cm. The sample volume used was ≥1 mL and was measured at a fixed wavelength of 400 nm. Samples were kept at their studied temperature between measurements.

For dissolution studies, UV-Vis Spectroscopy was carried out on a Biotek Synergy HT Multi-Mode 96 well micro titre plate reader. The sample volume used was ≥150 µL and measured at a fixed wavelength of 590 nm.

2.2.14 Magnetic Resonance Imaging (MRI)

Magnetic Resonance Imaging (MRI) measurements were carried out on a Bruker Avance III MR scanner at 7 Tesla. Prior to measurement, the Fe content was measured *via* ICP-OES. Samples were prepared in 1 % low melting temperature agarose with final concentrations of 0.25, 0.12 and 0.06 mM Fe. Imaging was carried out using a sequence based on RARe (Rapid Acquisition with Relaxation

Enhancement)[9] pulse sequence at base echo times TE = 11, 33, 55, 77 and 99 ms and at a repetition time TR = 5 s. Relaxation time T_2 was calculated based on an exponential fit of the signal intensity (S) as function of echo time (TE) using the following **Equation (2)**:

$$S = S_0 \exp\left(\frac{-TE}{T_2}\right) + S' \qquad \textbf{(2)}$$

Where: S_0 and S' are signal intensities at TE = 0 and infinity, respectively. The MRI measurements were performed by Ms Karen Davies at the University of Manchester, Department of Imaging Science and Biomedical Engineering.

2.2.15 Superconducting Quantum Interference Device (SQUID)

Superconducting quantum interference device (SQUID) magnetometry measurements were carried out on an MPMS SQUID 7T Quantum Design magnetometer. Samples were measured at 2 T under a helium atmosphere at 300 K. Samples were prepared as follows: dry samples (1-5 mg) were contained and fixed in a size 4 gelatin capsule which was then placed inside the middle of a plastic drinking straw. The SQUID measurements were performed by Dr. Pavel Borisov and Dr. Pranab Mandal at the University of Liverpool, Department of Chemistry. Help with the magnetic core characterisation using the Langevin expression was provided by Dr. Lara Bogart at the University of Liverpool, Institute of Integrative Biology.

2.2.15.1 Magnetic Core Characterisation

The magnetic size distribution of superparamagnetic NPs can be extracted from SQUID magnetisation curves by fitting experimentally measured curves using the simple Langevin expression modified by a log-normal distribution, **Equation (3)**. From this, extraction of the intracellular iron content from single cell magnetophoresis by cell tracking velocimetry can be achieved from the quantification of the magnetic radius of the iron oxide core.

Using room temperature SQUID magnetometry curves for iron oxide cores in samples, the best fit data of the magnetic radius can be extracted using the Langevin formula multiplied by the log-normal polydispersity function:

$$M(H) = \frac{M_{SP}}{\sqrt{2\pi}\,\sigma V}\exp\left(-\frac{\ln(V - V_c)^2}{2\sigma^2}\right)\left(\coth(b) - \frac{1}{b}\right) \quad \textbf{(3)}$$

Where M_{SP} and M_{SB} is the saturation magnetisation of the particles and of the bulk material, respectively in terms of volume by emu cm^{-1} Fe_3O_4, σ is the standard deviation of the population, *V* is the median physical volume, *Vc* is the volume of the magnetic core and the term *b* is given by **Equation (4)**:

$$b = \frac{\mu_0 \mathrm{M}_{SB} VH}{\mathrm{k_B} T} \quad \textbf{(4)}$$

2.2.16 Atomic Force Microscopy (AFM)

Atomic force microscopy measurements were collected in a Multimode atomic force microscope from Agilent. Samples were prepared by depositing a drop of NP solution from the appropriate solvent onto a clean Si wafer which was then allowed to air dry.

A μmasch/MikroMasch NSC15 LS15 hard Al BS long scanning SPM probe with tip radius with coating of <20 nm and tip cone angle of 40° (resonant frequency 325 kHz and a force constant 46 N/m) was used for tapping-mode in air at room temperature at a scan speed of 1ln/s.

Images were recorded with 512 x 512 pixel camera. Processing and analysis of the images were carried out using the PicoImage Software. Measurements were obtained using PicoView1.10.7. The AFM measurements were performed by Dr Natasha Flack at the University of Liverpool, Department of Chemistry.

2.2.17 Cell Tracking Velocimetry (CTV)

CTV measurements and analysis were prepared and performed by Dr. Lara Bogart at the University of Liverpool, Institute of Integrative Biology. Cells were first trypsinised and fixed with 4% paraformaldehyde for 10 minutes and then finally washed with PBS to remove excess fixative[10] before staining with 4′,6-diamidino-2-phenyindole, dilactate (DAPI), a fluorophore that intercolates with DNA (DAPI-DNA complex, λ_{ex} = 364 nm, λ_{em} = 454 nm)[11], to visualize the cell nucleus. The

cells were then suspended in a 30 % w/v glycerol solution and inserted into a square silicon borate glass capillary tube (I.D. 1 mm; CM Scientific). The capillary tube was then placed in a custom designed NdFeB magnet (acquired from/collaboration with Jeffrey J. Chalmers) with specially shaped pole pieces that yield a magnetic field gradient. The magnetic force generated by the magnetic field allowed for cells labeled with magnetic NP to move toward areas of high magnetic field with a velocity directly proportional to the number of magnetic NPs within the cell. Fluorescent cells were imaged using an Andor Neo sCMOS camera. The equipment was set up as found in **Figure 2.3C** and **Figure 2.4**.

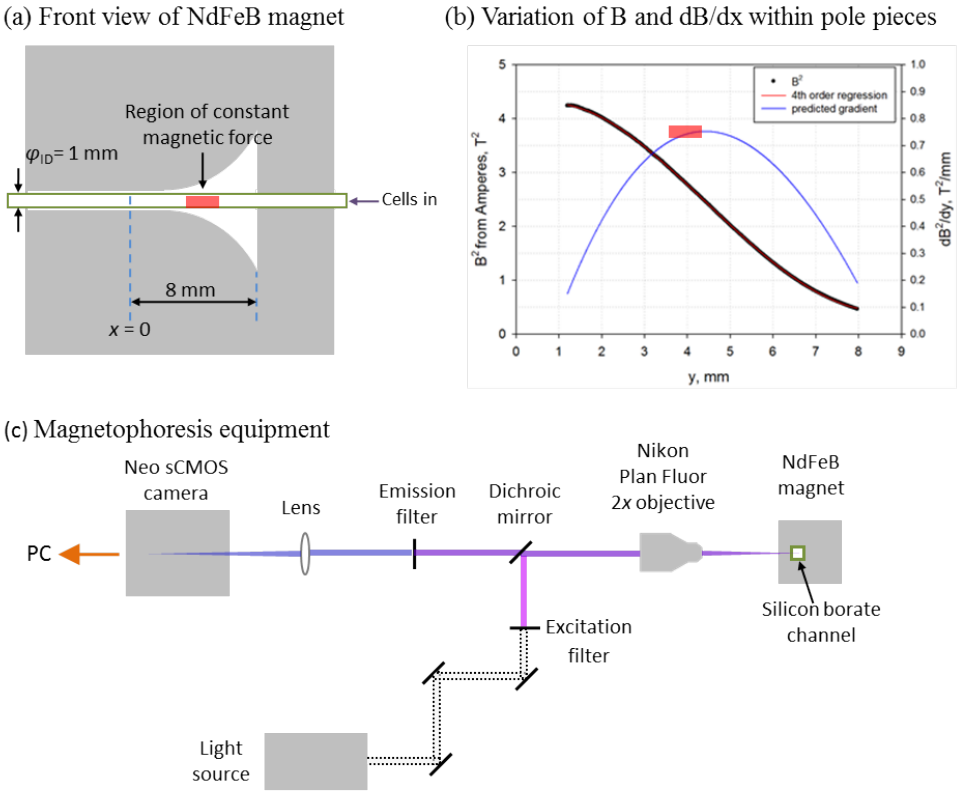

Figure 2.3. (a) Front view of the NdFeB magnet and channel in which cells are suspended in for magnetic characterisation (b) variation of magnetic field and field gradient within the pole pieces and indicating the magnetic pole pieces that give rise to the spatially varying magnetic field gradient and (c) simplified schematic of the magnetophoresis equipment used to measure magnetic velocity of cells.

Captured images were visualised by Solis imaging software, **Figure 2.5**. Cell trajectory plots within the area of uniform magnetic field gradient (**Figure 2.3**a) were drawn using ImageJ software with MTrack2 plugin. The horizontal component

of the velocity of cells through the capillary could then be measured using the co-ordinates (x,y) and the frame rate of each cell (**Figure 2.5**) to calculate the magnetic velocity, υ_m.

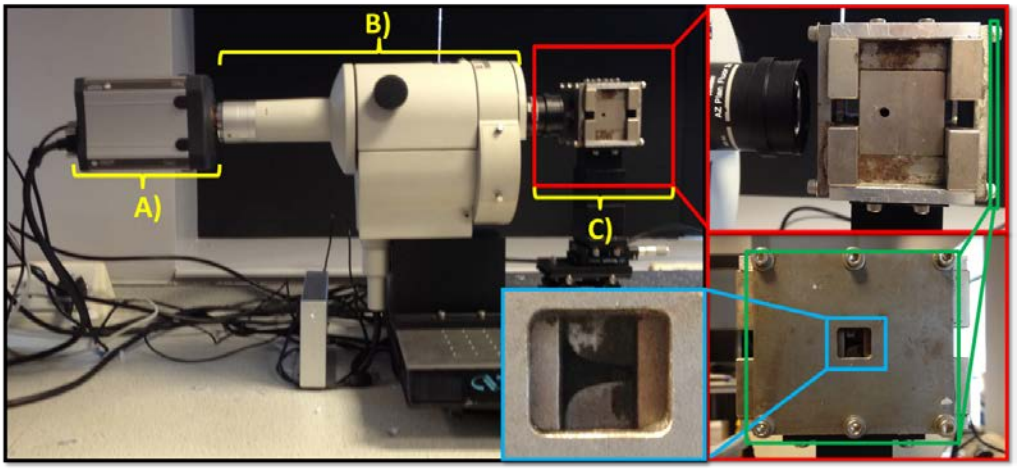

Figure 2.4. Cell tracking velocimetry (CTV) showing A) the fluorescent sensitive camera, B) the microscope, C) the magnet. Top right zoomed image of the magnet shows the hole where the glass capillary is placed and bottom right images show the front end of the magnet with cover slip removed to so the gap between the two fixed rare earth magnets can be seen.

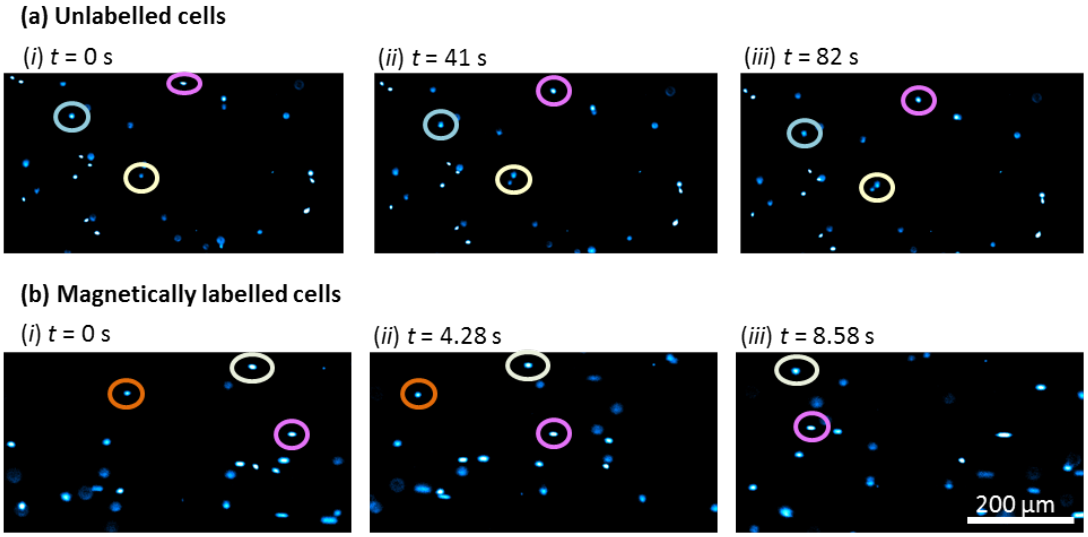

Figure 2.5. Series of fluorescence images of cell nuclei using DAPI taken from (a) unlabelled cells and (b) labelled cells. For each example, three cells are highlighted to indicate the direction of motion.

A mean magnetic velocity over a population (n = 200 cells minimum) was then used with the magnetic saturation (M_s) of the SPION sample (emu g^{-1} Fe_3O_4 or $1x10^3$

$A.m^2/kg$ Fe_3O_4), to calculate the average amount of magnetic material internalised within the cell using **Equation (8)**. At uniform magnetic field gradient, the magnetic force (F_m), **Equation (5)**, which is equal to the drag force (F_{stokes}) as found in **Equation (6)** of a cell containing magnetic NPs, **Equation (7)**. Hence, to deduce the number of magnetic NPs (N_m) in a cell, the magnetic velocity as deduced in **Equation (8)** is used and rearranged as found in **Equation (9)**:

$$F_m \propto N_m(M_s r^3)\frac{\partial B}{\partial x} \quad \textbf{(5)}$$

$$F_{stokes} = 6\pi r_{cell}\eta.\upsilon_m \quad \textbf{(6)}$$

$$F_m = F_{stokes} \quad \textbf{(7)}$$

$$\upsilon_m = \frac{2}{9}\frac{N_m.M_s {r_m}^3}{\eta r_{cell}}\frac{\partial B}{\partial x} \quad \textbf{(8)}$$

$$N_{\mathrm{m}} = \frac{9\upsilon_{\mathrm{m}}.r_{cell}\eta M_{SB}}{2M_{SB}r_m^3\,\partial B/\partial x} \quad \textbf{(9)}$$

Where B is the magnetic field; $\partial B/\partial x$ is the magnetic field gradient, N_m is the number of magnetic NPs, r_m is the radius of the magnetic NP, r_{cell} is the average cell radius, m and η is the viscosity of the suspending fluid.[12, 13]

2.2.18 Photothermal Microscopy

Photothermal imaging is a technique used to investigate the intracellular localisation of SPIONs. In a typical photothermal imaging experiment, a low powered laser is emitted onto a dish containing labelled cells. The NPs present inside the cell will conduct heat which is generated by the laser. The small difference in heat compared to the surrounding area of the cells in the dish is imaged using a heat sensitive infrared camera and thus allows for the visualisation of NPs inside the cell. **Figure 2.6** outlines the setup for the photothermal imaging equipment.

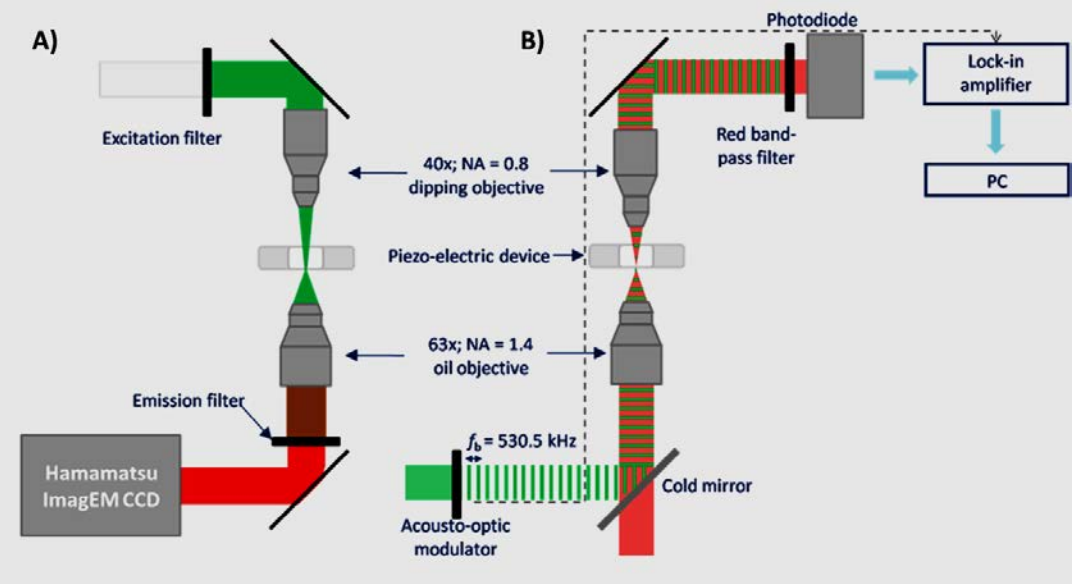

Figure 2.6. Schematic representations for the setup of the photothermal imaging equipment as taken from reference[14] for the measurement of "(A) fluorescence and (B) photothermal imaging of SPIONs in cells. In (B), the heating laser (green) is modulated by an acousto-optical modulator at a frequency of 530.5 kHz; the green laser is blocked before the photodiode, which measures the signal of the probe (red) beam only. A lock-in amplifier is used to extract the magnitude of the signal at the beatnote frequency, which is digitised to yield the photothermal signal. The system is based upon a modified Zeiss Axiovert 200 inverted microscope equipped with a microscope cage incubator".

Photothermal microscopy measurements were prepared and performed by Dr. Lara Bogart at the University of Liverpool, Institute of Integrative Biology. Imaging of SPIONs within stem cells were carried out on stem cells that were first fixed with 4% paraformaldehyde for 10 minutes and then finally washed with PBS to remove excess fixative prior to imaging The procedures for this technique can be found as reported.[14] "For imaging SPIONs in fixed cells, the sample in a glass dish was heated using a Laser Quantum ND:YAG frequency-doubled laser pump beam ($\lambda_{heating}$ = 523 nm) which was modulated at a frequency of 530.5 kHz by an acousto-optic modulator (Isomet Corporation) and set to a power of 2 mW. The local change in refractive index around the SPIONs was probed by a JDS Uniphase Corporation HeNe laser, (λ_{probe} = 633 nm). Both laser beams were focused to the same focal plane within the sample using a Zeiss Plan Apochromat 63×, NA = 1.4 oil objective lens. A Zeiss Achroplan 40×, NA = 0.8 water dipping objective was used to collect the forward interfering beam after its interaction with the sample. For cell sections, a Zeiss EC Plan-NEOFLUAR 40×, NA = 1.3 oil objective was used."

"All photothermal images were acquired 1 μm above the top surface of the glass bottom dish. The area of interest was raster scanned by moving a piezo-electric device (Physik Instrument) over the fixed laser beams, with the collected light focused onto a photodiode. For each pixel, the magnitude of the probe beam forward interfering field at 530.5 kHz was extracted using a lock-in amplifier and digitized, with the image constructed by integrating the signal in each pixel over a time of 10 ms."

For polymer coated SPIONs and silica coated SPIONs, a heating power (green laser) of 2 mW and a probe power (red laser) of 9.8 mW was used.

In the case of the Au-SPIONs, the fluorescence images were obtained using a Hammamastu camera illuminated with an X-Cite mecury lamp source. The DAPI images were obtained using a 1s exposure, whilst the immunostaining of the lysosomes was imaged using a 2s exposure. The colour image was performed using a ThorLabs camera. The photothermal image was obtained using a heating power (green laser) of 1 mW and a probe power (red laser) of 9.8 mW.

2.3 Protocols and Assays used Throughout the Thesis

2.3.1 Colorimetric Iron Quantification Assay

2.3.1.1 Stability of SPIONs in a Model of Lysosomal Environment

Measurements were performed by the author and by Dr Arthur Taylor at the University of Liverpool, Institute of Translational Medicine. The rate of degradation of NPs in a model lysosomal environment was based on procedures that have been previously described.[15, 16] NPs (5 μg Fe) were added to buffers at physiological or acidic pH and incubated at 37 ^{o}C for up to 40 days depending on the time taken to reach full dissolution of the iron core in solution. Alongside the samples incubated was a separate blank (0 μg Fe) and internal standard (5 μg Fe) in buffer solution at known pH. The buffers consisted of PBS supplemented with 20 mM of sodium citrate at a pH of 7.14, 5.5 or 4.5, the last two adjusted with hydrochloric acid. For each time point, a sample was taken for measurement of free iron ions in solution. The measurement was carried out by adding 20 % volume of a freshly prepared colorimetric reagent solution consisting of FerroZine (also known as 3-(2-Pyridyl)-

5,6-di(2-furyl)-1,2,4-triazine-5′,5″-disulfonic acid disodium salt) (6.5 mM) and ascorbic acid (10 mM).[17] After colour development for 30 minutes, the sample was transferred to a 96-well plate and the absorbance at 590 nm was measured by a microplate reader. The absorbance value was compared to that of a calibration curve obtained from serial dilutions of an iron standard (TraceCERT, Sigma) containing an additional 20 % volume of the colorimetric reagent. The concentration of free Fe obtained from each sample at a known time point was normalized to the amount of particles (Fe) added to each tube (5 µg Fe) yielding the percentage dissolved fraction. Three aliquots were taken from the blank, the internal standard, the calibration standards and all samples ran at each time point to yield an average measurement. For samples containing gold, a UV-Vis background absorbance measurement of the sample in buffer solution at known pH plus an additional 20 % volume of the buffer solution was taken at 590 nm and subtracted from the absorbance of the sample containing FerroZine colorimetric reagent prior to the calculation of free Fe in solution. The Fe concentration of the original samples was determined *via* ICP-OES prior to starting the dissolution assay to ensure 5 µg Fe mL^{-1} solutions were used.

2.3.1.2 Protocol for Iron Measurement in SPION Samples

Measurements were performed by the author and by Dr Arthur Taylor at the University of Liverpool, Institute of Translational Medicine. This protocol was used as an alternative method to ICP-OES analysis in order to quickly measure the iron concentration of polymer coated SPION samples. A freshly prepared FerroZine colorimetric reagent was first prepared which consisted of the following reagents added to deionised water (12.5 mL) in the following order with sufficient vortexing after each addition until dissolved: ammonium acetate (4.8 g, 5 M), ascorbic acid (4.4 g, 2 M), Ferrozine (40 mg (pre-dissolved in 500 µL of deionised water), 6.5 mM) and finally neocuproine (40 mg (pre-dissolved in 500 µL of ethanol), 13.1 mM). The FerroZine colorimetric reagent had a shelf life up to 3-6 weeks and was protected from light. Samples were prepared for digestion by adding 10-50 µl of SPION sample (the iron concentration of the original SPION sample should be between 0 and 1.5 µl) to a vial containing 1.2 M HCl (500 µL). The sealed sample vial was then heated to 50 °C for 1 h to speed up digestion. Once cooled, deionised

water (500 µL) was then added to the sample vial. The measurement was carried out by adding 20 % volume FerroZine colorimetric reagent (200 µL) to the sample vials containing digested SPIONs. After colour development for 30 minutes, the sample was transferred to a 96-well plate and the absorbance at 590 nm measured in a microplate reader. The absorbance value was compared to that of a calibration curve obtained from serial dilutions using 0.6 M HCl with an iron standard (TraceCERT, Sigma-Aldrich) containing an additional 20 % volume of the FerroZine colorimetric reagent. Three aliquots were taken from the blank, the calibration standards and all samples to yield an average measurement.[17]

2.3.2 *In Vitro* Studies

All *in vitro* studies were performed by Dr Arthur Taylor at the University of Liverpool, Institute of Translational Medicine. Kidney-derived murine stem cells[18] and mesenchymal stem cell lines were used for uptake and cytotoxicity studies. Cells were cultured in Dulbecco's modified Eagle's medium (DMEM) supplemented with 10 % fetal bovine serum (FBS; PAA), 1 % L-glutamine and 100 U mL^{-1} of penicillin and streptomycin. In all cases, cells were grown under standard culture conditions (37 °C, 5 % CO_2). All experiments involving KSC H6 were performed with cells between passage number of 10 and 30. Experiments using MSC D1 were performed with cells between passage number of 8 and 25. Cells were cryopreserved at their earliest passage number (10, 8), thus no cells at an earlier passage were used. At the later passage number (30, 25), these cells were known to preserve their stem cell like characteristics and had not undergone any phenotypic changes as a consequence of prolonged culture.

2.3.2.1 Cell Cytotoxicity/Viability Assay

For cytotoxicity screening of NP samples in a biocompatible solution, cells were seeded in 96 well plates and allowed to grow overnight. The culture medium was then replaced with fresh medium containing the NPs at a range of concentrations (0-50 µg Fe mL^{-1}) and the cells were allow to grow for a further 24 hours. The wells were then washed with PBS to remove excess NPs and replaced with fresh medium containing cell counting kit 8 (CCK-8) reagent (2-(2-methoxy-4-nitrophenyl)-3-(4-nitrophenyl)-5-(2,4-disulfophenyl)-2H-tetrazolium,monosodium salt) according the

manufacturer's specifications.[19] After 2 hours, the absorbance of each well was measured by a UV-Vis microplate reader at 450 nm, where the absorbance intensity at this wavelength is directly proportional to the number of viable cells in the well. Experiments were performed in triplicate and results were normalised to control conditions (cells that were not exposed to NPs). A negative control where cells were exposed to 0.1 % Triton-X instead of the NPs was used in each experiment.

2.3.2.2 Cell Uptake

Cells were sub-cultured in 3.5 cm dishes at a density that yielded 40-50% confluence on the following day. At this time point, the culture medium was replaced with fresh medium containing the NPs at a concentration of 5-50 µg Fe mL^{-1} and cells were allowed to grow for a further 24 hours.

After the incubation period, cells were washed twice with phosphate buffered saline (PBS) to remove excess SPIONs from the medium, fixed with 4% paraformaldehyde for 10 minutes and then finally washed with PBS to remove excess fixative. For imaging NPs taken up by cells those were stained with the Iron Stain Kit (Sigma Aldrich), which consists of a Prussian Blue staining for iron deposits and a Pararosaniline counterstain, followed by image acquisition under an optical microscope.

For staining of gold in cells, a silver enhancement kit (Sigma Aldrich) was used. Cells were labelled and fixed with 4% paraformaldehyde for 10 minutes and then finally washed with PBS to remove excess fixative and then the protocol for silver enhancement as per manufacturer's instructions were followed.[20]

2.4 Synthetic Material used Throughout the Thesis

2.4.1 Synthesis of Monodisperse oleic acid coated Magnetite SPIONs (Fe_3O_4) by Thermal Decomposition Reaction

2.4.1.1 Preparation of Iron(III) Oleate Complex

Iron(III) chloride hexahydrate ($Fe_3Cl_3.6H_2O$) (10.8 g, 40 mmol) and sodium oleate (36.5 g (120 mmol)) were dissolved in a solvent mixture of deionised water (60 mL),

ethanol (80 mL) and hexane (140 mL). The mixture was heated under reflux at 70 °C for 4 hours. **Scheme 1**outlines the synthesis procedure.

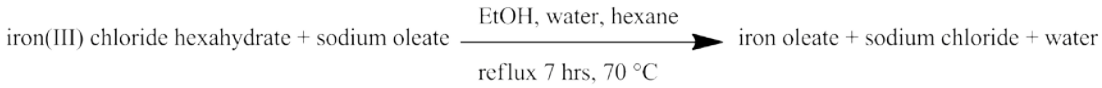

Scheme 1. Synthesis of iron(III) oleate complex

The resulting upper dark red organic layer containing iron(III)-oleate was washed three times with 30 mL deionised water in a separating funnel. The remaining organic layer was dried over anhydrous magnesium sulphate and hexane removed via rotary evaporation. FT-IR (KBr pellet) ν: 722, 1302, 1441, 1526, 1586, 1712, 2854, 2925 and 3006 cm^{-1}. Elemental analysis: expected C 72.05 %, H 11.08 %, actual C 70.73 %, H 11.69 %. TGA analysis: expected 91.14 %, actual 91.37 %.

2.4.1.2 Thermal Decomposition of Iron(III) Oleate to Synthesise Monodisperse Oleic Acid Coated SPIONs (OA-SPIONs)

Monodisperse oleic acid coated iron oxide NPs were synthesised as reported.[21] 7.0 g (8 mmol) of the iron-oleate complex synthesised as described above and 1.10 g of oleic acid (4 mmol) were dissolved in 38.88 g of 1-octadecene at room temperature. The reaction mixture was heated to 320 °C maintaining a heating rate of 3.3 °C min^{-1}, and then kept at 320 ^{o}C for 30 minutes. **Scheme 2** outlines the synthesis procedure.

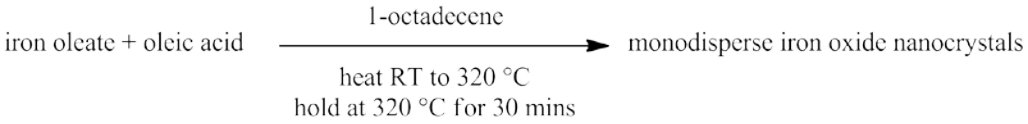

Scheme 2. Synthesis of monodisperse iron oxide nanocrystals

The resulting solution was then cooled to room temperature, and 100 mL of ethanol was added to the black solution to precipitate the oleic acid coated iron oxide NPs. The NPs were separated using a NdFeB magnet (Magnet Sales; size, 10 mm D 5 mm H; strength ~1.18 T) and stored as a solution of known concentration in chloroform in the fridge. Material submitted for characterisation using SQUID, FT-IR, TEM, DLS, PXRD, TGA and CHN. Results for all batches discussed in Chapters 3-5.

2.4.2 Ligand Exchange Reaction of OA-SPIONs with (3-amino)propyltrimethoxysilane (APTMS) to form Amino Silane Coated SPIONs (A-SPIONs).

In a 100 mL round bottom flask, dried toluene (114 mL (filled to this volume to remove excess air space), dried over 4Å molecular sieves) and dried oleic acid coated iron oxide NPs (50 mg by inorganic iron oxide mass) was added. The round bottom flask was then sealed using an air tight rubber suba seal and the air space above the solvent in the flask replaced by nitrogen. The sealed flask was then sonicated using an ultrasonic bath (Fisher Scientific, model FB15051, frequency = 30-40 kHz) for 5 minutes to ensure NPs were fully dispersed in the solvent. To this, 3-aminopropyltrimethoxysilane (APTMS) (320 µL, excess) was then injected into the sealed flask during another minute of sonication. The flask was then left to mix using a rotary mixer for a period of one week at 22 °C with a daily sonication for one minute. **Scheme 3** outlines the synthesis procedure. After this time, the solid was recovered using a NdFeB rare earth magnet. The supernatant was then decanted and the particles washed three times *via* sonication for one minute and centrifuged at 2,907 G for 5 minutes with 40 mL aliquots of toluene followed by three times *via* sonication for one minute and centrifugation at 7,441 G for 10 minutes with 15 mL aliquots of ethanol.

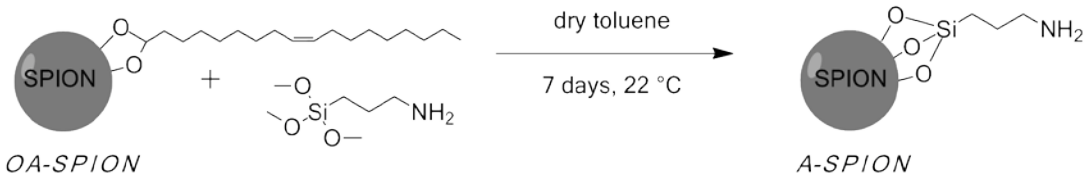

Scheme 3. Ligand exchange reaction for the synthesis of amino silane coated SPIONs.

The particles were then re-suspended in the appropriate amount of ethanol for storage at a concentration of 2 mg mL^{-1}. A dry sample of A-SPIONs was prepared for elemental and thermogravimetric analysis (TGA) by removing ethanol *via* rotary evaporation from a 5 mL sample which was then dried in the oven at 70 °C for 2 hours. Material submitted for characterisation using FT-IR, TEM, DLS, PXRD, TGA and CHN. Zeta potential measurements of the amino silane coated SPIONs (A-

SPIONs) in DIW and PBS pH 7.4 found as +25.6 ± 0.4 mV and +15.3 ± 0.8 mV respectively. Further results are discussed in Chapters 3 and 5.

2.5 Chapter 3 Experimental Procedures

2.5.1 Synthesis of *N*-succinimidyl-2-bromoisobutyrate Initiator for ATRP

In a 1 L round bottom flask, dry dichloromethane (DCM, 500 mL) was added and cooled to 0 °C under a nitrogen atmosphere. Under magnetic stirring, *N*-hydroxysuccinimide (NHS, 2.980 g, 26 mmol) and triethylamine (TEA, 7.1 mL, 51 mmol) were added. The mixture was left to stir under nitrogen until all the NHS had dissolved. 2-Bromoisobutyryl bromide (3.60 mL, 29 mmol) was then added to the mixture dropwise and the mixture was left to mix overnight and warm to room temperature. **Scheme 4** outlines the synthesis procedure. The TEA salts were filtered from the mixture and the remaining organic solution washed with 0.1 M HCl and 0.1 M Na_2CO_3 solutions. The DCM was then removed *via* rotary evaporation to leave an oil which was then precipitated using cold hexane. A fluffy cream solid was obtained and dried in a vacuum desiccator overnight.[22]

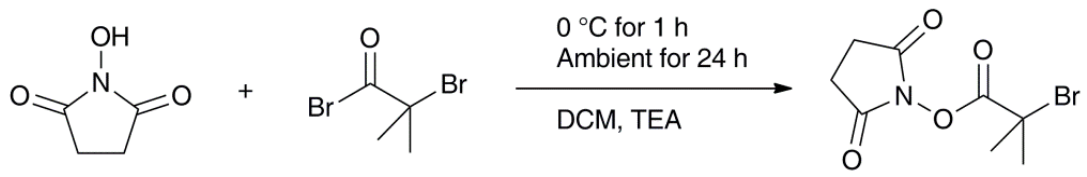

Scheme 4. Synthesis of *N*-succinimidyl-2-bromoisobutyrate (NSBriB) initator.

The structure and purity of the final product was confirmed by ^{1}H-NMR, ^{13}C-NMR and mass spectrometry, **Figure 2.7**. Chemical yield ~5 g (90 %). ^{1}H-NMR (400 MHz, chloroform-*d*, ppm): δ 2.2 (s, 6 H, CH_3), 2.9 (s, 4 H, CH_2). ^{13}C-NMR (100 MHz, chloroform-*d*, ppm): δ 168.9, 167.9, 31.1, 26.0. Elemental Analysis: expected C 36.39%, H 3.82%, N 5.30%, actual C 36.38%, H 3.81%, N 5.29%. Micromass LCT mass spectrometry expected (found): 264.07 g mol^{-1} (264.0 g mol^{-1}).

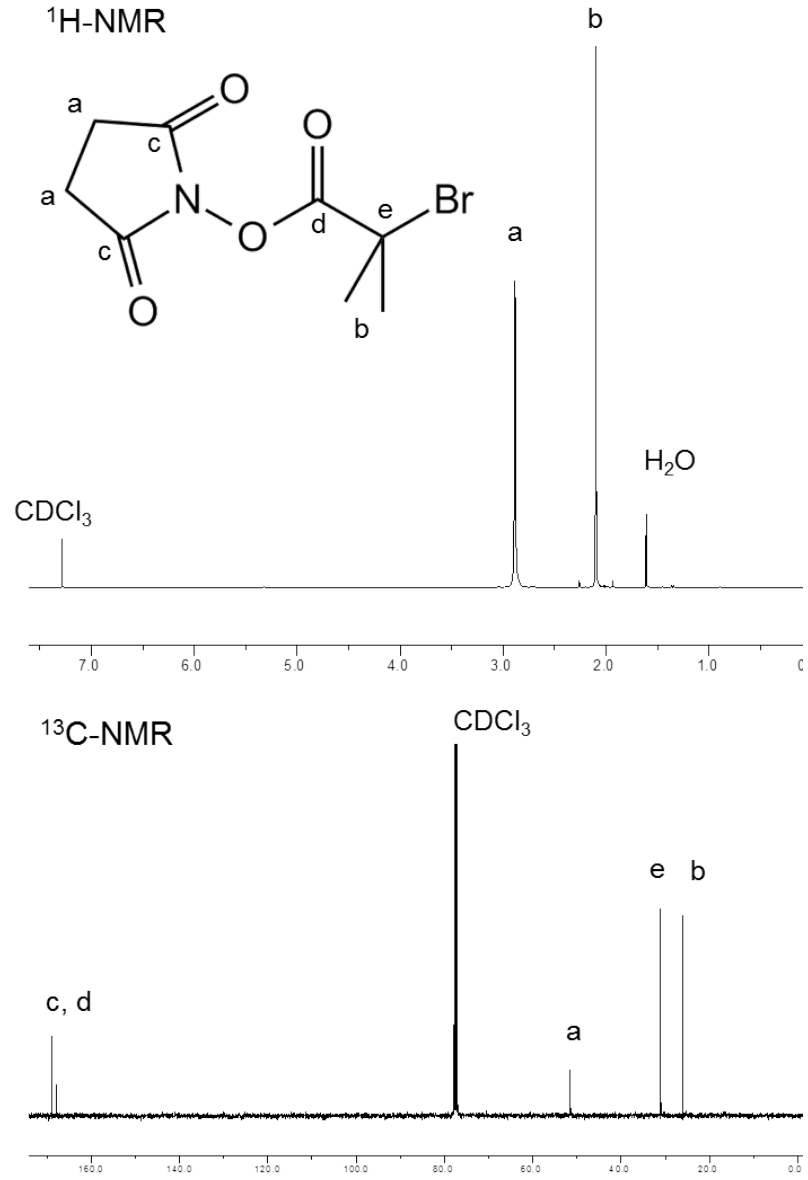

Figure 2.7. ^{1}H and ^{13}C NMR of *N*-succinimidyl-2-bromoisobutyrate (NSBriB) initator for ATRP.

2.5.2 Atom Transfer Radical Polymerisation (ATRP) of 2-methacryloylethyl phosphorylcholine (MPC) Using *N*-succinimidyl-2-bromoisobutyrate (NSBriB) Initiator

The ATRP reaction was carried out using molar ratios of [MPC]/[NSBriB]/[CuCl]/[bipy] = DP_n:1:1:2.1 in a solvent mixture ratio 2:3 (v/v) of methanol/DMSO. In a dry 100 mL round bottom flask, MPC monomer (5.00 g, DP_n equiv) was dissolved in degassed methanol (9.0 mL) over ice. In a separate flask, NSBriB initiator (1 equiv) was dissolved in DMSO (13.5 mL) with bipy ligand (2.1

equiv) and Cu(I)Cl (1 equiv). After purging both flasks with nitrogen for 30 min, the initiator/catalyst mixture in DMSO was added to the stirred MPC solution under nitrogen at 22 °C. **Scheme 5** outlines the ATRP reaction.

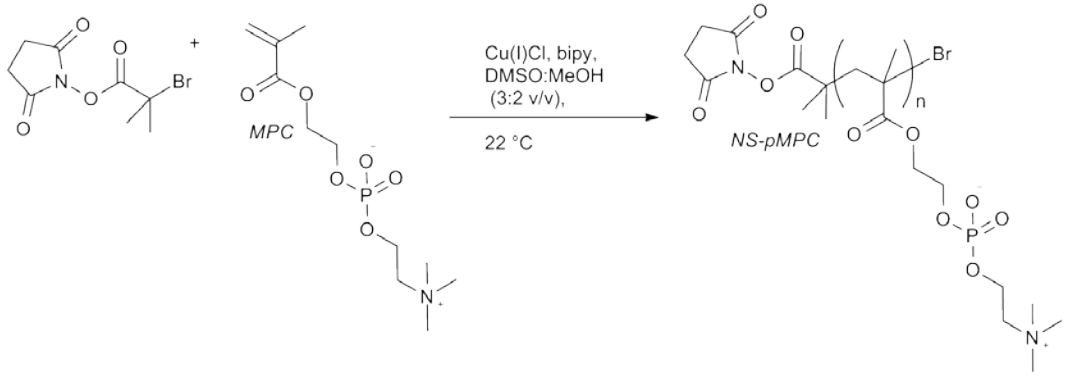

Scheme 5. ATRP of MPC using *N*-succinimidyl-2-bromoisobutyrate (NSBriB) initiator.

The reaction parameters for all *NS*-pMPC polymers synthesised are outlined in **Table 2.1**. The reaction mixture was left for the required amount of time to ensure full conversion. Conversion was monitored by ^{1}H NMR analysis by observing the disappearance of vinyl signals at δ 5.5−6.0. On exposure to air, the reaction solution turned blue, indicating aerial oxidation of the Cu(I) catalyst. The resulting *NS*−MPC homopolymer was mixed with Dowex Marathon MSC ion-exchange resin to remove Cu(II)Cl. The ion-exchange resin was then removed by filtration and remaining solution was rotary evaporated to remove methanol and precipitated into THF to remove DMSO. The precipitated polymer was then dried under vacuum and freeze dried. The sample was then stored in the fridge with sealed drying tube attached. The polymer was submitted for GPC and ^{1}H-NMR. Results for all *NS*-pMPC polymers synthesised are reported in Chapter 3.

Table 2.1. Summary of polymers synthesised by ATRP (to be used for amidation coupling reaction) and their respective reaction parameters. Where *NS* refers to the *N*-succinimidyl functional initiator used.

ID	Polymer synthesised (*I*-(monomer)$_n$	Target Polymer DP_n	Target polymer Mw (K g mol^{-1})	Initiator (*I*) weight (mg)	Monomer weight used (g)	Solvent (added to catalyst /added to monomer), volume	Catalyst mixture amounts (mg/mg) (Cu(I)Cl/bipy)
1	*NS*-(MPC)$_n$	15	4.5	112	2.06	DMSO/MeOH, 2 mL/ 1.3 mL	45/143
2	*NS*-(MPC)$_n$	50	15	94.9	5.31	DMSO/MeOH, 4.5 mL/3 mL	38/136
3	*NS*-(MPC)$_n$	100	29.5	44.5	5.03	DMSO/MeOH,, 9 mL/3 mL	16.9/56
4	*NS*-(MPC)$_n$	50	14.8	88.8	4.97	DMSO/MeOH, 4.5 mL/3 mL	33.3/110
5	*NS*-(MPC)$_n$	50	14.8	87.7	4.87	DMSO/MeOH, 4.5 mL/3 mL	35.7/112
6	*NS*-(MPC)$_n$	40	11.8	236	9.94	DMSO/MeOH, 27 mL/18 mL	83.3/276

2.5.3 Amidation Reaction of *N*-succinimidyl Functional Polymers with A-SPIONs.

Using the number of amino silane ligands per A-SPION calculated (L_{exp}), the amount of *NS*-pMPC polymer required for complete amidation reaction can be predicted.

The amount of *NS*-pMPC polymer required for a monolayer per 10 mg of A-SPIONs can be calculated: **Equation (10)**.

$$\left[\frac{\left(\left[\rho_{Fe_3O_4}.\left(\left[\frac{4}{3}\pi r^3\right]x10^{-21}\right)\right]+\left[\left(\frac{L_{exp}}{N_A}\right).MW_{reacted\ APTMS}\right]\right)^{-1}}{100}\right].\left[\frac{L_{exp}}{N_A}xMW_{polymer}\right] \qquad \textbf{(10)}$$

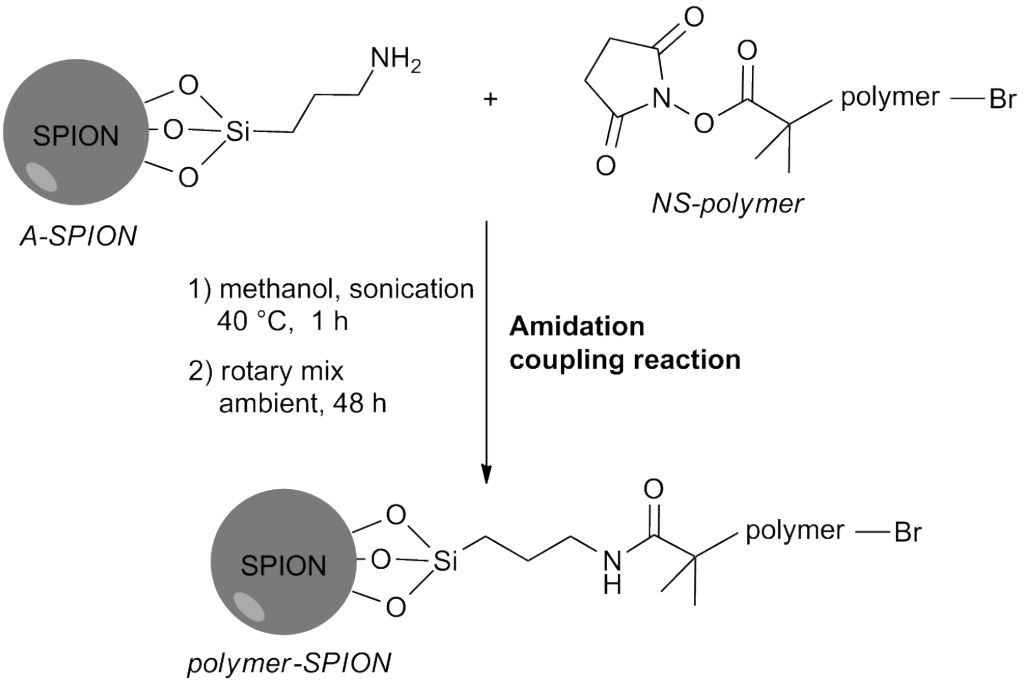

Scheme 6. Amidation reaction of *NS*-polymer with A-SPIONs.

It is expected that not all amino groups on the A-SPION are available for reaction due to unfavourable conformations.[23] Furthermore, it is expected that not all amino groups available could be reacted with a *NS*-polymer chain due to steric hindrance.[24] The amount of polymer used for amidation reaction was chosen as ~1 equivalents of all amino groups on the particle, which was expected to be in excess of actual available groups.

In a 15 mL vial, *NS*-pMPC polymer (0.41 g, 0.9 equiv) was dissolved in methanol to form a 10 % polymer/methanol solution. To this solution, amino silane coated iron oxide NPs (10 mg, pre-sonicated solution using an ultrasonic bath (Fisher Scientific, model FB15051, frequency = 30-40 kHz) dispersed in ethanol 5 mL) was added under bath sonicator set at 22 °C and further sonicated for 1 h. The reaction mixture was then left to rotary mix for 15 hours at 22 °C before dialysis into deionised water. The dialysis solution was changed with deionised water (4 L) five times over the course of a period of 8 hours. The dialysis bag was then left in the final change of deionised water (4 L) for 15 hours. **Scheme 6** outlines the amidation reaction procedure.

If polymer coated SPIONs were found to be colloidally stable in water for more than 24 hours, SPIONs were concentrated using a 50,000 MWCO Corning Spin-X UF centrifugal concentrator. The concentrated solution of polymer coated SPIONs were then passed through a Sephadex G25 gel filtration chromatography column in phosphate buffered saline (PBS) pH 7.4 to remove any unreacted polymer present. Samples as prepared were characterised by DLS, TEM and MRI. Samples were assessed for colloidal stability in PBS solution and for stability into citrate buffer solutions prior to biological studies. To determine polymer coverage, dry samples were prepared by dialysing polymer coated SPIONs back into deionised water to remove PBS salts prior to freeze drying. Samples were characterised by TGA, elemental analysis, SQUID, DLS and FT-IR. Characterisation and stability results are discussed in Chapter 3. Results from biological experiments are discussed in Chapter 6.

2.6 Chapter 4 Experimental Procedures

2.6.1 Synthesis of pH 2 Stable Maghemite SPIONs (γFe_2O_3) by Co-Precipitation Reaction

The procedure by Massart *et al.*[25] and Valero *et al.*[26] was followed. Aqueous solutions of iron (III) chloride (40 mL, 1 M) and iron (II) chloride (10 mL, 2 M in 2 M HCl solution) were prepared and mixed together. The iron chloride solution mixture was then slowly poured into ammonia solution (500 mL, 0.7 M, pH 11) in a 1 L conical flask under high vortex stirring using a magnetic stirrer bar to form a

black precipitate. Using a rare earth magnet, the black precipitate was separated and supernatant decanted. Under magnetic stirring, nitric acid solution (50 mL, 1 M) was added to the black precipitate to form pH 2 water dispersible maghemite colloid. TGA: 3.19 % (solvent), 3.19 % (organic), 2.36 %. Elemental analysis: 0.16 % (C), 0.26 % (H), 0.55 % (N). DLS measurements for SPIONs in DIW: $R_{h,\ intensity}$ = 20 ± 2 nm and 88 ± 13 nm, $R_{h,\ mass}$ = 19 ± 2 nm and 82 ± 12 nm and $R_{h,\ number}$ = 18 ± 8 nm. pXRD 8 nm.

2.6.2 Removal of Oleic Acid from the Surface of Oleic Acid Coated SPIONs (Fe_3O_4) to form pH 8 Water Dispersible SPIONs with a Bare Surface.

In a 40 mL vial, oleic acid coated SPIONs (65 mg based on iron oxide mass) were added to 1 M ammonium hydroxide in butan-1-ol (35 mL). The vial was sealed with screw top lid and sonicated using an ultrasonic bath (Fisher Scientific, model FB15051, frequency = 30-40 kHz) for 2 hours at 60 °C. After this time; the solid material was separated by magnetisation by placing a rare earth magnet at the side of the vial. The supernatant was decanted and pH 8 sodium hydroxide solution (35 mL) was then added. The SPIONs were re-dispersed in this solution via sonication for 30 minutes at 50 °C to yield pH 8 water dispersible SPIONs with a bare surface.[27] Elemental analysis: 1.54 % (C) and 0.34 % (H). TGA: 1.61 % (solvent and organic).

2.6.3 Pre-treatment of pH 2 Water Dispersible Maghemite (γFe_2O_3) NPs to make them pH 8 Water Dispersible in Preparation for Silica Coating.

The following pre-treatment was carried out on pH 2 stable SPIONs in order to prepare them for surface coating with tetra ethyl orthosilicate (TEOS) under basic conditions. The pre-treatment was carried out as follows: In a 40 mL vial, pH 2 stable SPIONs (65 mg) were added. To this, a pre-mix of butan-1-ol (35 mL) and ammonium hydroxide (1.35 mL) was added. The vial was sealed with screw top lid and sonicated using an ultrasonic bath (Fisher Scientific, model FB15051, frequency = 30-40 kHz) for 2 hours at 60 °C. After this time, the solid material was separated by magnetisation by placing a rare earth magnet at the side of the vial. The

supernatant was decanted and pH 8 sodium hydroxide solution (35 mL) was then added. The SPIONs were re-dispersed in this solution via sonication for 30 minutes at 50 °C to yield pH 8 water dispersible SPIONs with a bare surface. Material submitted for characterisation using DLS, PXRD, TGA and CHN. Characterisation results for all batches are discussed in Chapter 4.

2.6.4 Synthesis of Silica Coated Maghemite (γFe_2O_3) or Magnetite (Fe_3O_4) NPs using Sol-Gel Stöber Method

Method adapted from Lu *et al.*[28], in a two neck 100 mL round bottom flask, ammonia solution (30 %) (1.5 mL) was added to pH 8 water dispersible SPIONs (28 mg) dispersed in pH 8 sodium hydroxide solution (22.0 mL). The mixture was pre-mixed by overhead stirring (250 rpm) and sonicated using an ultrasonic bath (Fisher Scientific, model FB15051, frequency = 30-40 kHz) at 25 °C for 20 minutes. After this time, the stirring speed was increased to 715 rpm whilst under sonication. A mixture of a known amount of TEOS (50, 100, 150, 200 µL depending on required silica shell thickness) in 2-propanol (50 mL) was syringed into the reaction flask at a flow rate of 79 mL min^{-1}. After the addition of the TEOS 2-propanol mixture, the reaction was left to further mix at 715 rpm under sonication for 4 hours. **Scheme 7** outlines the synthesis procedure.

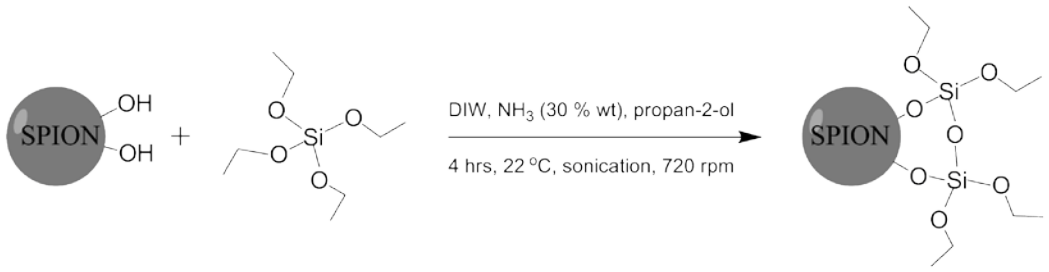

Scheme 7. Synthesis of silica coated SPION by sol-gel Stöber method.

Material was submitted for characterisation using SQUID, MRI, DLS, TGA and CHN. Samples of interest were submitted for biological studies. Characterisation results for all batches are discussed in Chapter 4. Results from biological experiments are discussed in Chapter 6.

2.7 Chapter 5 Experimental Procedures

2.7.1 Sonochemical Synthesis of Core/Shell Iron Oxide/Gold NPs using A-SPIONs

In this method, a procedure by Wu *et al.*[29] was followed. Amino silane SPIONs (1.5 mg mL^{-1}) dispersed in ethanol (10 mL) were pre-sonicated using an ultrasonic bath (Fisher Scientific, model FB15051, frequency = 30-40 kHz) for 30 minutes. A solution of $HAuCl_4.3H_2O$ (75 mg, 10.0 mL) was added to the amino silane coated iron oxide NPs and further sonicated for 10 minutes at 22 °C. Sodium citrate solution (20 mM, 20 mL) was added dropwise to the reaction mixture until a colour change from brown to black was observed (~19 mL). Once the colour change was observed, the reaction mixture was stopped and NPs centrifuged at 2,000 rpm for 2 minutes where the supernatant was then removed.

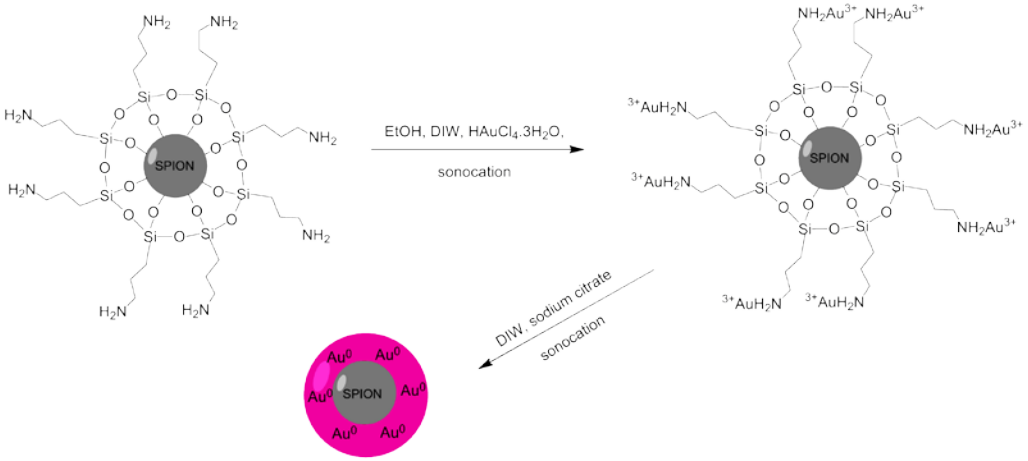

Scheme 8. Synthesis of gold coated amino silane SPIONs.

Scheme 8 outlines the synthesis procedure. The NPs were washed 3 times in ethanol (15 mL) *via* magnetic separation using a rare earth magnet and re-suspension assisted *via* sonication for 10 minutes. The NPs were finally stored in ethanol (15 mL) at 4 °C. Material was submitted for characterisation using SQUID, MRI, DLS, TGA, FT-IR and CHN. Results for all batches are discussed in Chapter 5.

2.7.2 Synthesis of Disulphide ATRP Initator bis[2-(2'-bromoisobutyryloxy) ethyl] disulfide (BriBOEDS)

Bis[2-(2'-bromoisobutyryloxy) ethyl] disulfide (BriBOEDS) was prepared by Dr Solène Cauët at the University of Liverpool, Department of Chemistry following the method as reported by Tsarevsky and Matyjaszewski.[30] **Scheme 9** outlines the synthesis procedure.

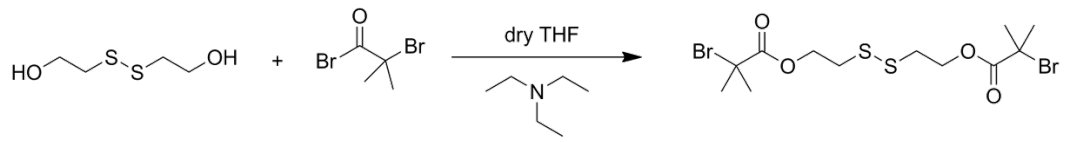

Scheme 9. Synthesis of Bis[2-(2'-bromoisobutyryloxy) ethyl] disulfide (BriBOEDS) ATRP initiator.

^{1}H NMR ($CDCl_3$, 400 MHz) δ (ppm) 4.43 (t, 2H, -CH_2OOC-), 2.97 (t, 2H, -CH_2S-), and 1.93 (s, 6H, $(CH_3)_2$C-). ^{13}C NMR ($CDCl_3$, 100.6 MHz) δ (ppm) 171.49 (-OOC-), 63.56 (-CH_2O-), 55.54(-C-$(CH_3)_2$), 36.81 (-CH_2S-) and 30.76 (CH_3). FTIR (ATR cell) 2975, 1731, 1267, 1152 and 1104 cm^{-1}. Micromass LCT mass spectrometry expected (found): 452.22 g mol^{-1} (451.91 g mol^{-1}). Elemental Analysis: expected C 31.87 %, H 4.46 %, S 14.18 %, actual C 31.90 %, H 4.45 %, S 13.81 %.

2.7.3 ATRP of MPC using Disulphide Initator bis[2-(2'-bromoisobutyryloxy) ethyl] disulfide (BriBOEDS)

The disulfide initiator synthesised above was used for the synthesis of disulfide functional MPC polymers which were prepared by ATRP by Dr Solène Cauët, University of Liverpool, Department of Chemistry.

2.7.4 Coating Au-SPIONs with pMPC

In a 10 mL vial, disulphide functional $pMPC_{81}$ (1.08 g) or $pMPC_{135}$ (1.0 g) was dissolved in distilled water (8 mL). To this, tris(2-carboxyethyl)phosphine (TCEP) (10 mg) was added and allowed to react with the polymer in solution *via* rotary

mixing for 10 minutes for the formation of thiol end groups. Au-SPIONs (10 mg, 2 mL) of in ethanol/ water mixture were then added and the mixture was allowed to sonicate using an ultrasonic bath (Fisher Scientific, model FB15051, frequency = 30-40 kHz) for 1 hour at 22 °C. **Scheme 10** outlines the reaction procedure.

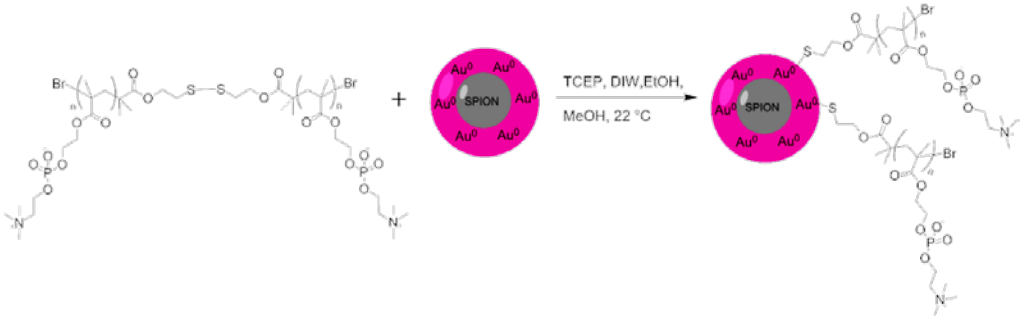

Scheme 10. Stabilisation of Au-SPIONs with thiol functionalised-pMPC polymer.

The reaction mixture was then left to rotary mix for 15 hours at 22 °C before dialysis into deionised water. The dialysis solution was changed with deionised water (4 L) five times over the course of a period of 8 hours. The dialysis bag was then left in the final change of deionised water (4 L) for 15 hours. Polymer-coated Au-SPIONs were concentrated using a 50,000 MWCO Corning Spin-X UF centrifugal concentrator. The concentrated solution of polymer coated Au-SPIONs were then passed through a Sephadex G100 gel filtration chromatography column in phosphate buffered saline (PBS) pH 7.4 to remove any unreacted polymer present. Samples of interest were submitted for biological studies. Characterisation results for all batches are discussed in Chapter 5. Results from biological experiments are discussed in Chapter 6.

2.7.5 Sonochemical Synthesis of A-SPIONs with a Thin Gold Shell.

In this method, a procedure by Wu *et al.*[29] was followed and modified. Amino silane SPIONs (1.5 mg mL^{-1}) dispersed in ethanol (10 mL) were pre-sonicated using an ultrasonic bath (Fisher Scientific, model FB15051, frequency = 30-40 kHz) for 30 minutes. A solution of $HAuCl_4.3H_2O$ (75 mg, 10.0 mL) was added to the SPIONs and further sonicated for 30 minutes at 22 °C. The reaction solution was then centrifuged at 5,000 rpm for 2 minutes and the yellow supernatant decanted. Particles were re-suspended in 10 mL of ethanol and sonicated for 15 minutes. Sodium citrate solution (20 mM, 15 mL) was added to the SPIONs and left to sonicate for 10 minutes. During sonication, the solution changed colour from brown

to dark brown/black. The reaction solution was then centrifuged at 5,000 rpm for 2 minutes. The supernatant was decanted and particles were re-suspended through sonication for 30 minutes in a 1:1 (v/v) solvent mixture of ethanol and water (15 mL). To this, $HAuCl_4.3H_2O$ solution (75 mg, 10 mL) was again added and sonicated for 5 minutes. During sonication, the colour of the solution turned red. The solution was again centrifuged at 5,000 rpm for 2 minutes and supernatant decanted. The NPs were again re-suspended through sonication for 15 minutes in a 1:1 (v/v) solvent mixture of ethanol and water (15 mL). Solution was then further separated using a rare earth magnet and re-suspended *via* sonication for 15 minutes into ethanol and water solvent mixture (15 mL) – the magnetic separation step was again repeated to yield a red stable suspension in ethanol/water (15 mL). Material was submitted for characterisation using SQUID, MRI, DLS, TGA, FT-IR and CHN. Samples of interest were submitted for biological studies. Characterisation results for all batches are discussed in Chapter 5. Results from biological experiments are discussed in Chapter 6.

2.7.6 Reaction of A-SPIONs with Auric Chloride Solution

Amino silane SPIONs (1.5 mg mL^{-1}) dispersed in ethanol (10 mL) were pre-sonicated using an ultrasonic bath (Fisher Scientific, model FB15051, frequency = 30-40 kHz) for 30 minutes. A solution of $HAuCl_4.3H_2O$ (75 mg, 10.0 mL) was added to the SPIONs and further sonicated for 30 minutes at 22 °C. The reaction solution was then centrifuged at 5,000 rpm for 2 minutes and the yellow supernatant decanted. Particles were re-suspended in 10 mL of ethanol and sonicated for 15 minutes. Material was submitted for characterisation using PXRD and TEM. Sample was assessed by dissolution stability assay. Results for all batches are discussed in Chapter 5.

2.8 References

Website references accessed 12th March 2014.

1. http://www.malvern.com/en/support/resource-center/Whitepapers/WP111214DLSTermsDefined.aspx

2. http://www.malvern.com/en/support/resource-center/technical-notes/TN101104IntensityVolumeNumber.aspx
3. V. Pecharsky and P. Zavalij, *Fundamentals of Powder Diffraction and Structural Characterization of Materials*, Springer US, 2005, ch. 3, 305-306.
4. http://www.nobelprize.org/educational/physics/microscopes/tem/
5. L. Reimer and H. Kohl, *Transmission Electron Microscopy : Physics of Image Formation*, Springer, New York, NY, 5th edn., 2008.
6. http://cnx.org/content/m34657/latest/?collection=col10699/latest
7. A. M. Striegel, W. W. Yau, J. J. Kirkland, *et al.*, *Modern Size-Exclusion Liquid Chromatography*, John Wiley & Sons, Inc., 2009, 1-17.
8. https://www.brainshark.com/malvern/vu?pi=984902997
9. J. Hennig, A. Nauerth and H. Friedburg, *Magn. Reson. Med.*, 1986, **3**, 823-833.
10. M. Schröder and P. Friedl, *Methods Cell Sci.*, 1997, **19**, 137-147.
11. J. Kapuscinski and W. Szer, *Nucleic Acids Res*, 1979, **6**, 3519-3534.
12. C. Wilhelm, C. Billotey, J. Roger, *et al.*, *Biomaterials*, 2003, **24**, 1001-1011.
13. J. J. Chalmers, Y. Zhao, M. Nakamura, *et al.*, *J. Magn. Magn. Mater.*, 1999, **194**, 231-241.
14. L. K. Bogart, A. Taylor, Y. Cesbron, *et al.*, *ACS Nano*, 2012, **6**, 5961-5971.
15. T. Skotland, P. C. Sontum and I. Oulie, *J Pharmaceut Biomed*, 2002, **28**, 323-329.
16. A. S. Arbab, L. B. Wilson, P. Ashari, *et al.*, *NMR Biomed.*, 2005, **18**, 383-389.
17. L. L. Stookey, *Anal. Chem.*, 1970, **42**, 779-781.
18. C. F. Mora, E. Ranghini, S. Bruno, *et al.*, *Stem Cells Dev*, 2012, **21**, 296-307.
19. https://www.sigmaaldrich.com/content/dam/sigma-aldrich/docs/Sigma/Datasheet/6/96992dat.pdf
20. http://www.sigmaaldrich.com/content/dam/sigma-aldrich/docs/Sigma-Aldrich/Bulletin/se100bul.pdf
21. J. Park, K. J. An, Y. S. Hwang, *et al.*, *Nat Mater*, 2004, **3**, 891-895.
22. D. H. Han and C. Y. Pan, *Polymer*, 2006, **47**, 6956-6962.
23. M. van de Waterbeemd, T. Sen, S. Biagini, *et al.*, *Micro Nano Lett.*, 2010, **5**, 282-285.

24. R. C. Advincula, W. J. Brittain, K. C. Caster, *et al.*, *Polymer Brushes: Synthesis, Characterization, Applications*, WILEY-VCH, 2004.
25. R. Massart, *IEEE Trans. Magn.*, 1981, **17**, 1247-1248.
26. E. Valero, S. Tambalo, P. Marzola, *et al.*, *J. Am. Chem. Soc.*, 2011, **133**, 4889-4895.
27. N. Kohler, G. E. Fryxell and M. Zhang, *J. Am. Chem. Soc.*, 2004, **126**, 7206-7211.
28. Y. Lu, Y. Yin, B. T. Mayers, *et al.*, *Nano Lett.*, 2002, **2**, 183-186.
29. W. Wu, Q. He, H. Chen, *et al.*, *Nanotechnology*, 2007, **18**, 145609.
30. N. V. Tsarevsky and K. Matyjaszewski, *Macromolecules*, 2002, **35**, 9009-9014.

3

Preparation of Poly(2-methacryloyloxyethyl phosphorylcholine) Functionalised SPIONs for Stem Cell Labelling

(Publication arising from this Chapter:
"**Poly[2-(methacryloyloxy)ethylphosphorylcholine]-coated iron oxide nanoparticles: synthesis, colloidal stability and evaluation for stem cell labelling**", Anita K. Peacock, Solène I. Cauët, Arthur Taylor, Patricia Murray, Steve R. Williams, Jonathan V. M. Weaver, Dave J. Adams and Matthew J. Rosseinsky, *Chem. Comm.*, 2012, 48, 9373-9375)

For experimental details related to this Chapter, see Chapter 2.

List of Figures

Figure 3.1. Steric stabilisation of iron oxide NPs. Showing (1) core, (2) anchor, (3) 'spacer'/ polymer.[5] 86

Figure 3.2. Diagram of a cell membrane highlighting the polar phosphorylcholine as the head group of the phospholipid.[26] 89

Figure 3.3. Characterisation data for oleic acid coated SPIONs showing A) intensity, mass and number solvodynamic radius peak height measurements by DLS B) PXRD pattern, C) TEM image and D) a size distribution taken from the TEM image. 91

Figure 3.4. TEM image and size distribution for A-SPIONs taken from >400 measurements..... 93

Figure 3.5. Fourier transform infrared (FT-IR) spectroscopy of A-SPIONs..... 93

Figure 3.6. Schematic representation of an amino silane footprint. 94

Figure 3.7. Representation of monolayer and multilayer arrangements through the polymerisation of the APTMS on the surface of a nanoparticle. Figure taken from reference.[31] 96

Figure 3.8. Thermal gravimetric analysis of A-SPIONs showing total weight loss of 34.88 %. The dashed vertical line shows the position of the isotherm held at 120 °C for the removal of adsorbed solvent. 97

Figure 3.9. GPC chromatograms of *NS*-pMPC polymers 1, 2 and 3 synthesised by ATRP showing refractive index (RI) and right angle light scattering (RALS) detector response (PBS solution pH 7.4 eluent, 50 °C, TD-GPC using PEO 22 kDa narrow standard). 101

Figure 3.10. Polymerisation kinetics of *NS*-$pMPC_{40}$ (GPC: PBS solution pH 7.4 eluent, 50 °C, set of PEO calibration standards with M_p values of 125,8, 909.5, 442.8, 116.3, 62.1, 23.5, 12.1, 12, 3.9, 1.5 kDa, differential refractive index (DRI) detector used). A) $M_{n(GPC)}$ versus conversion plot, B) monomer conversion versus time plot, C) polymer kinetic plot and D) GPC plot of the kinetic samples taken. . 102

Figure 3.11. Differential scanning calorimetry (DSC) themogram for 1 % *NS*-$pMPC_{50}$ in PBS solution carried out for the measurement of a lower critical solution temperature (LCST). 103

Figure 3.12. ^{1}H-NMR data showing the amide proton from the amidation reaction of APTMS with *N*-succinimidyl functional polymer. APTMS analysed in $CDCl_3$, polymer-containing samples analysed in DMSO-d6. 106

Figure 3.13. The effect of copper removal prior to amidation reaction. Vials show two different pMPC-SPION samples after reaction and dialysis into water. Vials show amidation reactions carried out with and without copper removal, vials labelled A) and B) respectively. 107

Figure 3.14. Initial screening of *NS*-pMPC$_n$ of different MW reacted with A-SPIONs. All samples are at the same SPION concentration..... 108

Figure 3.15. ^{1}H-NMR spectrum of the final precipitated *NS*-pMPC polymer in CD_3OD indicated a DP_n of 29, MW 9,000 g mol^{-1} deduced from the polymer chain end group protons 'g' against integration for H protons on polymer 'a' and 'b'. ... 109

Figure 3.16. Images of pMPC$_{29}$-SPIONs through the sample preparation process. A) NPs after amidation in methanol/ethanol, B) NPs during dialysis into DIW, C) NPs after dialysis into water, D) NPs in PBS pH 7.4 passing through G25 sephadex column, E) NPs after G25 in PBS pH 7.4, F) NPs at 1 mg Fe mL^{-1} in PBS pH 7.4, G) NPs after freeze drying..... 110

Figure 3.17. FT-IR absorbance spectra for A) OA-SPIONs, B) A-SPIONs and C) pMPC$_{29}$-SPIONs (after passing through a G25 gel filtration column). The wavenumber bands are collected as a percentage of transmission. 111

Figure 3.18. TGA spectra for A-SPIONs (red) and pMPC$_{29}$-SPIONs (blue). The dotted line represents the isotherm at temperature of 120 °C for the removal of adsorbed solvent. 112

Figure 3.19. DLS solvodynamic and hydrodynamic radius peak height measurements for OA-SPION starting material in THF compared with pMPC$_{29}$-SPIONs in PBS solution pH 7.4. 113

Figure 3.20. TEM images of pMPC$_{29}$-SPIONs unstained. Here, only the iron oxide cores can be visualised. 114

Figure 3.21: TEM images of pMPC$_{29}$-SPIONs stained with 3 % PTA solution demonstrating the consistency of polymer coverage and core-shell architecture across the sample. 115

Figure 3.22. MIRB TEM image of SPIONs without stain and hydrodynamic radius peak height measurements by DLS in PBS solution pH 7.4. 116

Figure 3.23. AFM topography (images A and B), 3D topography (C and D) and intensity profiles (E and F) of $pMPC_{30}$-SPIONs. 117

Figure 3.24. Hydrodynamic radius peak height measurements by DLS of $pMPC_{29}$-SPIONs compared with reconstituted $pMPC_{29}$-SPIONs in PBS solution pH 7.4. .. 118

Figure 3.25: Structure of surface reacted APTMS ligand and pMPC ligand. 122

Figure 3.26: Relative viability of kidney murine stem cells exposed to a range of concentrations of pMPC coated SPIONs or MIRB nanoparticles. The cells were incubated in culture medium containing the nanoparticles for 24 h followed by viability measurement with CCK-8 reagent. Results are plotted as the relative viability in respect to control conditions as a function of nanoparticle concentration and error bars represent the standard deviation from three replicates. 123

Figure 3.27. $pMPC_{29}$-SPIONs stability study in PBS at 25 °C and 37 °C with images of solutions at t = 0 and at the end points of the 4 studies..... 125

Figure 3.28. Dissolution assay of $pMPC_{29}$-SPIONs and MIRB in citrate buffer solution at 37 °C. 127

Figure 3.29: Magnetisation-field magnetic hysteresis curves for OA-SPION and $pMPC_{29}$-SPION at 300K. The 2 T magnetisation for OA-SPION is 53.50 emu g^{-1} iron oxide and $pMPC_{29}$-SPION 33.20 emu g^{-1} iron oxide. 128

Figure 3.30. Ambient temperature magnetisation curves of (a) Fe_3O_4 cores as synthesised in oleic acid (b) Following addition of amino-silanisation (c) after polymerisation with MPC block polymer and (d) MIRB SPIONs. Grey line indicates best model fit using simple Langevin expression modified by the log-normal polydispersity function. Best fit parameters for all fits are provided in **Table 3.5**. 129

Figure 3.31. Relaxivity data for $pMPC_{29}$-SPIONs as prepared and reconstituted vs. Endorem and MIRB contrast agents. 131

List of Tables

Table 3.1. Predicted elemental percentage weight and TGA weight loss values for one monolayer of amino silane ligands surrounding a 7.6 nm SPION..... 96

Table 3.2. Experimental and calculated elemental analysis and TGA weight loss values for dried A-SPION. Shaded areas show actual experimental values..... 98

Table 3.3. GPC and ^{1}H-NMR results for *NS*-pMPC polymers. GPC samples were ran in PBS solution pH 7.4 eluent at 50 °C. Samples were analysed by TD-GPC using a narrow standard of polyethylene oxide (PEO) with MW of 22 kDa. Data in brackets represents samples analysed using PEO conventional calibration standards. 100

Table 3.4. Percentage elemental mass break down of surface reacted $pMPC_{29}$-ligand as interpreted by the number of reacted and unreacted amino silane ligands (column 1). From this and the TGA percentage weight measured for the organic shell and water contribution, C, H and N values could be predicted. 122

Table 3.5. Best fit parameters extracted from ambient temperature magnetisation curves presented in Figure 3.30. Where M_{SP} and M_{SB} is the saturation magnetisation of the particles and of the bulk material, respectively. Where D_t is the total SPION core diameter and D_m is the magnetic core diameter..... 130

List of Schemes

Scheme 3.1. Condensation of the propyl amine functional silane ligand and its attachment to the SPION surface.[28, 29] 92

3.1 Introduction

Polymers are versatile materials that can be tailored in numerous ways.[1] Using controlled free radical polymerisation methods, polymers can be designed by controlling molecular weight (MW) or chain length (degree of polymerisation (DP_n)), dispersity (Đ), solubility and their behaviour under a variety of conditions

(such as pH, temperature, light) and the ability to incorporate functional groups for bio-conjugation or surface chemistry.[2]

Uncoated nanoparticles (NPs) in physiological buffer solution (such as phosphate buffered saline (PBS)) or cell culture medium interact with each other mainly by van der Waals forces, which induce aggregation. Salts present in the NP solution will additionally destabilise NP surface charges thus contributing to the aggregation process.[3] Polymers are used as NP surface coatings because they create space between NP cores therefore allowing colloidal stability through a steric stabilisation mechanism, **Figure 3.1**.[4]

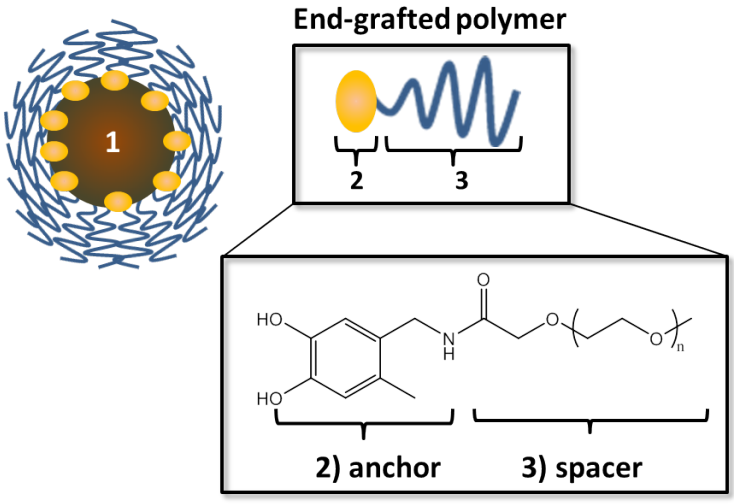

Figure 3.1. Steric stabilisation of iron oxide NPs. Showing (1) core, (2) anchor, (3) 'spacer'/ polymer.[5]

In this Chapter, well-defined end functional hydrophilic polymers are prepared by atom transfer radical polymerisation (ATRP). To end-graft these polymers to the surface of superparamagnetic iron oxide NPs (SPIONs), a reactive *N*-succinimidyl activated ester group is incorporated onto the end of the hydrophilic polymer chain through the ATRP initiator which anchors onto the SPION surface through amidation conjugation/coupling reaction with amino silane surface functionalised SPIONs (A-SPIONs). An example of end-grafted polymer coating onto a SPION is represented in **Figure 3.1**.[6, 7] The polymers synthesised will be characterised to determine MW, DP_n and Đ prior to their use for the coating procedure. The idea of using well-defined polymers with narrow distribution of known molecular weight (MW) synthesised by controlled radical polymerisation is attractive due to the ability

to accurately quantify the polymer coverage when using monodisperse SPIONs with known surface area and known available functional surface groups for conjugation. Polymers that are covalently bound through a strong stable bond to the SPION surface are likely to provide stability, which is attractive for the application of long-term stem cell tracking.[8, 9]

To achieve optimal colloidal stability through steric stabilisation, the mechanism of creating space between NPs through steric polymer chains, provides : 1) there needs to be sufficient polymer coverage or surface grafting density and 2) the optimal polymer chain length and molecular weight needs to be determined.[10] Longer polymer chains are typically known to provide greater colloidal stability and steric stabilisation.[11] There is however a trade-off when it comes to selecting polymer chain length versus achieving high surface grafting density. Steric hindrance issues exist surrounding the use of polymers with increased chain length/branching/molecular weight for grafting-to reactions with NP surfaces (thus leading to a decrease in surface grafting density during the grafting-to procedure). A balance between these two parameters is therefore required if optimal colloidal stabilisation of NPs in solution is to be achieved.[12]

Selecting a suitable polymeric NP surface coating for optimal colloidal stability does require some understanding of the environmental conditions that the NP will face. In this project, the aim is to prepare stable SPIONS that can be stored for long periods at temperatures mimicking those in a fridge and ambient of 4 and 25 °C respectively. The NPs are expected to be stored in water, physiological buffer at pH 7.4 or cell culture media. 1 % penicillin or 0.05 % sodium azide will also be added to the storage solutions for the prevention of bacterial growth. Ideally, the concentration of the SPION suspension for storage should be at least 1 mg Fe mL^{-1}. This is so that minimal sample volume can be used (~10 % v/v, maximum SPION cell labelling concentration of 100 and 50 µg Fe mL^{-1}) so as to further avoid any bacterial contamination in the cell culture petri dishes during the cell labelling procedure. The SPION sample is to be diluted in bioactive media consisting of Dulbecco's modified Eagle's medium (DMEM) supplemented with 10 % foetal bovine serum (FBS; PAA), 1 % L-glutamine and 100 U/mL of penicillin and streptomycin. Stem cells were incubated at 37 °C, 5 % CO_2 for 24 to 48 hours. The polymer of choice for this

project will therefore be one that can withstand these conditions and prevent NP precipitation at concentrations of 1 mg Fe mL^{-1} upon storage.[3] The polymer must be highly hydrophilic and soluble in aqueous and bioactive solutions, be non-cytotoxic or have low cytotoxicity, be bio-compatible (i.e. it must not change any biological mechanisms or the overall function of the cell), and maintain the polymer coated SPION with nanoscale dimensions for easy internalisation into the stem cell.

The polymer will also need to be soluble in solvents required for the coating reaction. Amino silane coated SPIONs (A-SPIONs) are found to only be dispersible in alcohols, so a polymer that is soluble in a solvent that is miscible with alcohols will be required for good reactivity and access to the amino sites on the NP surface.[13]

The solution behaviour of polymers in ionic solutions at different temperatures can be studied to determine their suitability as a coating for colloidal stability. Coil-to-globule formation or "salting-out" of hydrophilic polymers can be induced through dehydration from salt/dissolved ions in solution (e.g. PBS solution) which compete for water hydration and thus can effectively lower the lower critical solution temperature (LCST) of specific polymers.[14-17] Interestingly, some zwitterionic polymers possess an upper critical solution temperature (UCST) in water or salt containing solutions whereby at a critical temperature, polymers become more soluble in solution upon increasing temperature.[18] Salt has also been found to behave as counter ions in solution for zwitterionic polymers which can thus help the solubility of polymer in solution.[19]

At the start of this Ph.D project, several polyethylene glycol (PEG) based polymers were prepared and screened due to having known colloidal stability and bio-compatibility. The studies are found in Appendix B. In this Chapter, poly(2-methacryloyloxyethyl phosphorylcholine) (pMPC) is discussed since at the beginning of this project (in 2011), there were only a few reports where pMPC had been used as a surface coating for SPIONs.[20-22] PolyMPC a zwitterionic polymer is of interest for bio-applications mainly due to its biomimetic property and similar molecular composition to the hydrophilic head group of the phospholipid cell membrane, **Figure 3.2**. Like a cell membrane, the arrangement of the choline moiety on the end of the monomer provides polymers with anti-biofouling and stealth properties. PolyMPC homopolymer has been prepared by controlled radical

polymerisation methods to form well-defined polymers with controlled chain lengths and narrow distribution.[23, 24] Interestingly, a similar monomer to MPC has been synthesised known as 2-(methacryloyloxy)ethyl choline phosphate (MCP) where the phosphate and choline moiety arrangement is reversed allows polyMCP to act as a bio membrane adhesive.[25] Despite the interesting biomimetic properties of pMPC, very little biological studies have been carried out or reported with pMPC coated SPIONs. Yuan *et al.*[21] synthesised superparamagnetic magnetite NPs by co-precipitation of ferric and ferrous salts in the presence of a double hydrophilic copolymer poly[2-(methacryloyloxy)ethyl phosphorylcholine]-*block*-glycerol monomethacrylate ($pMPC_{30}$–$pGMA_{30}$) upon the addition of ammonium hydroxide. The double hydrophilic copolymer was prepared prior to SPION synthesis *via* ATRP. The $pMPC_{30}$ chains acted as the stabilising block and the $pGMA_{30}$ block were used to adsorb onto the surface of the SPIONs. PolyMPC-SPIONs were also prepared using a grafting from approach by surface initiated ATRP.

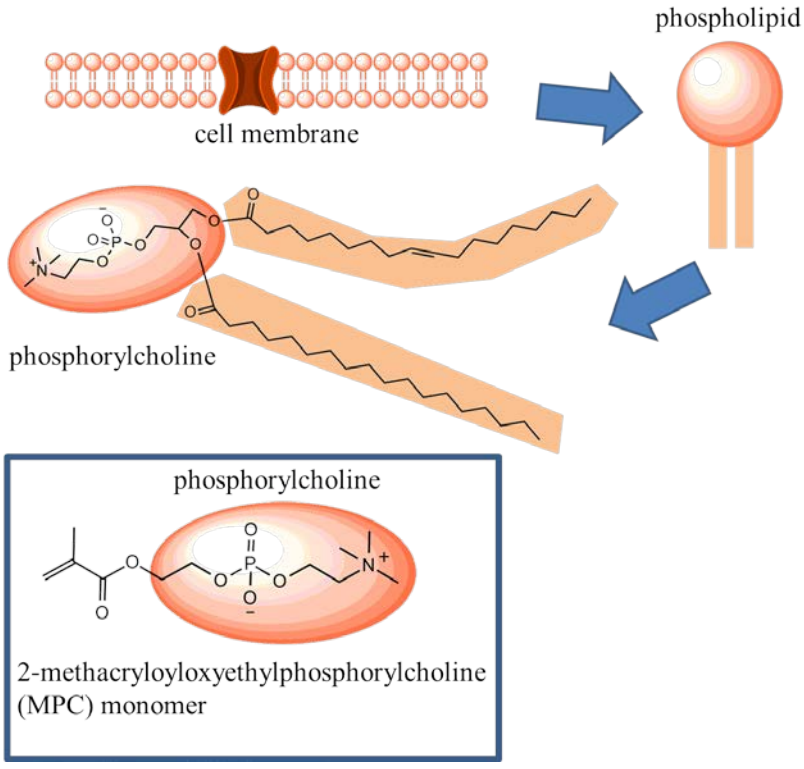

Figure 3.2. Diagram of a cell membrane highlighting the polar phosphorylcholine as the head group of the phospholipid.[26]

Sun *et al.*[20] surface functionalised SPIONs with average particle diameter of 9 ± 1 nm using 2-(4-chlorosulfonylphenyl)ethyltrichlorosilane (CTCS) in dry

toluene. Sui *et al.*[22] also surface functionalised hydroxyl-functional SPIONs with diameter of 7 nm using a grafting from approach this time using 2-bromoisobutyryl bromide (BriBBr) initiator which were attached to the bare hydroxyl SPION surface *via* esterification. PolyMPC homopolymers were then prepared by surface initiated ATRP in methanol at ambient for 2 hours. In this Chapter, poly(2-methacryloyloxyethyl phosphorylcholine) coated SPIONs (pMPC-SPIONs) were prepared using a grafting-to approach and were investigated as a potential R_2 MRI contrast agent through the assessment of biocompatibility, colloidal stability prior to biological studies of the polymer coated SPIONs with stem cells.

3.2 Results and Discussion

3.2.1 Preparation of Oleic Acid Coated Superparamagnetic Iron Oxide Nanoparticles (OA-SPIONs)

Monodisperse oleic acid coated superparamagnetic iron oxide nanoparticles (OA-SPIONs) were prepared following the method reported by Hyeon and co-workers.[27] Dynamic light scatting (DLS) measurements of the OA-SPIONs in tetrahydrofuran (THF) gave solvodynamic radius peak height measurements by intensity, mass and number as the following: $R_{s,\ intensity} = 14 \pm 3$ nm, $R_{s,\ mass} = 12 \pm 2$ nm and $R_{s,\ number} = 11 \pm 2$ nm (**Figure 3.3A**). The DLS distribution of sizes are produced from a set of correlation functions using a variation of the Stokes-Einstein equation. Each function has its own amplitude and decay rate. Cumulants analysis proposed by ISO whereby a single or cumulant exponential fit of the correlation function to give an intensity weighted average or Z average hydrodynamic size using the Stokes-Einstein equation was not provided by the software. Hydrodynamic/solvodynamic radius peak height measurements were instead provided here.

Powder X-ray diffraction (PXRD) was also obtained for the OA-SPIONs which showed good agreement with the reference pattern for magnetite (ICDD no. 00-019-0629) and indicated the material was crystalline, **Figure 3.3B**. The average particle size diameter measured was 7.6 nm as derived from the Scherrer equation. A size distribution from over 400 measurements using a Transmission Electron Microscopy (TEM) image of OA-SPIONs was obtained using ImageJ software. The average

diameter of the cores were measured at 8 ± 3 nm with the mode found at 9 nm, **Figure 3.3C and D**.

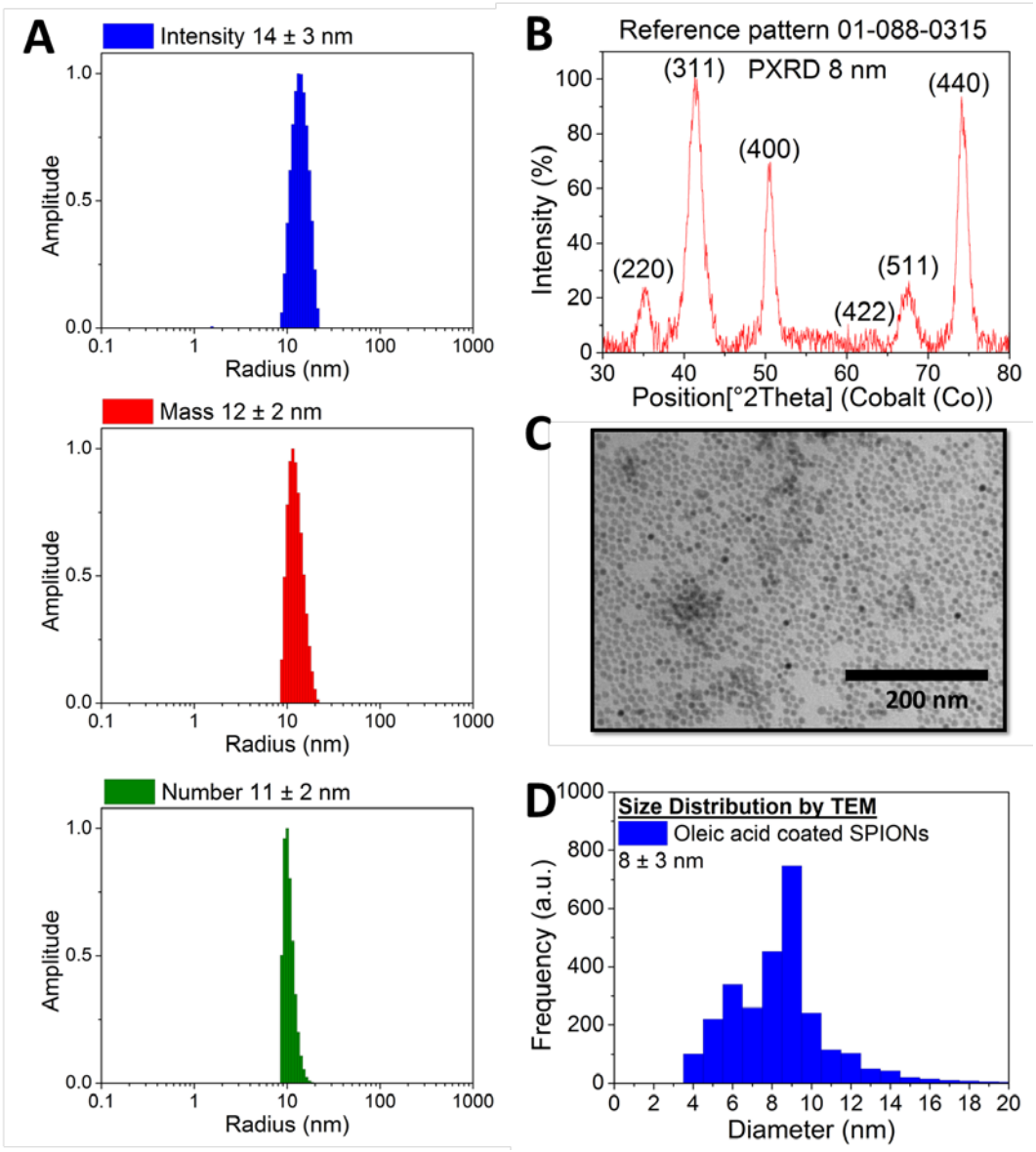

Figure 3.3. Characterisation data for oleic acid coated SPIONs showing A) intensity, mass and number solvodynamic radius peak height measurements by DLS B) PXRD pattern, C) TEM image and D) a size distribution taken from the TEM image.

3.2.2 Preparation of Amino Silane Functionalised SPIONs (A-SPIONs)

To prepare SPIONs for end-grafted polymer coating, chemical modification of the SPION surface was performed to convert the SPIONs from hydrophobic to

hydrophilic. Ligand exchange reaction was used to remove hydrophobic ligands from the SPION surface whilst the hydrophilic ligand was attached to the NP surface *in situ*. An amino functional silane, (3-amino)propyltrimethoxysilane (APTMS) was used as the ligand to provide a hydrophilic surface in addition to providing a stable covalently bound ligand to the SPION surface. Here, amino groups act as anchor for end-grafted conjugation of polymers to the surface.

To control the condensation procedure of the amino silane ligand, the reaction was carried out in dry conditions using dried toluene under an inert atmosphere (N_2 gas). The reaction took a period of one week whereby the reaction mixture was agitated continuously using a rotary mixer at 22 °C with a brief daily sonication throughout this timeframe. The mechanism for the condensation of the amino silane ligand and its attachment to the SPION surface is shown in **Scheme 3.1**, where R represents the propyl amine functional group.

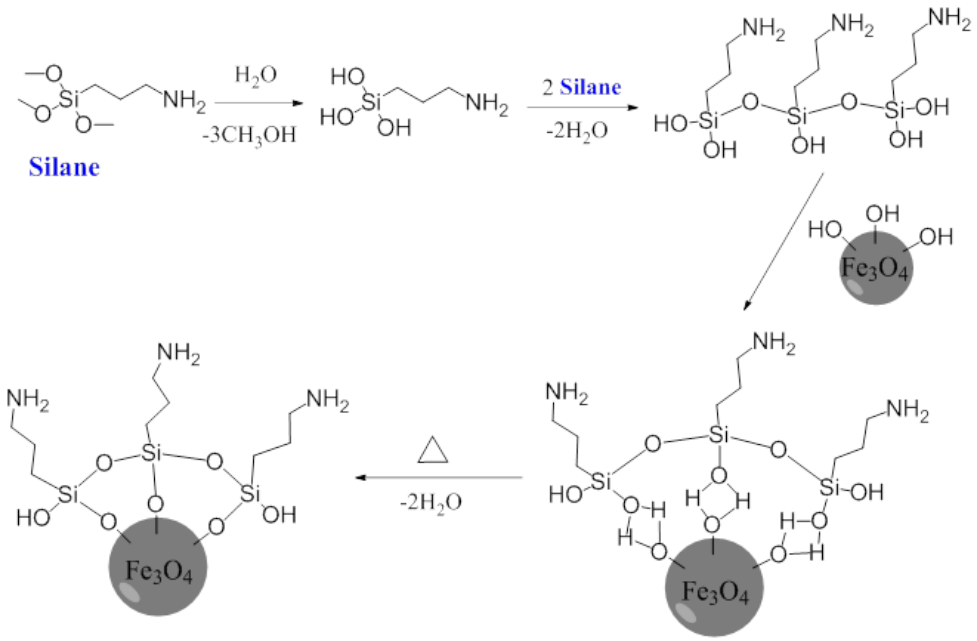

Scheme 3.1. Condensation of the propyl amine functional silane ligand and its attachment to the SPION surface.[28, 29]

A size distribution of A-SPIONs measured by TEM (>400 measurements) gave an average core diameter of 8 ± 2 nm, **Figure 3.4**, which was found to be similar to that measured for the OA-SPIONs by TEM.

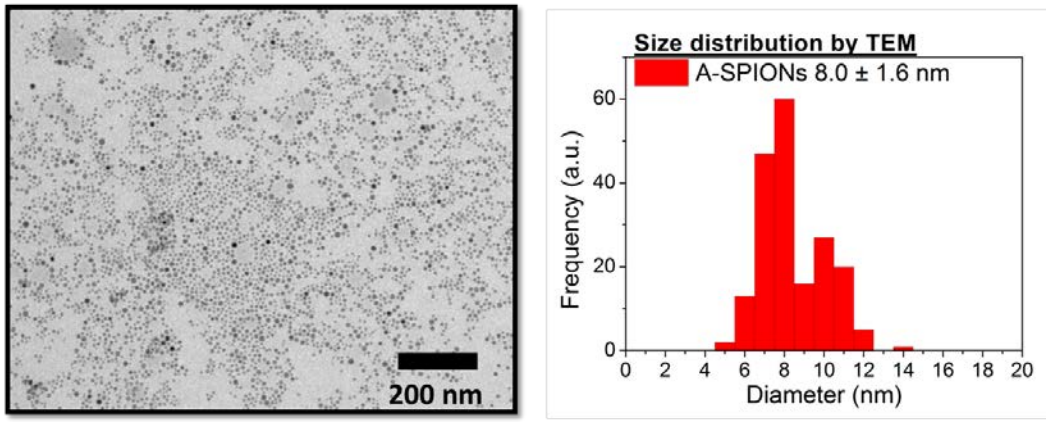

Figure 3.4. TEM image and size distribution for A-SPIONs taken from >400 measurements.

The presence of amine groups on the surface of A-SPIONs was confirmed by zeta potential measurements. The zeta-potential for the A-SPIONS was +25.6 ± 0.4 mV in deionised water (DIW), pH 8. Fourier transform infrared (FT-IR) spectroscopy also confirmed the presence of primary amine groups, as shown by the band at ~1400 cm^{-1}. Bands found at wavenumbers of 1100 cm^{-1} and lower also confirmed the presence of silane bonds, **Figure 3.5.**

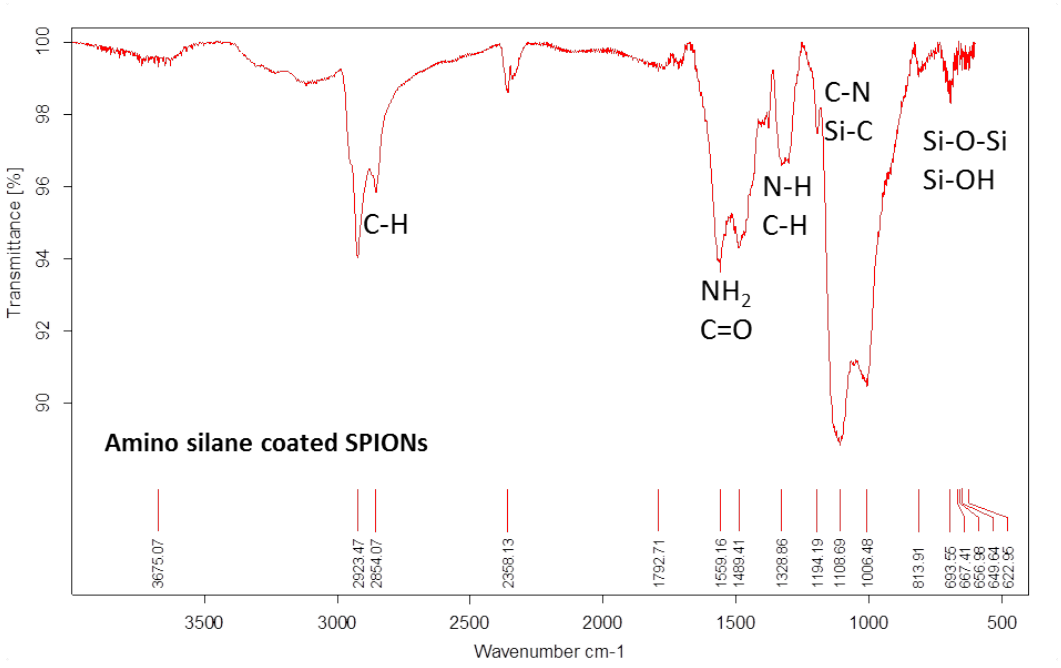

Figure 3.5. Fourier transform infrared (FT-IR) spectroscopy of A-SPIONs.

3.2.2.1 Quantification of Amine Groups Reacted to the SPION Surface

The average number of actual amino silane ligands available on the surface of iron oxide nanoparticles was determined using both thermal gravimetric analysis (TGA) and nitrogen content obtained from elemental analysis measured. Using the surface area of the footprint from the tridentate amino silane ligand as 0.073 nm^2,[30] **Figure 3.6**, the theoretical number of amine ligands for one mono-layer on the surface of a 7.6 nm diameter nanoparticle (as determined by PXRD using the Scherrer equation, see above) was calculated as 2505 ± 249. This was determined by the following:

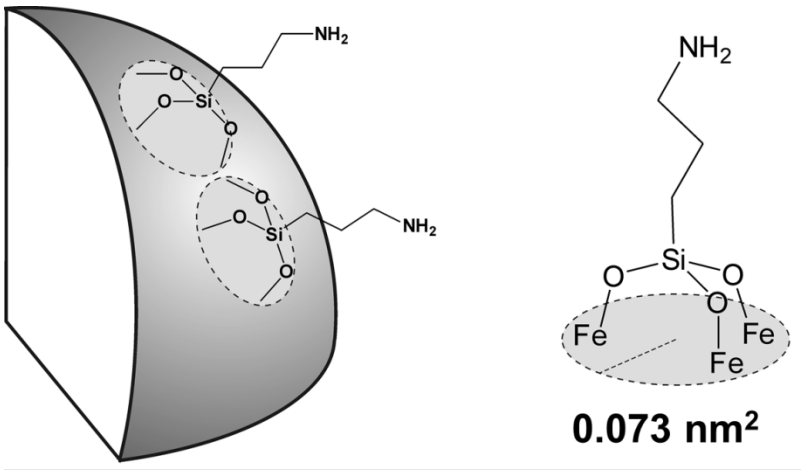

Figure 3.6. Schematic representation of an amino silane footprint.

The surface area (SA) of a 7.6 nm SPION:

$$SA_{SPION} = 4\pi r^2$$

SA_{SPION} = 183 ± 18 nm^2

Predicted number of reacted APTMS ligands that can fit as one monolayer on a 7.6 nm SPION (L_{pred}):

$$L_{pred} = \frac{SA_{SPION}}{Footprint_{APTMS}}$$

L_{pred} = 2505± 249 ligands

Predicted elemental and thermal gravimetric analysis (TGA) percentage weight values for one monolayer of amino silane around a 7.6 nm SPION could also be calculated and compared with actual results.

$$Mass\ of\ one\ SPION = \rho_{Fe_3O_4} x \left(\left[\frac{4}{3} \pi r^3 \right] x 10^{-21} \right)$$

$$Mass\ of\ one\ SPION = 1.20 \times 10^{-18} \pm 1.90 \times 10^{-19}\ g$$

$$Mass\ of\ ligand\ monolayer\ per\ SPION = \left[\frac{L_{pred}}{N_A} x MW_{reacted\ amino\ silane\ ligand} \right]$$

$$Mass\ of\ ligand\ monolayer\ per\ SPION = 5.58 \times 10^{-19} \pm 5.57 \times 10^{-20}\ g$$

Therefore,

the total mass of one A-SPION

$$= Mass\ of\ 1\ SPION + Mass\ of\ ligand\ monolayer\ per\ SPION$$

the total mass of one A-SPION = $1.76 \times 10^{-18} \pm 2.40 \times 10^{-19}$ g

$$\%\ mass\ of\ Fe_3O_4 = \frac{Mass\ of\ one\ SPION}{Total\ mass\ of\ a\ ligand\ coated\ SPION}\ x\ 100$$

$$\%\ mass\ of\ Fe_3O_4 = 68.29 \pm 2.99\ \%$$

$$\%\ mass\ of\ ligand\ shell = \frac{Mass\ of\ ligand\ monolayer\ per\ SPION}{Total\ mass\ of\ a\ ligand\ coated\ SPION}\ x\ 100$$

$$\%\ mass\ of\ ligand\ shell = 31.71 \pm 2.99\ \%$$

Using the percentage mass values for the contribution of Fe_3O_4 versus the contribution of the ligand shell, the molar composition of A-SPION with one monolayer of reacted APTMS could be written as $(Fe_3O_4)_1(C_3H_8NSiO_3)_{0.8}$.

The theoretical percentage mass for one monolayer of reacted amino silane ligands around a 7.6 nm Fe_3O_4 core was found as 31.71 ± 2.99 %. This percentage mass value includes the percentage mass contribution from the inorganic silane, which is not thermally decomposed during the TGA. The theoretical percentage mass contribution of the silane (SiO_2) was therefore deducted to give a predicted TGA percentage for one monolayer of reacted APTMS. The theoretical percentage mass

contribution from C, H and N was also used to predict the elemental analysis. The predicted results are shown in **Table 3.1**.

Table 3.1. Predicted elemental percentage weight and TGA weight loss values for one monolayer of amino silane ligands surrounding a 7.6 nm SPION.

Element	% mass for reacted amino silane ligand	% mass for reacted amino silane ligand (scaled to 31.71 %)
C	26.85	8.51
H	6.01	1.91
N	10.44	3.31
O	35.77	11.34
Si	20.93	6.64
Predicted TGA weight loss	43.30	13.73
Total % mass	100	31.71

The actual measured results obtained from the elemental analysis and TGA were used to determine the actual composition of A-SPION, **Table 3.2**. The actual results could then be used to calculate the average number of APTMS ligands reacted with the SPION surface with diameter of 7.6 nm and thus determine the average number of monolayer(s) of amino silane (**Figure 3.7**).

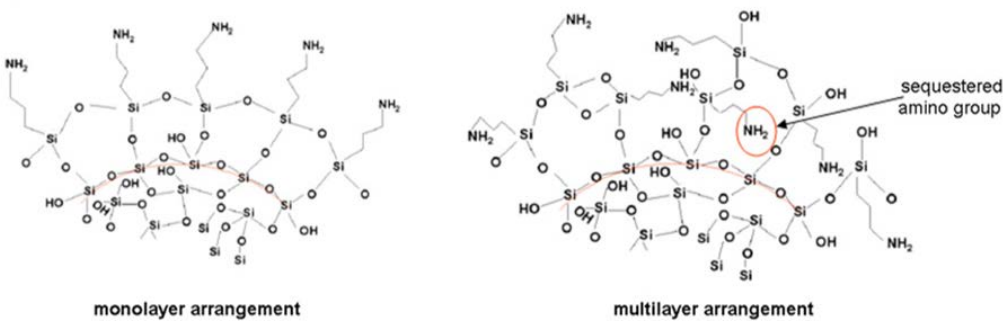

Figure 3.7. Representation of monolayer and multilayer arrangements through the polymerisation of the APTMS on the surface of a nanoparticle. Figure taken from reference.[31]

From the TGA measurements taken for A-SPIONs, there was 6.72 % weight loss measured from ambient to 120 °C which was considered to be residual solvent

(ethanol and toluene). The total weight loss found for A-SPIONs was 34.88 %, **Figure 3.8**.

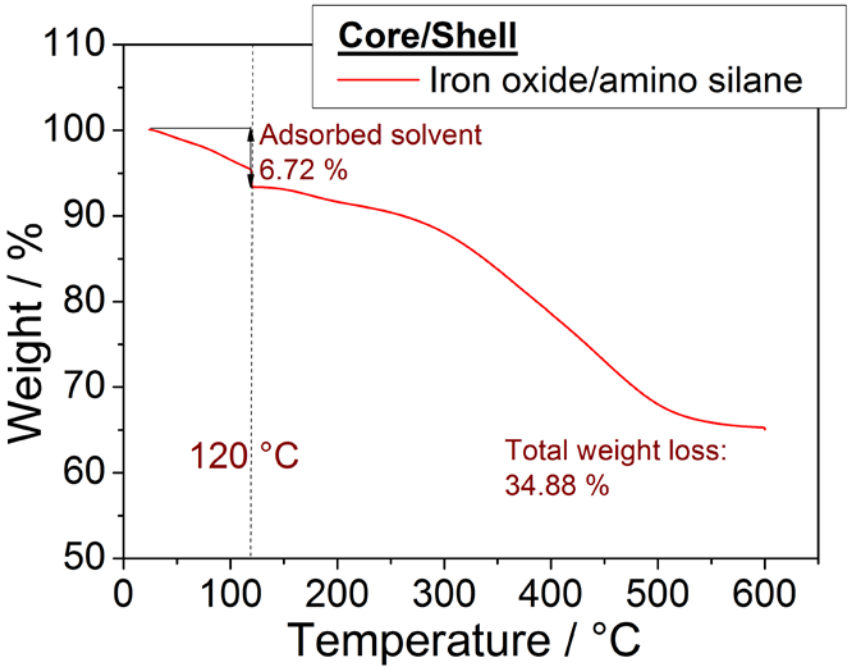

Figure 3.8. Thermal gravimetric analysis of A-SPIONs showing total weight loss of 34.88 %. The dashed vertical line shows the position of the isotherm held at 120 °C for the removal of adsorbed solvent.

Table 3.2 summarises experimental elemental analysis results, TGA weight loss and calculations of weight contributions from APTMS, residual oleic acid, adsorbed solvent and SPION core. From the experimental procedure, the nitrogen content of the A-SPION product could only be attributed to APTMS ligands reacted onto the surface. Using the weight percentage measured for nitrogen, it was possible to calculate the carbon and hydrogen contribution for APTMS. **Table 3.2** shows that, from the elemental analysis data, an excess of carbon and hydrogen was observed compared to the expected values for a pure APTMS coverage. The excess contaminant carbon and hydrogen values left over of 9.17 % were attributed to residual oleic acid, the theoretical percentage C, H and O has been predicted in **Table 3.2**.

Table 3.2. Experimental and calculated elemental analysis and TGA weight loss values for dried A-SPION. Shaded areas show actual experimental values.

		Actual experimental values	Calculated from Nitrogen content	Calculated from TGA weight loss			
			APTMS	Residual Oleic Acid	Residual solvent	Total values	SPION (as Fe_3O_4)
Elemental analysis	C	23.6	11.78	7.02	4.8	23.6	
	H	4.3	2.64	1.11	0.55	4.3	
	N	4.58	4.58			4.58	
	O		15.69	1.04	*1.37*	18.1	11.52
	Si		9.18			9.18	
	Fe						28.72
	Total weight %	32.48	43.87	9.17	6.72	59.76	40.25
TGA	Weight loss	34.88	18.99	9.17	6.72	34.88	

The weight composition of A-SPION was determined as (Fe_3O_4), 40.25 %, (APTMS), 43.87 % (oleic acid), 9.17 % and (solvent), 6.72 %. The molar composition of A-SPION was determined as $(Fe_3O_4)_1(C_3H_8NSiO_3)_{1.9}$ $(C_{18}H_{34}O_2)_{0.2}(C_6H_8O_1)_{0.4}$. The amount of APTMS on the A-SPION (with residual organic contaminate removed) corresponded to 2.2 equivalents of the value calculated earlier for a monolayer so the number of APTMS ligands on the surface (L_{exp}) was estimated at 5541 (5.29 % N).

3.2.3 Preparation of *N*-Succinimidyl Functional Poly[2-(methacryroyloxy)ethylphosphorylcholine] (*NS*-pMPC) Homopolymers by Atom Transfer Radical Polymerisation (ATRP)

The conditions for the ATRP of MPC were adapted from those reported by Samanta *et al.*[24] who synthesised pMPC hompolymers by ATRP using *N*-succinimidyl-2-bromoisobutyrate (NSBriB) initiator in a methanol/dimethyl sulfoxide (DMSO) (1/3 v/v) solvent mix at ambient using Cu(I)Br/2,2-bipyridine (bipy) catalyst. For the ATRP of MPC carried out here, Cu(I)Cl/bipy catalyst was used with NSBriB initiator in methanol/DMSO (2/3 v/v) at 22 °C. The solvent ratio modified by reducing the amount of DMSO in order to improve control since the Đ reported for pMPC polymers with target DP_n of 7.5 kDa and 11kDa were found at 1.3 and 1.5 respectively. To demonstrate if the MPC polymers were suitable for the colloidal stabilisation of SPIONs in PBS solution at pH 7.4 and 37 °C, MPC polymers with target DP_n of 15, 50 and 100 were prepared (labelled with *NS*-pMPC ID of 1, 2 and 3 respectively) and later on reacted with A-SPIONs. Proton nuclear magnetic resonance (^{1}H-NMR) and gel permeation chromatography (GPC) results for polymers 1-3 (**Figure 3.9** and **Table 3.3**) indicated *NS*-pMPC_n polymers were successfully prepared. The DP_n obtained by triple detection-GPC (TD-GPC) were found as 15, 45 and 133 with Đ of 1.09, 1.12 and 1.21 respectively. By ^{1}H-NMR, a DP_n of 24, 75 and 144 was found. Differences in DP_n and M_n for both techniques were likely to be observed since GPC determines molecular weight based on hydrodynamic volume against a narrow standard that is not of the same composition as the polymer samples measured. The samples measured are not likely to have the same degree of solubility and thus hydrodynamic volume at a particular molecular

weight in the solvent so results measured are only relative to the standard. For ^{1}H-NMR, no calibration was required so DP_n and M_n results are fairly accurate.[32]

Table 3.3. GPC and ^{1}H-NMR results for *NS*-pMPC polymers. GPC samples were ran in PBS solution pH 7.4 eluent at 50 °C. Samples were analysed by TD-GPC using a narrow standard of polyethylene oxide (PEO) with MW of 22 kDa. Data in brackets represents samples analysed using PEO conventional calibration standards.

***NS*-pMPC ID**	**DP_{nTheo}**	**^{1}H-NMR**		**GPC**		
		DP_n	**M_n / g mol^{-1}**	**DP_n**	**M_n / g mol^{-1}**	**Đ**
1	15	24	7,000	15	4,500	1.09
2	50	75	22,100	45	13,400	1.12
3	100	144	42,500	133	39,200	1.21
4	50	50	15,000	139 (42)	41,000 (12,500)	1.10 (1.20)
5	40	29	9,000	34	10,100	1.08

The kinetics for the polymerisation of MPC were studied to understand if the reaction conditions were suitable to obtain a low Đ and expected M_n. Samples were taken during an ATRP reaction of MPC with target DP_n of 50 and analysed by ^{1}H-NMR and GPC,(*NS*-pMPC ID 4, **Table 3.3**) with the results plotted in **Figure 3.10**. Polymer conversion was monitored by ^{1}H-NMR through the disappearance of vinyl signals at δ 5.5−6.0. The $M_{n(GPC)}$ versus conversion plot and kinetic plot, **Figure 3.10A and C**, shows a step at low conversion with higher M_n than theoretically predicted. The rapid increase in M_n at low conversion corresponds to a slow initiation step.[33] This behaviour is typically found when chains containing several monomer units are more reactive than the initiator itself.[34] The chains that are already formed propagate more readily than the activation of the initiator allowing polymer chains with higher M_n to be formed than theoretically expected at low conversion. This could be explained by looking at the solubility of the NSBriB initiator, which is more hydrophobic than the highly hydrophilic MPC monomer. The rate of reactivity of the more hydrophobic NSBriB initiator with highly

hydrophilic MPC monomer could initially be lower when compared with the rate of reactivity of NSBriB initator containing several MPC monomer units attached since the initiator containing reacted hydrophilic monomer groups increases the overall hydrophilicity. It is possible to improve the initiating rate by increasing the temperature of the reaction. The activation energy of NSBriB initiator could be lowered if the temperature of the ATRP reaction was increased. Increasing the temperature could however increase the rate of polymerisation and termination thus potentially yielding polymers with higher Đ.

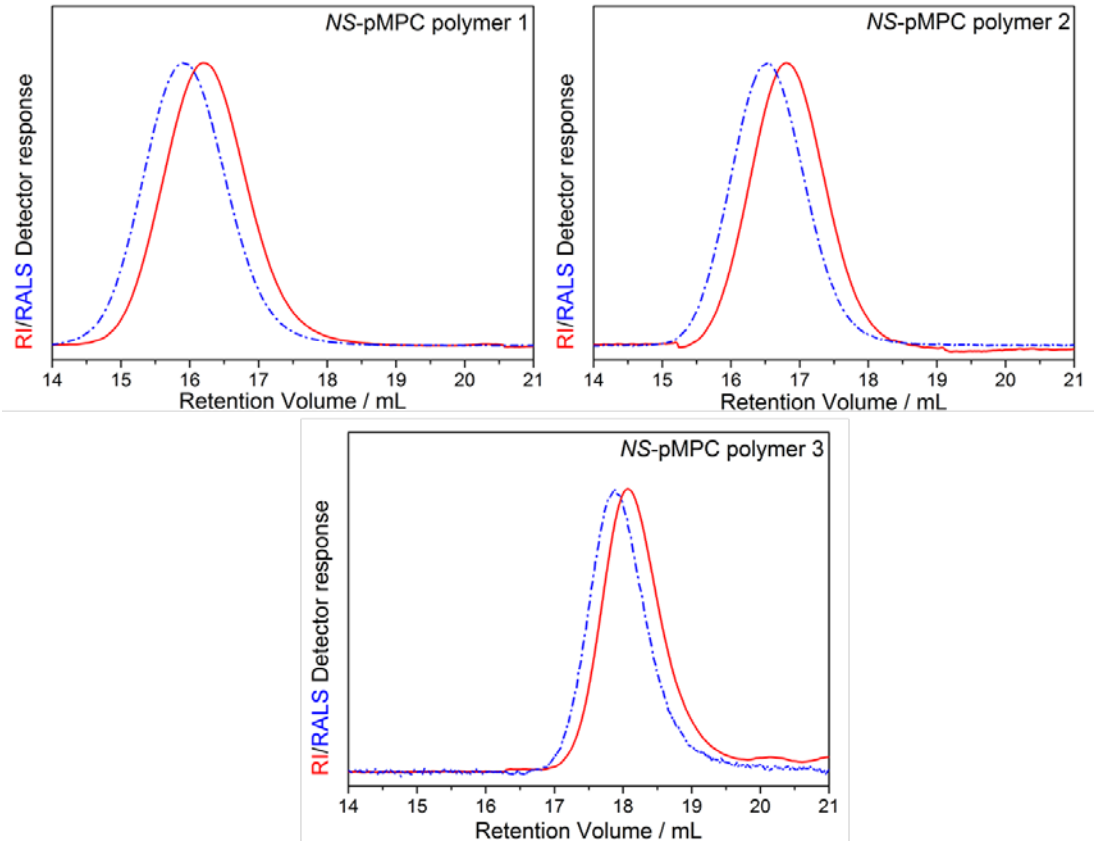

Figure 3.9. GPC chromatograms of *NS*-pMPC polymers 1, 2 and 3 synthesised by ATRP showing refractive index (RI) and right angle light scattering (RALS) detector response (PBS solution pH 7.4 eluent, 50 °C, TD-GPC using PEO 22 kDa narrow standard).

Despite the step at low conversion (3,500 g mol^{-1} at 5% conversion which should be 590 g mol^{-1}) with high M_n polymers, the Đ remained around 1.20 throughout the polymerisation (**Figure 3.10A**), which indicates the dispersity created at the start is maintained throughout the polymerisation which is expected during a controlled polymerisation reaction. **Figure 3.10C** also shows that the reaction follows near

linear 1st order kinetics, indicating the concentration of radicals in the reaction remains the same throughout the polymerisation.

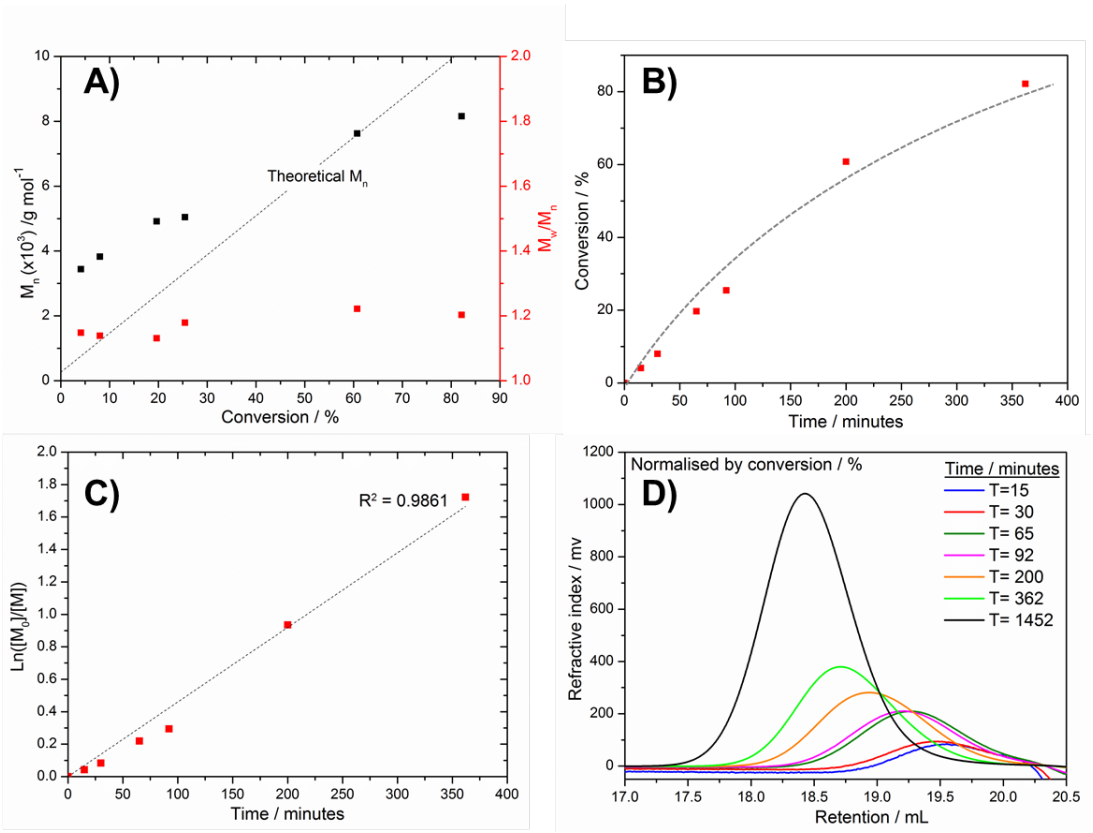

Figure 3.10. Polymerisation kinetics of *NS*-pMPC$_{40}$ (GPC: PBS solution pH 7.4 eluent, 50 °C, set of PEO calibration standards with M_p values of 125,8, 909.5, 442.8, 116.3, 62.1, 23.5, 12.1, 12, 3.9, 1.5 kDa, differential refractive index (DRI) detector used). A) $M_{n(GPC)}$ versus conversion plot, B) monomer conversion versus time plot, C) polymer kinetic plot and D) GPC plot of the kinetic samples taken.

At 200 minutes, the polymer conversion had reached 60 % at 22 °C (**Figure 3.10B**). GPC results show as expected, **Figure 3.10D,** a reduction in the retention time of each kinetic sample whilst the refractive index (RI) normalised by percentage conversion increases with the growth of polymer with time. GPC results were obtained using conventional calibration with a set of polyethylene oxide (PEO) calibration standards to produce a calibration curve using the DRI detector, **Table 3.3** (*NS*-pMPC ID 4). This calibration method is commonly used for analysing kinetic samples when the concentration of polymer is unknown. The results obtained are only relative to the standards as they could be somewhat far from the theoretical values. The calibration standards used have a different composition to the samples

and therefore the solubility and thus hydrodynamic size in solution would be different compared to the measured samples.

The solution behaviour of pMPC with target DP_n of 50 (*NS*-pMPC ID 4) was checked by differential scanning calorimetry (DSC) using 1 % pMPC in PBS. DSC was chosen as the technique to measure LCST because it has been found to be more reliable regardless of polymer concentration when compared to the LCST value determined by UV-Vis.[35] A DSC thermogram of $pMPC_{50}$ is shown in **Figure 3.11**. An LCST peak would be expected in the endothermic direction at which the temperature at the minimum point of the endotherm peak would be referred to as the LCST. From the DSC measurement, an LCST was not observed suggesting that the LCST occurs higher than that measured up to 80 °C or that pMPC simply does not have an LCST. There is a slight dip in the curve around 43 °C, but this is not prominent enough to suggest a peak for the LCST of *NS*-$pMPC_{50}$.

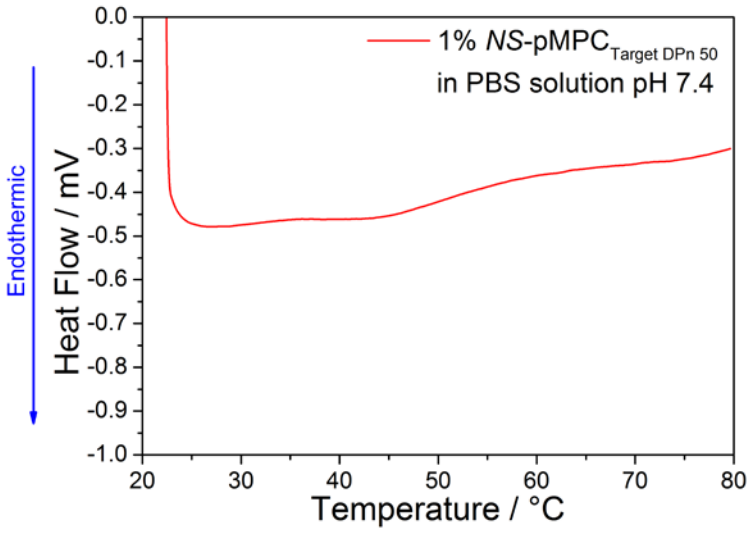

Figure 3.11. Differential scanning calorimetry (DSC) themogram for 1 % *NS*-$pMPC_{50}$ in PBS solution carried out for the measurement of a lower critical solution temperature (LCST).

3.2.4 Amidation Reaction of *NS*-pMPC Homopolymers with A-SPIONs.

As mentioned previously, A-SPIONs are only dispersible in alcohols and will aggregate and eventually precipitate when in water or PBS. Ethanol was found to provide the best dispersion of A-SPIONs. However, A-SPIONs are not fully

dispersible and colloidally stable in this solvent since A-SPIONs slightly aggregate/cluster in the dispersion. This was confirmed by the difficulty in obtaining size measurements by DLS. Protonation of the A-SPION surface by use of a weak acid solution breaks up aggregates into a colloidal dispersion through peptization whereby hydrogen protons protonate amines present on the SPION surface and provides better stability, however in terms of storage this is unsuitable since acidic solutions will dissolve the SPION core.[31, 36, 37] The conditions for the amidation coupling reaction of A-SPIONs with *NS*-pMPC$_n$ were determined by assessing the solubility of *NS*-pMPC (of all MWs, *NS*-pMPC ID 1-3) with various solvents (which were miscible with ethanol). It was found that *NS*-pMPC polymers were insoluble in a wide range of solvents (such as dioxane, ethyl acetate, THF, DMSO, dimethylformamide (DMF)). The insolubility in DMSO and DMF led to difficulties; DMSO–d_6 could not be used as a solvent for NMR analysis and that DMF could not be used as the eluent for GPC analysis. The only solvents found to solubilise *NS*-pMPC$_n$ were water (or water-based solutions such as PBS), ethanol and methanol. The solubility of *NS*-pMPC$_n$ in methanol was higher than that found for ethanol, as indicated by the time taken to full dissolve the polymer. The solubility of *NS*-pMPC$_n$ in water was excellent (instant dissolution), however due to induced aggregation of the A-SPIONs in water and the issue that the *N*-succinimidyl activated ester would be actively hydrolysed in the presence of water and hence have a negative effect on the reactivity of the *N*-succinimidyl functional group, water was ruled out as a solvent for amidation.[38] Instead, methanol was used as the solvent for *NS*-pMPC for the amidation reaction with A-SPIONs pre-dispersed in ethanol since *NS*-pMPC had a greater solubility in methanol compared to ethanol. *NS*-pMPC was pre-dissolved in methanol prior to the amidation reaction and remained miscible after addition into A-SPIONs dispersed in ethanol.

The amount of *NS*-pMPC$_n$ required for the complete amidation reaction with A-SPIONs was predicted using the number of APTMS ligands per A-SPION (L_{exp}) and the MW of the polymer, which was calculated using the equations below:

$$SA_{SPION} = 4\pi r^2$$

Predicted number of APTMS ligands that can fit as one monolayer on a 7.6 nm SPION, L_{pred} 2505± 249 ligands.

$$L_{exp} = \frac{SA_{SPION}}{Footprint_{APTMS}} . N_{APTMS\ monolayers}$$

$$L_{exp} = 2505 \pm 249 \text{ ligands}$$

For example, the amount of *NS*-pMPC$_n$, *A*, with DP$_n$ of 29 (MW of 9,000 g mol^{-1}) required for 10 mg of A-SPIONs containing one monolayer of amino silane ligands:

$$A = \left[\frac{\left(\left[\rho_{Fe_3O_4}.\left(\left[\frac{4}{3}\pi r^3\right]x10^{-21}\right)\right]+\left[\left(\frac{L_{exp}}{N_A}\right).MW_{reacted\ APTMS}\right]\right)^{-1}}{100}\right] . \left[\frac{L_{exp}}{N_A} xMW_{polymer}\right]$$

$$A = 0.462 \text{ g (1 equivalent)}$$

During a typical amidation coupling reaction for the synthesis of pMPC$_n$-SPIONs, a solution of pre-sonicated A-SPIONs in ethanol was added to the *NS*-pMPC$_{29}$ polymer which was solubilised in methanol was sonicated for 1 hour and left to rotary mix for 15 hours at 22 °C before dialysis into DIW.

To check if the amidation reaction was successful, an experiment was set up where APTMS would be reacted with *NS*-homopolymer using the same polymer concentration of *NS*-homopolymer in methanol added to the same molar ratio of APTMS in ethanol to that of a standard amidation reaction of *NS*-polymer with A-SPIONs. A-SPIONs were not used in this test experiment due to the magnetic interference from the SPIONs during ^{1}H-NMR analysis. The test experiment reaction conditions were simulated to those of the standard amidation procedure. Briefly, the 15 mL reaction vial was sonicated for 1 hour and left to mix on a rotary mixer for >15 hours. **Figure 3.12** shows the ^{1}H-NMR data for comparison of APTMS in deuterated chloroform ($CDCl_3$), *NS*-polymer in deuterated methanol (MeOD) and APTMS plus *NS*-Polymer in MeOD after amidation reaction.

The ^{1}H-NMR spectra, **Figure 3.12**, confirmed the successful amidation reaction of the primary amine present in the APTMS molecule with the *N*-succinimidyl activated ester group on the polymer. The 1 H singlet found around δ 8.5 ppm indicated the formation of the amide bond which is not present in the ^{1}H-NMR spectra for the NHS initiator (400 MHz, chloroform-*d*, ppm): δ 2.2 (s, 6 H, CH_3), 2.9 (s, 4 H, CH_2) (see Chapter 2 Figure 2.7 section 2.5.1).

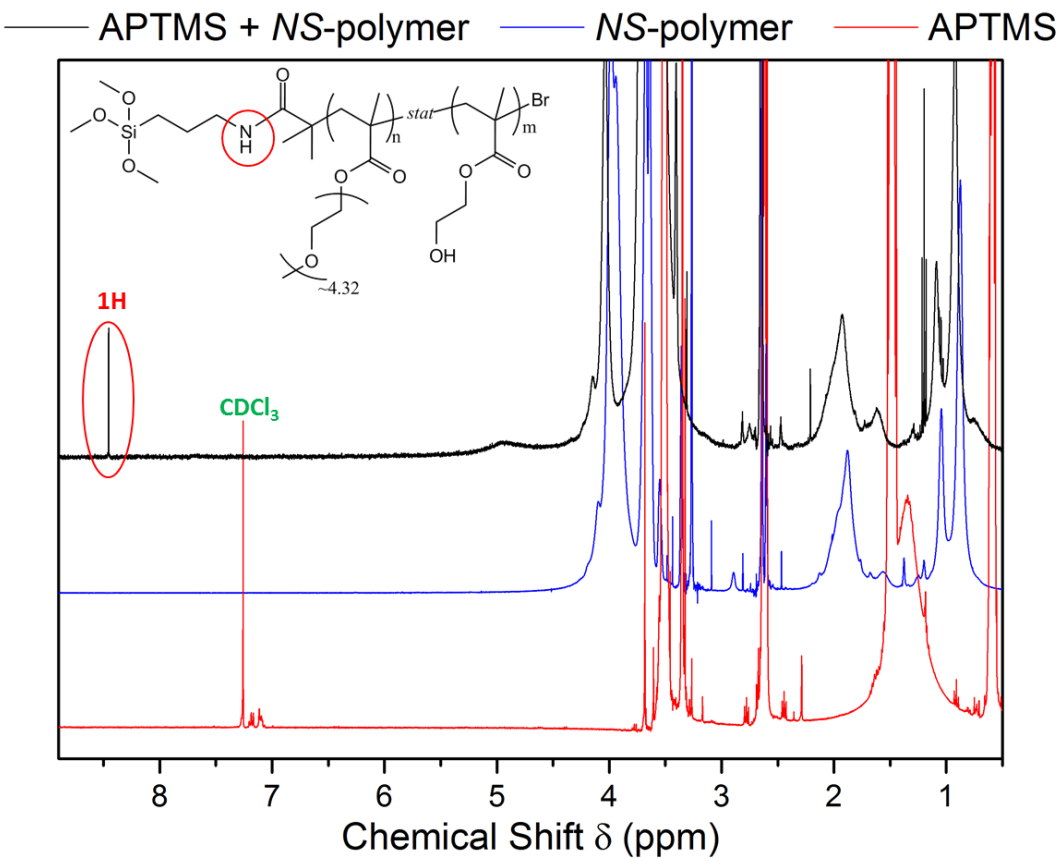

Figure 3.12. [1]H-NMR data showing the amide proton from the amidation reaction of APTMS with *N*-succinimidyl functional polymer. APTMS analysed in $CDCl_3$, polymer-containing samples analysed in DMSO-d6.

FT-IR was also used to confirm the formation of the amide bond through the measurement of *NS*-$pMPC_{29}$ reacted A-SPIONs, **Figure 3.17C**. Two bands with wavenumbers 1600 to 1700 cm^{-1} were observed and can be assigned as C=O or/and N-H bonds from an amide linkage.[39]

Amine functional iron oxide nanoparticles have been known to be used in the removal of Cu(II) and other heavy metal ions from solution.[40-42] The co-ordination interaction of the amine on the surface of the SPIONs with Cu(II) ions in solution can potentially interfere with the amidation reaction. To test whether this would be the case, two amidation reactions were set up. In one reaction vial, *NS*-$pMPC_{29}$ with copper removed (using Dowex MSC-1 ion exchange resin) was reacted with A-SPIONs in ethanol/methanol mixture. In another reaction vial, *NS*-$pMPC_{29}$ without removing copper was reacted with A-SPIONs in ethanol/methanol mixture. The co-ordination of amine groups with Cu(II) ions in solution and thus interference of the

amidation reaction was confirmed as indicated by the differences in the colloidal stability of the NPs in water, **Figure 3.13**. Here, vials A and B represent the reaction of A-SPIONs with *NS*-pMPC$_{30}$ whereby for vial A, Cu(II) ions were removed from the mixture prior to the reaction using Dowex MSC-1 ion exchange resin. For vial B, no Dowex MSC-1 ion exchange resin was used so that Cu(II) ions could be kept in the mixture during the reaction. The NPs in both vials were then transferred to water through dialysis and the appearance and stability of the solutions were then assessed. The transparent appearance of the liquid in vial A confirmed a colloidally-stable suspension was achieved whereas vial B confirmed the interference of Cu(II) ions with the amidation reaction through the co-ordination of amine groups which was indicated by the cloudy appearance. Cloudy dispersions are an indication of aggregates in the solution/suspension.

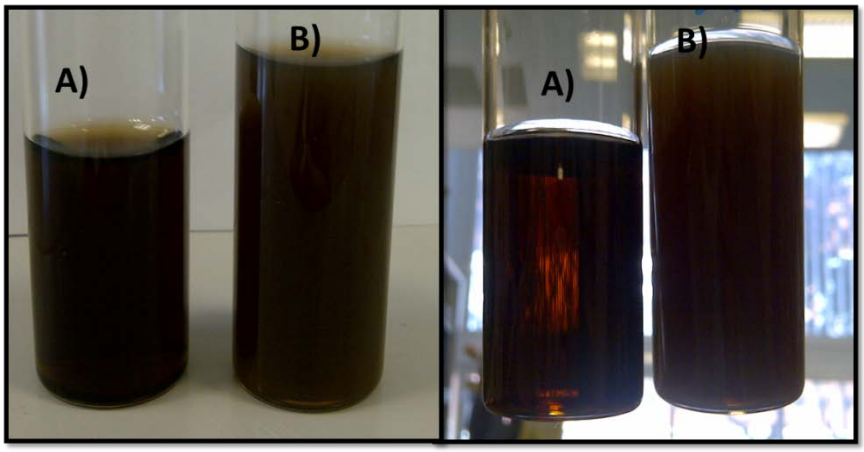

Figure 3.13. The effect of copper removal prior to amidation reaction. Vials show two different pMPC-SPION samples after reaction and dialysis into water. Vials show amidation reactions carried out with and without copper removal, vials labelled A) and B) respectively.

To determine the optimum polymer chain length and MW to be used for the stabilisation of SPIONs in PBS, three *NS*-pMPC$_n$ homopolymers (*NS*-pMPC ID 1-3), which had been prepared with DP$_n$ of 15, 45 and 133 (original DP$_n$s of 15, 50 and 100 were originally targeted to start with. See Chapter 2, Table 2.1), were pre-dissolved in methanol before reaction of each with A-SPIONs which were dispersed in ethanol. The samples were transferred to water *via* dialysis and then PBS at pH 7.4. The colloidal stability was assessed through the appearance of the suspension over a period of 24 h since it has been established that A-SPIONs are unstable in water or PBS. Colloidal stability after this time is an indication of

successful amidation reactions on the A-SPION surface. **Figure 3.14** shows images of the three pMPC$_n$-SPION samples at the same SPION concentration in PBS after a period of 24 h. An image of a sample containing just A-SPIONs was also shown to demonstrate their instability in PBS.

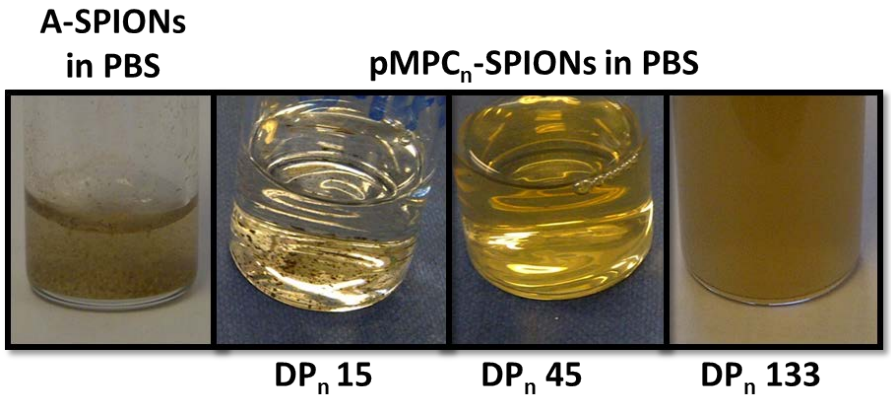

Figure 3.14. Initial screening of *NS*-pMPC$_n$ of different MW reacted with A-SPIONs. All samples are at the same SPION concentration.

The results from observation of the initial screening indicated that the sample reacted with *NS*-pMPC$_n$ with highest DP$_n$ of 133 gave suspended NPs in solution but the cloudy appearance of the sample indicated the presence of small aggregates. This is most likely to be caused by a low coupling efficiency of the polymer with the NP surface due to steric hindrance issues caused by the long polymer chain length. For the sample reacted with *NS*-pMPC$_n$ containing the lowest DP$_n$ of 15, SPION aggregates were observed thus indicating the polymer chain length was too short and insufficient at providing space between NPs for steric stabilisation. For the sample containing *NS*-pMPC$_n$ with DP$_n$ of 45, SPIONs were provided with the best colloidal stability which was indicated by the transparency of the sample, which suggested a good balance of polymer coupling and polymer chain length for steric stabilisation in PBS was achieved. At this stage, pMPC coated SPIONs (pMPC-SPIONs) with polymer DP$_n$ around 45 were thus prepared and further investigated.

3.3 Poly[2-(methacryroyloxy)ethylphosphorylcholine]-Coated SPIONs (pMPC-SPIONs): Synthesis, Colloidal Stability and Evaluation for Stem Cell Labelling.

3.3.1 Preparation of pMPC-SPIONs

For the preparation of pMPC$_n$-SPIONs with optimal polymer chain length, the synthesis of pMPC$_n$ homopolymer with target DP$_n$ of 40 and MW of 12,000 g mol^{-1} was carried out (**Table 3.3**, *NS*-pMPC ID 5). The characterisation of the final precipitated freeze-dried polymer by ^{1}H-NMR in CD_3OD indicated a DP$_n$ of 29 and an MW 9,000 g mol^{-1} was obtained, **Figure 3.15**. This was deduced by setting the integration for the 6H end group methyl protons as 6 found on the *N*-succinimidyl initiating group (**Figure 3.15** labelled 'g') and then integrating either the 6H or 2H protons from the phosphorylcholine group on the polymer chain which were found as 174 and 57 respectively (**Figure 3.15** labelled 'a' and 'b'). Dividing 174 by 6 or 57 by 2 gives DP$_n$ as 29. PolyMPC is highly hygroscopic and readily absorbs moisture.[43]

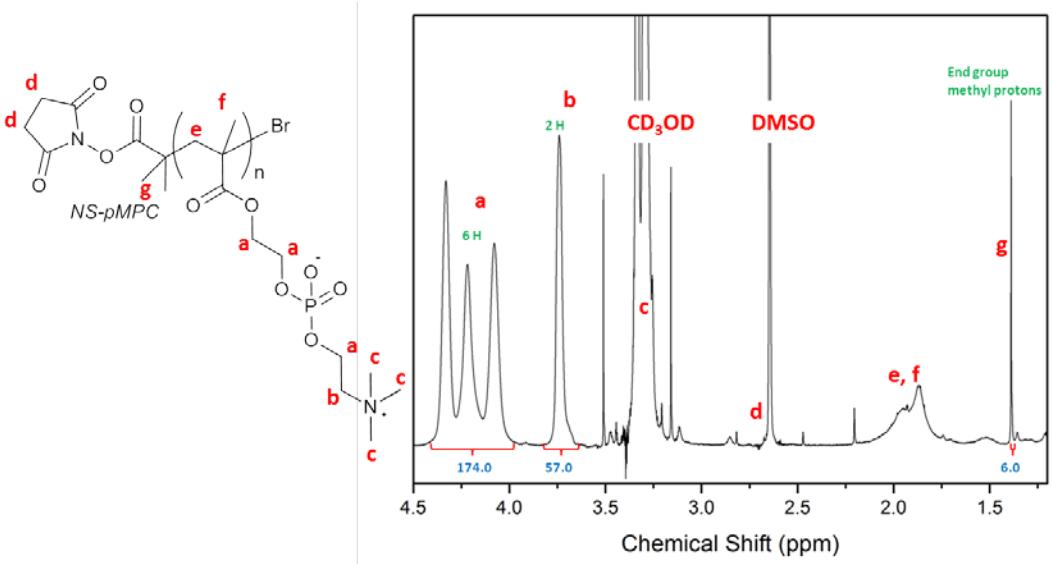

Figure 3.15. ^{1}H-NMR spectrum of the final precipitated *NS*-pMPC polymer in CD_3OD indicated a DP$_n$ of 29, MW 9,000 g mol^{-1} deduced from the polymer chain end group protons 'g' against integration for H protons on polymer 'a' and 'b'.

To accurately determine the mass of pMPC weighed for TD-GPC analysis, a sample was measured by TGA at the same time pMPC was weighed for GPC analysis in

order to determine the percentage weight contribution by water. This was then deducted from the weight of pMPC weighed. Aqueous TD-GPC showed the polymer had a monodisperse distribution with M_n 10,100 g mol^{-1} and M_n/M_w of 1.08.

In the case for the synthesis of pMPC$_{29}$-SPIONs, previously prepared A-SPIONs were used. As multiple amino silane layers are present on the surface (2.2 monolayers, 5541 amino silane ligands), it is expected that not all amino-groups will be available for reaction. To ensure maximum coverage, 1 equivalent of polymer per amino silane ligand on the A-SPION was used for the coupling reaction. The appearance of pMPC$_{29}$-SPIONs after the amidation reaction provided a transparent and clear liquid, **Figure 3.16A**. After dialysis, **Figure 3.16B and C**, free polymer remaining from pMPC$_{29}$-SPIONs was separated by passing the particles in PBS pH 7.4 through a Sephadex G25 gel filtration chromatography column, **Figure 3.16D**. Two 1 mL aliquots of the pMPC$_{29}$-SPIONs were placed in UV-Vis cuvettes, **Figure 3.16E**, for colloidal stability studies at ambient and at 37 °C, **section 3.3.3**.

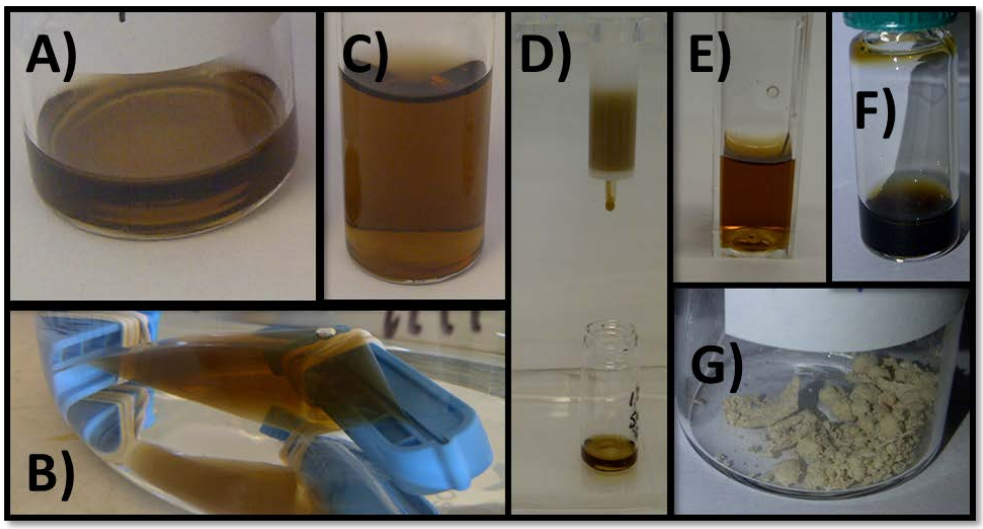

Figure 3.16. Images of pMPC$_{29}$-SPIONs through the sample preparation process. A) NPs after amidation in methanol/ethanol, B) NPs during dialysis into DIW, C) NPs after dialysis into water, D) NPs in PBS pH 7.4 passing through G25 sephadex column, E) NPs after G25 in PBS pH 7.4, F) NPs at 1 mg Fe mL^{-1} in PBS pH 7.4, G) NPs after freeze drying.

For the determination of polymer coverage, pMPC$_{29}$-SPIONs were dialysed back into DIW for the removal of inorganic PBS salt prior to being cryogenically frozen in liquid nitrogen and freeze-dried, **Figure 3.16G**, in preparation for TGA and

elemental analysis. After freeze-drying, the $pMPC_{29}$-SPIONs appeared cream in colour with a light fluffy texture.

3.3.2 Nanoparticle Characterisation

Figure 3.17 shows FT-IR spectra comparing OA-SPIONs, A-SPIONs and $pMPC_{29}$-SPIONs, which show bands confirming their surface chemistry indicated by the assigned bonds to peaks at the relevant wavenumbers. In particular, bands for amide bonds (N-H and C=O) were found around 1500 - 1700 cm^{-1} and secondary amide band found at 3400 cm^{-1}.

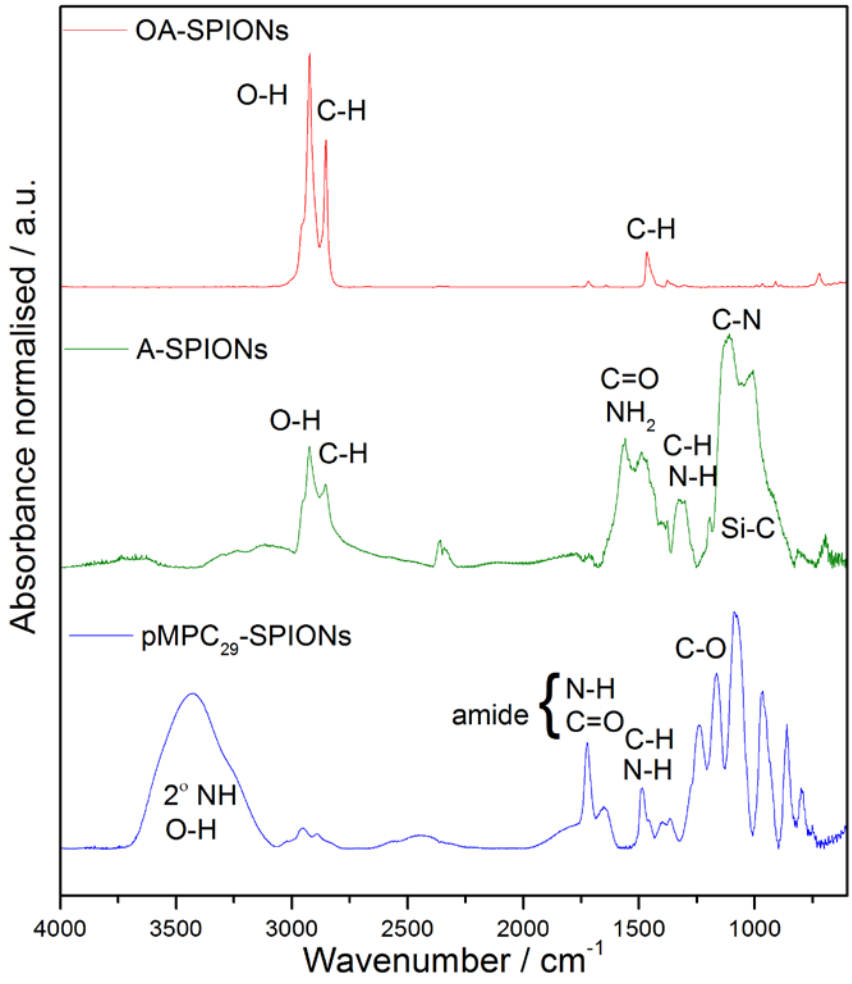

Figure 3.17. FT-IR absorbance spectra for A) OA-SPIONs, B) A-SPIONs and C) $pMPC_{29}$-SPIONs (after passing through a G25 gel filtration column). The wavenumber bands are collected as a percentage of transmission.

The pMPC-SPION sample was found to be wet due to the highly hygroscopic pMPC polymer, which was confirmed by TGA, **Figure 3.18**. The weight contribution of water was determined as 12.2%, which was the percentage weight loss calculated from ambient to 120 °C.

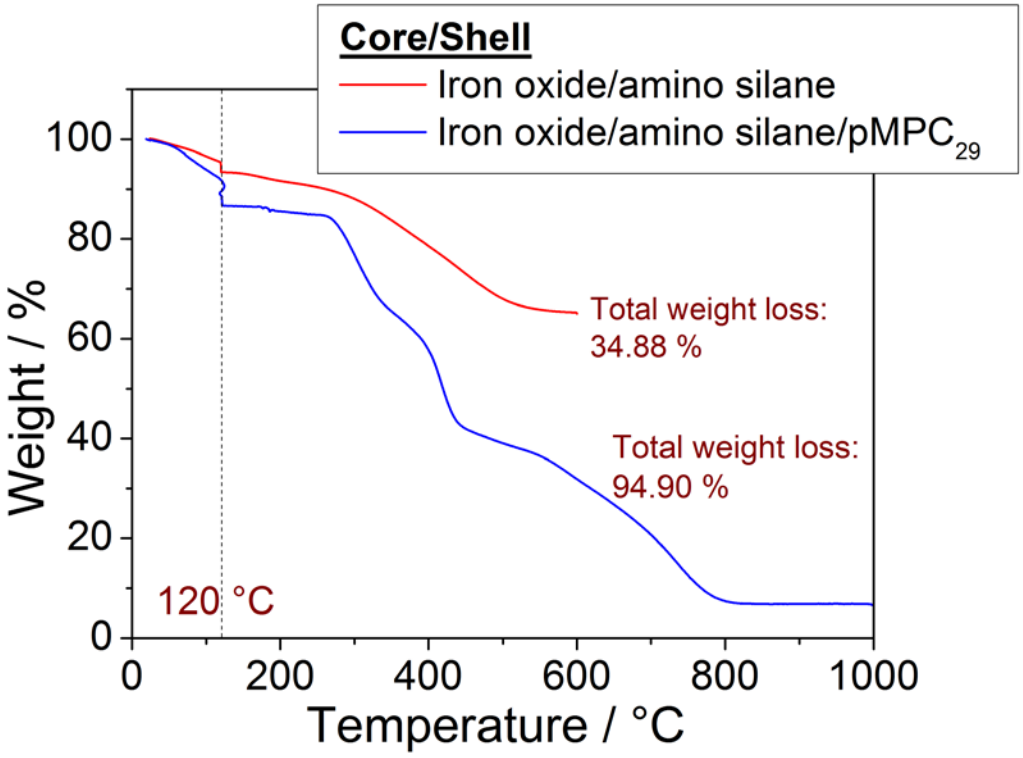

Figure 3.18. TGA spectra for A-SPIONs (red) and $pMPC_{29}$-SPIONs (blue). The dotted line represents the isotherm at temperature of 120 °C for the removal of adsorbed solvent.

The weight composition of the sample was determined as Fe_3O_4: 5.1%; APTMS/pMPC-coating: 82.7%. TGA total weight loss was found to be 94.90 %. Further determination of the composition of the coating of pMPC-SPION was achieved using TGA data (see **section 3.3.3 polymer coverage**). Size measurements by DLS of $pMPC_{29}$-SPIONs in PBS pH 7.4 showed that the SPIONS have two hydrodynamic radius peak height populations observed by the intensity weighted distribution: $R_{h,\ intensity}$ = 20 ± 2 nm and 108 ± 21 nm, $R_{h,\ mass}$ = 19 ± 2 nm, $R_{h,number}$ = 18 ± 2 nm, **Figure 3.19**.

TEM measurements of the core diameter = 8 ± 2 nm and polymer-coated particle diameter = 17 ± 2 nm, **Figure 3.20** and **Figure 3.21**. TEM images of

pMPC$_{29}$-SPIONs initially showed the presence of iron oxide cores only and no visualisation of pMPC shell due to having insufficient electron density.

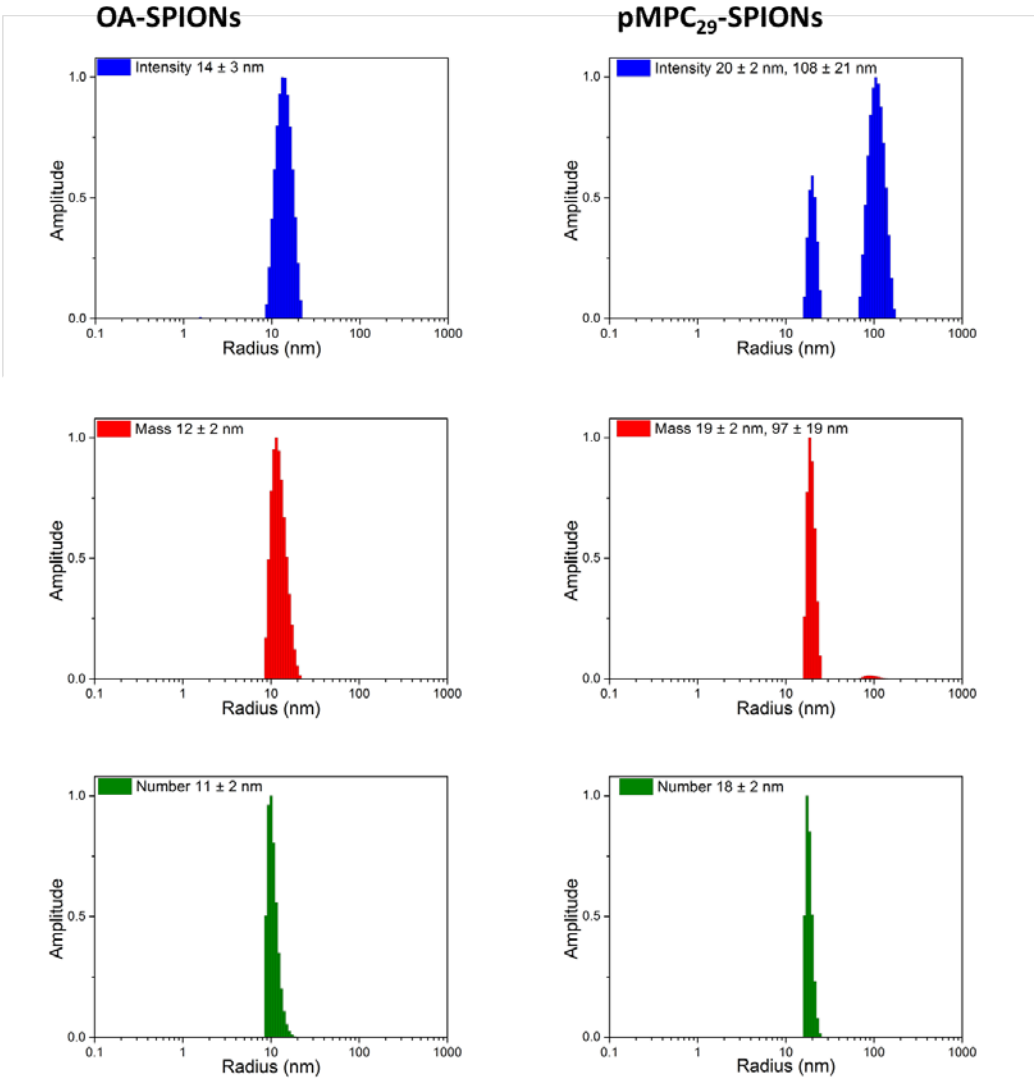

Figure 3.19. DLS solvodynamic and hydrodynamic radius peak height measurements for OA-SPION starting material in THF compared with pMPC$_{29}$-SPIONs in PBS solution pH 7.4.

To visualise the shell, several negative stain solutions containing an electron dense chemical were used which included uranyl acetate and phosphotungstic acid (PTA). The interaction and retention of a stain with the polymer shell provides visualisation of the polymeric shell. This was achieved using a 3 % PTA solution and not with uranyl acetate. The pMPC shell stained using PTA allowed for polymer visualisation around the core, **Figure 3.21**. To prepare samples for staining, a 100 µL aliquot of 3% PTA was added to 100 µL aliquot of a dilute pMPC$_{29}$-SPION sample.

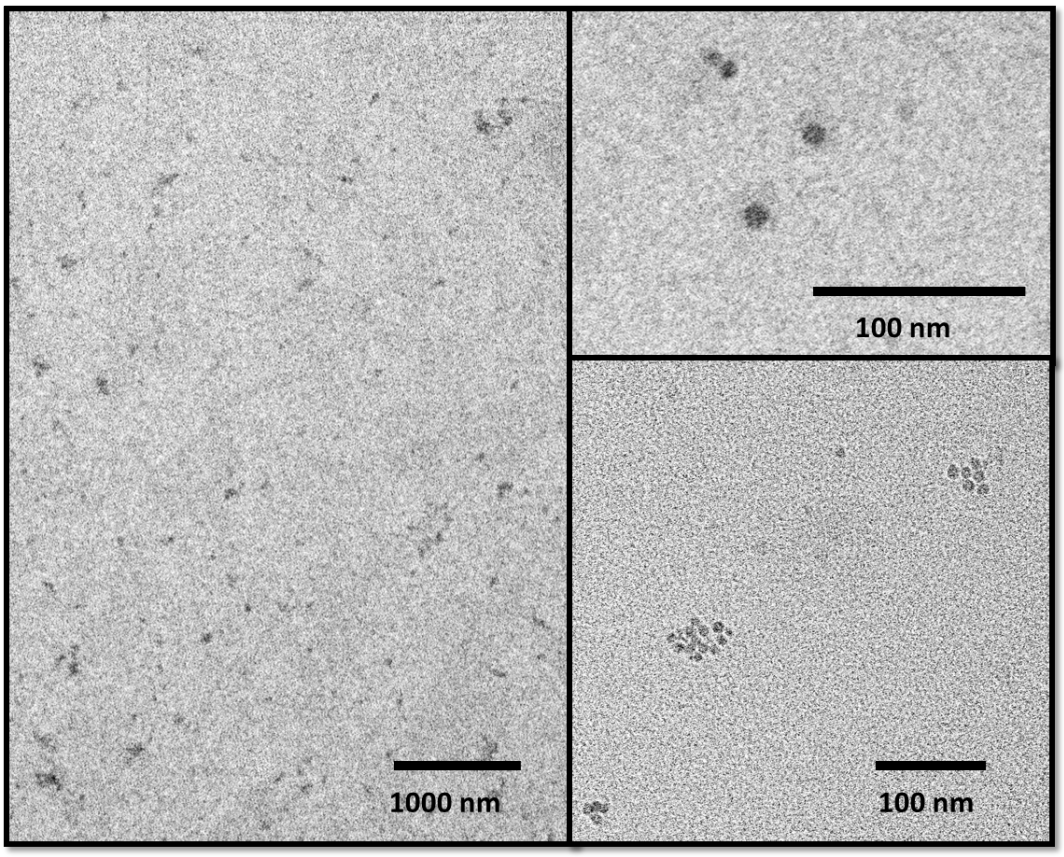

Figure 3.20. TEM images of $pMPC_{29}$-SPIONs unstained. Here, only the iron oxide cores can be visualised.

A drop of this mixture was placed onto parafilm and a carbon coated piloform TEM grid was placed upside down onto the surface of the drop. $pMPC_{29}$-SPIONs were left to adsorb to the TEM grid for 5-10 minutes. The TEM grid was then washed a couple of times with DIW and left to air dry. The average zeta potential value of $pMPC_{29}$-SPIONs in DIW pH 7 was near to neutral at +3.0 ± 0.3 mV indicating a good coverage with pMPC was achieved when compared to +25.6 ± 0.4 mV in DIW pH 8 measured for A-SPIONs.

To demonstrate whether $pMPC_{29}$-SPIONs were suitable for biomedical applications, R_2 relaxivity, cytotoxicity and stability to dissolution in conditions to those mimicking the lysosomal environment inside the cell were studied prior to cell labelling studies and the level of cell uptake (Chapter 6). To compare the results for the $pMPC_{29}$-SPIONs, a commercially available SPION reference material Molday Ion Rhodamine B (MIRB) from Biopal was used as a reference/control standard.

MIRB has been reported to contain a similar core size of 8 nm coated with cationic dextran containing a Rhodamine B fluorophore.[44]

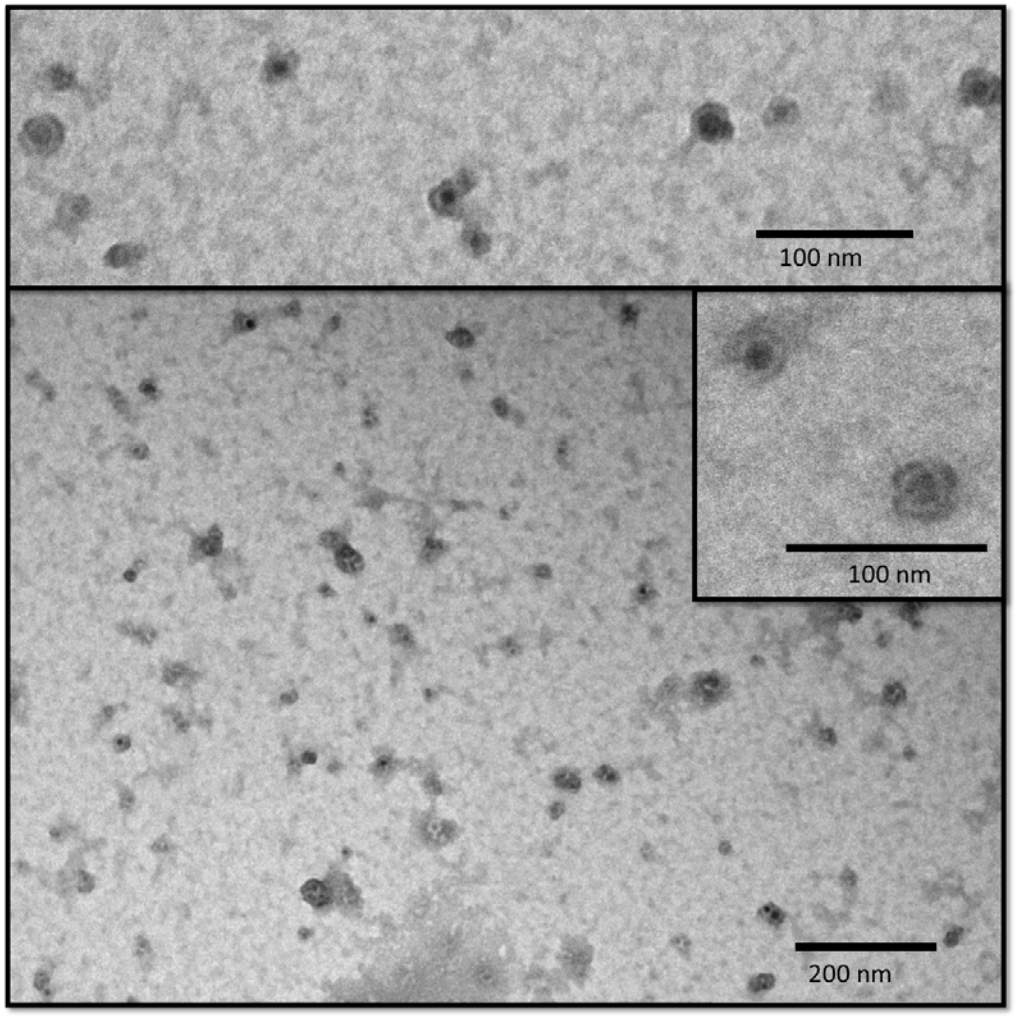

Figure 3.21: TEM images of $pMPC_{29}$-SPIONs stained with 3 % PTA solution demonstrating the consistency of polymer coverage and core-shell architecture across the sample.

Size measurements by DLS of MIRB in PBS pH 7.4 gave two hydrodynamic radius peak height populations observed by the intensity weighted distribution: $R_{h,\ intensity}$ = 19 ± 2 nm and 107 ± 45 nm, $R_{h,\ mass}$ = 18 ± 2 nm, $R_{h,number}$ = 17 ± 2 nm, **Figure 3.22**. By TEM, MIRB appeared to be distributed evenly on the grid. The iron oxide cores were not found to be spherical in shape, as expected from their co-precipitation synthetic route.[45] Endorem (a well-known former commercial clinical contrast agent which was withdrawn for commercial reasons) was also used for MRI measurements, as an additional reference due to its well-known high R_2 relaxivity.

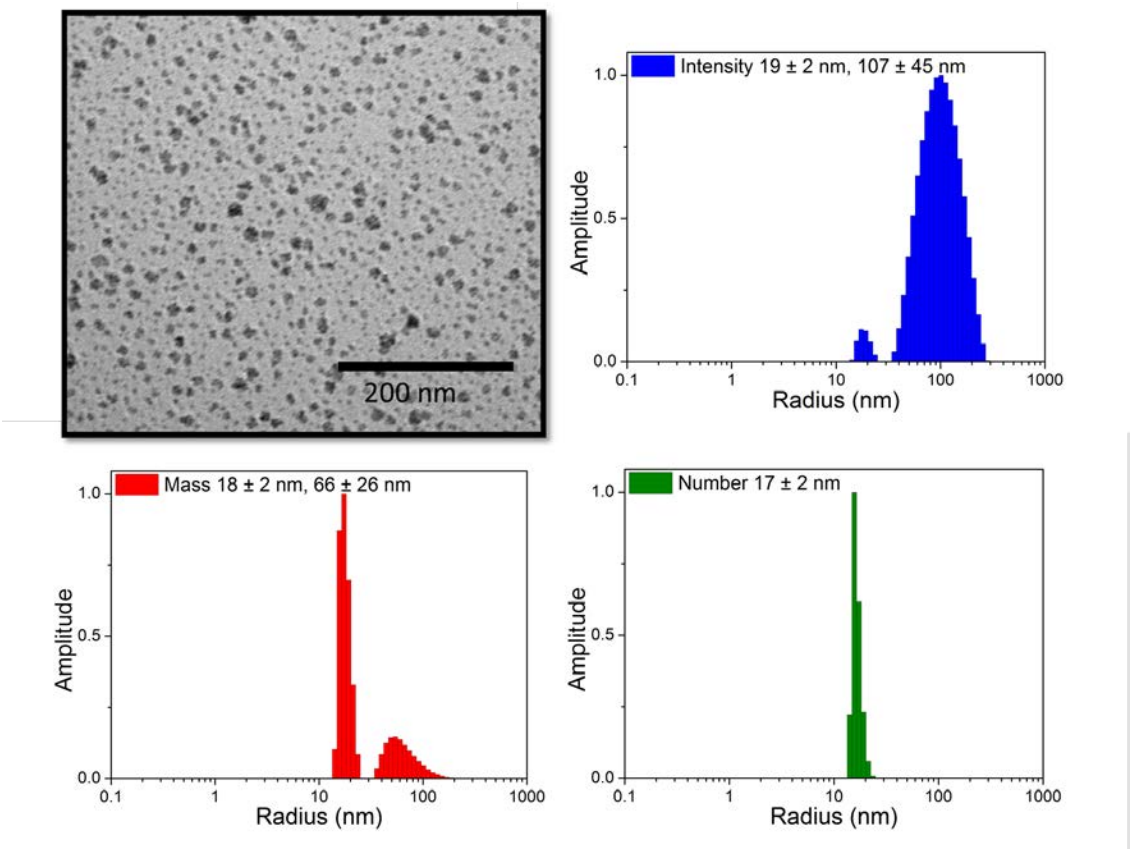

Figure 3.22. MIRB TEM image of SPIONs without stain and hydrodynamic radius peak height measurements by DLS in PBS solution pH 7.4.

The size of $pMPC_{29}$-SPIONs was also measured by Atomic Force Microscopy (AFM). $pMPC_{29}$-SPIONs were first dispersed onto a silicon wafer which was then left to air dry. Using tapping mode, AFM topography images, **Figure 3.23A and B**, showed spherical particles which were evenly dispersed. The 3D topography images found in **Figure 3.23C and D** show spherical crater like shapes are likely to resemble the polymeric shell. Some of the craters showed a raised spherical centre suggesting the presence of a hard iron oxide core in the centre of the soft polymer shell. Intensity profiles of the 2D topography images were taken (**Figure 3.23E and F**) to measure the size of the particles. The sizes were found to range from 18 to 28 nm in diameter with a height range of 6 to 15 nm. It was found that a sample of the freeze-dried $pMPC_{29}$-SPIONs material could be reconstituted back into water or PBS to provide a colloidally-stable solution. $PolyMPC_{29}$-SPIONs appeared to re-disperse easily and rapidly in PBS/water with only a short sonication required to break up any particulates. The solution appeared transparent and colloidally stable.

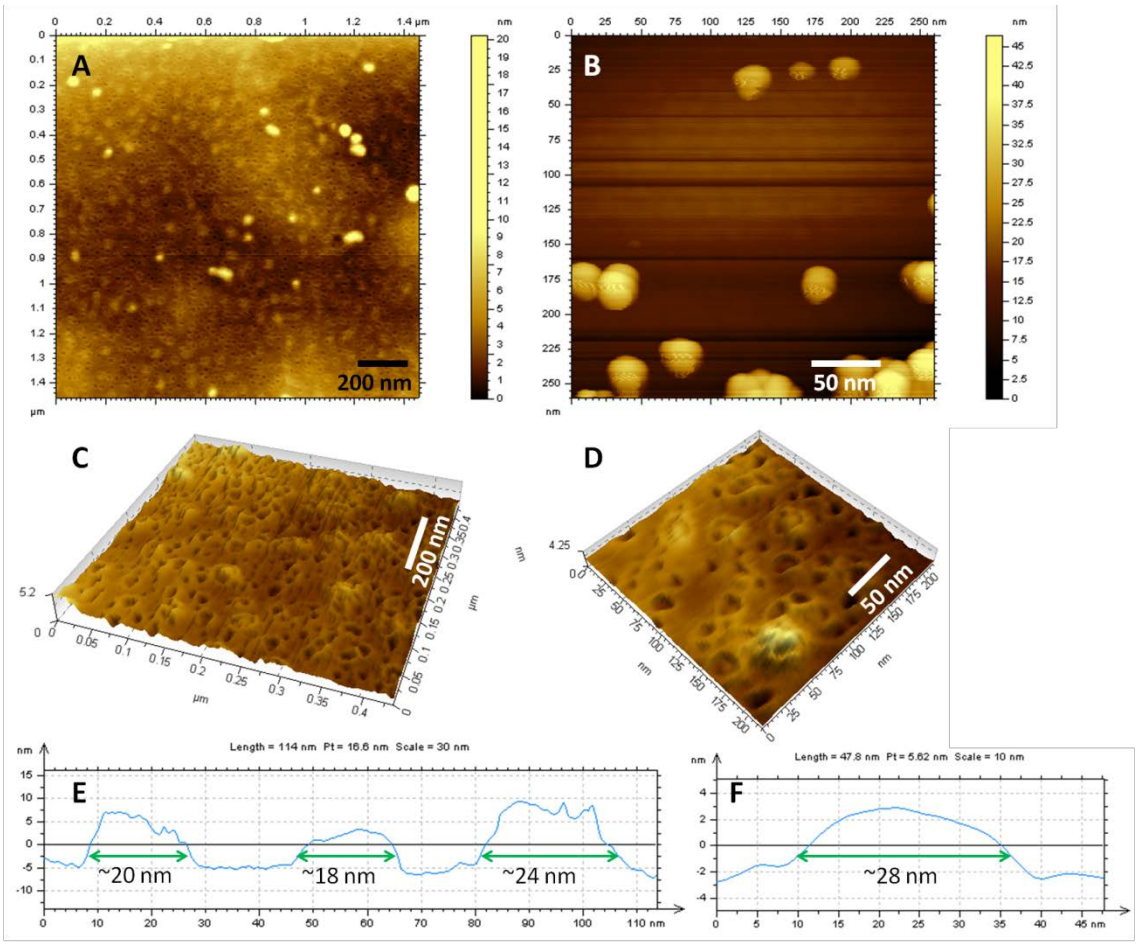

Figure 3.23. AFM topography (images A and B), 3D topography (C and D) and intensity profiles (E and F) of $pMPC_{30}$-SPIONs.

No aggregation of the reconstituted sample was found after standing for 1 day at ambient. This is an interesting observation since lyophilisation is a widely used method for long-term storage of polymer-coated nanoparticles. In addition, this provides an easy method for the preparation of solutions with known Fe concentration and limits the exposure of nanoparticles to bacterial growth for cell labelling experiments. Reconstituted $pMPC_{29}$-SPIONs in PBS solution pH 7.4 gave two hydrodynamic radius peak height populations observed by the intensity weighted DLS distribution: $R_{h,\ intensity}$ = 22 ± 2 nm and 99 ± 13 nm, $R_{h,\ mass}$ = 22 ± 2 nm and 94 ± 13 nm, $R_{h,number}$ = 21 ± 2 nm, **Figure 3.24**. The DLS measurements of reconstituted $pMPC_{29}$-SPIONs in PBS solution pH 7.4 showed the NP distribution was restored to its original measurements prior to lyophilisation, **Figure 3.24**.

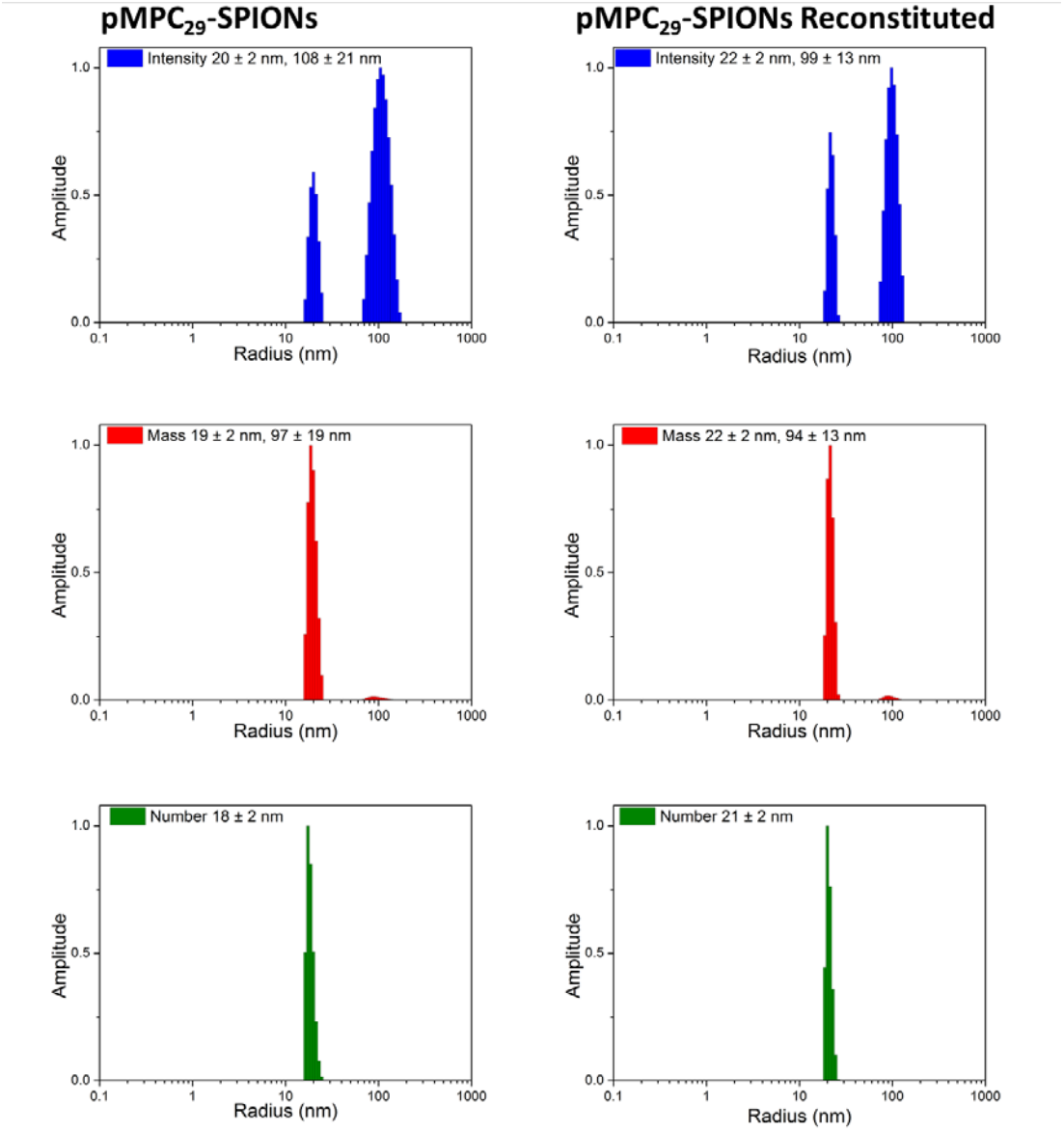

Figure 3.24. Hydrodynamic radius peak height measurements by DLS of $pMPC_{29}$-SPIONs compared with reconstituted $pMPC_{29}$-SPIONs in PBS solution pH 7.4.

3.3.3 Polymer Coverage Calculations

Predicted elemental and TGA percentage weight values for the reaction of *NS*-$pMPC_{29}$ with A-SPION containing an estimated 5541 surface APTMS ligands (L_{exp}) which corresponded to 2.2 monolayers of amino silane around a 7.6 nm SPION could also be calculated and compared with actual results.

Theoretical $pMPC_{29}$-SPION particle composition after complete reaction with all 5541 amino groups:

$$mass_{SPION\ core} = \rho_{Fe_3O_4} x \left(\left[\frac{4}{3} \pi r^3 \right] x 10^{-21} \right) = 1.20 \text{ x } 10^{-18} \text{ g}$$

$$Mass\ of\ pMPC\ ligand\ per\ SPION = \left[\frac{L_{exp}}{N_A} x MW_{pMPC-ligand} \right] = 8.16 \text{ x } 10^{-17} \text{ g}$$

$$Therefore:$$

$$Total\ mass\ of\ one\ pMPC\text{-}SPION = mass_{SPION\ core} + Mass\ of\ ligand\ per\ SPION$$

$$Total\ mass\ of\ one\ pMPC\text{-}SPION = 8.28 \text{ x } 10^{-17} \text{ g}$$

$$Theoretical\ \%\ mass\ of\ Fe_3O_4 = \frac{mass_{SPION\ core}}{Total\ mass\ of\ 1\ pMPC - SPION} x\ 100$$

$$Theoretical\ \%\ mass\ of\ Fe_3O_4 = 1.45\ \%$$

$$Theoretical\ \%\ mass\ of\ pMPC\ amino\ silane\ ligand\ coating = \frac{Mass\ of\ ligand\ monolayer\ per\ SPION}{Total\ mass\ of\ 1\ pMPC-SPION} x\ 100 = 98.55\ \%$$

A sample of freeze dried $pMPC_{29}$-SPION was taken for TGA analysis and measurement of iron content based on previously published methods.[46] The TGA data revealed a weight loss of 12.20 % between 20 and 120 °C, which was attributed to adsorbed water due to the highly hygroscopic nature of pMPC. The weight composition of the sample was determined as SiO_2/Fe_3O_4, 5.10 %; propyl amine/pMPC-coating, 82.70 %. TGA total weight loss was found to be 94.90 %. By elemental analysis, the Fe content was found to be 0.0360 mg/mg of sample (3.60 %). Considering a Fe_3O_4 SPION, the iron oxide content of the sample was calculated as 0.0498 mg Fe_3O_4/mg of sample (4.98 %) and SiO_2 content deduced as 0.12 %.

By removing the water contaminate mass, we can deduce that the organic shell mass actually contributes as 94.19 % and the Fe_3O_4/SiO_2 core mass contributes to 5.81 %. The organic shell mass including SiO_2 would therefore be 94.33 % and Fe_3O_4 as 5.67 %. Using this data it was possible to calculate the weight fraction of coating (f_c), in pMPC-SPION.

$$Coating\ weight\ fraction = f_c = \frac{mass\ of\ coating}{overall\ \text{pMPC-SPION}\ mass} = \frac{mass\ dry\ sample(from\ TGA) - mass\ of\ SPION\ core(from\ titration)}{mass\ dry\ sample(from\ TGA)}$$

$$Coating\ weight\ fraction = \ f_c = \frac{(1 - 0.1220) - 0.0498}{(1 - 0.1220)} = 0.9433$$

Using a different method to express f_c, it was possible to calculate the fraction of all amino groups on the particle reacted with a polymer chain and then the percentage polymer coverage of reacted amino groups. The calculations are as follows:

$$Coating\ weight\ fraction = f_c = \frac{mass\ of\ coating}{overall\ \text{pMPC-SPION}\ mass} =$$

$$\frac{2.00x10^{-17}\ g}{2.12x10^{-17}\ g} = 0.9433$$

Where:

$$mass\ of\ coating = mass_{pMPC-ligand} + mass_{unreacted\ APTMS-ligands}$$

$$mass\ of\ coating = 1.90 \text{ x } 10^{-17} + 9.46 \text{ x } 10^{-19} = 2.00 \text{ x } 10^{-17} \text{ g}$$

$$overall\ pMPC\text{-}SPION\ mass = mass_{SPION\ core} + mass\ of\ coating$$

$$overall\ pMPC\text{-}SPION\ mass = 1.20 \text{ x } 10^{-18} \text{ g} + 2.00 \text{ x } 10^{-17} \text{ g} = 2.12 \text{ x } 10^{-17} \text{ g}$$

With $mass_{pMPC\text{-}ligand}$, the total mass of pMPC ligand reacted on a particle, see **Figure 3.25** for structure.

Terms defined as:

$$mass_{pMPC-ligand} = N_{reacted} \times \frac{MW_{pMPC-ligand}}{N_A} = 1.90\ x\ 10^{-17}\ g$$

With $mass_{unreacted APTMS\text{-}ligand}$, the mass of unreacted APTMS ligand on a particle, see **Figure 3.25** for structure.

$$mass_{unreacted\ APTMS-ligand} = N_{unreacted} \times \frac{MW_{APTMS-ligand}}{N_A} = 9.46\ x\ 10^{-19}\ g$$

$$\text{Where } N_{reacted} = L_{exp} \times coverage$$

$N_{reacted}$= 1294 pMPC chains per SPION or the number of amino silane ligands reacted per SPION and $N_{unreacted} = L_{exp} \times (1 - coverage) =$ 4247 unreacted amino silane ligands per SPION.

Since $N_{reacted}$ and $N_{unreacted}$ are values that cannot be determined without knowing the coverage value, coverage values are entered into the equation below (found to be 23.35 %) in order to fit the weight fraction of coating value f_c of 0.9433 and hence deduce the percentage polymer coverage of reacted amino groups.

The expression of the coating weight fraction could then be developed:

$$f_c = \frac{N_{reacted}\frac{MW_{pMPC-ligand}}{N_A} + N_{unreacted}\frac{MW_{APTMS-ligand}}{N_A}}{M_{SPION} + N_{reacted}\frac{MW_{pMPC-ligand}}{N_A} + N_{unreacted}\frac{MW_{APTMS-ligand}}{N_A}}$$

Which is also written as:

$$f_c = \frac{(L_{exp} \times coverage)\frac{MW_{pMPC-ligand}}{N_A} + L_{exp} \times (1 - coverage)\frac{MW_{APTMS-ligand}}{N_A}}{M_{SPION} + (L_{exp} \times coverage)\frac{MW_{pMPC-ligand}}{N_A} + L_{exp} \times (1 - coverage)\frac{MW_{APTMS-ligand}}{N_A}}$$

The equation could be rearranged to calculate the coverage.

$$coverage = \frac{(1 - f_c)MW_{APTMS-ligand} - \frac{f_c \times mass_{SPION\ core} \times N_A}{L_{exp}}}{(f_c - 1) \times (MW_{pMPC-ligand} - MW_{APTMS-ligand})}$$

The values of the parameters required to calculate the coverage are as such:

$$f_c = 0.9433$$

$L_{exp} = 5541$ ligands expected for 2.2 monolayers

$MW_{APTMS-ligand} = 134.19$ g mol^{-1}

$MW_{pMPC-ligand} = 8846$ g mol^{-1}

Thus, the coverage was determined as 23.35 %, which is the percentage of amino groups which were reacted with a $pMPC_{29}$ polymer chain resulting in 1294 polymer chains attached to the SPION surface based on 5541 amino groups on the A-SPION. Since the number of available amino groups represent an average 2.2 monolayers surrounding each nanoparticle, in terms of space for grafting pMPC, one monolayer provides 2505 amino groups so the polymer graft density would be 51.66 % based

on an average of 1294 polymer chains or 52 polymer chains grafted per 100 amino groups in a surface area of 7 nm^2.

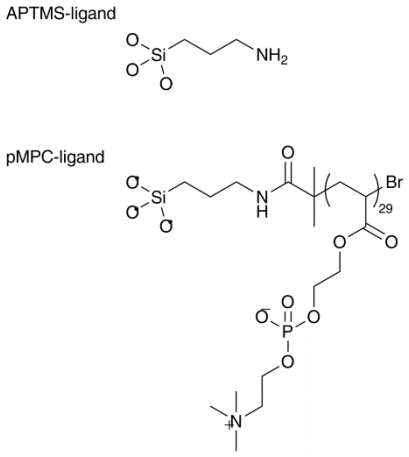

Figure 3.25: Structure of surface reacted APTMS ligand and pMPC ligand.

Table 3.4. Percentage elemental mass break down of surface reacted $pMPC_{29}$-ligand as interpreted by the number of reacted and unreacted amino silane ligands (column 1). From this and the TGA percentage weight measured for the organic shell and water contribution, C, H and N values could be predicted.

Element	% mass of surface reacted $pMPC_{29}$-ligand (1)	% mass of organic surface reacted $pMPC_{29}$-ligand (TGA)	% mass contribution from water contaminate (TGA)	Total % mass of organic (TGA)
C	**40.90**	**37.16**		**37.16**
H	**6.92**	**6.29**	**1.37**	**7.65**
N	**4.73**	**4.30**		**4.30**
O	28.55	25.94	10.83	36.78
P	9.11	8.27		8.27
Br	0.81	0.74		0.74
Si	1.22			
O3	2.08			
Sum	**94.33**	**82.70**	**12.20**	**94.90**

Taking into account the amount of water present in this particular sample, the molar composition of $pMPC_{29}$-SPION could be expressed as:

$(Fe_3O_4)_1(C_3H_8NSiO_3)_{1.4}(Br\text{-}pMPC_{29}\text{-}C_7H_{13}NSiO_3)_{0.4}(H_2O)_{27}$.

Using the polymer coverage value to determine the number of amino groups reacted and unreacted, the total percentage elemental mass was broken down for the coating shell which could be deduced, **Table 3.4 column 1**. Using this information and the TGA percentage mass data measured for the contribution of water in the sample analysed (12.20 %) and the percentage mass of organic for the coating (87.20 %), C, H and N values could be predicted for the total percentage mass of organic measured in the TGA (94.90 %). This was found as C:37.16, H:7.65, N:4.30. When compared with actual elemental C, H and N values measured, C:38.35, H:7.57, N:3.92, the percentage elemental mass values predicted are found to be very close to those measured by elemental analysis.

3.3.4 Cytotoxicity

To determine if $pMPC_{29}$-SPIONs were suitable for cell labelling studies, nanoparticles were first tested for cytotoxicity *via* a colorimetric assay, using cell-counting kit-8 (CCK-8) for the quantification for the number of viable cells after a period of 24 to 48 hours.

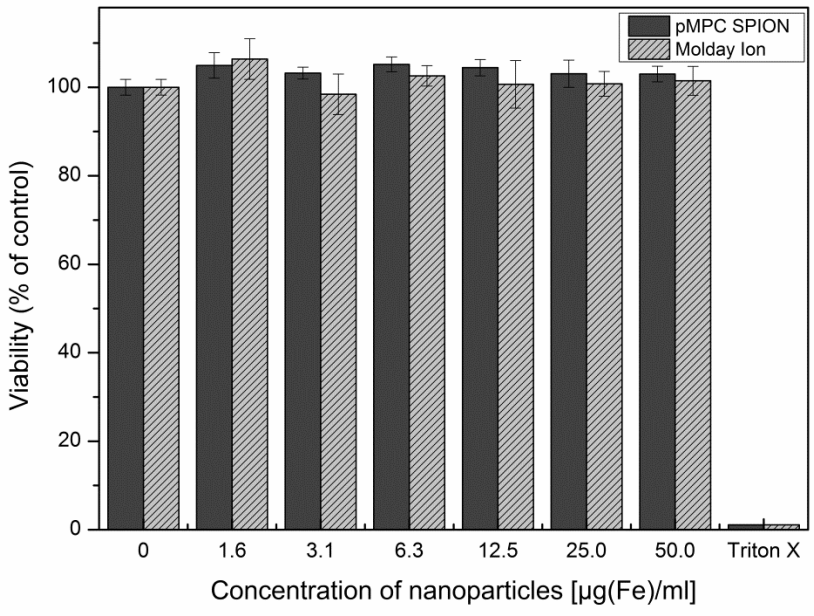

Figure 3.26: Relative viability of kidney murine stem cells exposed to a range of concentrations of pMPC coated SPIONs or MIRB nanoparticles. The cells were incubated in culture medium containing the nanoparticles for 24 h followed by viability measurement with CCK-8 reagent. Results are plotted as the relative viability in respect to control conditions as a function of nanoparticle concentration and error bars represent the standard deviation from three replicates.

A kidney-derived murine stem cell line[47] was used and exposed to cell culture medium containing concentrations of nanoparticles ranging up to 50 μg Fe mL^{-1} for 24 hours after which cell viability was then determined. It was found that cell viability was maintained after 24 hours despite exposure to $pMPC_{29}$-SPIONs at different concentrations, **Figure 3.26**. At higher concentrations of $pMPC_{29}$-SPIONs, the cell viability assay showed slightly higher percentages in the control of viability when compared to cells exposed to MIRB thus indicating pMPC has low cytotoxicity even at high concentrations and supports the selection of pMPC as a biocompatible surface coating for bio-application.[48, 49] Percentages of viability above 100 % could suggest pMPC and dextran are providing the stem cells with material to encourage cell proliferation (i.e. dextran is a sugar and may provide the cell with energy. Phophorylcholine found in pMPC is also a component found in the phospholipid bilayer of a cell membrane). The cell viability assay was carried out by Dr Arthur Taylor at the University of Liverpool, Institute of Translational Medicine

3.3.5 Stability Studies

3.3.5.1 Colloidal Stability

To assess whether $pMPC_{29}$-SPIONs would be suitable for cell labelling experiments, their colloidal stability in PBS at 37 °C for at least 24 hours was evaluated. In addition, $pMPC_{29}$-SPIONs need be colloidally stable at temperatures of 25 °C and lower for storage. The maximum nanoparticle concentrations used for cell labelling experiments is 100 and 50 μg Fe mL^{-1} with incubation periods of up to 48 hours.[50] For this reason, the colloidal stability of $pMPC_{29}$-SPIONs with Fe concentration of 53 and 187 μg Fe mL^{-1} at 37 °C was investigated. Colloidal stability studies of $pMPC_{29}$-SPION samples at concentrations between 50 and 237 μg Fe mL^{-1} at both 25 and 37 °C were carried out using UV-Vis spectroscopy by measuring the absorbance of the particles suspended in PBS at 400 nm over a period of days, **Figure 3.27**. An absorbance of 400 nm was selected since it gave the best correlation to Fe concentration of $pMPC_{29}$-SPIONs, which was determined using a range of $pMPC_{29}$-SPION samples prepared by serial dilution using a concentrated $pMPC_{29}$-SPION sample with known Fe concentration quantified by elemental analysis. A calibration curve with R^2 value of 0.998 was obtained.

Figure 3.27 shows that $pMPC_{29}$-SPIONs at 53 and 187 µg Fe mL^{-1} were colloidally stable for up to 7 days and 53 hours at 37 °C respectively. Interestingly, the difference in the colloidal stability periods were of a factor of 3.5 which is the same dilution factor between the two concentrations measured. This not likely to be a coincidence since diluted NPs are likely to have extended colloidal stability periods due to less NP interactions by Brownian motion. Further colloidal stability measurements at 37 °C using different NP concentrations would support the idea that the colloidal stability period could be predicted based on dilution of NPs.

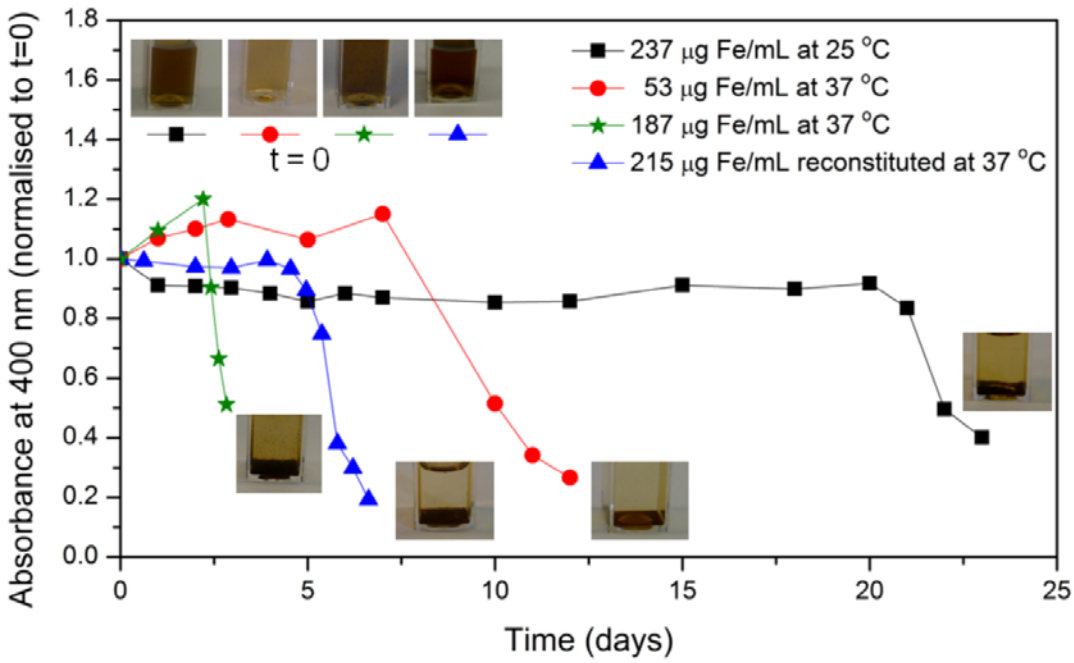

Figure 3.27. $pMPC_{29}$-SPIONs stability study in PBS at 25 °C and 37 °C with images of solutions at t = 0 and at the end points of the 4 studies.

The colloidal stability of $pMPC_{29}$-SPIONs achieved past 48 hours in PBS at 37 °C confirmed the suitability of $pMPC_{29}$ as a NP surface coating for the colloidal stabilisation of nanoparticles required for cell internalisation experiments.[51] Reconstituted $pMPC_{29}$-SPIONs with a concentration of 215 µg Fe mL^{-1} in PBS at 37 °C were also investigated and showed increased colloidal stability up to 94 hours. Thus, the freeze-drying and reconstitution procedure improves colloidal stability by ~40 hours compared to standard $pMPC_{29}$-SPIONs without a freeze-drying step. The difference in colloidal stability could be due to a difference in density of $pMPC_{29}$-SPIONs compared to freeze dried $pMPC_{29}$-SPIONs. The polymer/amino

silane shell in freeze dried $pMPC_{29}$-SPIONs may not be fully hydrated and may contain pockets of air. Particles with higher density sediment at a faster rate compared to less dense particles (Stokes law). The increase in colloidal stability therefore supports the potential of freeze-drying $pMPC_{29}$-SPIONs for long-term storage without facing colloidal stability issues.

The colloidal stability of $pMPC_{29}$-SPIONs with concentration of 237 μg Fe mL^{-1} at 25 °C was also investigated to determine the suitability and stability for storage. A concentration of 237 μg Fe mL^{-1} was used as the highest concentration in this study measured by UV-Vis spectroscopy at 400 nm since this concentration was just under the absorbance saturation limit for the instrument. This sample showed colloidal stability for 20 days at 25 °C, indicating a good shelf life could be obtained for concentrated samples in PBS.

3.3.5.2 Chemical Stability

The most likely cell internalisation mechanism for nanoparticles is *via* endocytosis whereby nanoparticles enter the cell through the endosome organelle which is created by the invagination of the cell wall to form a small vesicle.[52] Early endosome pH is typically the same as the cell culture medium on the outside of the cell of pH 7.4. However, endosome pH gradually decreases to pH 4.5 due to an increased concentration of the acid hydrolyase enzyme present (produced by the golgi body) which turns the late endosome into a lysosome.[53-55] In this situation, SPIONs could be degraded by the acidic environment.[56] The SPION core therefore needs to be stable to acidic conditions in order to maintain a R_2 relaxivity for long-term cell labelling.

To investigate the chemical stability, $pMPC_{29}$-SPIONs were subjected to conditions modelling the lysosomal environment of a stem cell, **Figure 3.28**. Briefly, NPs (5 μg Fe) were added to buffers at physiological or acidic pH and incubated at 37 ^{o}C alongside a blank (0 μg Fe) and internal standard (5 μg Fe). For each time point, a sample was taken for measurement of free iron ions in solution by adding a colorimetric reagent solution consisting of FerroZine (6.5 mM).[46] After colour development, the absorbance at 590 nm was measured and compared to a calibration curve containing colorimetric reagent. The free iron content in solution was then

deduced and the degree of dissolution of the sample was determined (see Chapter 2 section 2.3.1.1 for full experimental details).[47, 57]

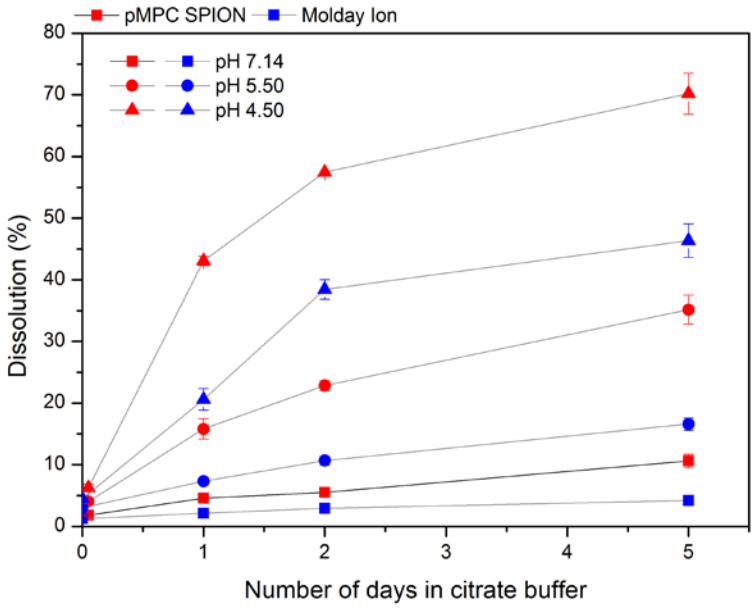

Figure 3.28. Dissolution assay of $pMPC_{29}$-SPIONs and MIRB in citrate buffer solution at 37 °C.

The dissolution assay results showed that both $pMPC_{29}$-SPION and MIRB possessed rapid dissolution of the iron oxide core at pH 4.5 over a period of 5 days with $pMPC_{29}$-SPION showing an additional 20 % dissolution, **Figure 3.28**. As expected, $pMPC_{29}$-SPION and MIRB samples exposed to less acidic pH environments at 5.5 and 7.14 showed much slower dissolution rates. The dissolution of $pMPC_{29}$-SPIONs after 5 days of exposure in pH 5.5 environment had reached 35 % dissolution which was over twice as high than that observed for MIRB which had reached only 15 % dissolution at 5 days exposure in pH 5.5 environment. For SPIONs with long-term stability inside the cell, further developments to the surface coating would be required to ensure long-term stability at pH 4.5 inside the cell.

3.3.6 Magnetic Measurements

3.3.6.1 Magnetisation Saturation (M_s) Measurements

Superconducting quantum interference device (SQUID) magnetometry was used to determine whether OA-SPIONs and $pMPC_{29}$-SPIONs were superparamagnetic and

to measure their magnetisation saturation (M_s) values. The M_s value of $pMPC_{29}$-SPIONs were measured at 33 emu g^{-1} $Fe_3O_4^{-1}$ which was found to be a decrease of 20 emu g^{-1} $Fe_3O_4^{-1}$ when compared with OA-SPIONs of 53 emu g^{-1} $Fe_3O_4^{-1}$, **Figure 3.29**. The drop in M_s suggests that transferring SPIONs into water induces the oxidation of the surface of Fe_3O_4 SPIONs to form Fe_2O_3 thus causing a magnetic dead layer and a decrease in M_s value.[58, 59] Both magnetisation-field magnetic hysteresis curves show typical superparamagnetic behaviour (as indicated by the s shape curve and position of the curves through the origin **Figure 3.29** inset) with minimal remanence and coercivity (magnetism is not retained (observed when SPIONs are demagnetised at 0 kOe)).[60] The M_s values measured here will be used to calculate the level of uptake of $pMPC_{29}$-SPION *vs.* MIRB and hence quantify the number of SPIONs up taken per cell and thus amount of Fe using cell tracking velocimetery (CTV) as discussed in Chapter 6.

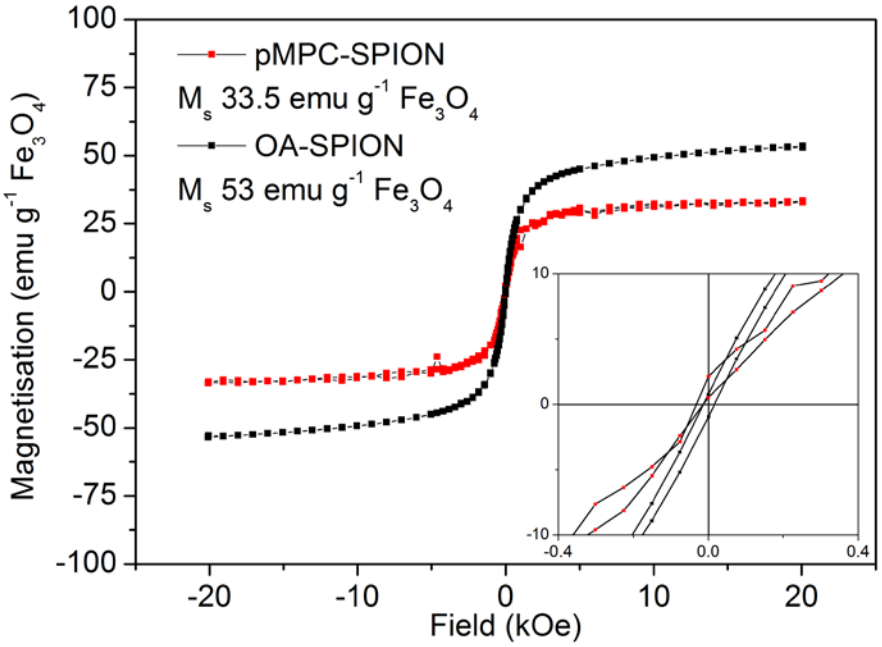

Figure 3.29: Magnetisation-field magnetic hysteresis curves for OA-SPION and $pMPC_{29}$-SPION at 300K. The 2 T magnetisation for OA-SPION is 53.50 emu g^{-1} iron oxide and $pMPC_{29}$-SPION 33.20 emu g^{-1} iron oxide.

Magnetic Core Characterisation

Dr. Lara Bogart at the University of Liverpool, Institute of Integrative Biology determined the magnetic SPION cores sizes using SQUID magnetometry curves

obtained from measurements taken for p(MPC)$_{29}$-SPIONs, OA-SPIONs and MIRB particles. The curves which were originally represented in terms of mass (emu g^{-1} Fe_3O_4) were converted in terms of volume (emu cm^{-3} Fe_3O_4), **Figure 3.30**. A Langevin expression modified by the log-normal polydispersity function was used to determine the magnetic SPION cores sizes and have been summarized in **Table 3.5**. The data confirm core sizes of OA-SPIONs and pMPC$_{29}$-SPIONs are similar in size to those obtained from previous size measurements (**Table 3.5**). It was found that OA-SPIONs, pMPC$_{29}$-SPIONs and MIRB had total core diameter of 8 nm, 8 nm and 11 nm respectively and magnetic core diameter of 7 ± 0.1 nm, 7 ± 0.1 nm and 9 ± 0.1 nm respectively. Magnetic core sizes have also been deduced from the intracellular iron content in single cell magnetophoresis measurements, which are discussed further in detail in Chapter 6.

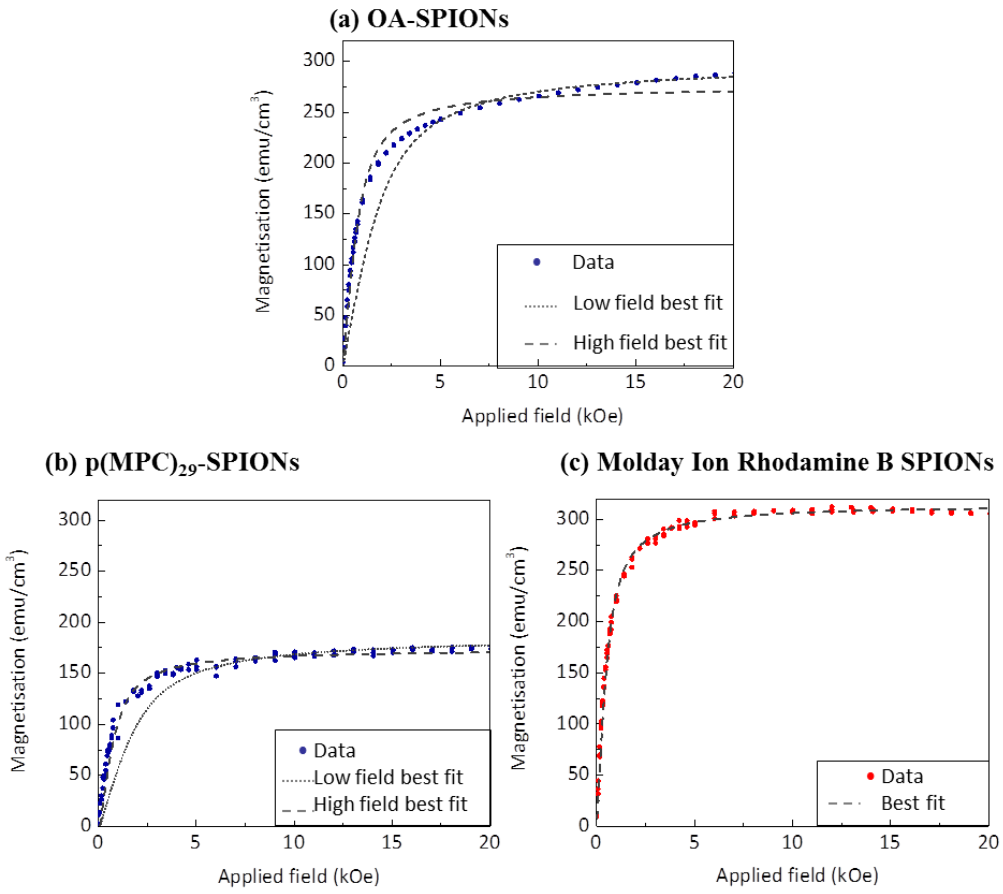

Figure 3.30. Ambient temperature magnetisation curves of (a) Fe_3O_4 cores as synthesised in oleic acid (b) Following addition of amino-silanisation (c) after polymerisation with MPC block polymer and (d) MIRB SPIONs. Grey line indicates best model fit using simple Langevin expression modified by the log-normal polydispersity function. Best fit parameters for all fits are provided in **Table 3.5**.

Table 3.5. Best fit parameters extracted from ambient temperature magnetisation curves presented in Figure 3.30. Where M_{SP} and M_{SB} is the saturation magnetisation of the particles and of the bulk material, respectively. Where D_t is the total SPION core diameter and D_m is the magnetic core diameter.

Sample	M_{SP} (emu/cm^3)	M_{SB} (emu/cm^3)	D_t (nm)	D_m (nm)	Standard deviation	Comment
OA-SPIONs	270	480	8	7	0.1	Powdered sample
p(MPC)$_{29}$-SPIONs	160		8	7	0.1	
MIRB	320		11	9	0.1	Sample in water

3.3.6.2 Magnetic Resonance Imaging (MRI)

pMPC$_{29}$-SPION samples were evaluated for their potential for use as an MRI contrast agent. pMPC$_{29}$-SPION samples (as prepared and reconstituted) with concentrations ranging from 0 to 1.0 mM Fe fixed in 1 % agarose were analysed by MRI to measure their R_2 relaxivity. The R_2 relaxivity for pMPC$_{29}$-SPION samples as prepared and reconstituted were found at 127 and 112 mMFe^{-1} s^{-1} respectively compared with MIRB which had a lower R_2 relaxivity of 77 mMFe^{-1} and Endorem which showed a higher R_2 relaxivity of 159 s^{-1}, **Figure 3.31**. The difference in R_2 relaxivity results observed for pMPC$_{29}$-SPIONs and reconstituted pMPC$_{29}$-SPIONs may support the idea proposed by differences observed for colloidal stability results for pMPC$_{29}$-SPIONs and reconstituted pMPC$_{29}$-SPIONs. The suggestion was that not all of the pMPC shell present for reconstituted pMPC$_{29}$-SPIONs had become fully rehydrated. This would explain the lower R_2 value observed for reconstituted pMPC$_{29}$-SPIONs since the relaxation of more water protons surrounding the SPION cores would provide higher R_2 values. Overall, the relaxivity results show that both pMPC$_{29}$-SPION and reconstituted samples could be used as a potential contrast agent since the R_2 relaxivity values both exceeded that observed for the commercial available contrast agent, MIRB.

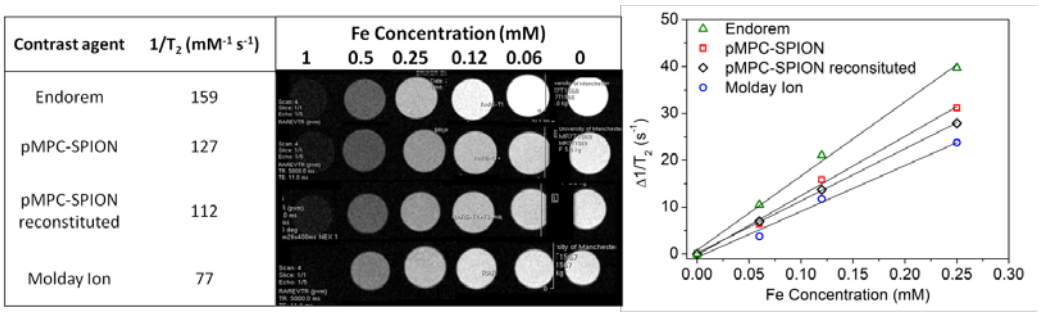

Figure 3.31. Relaxivity data for $pMPC_{29}$-SPIONs as prepared and reconstituted vs. Endorem and MIRB contrast agents.

The relaxivity performance of $pMPC_{29}$-SPIONs suggests that the highly hydrophilic characteristics of the pMPC coating provide good water contact and diffusion/supply with the SPION surface which is favourable for enhancing the R_2 contrast signal.

3.4 Conclusion

To conclude, well defined bio-compatible *NS*-pMPC were prepared by ATRP and screened for the colloidal stabilisation of amino silane functional SPIONs in PBS at 25 and 37 °C. Well defined *N*-succinimidyl functional poly MPC homopolymer with a DP_n 29 or M_n ~9,000 g mol^{-1} was found to be a suitable polymer for the covalent grafting to amino silane coated SPIONs and providing SPIONs in PBS at 37 °C with good colloidal stability for more than 48 hours and up to 7 days with cell labelling concentrations of 187 µg Fe mL^{-1} and 53 µg Fe mL^{-1} respectively. A cell viability assay showed that $pMPC_{29}$-SPIONs had non-cytotoxic behaviour when placed with kidney murine stem cells. This confirms the suitability of pMPC as a surface coating for SPIONs for potential cell labelling. The coverage of $pMPC_{29}$ on the surface of A-SPIONs was also measured using TGA and CHN elemental analysis. From the average number of available amine sites predicted on the surface of the A-SPIONs (5541 amino groups, 2.2 monolayers), an average of 23.35 % of amines were found to be reacted with *NS*-$pMPC_{29}$. Further pre-biological studies showed as prepared and reconstituted $pMPC_{29}$-SPIONs had an R_2 relaxivity of 127 and 112 mM^{-1} s^{-1} respectively which was found to be higher than the commercially available contrast agent MIRB which had a R_2 relaxivity of 77 mM^{-1} s^{-1}.

$PolyMPC_{29}$-SPIONs also had a magnetisation saturation value (M_s) of 33 emu g^{-1} $Fe_3O_4^{-1}$ which was a reduction of 20 emu g^{-1} Fe_3O_4 from the starting material of oleic

acid coated SPIONs of 53 emu g^{-1} Fe_3O_4. This suggested that transferring SPIONs into water using $pMPC_{29}$ caused possible oxidation of the surface of Fe_3O_4 SPIONs into Fe_2O_3 thus causing a magnetic dead layer and a decrease in M_s value.[58, 59]

$PolyMPC_{29}$-SPIONs were subjected to citrate buffers at pH 7.4 to 4.5 incubated at 37 °C in order to mimic the endosomal and lysosomal environments inside a stem cell. The dissolution assay showed that the SPION cores rapidly digested at pH 4.5 within a period of 5 days with dissolution of 70 %. MIRB NPs showed a slightly slower rate of dissolution at pH 4.5 with 45 % of the core dissolved at T= 5 days. The rapid dissolution of the SPION core of $pMPC_{29}$-SPIONs thus indicates that the MRI signal will rapidly be lost with time and therefore indicates that further improvements of the SPION coating is required in order to achieve SPIONs for long term stem cell labelling.

Overall, the suitability of $pMPC_{29}$-SPIONs as a contrast-labelling agent for bio application has been studied. The biological studies for $pMPC_{29}$-SPIONs have been investigated and are discussed in the stem cell biology Chapter 6.

3.5 References

1. D. Braun, H. Cherdron, M. Rehahn, *et al.*, *Polymer Synthesis: Theory and Practice. Fundamentals, Methods, Experiments*, Springer eBooks, 5th edn., 2013.
2. W. A. Braunecker and K. Matyjaszewski, *Prog. Polym. Sci.*, 2007, **32**, 93-146.
3. S. A. Macpherson, G. B. Webber and R. Moreno-Atanasio, *Adv. Powder Technol.*, 2012, **23**, 478-484.
4. J.-R. Roan, *Int. J. Mod. Phys. B*, 2003, **17**, 2791-2820.
5. E. Amstad, M. Textor and E. Reimhult, *Nanoscale*, 2011, **3**, 2819-2843.
6. K. Matyjaszewski and J. Xia, *Chem. Rev.*, 2001, **101**, 2921-2990.
7. W. He, H. Jiang, L. Zhang, *et al.*, *Polym. Chem.*, 2013, **4**, 2919-2938.
8. C. Fang, N. Bhattarai, C. Sun, *et al.*, *Small*, 2009, **5**, 1637-1641.
9. C. Boyer, M. R. Whittaker, V. Bulmus, *et al.*, *NPG Asia Mater.* , 2010, **2**, 23-30.
10. D. S. Achilleos and M. Vamvakaki, *Materials*, 2010, **3**, 1981-2026.

11. T. Liu and B. Thierry, *Langmuir*, 2012, **28**, 15634-15642.
12. B. Zhao and W. J. Brittain, *Prog. Polym. Sci.*, 2000, **25**, 677-710.
13. T. Sen and I. J. Bruce, *Sci. Rep.*, 2012, **2**.
14. J. R. Hughey, J. M. Keen, D. A. Miller, *et al.*, *Eur. J. Pharm. Sci.*, 2013, **48**, 758-766.
15. S. R. Pygall, S. Kujawinski, P. Timmins, *et al.*, *Int. J. Pharm.*, 2009, **370**, 110-120.
16. R. C. D. Silva and W. Loh, *J. Colloid Interface Sci.*, 1998, **202**, 385-390.
17. P. Bahadur, K. Pandya, M. Almgren, *et al.*, *Colloid. Polym. Sci.*, 1993, **271**, 657-667.
18. P. K. Singh, V. K. Singh and M. Singh, *E-polymers*, 2007, **7**, 30.
19. P. Mary, D. D. Bendejacq, M. P. Labeau, *et al.*, *J. Phys. Chem. B*, 2007, **111**, 7767-7777.
20. X.-Y. Sun, S.-S. Yu, J.-Q. Wan, *et al.*, *J. Biomed. Mater. Res. A*, 2013, **101A**, 607-612.
21. J. J. Yuan, S. P. Armes, Y. Takabayashi, *et al.*, *Langmuir*, 2006, **22**, 10989-10993.
22. J. H. Sui, C. Y. Cao and W. Cai, *J. Nanosci. Nanotechnol.*, 2011, **11**, 8469-8473.
23. E. J. Lobb, I. Ma, N. C. Billingham, *et al.*, *J. Am. Chem. Soc.*, 2001, **123**, 7913-7914.
24. D. Samanta, S. Mcrae, B. Cooper, *et al.*, *Biomacromolecules*, 2008, **9**, 2891-2897.
25. X. Yu, X. Yang, S. Horte, *et al.*, *Chem. Commun.*, 2013, **49**, 6831-6833.
26. http://www.nature.com/scitable/topicpage/cell-membranes-14052567
27. J. Park, K. An, Y. Hwang, *et al.*, *Nat Mater*, 2004, **3**, 891-895.
28. W. Wu, Q. He and C. Jiang, *Nanoscale Res. Lett.*, 2008, **3**, 397-415.
29. http://www.gelest.com/goods/pdf/Library/08Tailor.pdf
30. L. Bouffier, H. H. P. Yiu and M. J. Rosseinsky, *Langmuir*, 2011, **27**, 6185-6192.
31. M. van de Waterbeemd, T. Sen, S. Biagini, *et al.*, *Micro Nano Lett.*, 2010, **5**, 282-285.
32. J. U. Izunobi and C. L. Higginbotham, *J. Chem. Educ.*, 2011, **88**, 1098-1104.

33. M. Pierre-Eric, C. M. Nathalie, B. Alexander, *et al.*, *Controlled/Living Radical Polymerization: Progress in ATRP*, American Chemical Society, 2009, vol. 1023, ch. 9, 127-137.
34. H. F. Mark, *Encyclopedia of Polymer Science and Technology*, John Wiley & Sons, New Jersey, 2013, ch. Living Radical Polymerization, 641-642.
35. M. Constantin, *eXPRESS Polym. Lett.*, 2011, **5**, 839-848.
36. M.-E. Meyre, R. Clerac, S. Mornet, *et al.*, *PCCP*, 2010, **12**, 12794-12801.
37. K. Hervé, L. Douziech-Eyrolles, E. Munnier, *et al.*, *Nanotechnology*, 2008, **19**, 465608.
38. G. T. Hermanson, *Bioconjugate Techniques (Second Edition)*, ed. G. T. Hermanson, Academic Press, New York, 2008, 169-212.
39. J. B. Lambert, *Introduction to Organic Spectroscopy*, Macmillian, New York, 1987.
40. A. Megia-Fernandez, M. Ortega-Muñoz, J. Lopez-Jaramillo, *et al.*, *Adv. Synth. Catal.*, 2010, **352**, 3306-3320.
41. Y. Hao, C. Man and Z. Hu, *J. Hazard. Mater.*, 2010, **184**, 392-399.
42. J. Wang, S. Zheng, Y. Shao, *et al.*, *J. Colloid Interface Sci.*, 2010, **349**, 293-299.
43. A. Lewis, Y. Tang, S. Brocchini, *et al.*, *Bioconjugate Chem.*, 2008, **19**, 2144-2155.
44. B. Addicott, M. Willman, J. Rodriguez, *et al.*, *Contrast Media Mol. Imaging*, 2011, **6**, 7-18.
45. R. S. Molday and D. Mackenzie, *J. Immunol. Meth.*, 1982, **52**, 353-367.
46. L. L. Stookey, *Anal. Chem.*, 1970, **42**, 779-781.
47. A. S. Arbab, L. B. Wilson, P. Ashari, *et al.*, *NMR Biomed.*, 2005, **18**, 383-389.
48. Y. Iwasaki and K. Ishihara, *Anal. Bioanal. Chem.*, 2005, **381**, 534-546.
49. H. K. Cho, H. J. Cho, S. Lone, *et al.*, *J. Mater. Chem.*, 2011, **21**, 15486-15493.
50. J. D. Goff, P. P. Huffstetler, W. C. Miles, *et al.*, *Chem Mater*, 2009, **21**, 4784-4795.
51. R. R. Qiao, C. H. Yang and M. Y. Gao, *J. Mater. Chem.*, 2009, **19**, 6274-6293.

52. B. Alberts, A. Johnson, J. Lewis, *et al.*, *Molecular Biology of the Cell*, Garland Science, New York, 4th edn., 2002.
53. T. Kurz, A. Terman and U. T. Brunk, *Arch. Biochem. Biophys.*, 2007, **462**, 220-230.
54. S. Mukherjee, R. N. Ghosh and F. R. Maxfield, *Physiol Rev.*, 1997, **77**, 759-803.
55. B. M. Myers, F. G. Prendergast, R. Holman, *et al.*, *J. Clin. Invest.*, 1991, **88**, 1207-1215.
56. N. Singh, G. J. S. Jenkins, R. Asadi, *et al.*, *Nano reviews*, 2010, **1**.
57. T. Skotland, P. C. Sontum and I. Oulie, *J Pharmaceut Biomed*, 2002, **28**, 323-329.
58. K. Yong Seok, L. Hyun Jong, P. Govindaiah, *et al.*, *Materials*, 2014, **7**, 195-205.
59. H. Mohammad-Beigi, S. Yaghmaei, R. Roostaazad, *et al.*, *Physica E*, 2011, **44**, 618-627.
60. D. L. Huber, *Small*, 2005, **1**, 482-501.

PAGE LEFT INTENTIONALLY BLANK

4

Synthesis of Silica Coated SPIONs: The Development of SPIONs Stable to the Conditions of the Lysosomal Environment

For experimental details related to this Chapter, see Chapter 2.

List of Figures

Figure 4.1. Chemical stability of maghemite and magnetite showing the rate of dissolution of iron oxides in 0.5 M HCl (pH 0.3) at 25 °C over a period of 100 hours (4.16 days) Image taken from reference.[15] 143

Figure 4.2. Chemical stability of maghemite and magnetite showing the correlation between iron oxide dissolution/chemical stability and their toxicity. E_h represents the redox potential. Image adapted from reference.[16] 144

Figure 4.3. "(a) Frequency-domain photoacoustic (FD-PA) array image of a silica coated SPION-filled tube inside chicken breast tissue. (b) Two-dimensional FD-PA image of a rat thigh containing silica-coated SPION obtained using a 3.5-MHz focused transducer." Image taken from reference.[5] 145

Figure 4.4. Characterisation data for oleic acid coated SPIONs showing A) solvodynamic radius peak height distributions by DLS, B) TEM image and size distribution C) and D) PXRD pattern..... 146

Figure 4.5. Characterisation data for pH 2 dispersible γFe_2O_3 SPIONs showing A) hydrodynamic radius peak height distributions by DLS, B) TEM image and C) PXRD pattern..... 148

Figure 4.6. Room temperature magnetisation curves of (a) γFe_2O_3 and (b) Fe_3O_4 cores as synthesised. The grey line indicates best model fit using simple Langevin expression modified by the log-normal polydispersity function. Best fit parameters are provided in **Table 4.1.** 150

Figure 4.7. Image showing vials of pH 8 dispersible A) maghemite γFe_2O_3 and B) magnetite Fe_3O_4 SPIONs at the same concentration showing orange and brown suspensions respectively..... 150

Figure 4.8. TGA data for pH 8 dispersible magnetite Fe_3O_4 SPIONs (red line) and pH 2 dispersible maghemite γFe_2O_3 SPIONs (blue line). The line represents the isotherm held at 120 °C for the removal of adsorbed solvent. Air atmosphere at 100 mL/min. 151

Figure 4.9. TGA pans containing 1) pH 8 dispersible magnetite Fe_3O_4 SPIONs and 2) pH 8 dispersible maghemite γFe_2O_3 SPIONs showing (A) before and (B) after heating the dry sample in the TGA to 600 °C in air. (C) shows colour plates for Magnetite and Maghemite taken from reference.[35] 152

Figure 4.10. TEM images of silica coated γFe_2O_3 SPIONs using TEOS aliquots of A) 150 µL, B) 100 µL and C) 50 µL in the reaction. Image A) shows presence of silica NPs formed and A) and B) showing increased numbers of multiple SPION cores surrounds by a silica coating. 155

Figure 4.11. Size distribution of silica coated γFe_2O_3 SPIONs by TEM. Average diameter 33 ± 15 nm taken from >200 measurements..... 156

Figure 4.12. TEM images of A) γFe_2O_3 SPION starting material and B) silica coated γFe_2O_3 SPIONs using TEOS aliquot of 50 µL with zoomed in areas highlighted in red and green inset. 156

Figure 4.13. DLS hydrodynamic radius peak height measurements of silica coated maghemite SPIONs..... 157

Figure 4.14. FT-IR spectra of A) pH 8 dispersible γFe_2O_3 SPIONs (before coating procedure) and B) silica coated γFe_2O_3 SPIONs (after coating procedure). The red dashed line represents the start of the fingerprint region to identify iron oxide composition using **Figure 4.16.** 158

Figure 4.15. FT-IR spectra fingerprint region of **Figure 4.14A** against **Figure 4.20A**. Peaks picked using reported wavenumbers for maghemite, **Table 4.2**. Red dash lines show the wavenumbers for when the broad peaks plateau with the baseline..... 159

Figure 4.16. FT-IR spectra of iron oxides showing the fingerprint region of the FT-IR spectrum of iron oxides. Image taken from reference.[38] Red lines added to figure to highlight the wavenumbers for when the broad peaks plateau with the baseline. 160

Figure 4.17. Size distribution of silica coated γFe_2O_3 SPIONs by TEM. Average diameter of 25 ± 12 nm taken from >100 measurements..... 161

Figure 4.18. TEM images of A) oleic acid coated Fe_3O_4 SPION starting material and B) silica coated Fe_3O_4 SPIONs using TEOS aliquot of 50 µL with zoomed in area highlighted in red inset. Bottom left shows a frequency histogram for the number of SPION cores counted per silica coated composite particle..... 162

Figure 4.19. DLS hydrodynamic radius peak height measurements of silica coated magnetite Fe_3O_4 SPIONs. 163

Figure 4.20. FT-IR spectra of A) pH 8 dispersible Fe_3O_4 SPIONs (before coating procedure) and B) silica coated Fe_3O_4 SPIONs (after coating procedure). The red

dashed line represents the start of the fingerprint region to identify iron oxide composition using **Figure 4.16.**..... 164
Carbon dioxide for both samples were observed around 2300 cm^{-1}. Again, the CH band found around 3000 cm^{-1} in FT-IR spectrum B for SiO_2 coated γFe_2O_3 SPIONs is likely to come from un-hydrolysed TEOS on the surface of the coated NPs. The iron oxide composition of pH 8 dispersible Fe_3O_4 SPIONs was associated with magnetite, **Figure 4.15** taken from **Figure 4.21A** compared to **Figure 4.16** and **Table 4.2**, as observed by a single broad peak with a characteristic left hand slope shape found around 590 cm^{-1}..... 164
Figure 4.22. Relative viability of KSCs exposed to a range of concentrations of SiO_2-SPIONs (γFe_2O_3 SPION core) or Molday Ions. The cells were incubated in culture medium containing the NPs for 24 hours followed by viability measurement with CCK-8 reagent. Results are plotted as the relative viability as a function of NP concentration and error bars represent the standard deviation from three replicates. Cell viability with SiO_2-SPIONs (Fe_3O_4 SPION core) was not measured. 165
Figure 4.23. Dissolution assay of uncoated SPIONs (pH 8 and pH 2 dispersible) vs. silica coated-SPIONs in pH 4.5 citrate buffer solution at 37 °C. 166
Figure 4.24. Magnetisation-field magnetic hysteresis curves for uncoated SPIONs vs. silica coated-SPIONs at 300K. The results show samples containing A) Fe_3O_4 and B) γFe_2O_3 cores. 168
Figure 4.25. R_2 ($1/T_2$) Relaxivity data for SiO_2-SPION samples containing Fe_3O_4 and γFe_2O_3 cores. 169

List of Tables

Table 4.1. Best fit parameters extracted from magnetisation curves presented in **Figure 4.6.**..... 149
Table 4.2. Infrared bands of iron oxides. 159

4.1 Introduction

In Chapter 3, poly(2-methacryloyloxyethyl phosphorylcholine) functionalised superparamagnetic iron oxide nanoparticles (pMPC-SPIONs) were developed, which

showed excellent colloidal stability in PBS at 37 °C for up to 7 days at stem cell labelling concentrations of 50 μg Fe mL^{-1}. Unfortunately, pMPC-SPIONs showed poor chemical stability under low pH conditions (conditions mimicking those of a lysosomal environment found in a stem cell) which thus determined their unsuitability for long term stem cell tracking. In this Chapter and Chapter 5, we focus on coating strategies for the protection of the iron oxide core from erosion under acidic conditions.

Coating strategies are divided by composition using either organic or inorganic coatings (or a hybrid of both).[1] Proposed ideas/strategies to tailor an organic shell by preventing the diffusion of acidic protons reaching the iron oxide core to improve chemical stability are i) incorporating a hydrophobic section in the shell, ii) incorporating a section of the polymer shell which acts as a buffer such as the presence of basic moieties which could slowly protonate or iii) incorporating a cross-linkable section in the polymeric shell.

In general, inorganic coatings compared to organic coating are best known for their chemical stability and are therefore likely to be successful at protecting the iron oxide core from dissolution on a long-term timescale.[2] Most inorganic coatings provide nanoparticles (NPs) with imaging capabilities (such as silica, gold, silver, cadmium based). In terms of designing contrast agents for cell labelling, nanomaterials possessing multimodal imaging capabilities are an attractive target. In this Chapter, we focus on inorganic coating strategies using silica and in Chapter 5, we focus on coating strategies using gold. These coatings are selected for further investigation for this project since they are known to possess chemical stability and interesting imaging properties which thus appeal to the synthesis of a magnetic nanomaterial as a contrast agent for long term stem cell tracking.[3-5]

Silica precursors (i.e. tetraethyl orthosilicate (TEOS), sodium silicate or silicic acid) are relatively cheap reagents to use for the preparation of silica coated NPs. As a NP surface coating, silica provides a hydrophilic surface which allows NPs to be colloidally stable in a range of aqueous solvents.[6, 7] Silica has been known to stabilise magnetic NPs by shielding the magnetic dipole interaction.[8] In addition, silica coatings can enhance the coulomb repulsion of magnetic NPs which is caused by electrostatic repulsion from its highly negatively charged surface.[9] Silica is

porous due to its molecular framework to which oxygen or other species such as hydrogen protons could diffuse through.[10] Silica can provide a surface for further surface modification due to the presence of surface silanol groups which can covalently react with a variety of coupling groups.[11]

Disadvantages to using silica are that the co-ordination of orthosilicate ligands with the iron oxide NP surface can modify the magnetic moment and anisotropy of NP surface metal ions through surface pinning.[12, 13] In addition, it has been proposed that surface magnetic moments are quenched through the bonding of surface ligands leading to a reduction in magnetisation.[14] Therefore, direct reaction of silica to the surface of uncoated iron oxide NPs can lead to the creation of a magnetic dead layer through the oxidation of Fe_3O_4 to form γFe_2O_3 which can thus lead to a decrease in the magnetisation saturation (M_s) value of silica coated NPs. It would be interesting to see if the same would be observed if reacting silica onto γFe_2O_3 NPs and if this also lowers the M_s value. In addition to this, the chemical stability of silica coated SPIONs containing an γFe_2O_3 core versus an Fe_3O_4 core and their relative rate of dissolution to conditions mimicking those found in a lysosome would provide information regarding the stability of the silica shell versus stability of the core. Chemical stability of iron oxides in 0.5 M HCl (pH 0.3) at 25 °C and their rates of dissolution over a period of 100 hours (4.16 days) has been investigated and reported, **Figure 4.1**.[15] At 80 hours (3.3 days), the dissolution of magnetite reached a dissolution fraction of 0.37 (37 %) and at 100 hours (4.16 days) a dissolution fraction of 0.45 (45 %) was observed. However, for maghemite, a dissolution fraction of around 0.12 (12 %) was reported at 80 hours thus a slower rate of dissolution was observed. These results therefore show that maghemite is more chemically stable than magnetite which may be an advantage when considering the development of chemically stable SPIONs for long term stem cell tracking. To support the chemical stability of maghemite compared to magnetite further, maghemite has been found to be stable in biological media and has thus showed a lower cytotoxicity when compared to magnetite. It has been suggested that the increased chemical stability of maghemite is due to the material containing fully oxidised Fe^{3+} ions only whereas magnetite contains Fe^{2+} which allows for ionic or electronic transfers (redox (reduction of O_2)), **Figure 4.2**.[16] Mineral surfaces containing transition metals may induce reactive oxygen species (ROS) through dissolution and release of metals,

thereby inducing oxidative stress (cytotoxicity). For the case of iron, the reaction of Fe^{2+} with O_2 is fast when Fe^{2+} ions are adsorbed at the mineral surface than when Fe^{2+} ions are dissolved. Other factors affecting the rate of dissolution include the NP surface area, surface roughness and surface curvature.[17] These findings support the need to compare and investigate the chemical stability and dissolution of the two different iron oxide core species (magnetite and maghemite) which will be studied in this Chapter. Biological studies with SiO_2-SPION samples containing Fe_3O_4 and γFe_2O_3 cores will also be investigated in Chapter 6.

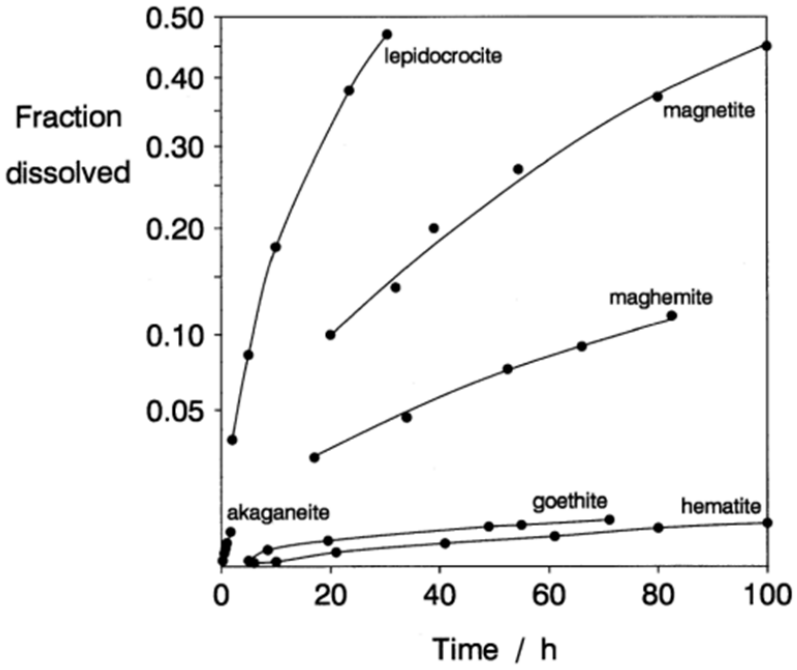

Figure 4.1. Chemical stability of maghemite and magnetite showing the rate of dissolution of iron oxides in 0.5 M HCl (pH 0.3) at 25 °C over a period of 100 hours (4.16 days) Image taken from reference.[15]

The main method to synthesise silica surface coatings on NPs is *via* the sol-gel Stöber method whereby hydrolysis and condensation of a sol-gel precursor (such as tetraethyl orthosilicate (TEOS)) polymerises in the presence of a base such as ammonia to form silica *in situ*.[18] The conventional procedure for carrying out the sol-gel Stöber method to form a surface NP coating involves the direct hydrolysis of TEOS with water dispersible bare NPs containing surface hydroxyl groups to which silica readily binds. Lu *et al.*[19] have demonstrated control of the silica shell thickness onto 5-10 nm SPIONs by varying the ammonia concentration and the ratio of TEOS to water. Adapted methods of this procedure have been carried out by miniemulsion

using micelles or reverse micelles through the use of a surfactant which forms a nanoreactor to achieve control over the silica coating thickness.[20-23]

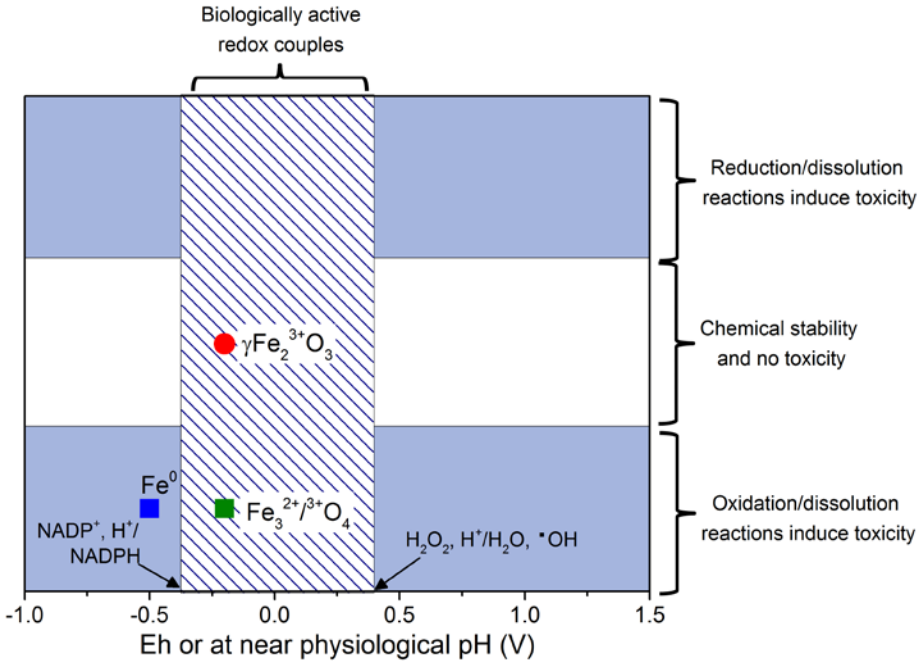

Figure 4.2. Chemical stability of maghemite and magnetite showing the correlation between iron oxide dissolution/chemical stability and their toxicity. E_h represents the redox potential. Image adapted from reference.[16]

An advantage to this latter approach is that NPs synthesised with a hydrophobic shell such as oleic acid can be used directly without modification of the surface prior to the micellisation reaction. A serious disadvantage to this approach is the surfactant which is used during the reaction is cytotoxic to cells and can be difficult to remove after coating reaction. For the removal of surfactant, silica coated SPIONs require harsh treatment through washing in acid which can lead to dissolution of the SPION core.

The synthesis of a monodisperse distribution consisting of individual SPION cores coated with silica is difficult to achieve. A distribution of silica coated NPs containing two or more cores is likely to be formed during the reaction.[19] An alternative method to depositing silica on the surface of NPs is to use sodium silicate or silicic acid solution in the presence of a base such as tetramethylammonium hydroxide with water dispersible bare NPs containing surface hydroxyl groups.[24, 25] Studies have shown the deposition of silica by this method provides better coverage

onto the NP surface than by *via* the TEOS sol-gel precursor route.[26] Disadvantages found with this approach surround issues with control of the silica shell size and uniformity around the core.[26] With regards to multimodal imaging, silica coated iron oxide NPs have been found to possess a photoacoustic absorbance in the near-IR spectral range at a laser excitation wavelength of 1064 nm.[5] The 3 nm thick silica shell coated onto 8 nm core SPIONs were prepared by Alwi *et al.* and used as a contrast agent for photoacoustic imaging *ex vivo*, **Figure 4.3**.

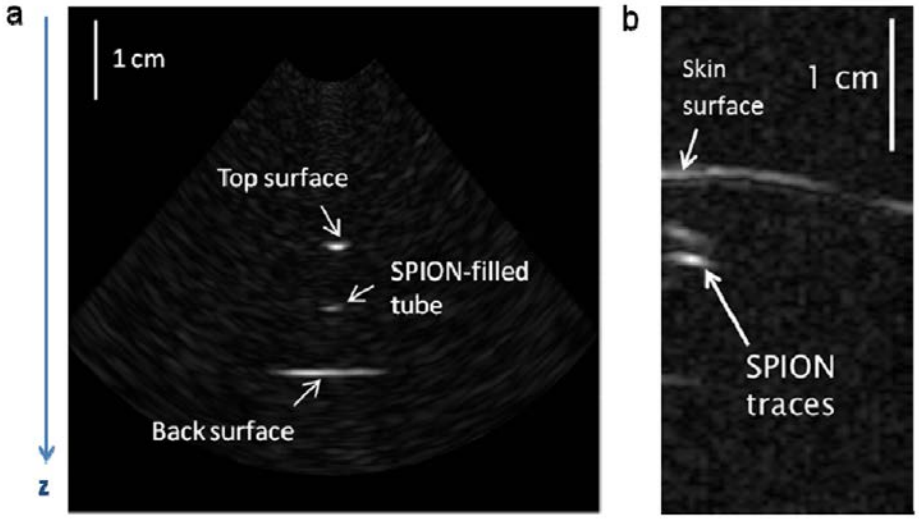

Figure 4.3. "(a) Frequency-domain photoacoustic (FD-PA) array image of a silica coated SPION-filled tube inside chicken breast tissue. (b) Two-dimensional FD-PA image of a rat thigh containing silica-coated SPION obtained using a 3.5-MHz focused transducer." Image taken from reference.[5]

4.2 Results and Discussion

Silica coated SPIONs were prepared using the conventional sol-gel Stöber method involving the hydrolysis of TEOS onto the surface of water dispersible bare SPIONs containing surface hydroxyl groups. The conventional method was selected since it avoided the use of surfactants and thus prevented harsh treatment for the removal of surfactant from samples prior to biological studies. The overall aim for the silica shell synthesis procedure was to obtain a method whereby a uniform silica shell could be achieved and the silica shell thickness could be controlled. Two different SPION cores were used to assess if silica coated SPIONs of different composition (i.e. maghemite (γFe_2O_3) (synthesised by co-precipitation) and magnetite (Fe_3O_4) (synthesised by thermal decomposition process involving the use of oleic acid to form OA-SPIONs)) would affect their overall performance and properties.

4.2.1 Synthesis and Characterisation of Magnetite Fe_3O_4 SPIONs

Monodisperse oleic acid coated superparamagnetic iron oxide NPs (OA-SPIONs) were prepared following the thermal decomposition method reported by Hyeon and co-workers.[27]

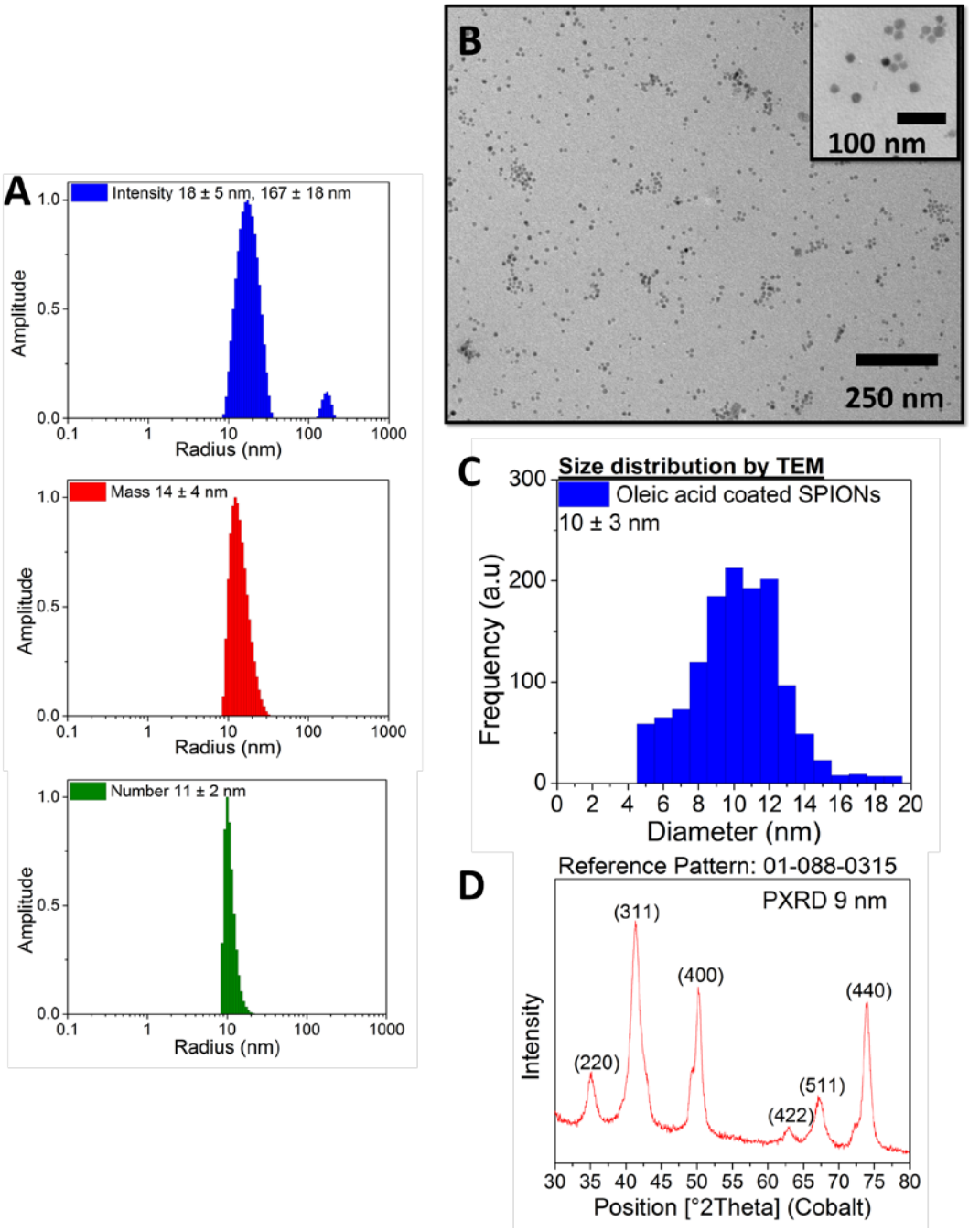

Figure 4.4. Characterisation data for oleic acid coated SPIONs showing A) solvodynamic radius peak height distributions by DLS, B) TEM image and size distribution C) and D) PXRD pattern.

Dynamic light scatting (DLS) size measurements of the OA-SPIONs in tetrahydrofuran (THF) gave solvodynamic hydrodynamic radius peak height measurements by intensity, mass and number of: $R_{s,\ intensity}$ = 18 ± 5 nm and 167 ± 18 nm, $R_{s,\ mass}$ = 14 ± 4 nm, $R_{s,\ number}$ = 11 ± 2 nm (**Figure 4.4A**). Transmission electron microscopy (TEM) showed OA-SPIONs were spherical in shape. From the TEM image, a size distribution from over 400 measurements was obtained using ImageJ software. The average diameter of the cores was measured at 10 ± 3 nm, **Figure 4.4B and C**. Powder X-ray diffraction (PXRD) was also used to characterise the SPIONS and the PXRD pattern obtained for the OA-SPIONs showed good agreement with the reference pattern for magnetite (ICDD no. 01-088-0315) and indicated the material was crystalline, **Figure 4.4B**. The average particle size diameter measured was 9 nm as derived from the Scherrer equation.

4.2.2 Synthesis and Characterisation of Maghemite γFe_2O_3 SPIONs

SPIONs stable and dispersible in pH 2 solution were prepared following the co-precipitation methods reported by Massart and Valero *et al.*[28, 29] The size of maghemite (γFe_2O_3) SPIONs was assessed by DLS in deionised water (DIW) pH 2 and gave hydrodynamic radius peak height measurements of: $R_{h,\ intensity}$ = 20 ± 2 nm and 88 ± 13 nm, $R_{h,\ mass}$ = 19 ± 2 nm and 82 ± 12 nm and $R_{h,\ number}$ = 18 ± 8 nm (**Figure 4.5A**). The co-precipitation method is known for producing NPs with uncontrolled shape and size.[30, 31] This was confirmed by TEM of a sample of pH 2 dispersible SPIONs, **Figure 4.5B**. A size distribution of the SPIONs was therefore not produced from the image using ImageJ software since the software had difficulty scanning NPs which were non-spherical in shape. PXRD was again used and the pattern obtained for the pH 2 dispersible SPIONs showed good agreement with the reference pattern for maghemite (ICDD no. 00-025-1402) and indicated the material was crystalline, **Figure 4.5C**. The average particle size diameter measured was 8.4 nm as derived from the Scherrer equation. The core size obtained by PXRD was used to calculate and deduce silica shell thicknesses in samples produced from further reactions.

Dr. Lara Bogart at the University of Liverpool, Institute of Integrative Biology determined the magnetic SPION cores sizes using superconducting quantum interference device (SQUID) magnetometry curves obtained from measurements taken for γFe_2O_3 and Fe_3O_4 SPIONs, **Figure 4.6**.

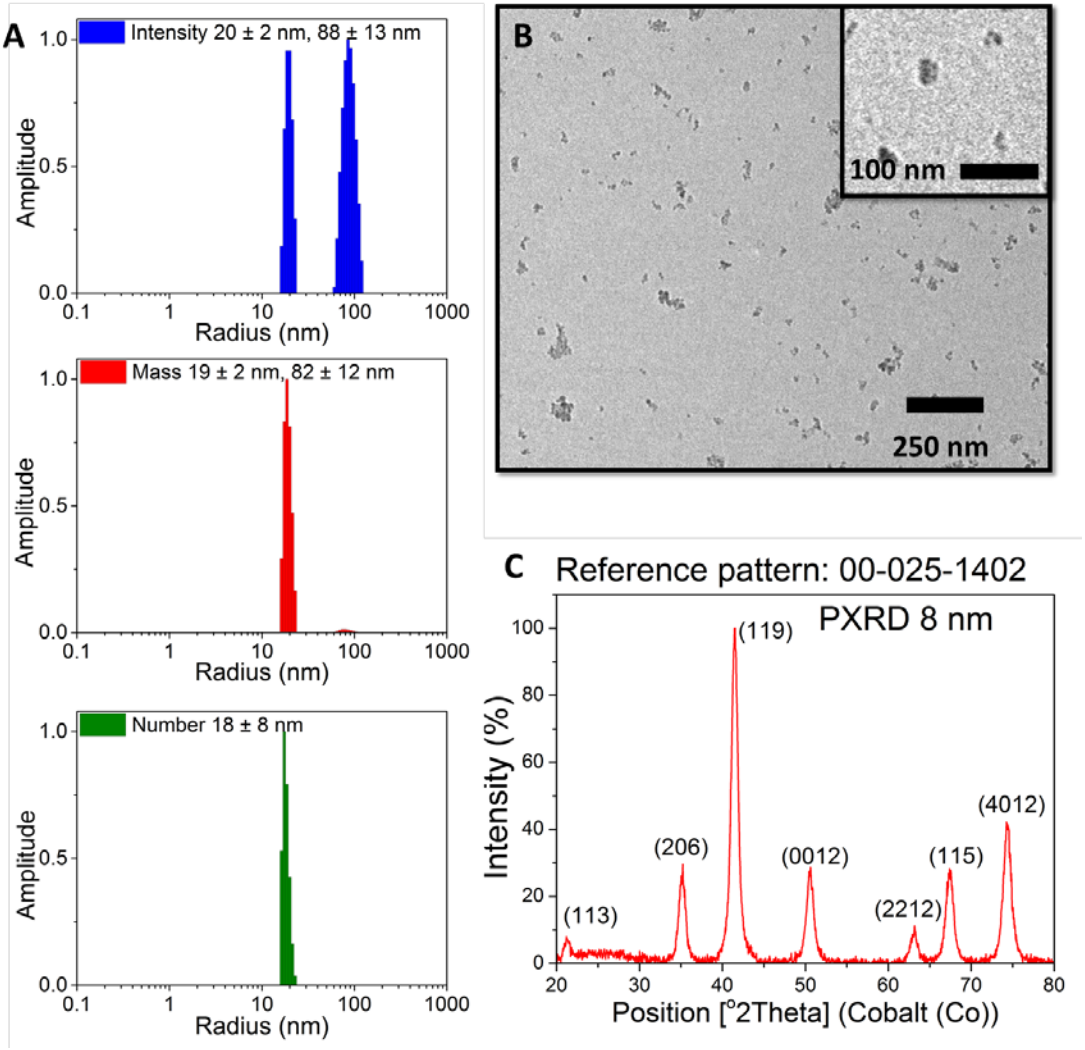

Figure 4.5. Characterisation data for pH 2 dispersible γFe_2O_3 SPIONs showing A) hydrodynamic radius peak height distributions by DLS, B) TEM image and C) PXRD pattern.

The sizes were determined using a simple Langevin expression modified by the log-normal polydispersity function, summarised in **Table 4.1**, where M_{SP} and M_{SB} is the saturation magnetisation of the particles and of the bulk material, respectively and where D_t is the total SPION core diameter and D_m is the magnetic core diameter. Size measurements obtained using this method (**Table 4.1**) for the core sizes of γFe_2O_3 and Fe_3O_4 were very similar to those obtained from PXRD, TEM and DLS. It was found that both γFe_2O_3 and Fe_3O_4 had total core diameter of 10 nm and magnetic

core diameter of 9 ± 0.1 nm and 8 ± 0.1 nm respectively. Magnetic core sizes have also been determined from the intracellular iron content in single cell magnetophoresis measurements, which are discussed further in detail in Chapter 6.

Table 4.1. Best fit parameters extracted from magnetisation curves presented in **Figure 4.6.**

Sample	M_{SP} (emu/cm^3)	M_{SB} (emu/cm^3)	D_m (nm)	D_t (nm)	Standard Deviation	Comment
γFe_2O_3	375	375	9	10	0.1	Powdered sample
Fe_3O_4	265	480	8	10	0.1	

4.2.3 Preparation of pH 8 Dispersible SPIONs from OA-SPIONs

To prepare SPIONs for silica coating by the sol-gel Stöber method, chemical modification of the SPION surface was performed to convert the hydrophobic OA-SPIONs to hydrophilic through the removal of oleic acid from the surface of the SPIONs, producing a bare surface containing only surface hydroxyl groups. The procedure to remove oleic acid from the surface of OA-SPIONs was adapted from a method reported by Kohler *et al.*[32] The method involved conditioning OA-SPIONs in 1 M ammonium hydroxide in butan-1-ol solution *via* sonication using an ultrasonic bath for 2 hours at 60 °C. SPIONs with a bare surface containing only surface hydroxyl groups could then be separated using a rare earth magnet at the side of the vial and later on dispersed into pH 8 sodium hydroxide solution using further sonication. The removal of oleic acid from the surface was confirmed by elemental analysis which showed C: 0.74 % and H: 0.23 % and by TGA (air atmosphere at 100 mL/min), which showed a total organic and adsorbed solvent content of 1.09 %, **Figure 4.8 red line**. Hydrodynamic radius peak height measurements by DLS indicated the pH 8 dispersible SPIONs were not fully colloidally stable since size distributions found were much larger than those measured for OA-SPIONs. This suggests aggregates were present in the dispersion which is likely to be caused by interactions of SPIONs with each other through van der Waals forces. Dispersibility was demonstrated by the ability of the SPIONs to remain in suspension in pH 8 solution, **Figure 4.7**.

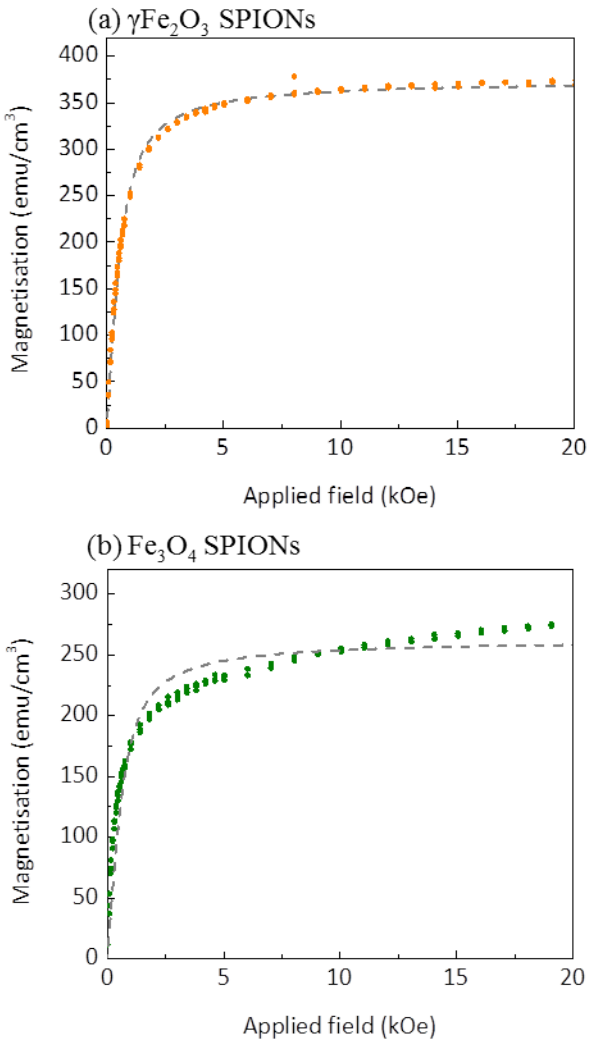

Figure 4.6. Room temperature magnetisation curves of (a) γFe_2O_3 and (b) Fe_3O_4 cores as synthesised. The grey line indicates best model fit using simple Langevin expression modified by the log-normal polydispersity function. Best fit parameters are provided in **Table 4.1.**

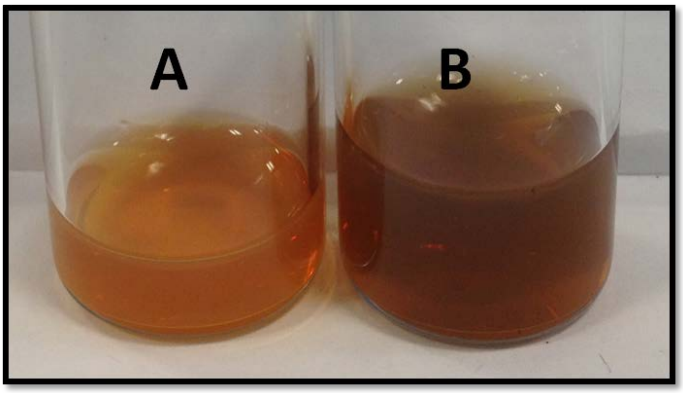

Figure 4.7. Image showing vials of pH 8 dispersible A) maghemite γFe_2O_3 and B) magnetite Fe_3O_4 SPIONs at the same concentration showing orange and brown suspensions respectively.

A confirmation of the maghemite composition was carried out using TGA (**Figure 4.8**), through the observation of the colour of the SPIONs in solution (**Figure 4.7A)** and by FT-IR spectroscopy (**Figure 4.14** fingerprint region using **Figure 4.16**).

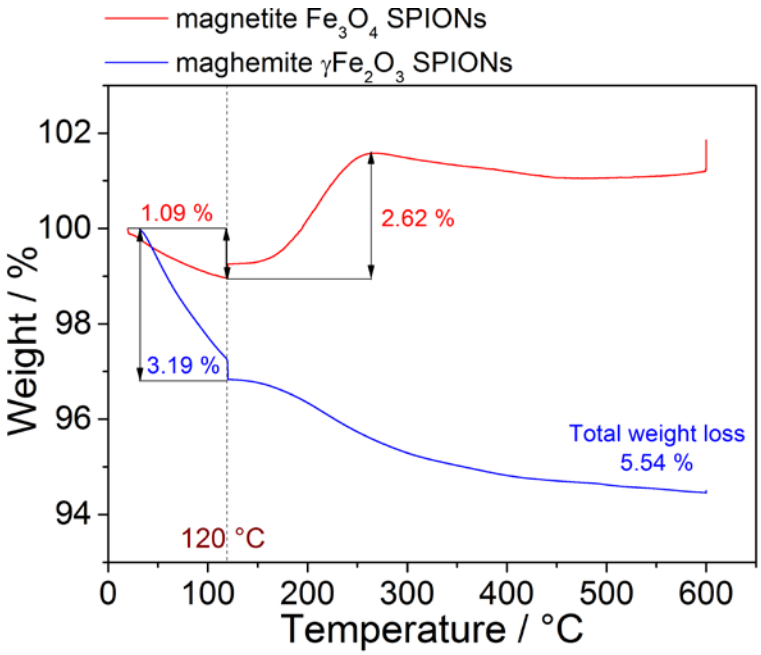

Figure 4.8. TGA data for pH 8 dispersible magnetite Fe_3O_4 SPIONs (red line) and pH 2 dispersible maghemite γFe_2O_3 SPIONs (blue line). The line represents the isotherm held at 120 °C for the removal of adsorbed solvent. Air atmosphere at 100 mL/min.

The TGA measurement of pH 8 dispersible SPIONs, **Figure 4.8 red line,** shows a 2.62 % weight increase from 150 to 280 °C which indicates oxidation of Fe^{2+} during the heating process in air. The theoretical percentage weight increase for the oxidation of pure magnetite to maghemite is 3.45 % since each Fe_3O_4 can combine with half an oxygen unit ($2Fe_3O_4 + ½\ O_2 \rightarrow 3(\gamma Fe_2O_3)$).[24,25] The percentage weight increase obtained from the TGA (2.62 %) thus indicates the SPIONs are likely to consist mainly of magnetite Fe_3O_4 (76 %) with a small amount of maghemite also likely to be present (34 %).[33, 34] The colour of a dry sample of pH 8 dispersible magnetite Fe_3O_4 SPIONs produced were found to be black, **Figure 4.9(1A)**, which according to colour plates of iron oxide produced by R. Cornell indicates the sample is magnetite Fe_3O_4, **Figure 4.9C**.[35] After the heating procedure from the TGA in air, the dry sample turned from black to brown, which indicates the formation of maghemite, **Figure 4.9(1B)**.[35]

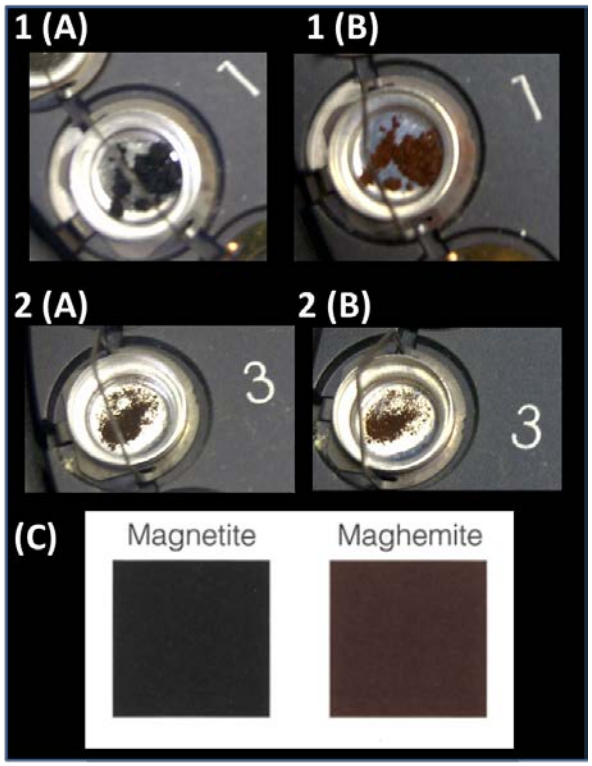

Figure 4.9. TGA pans containing 1) pH 8 dispersible magnetite Fe_3O_4 SPIONs and 2) pH 8 dispersible maghemite γFe_2O_3 SPIONs showing (A) before and (B) after heating the dry sample in the TGA to 600 °C in air. (C) shows colour plates for Magnetite and Maghemite taken from reference.[35]

The colour change therefore suggests maghemite had been formed *via* oxidation of magnetite after heating in the TGA. When compared to pH 2 dispersible SPIONs synthesised by co-precipitation procedure, the colour of the dry SPION sample was brown, **Figure 4.9(2A)**, and remained brown after heating, **Figure 4.9(2B)**. The SPION sample also showed no increase in percentage weight by the TGA, **Figure 4.8 blue line**, which thus indicated these SPIONs were maghemite γFe_2O_3 in composition. Interestingly, when samples of pH 8 dispersible maghemite γFe_2O_3 and magnetite Fe_3O_4 SPIONs in suspension at the same concentration were compared visually, the samples appear orange and brown respectively, **Figure 4.7A and B**.

4.2.4 Preparation of pH 8 Water Dispersible SPIONs from pH 2 Water Dispersible SPIONs

For the silica coating procedure *via* the sol-gel Stöber method, alkaline conditions were required. It was found from observations that pH 2 dispersible SPIONs

aggregate at high pH. This aggregation behaviour in alkaline conditions for the silica coating procedure was not favourable since good dispersibility of SPIONs is required during the silica coating procedure to achieve a uniform coating around an individual SPION core.

Since the method used previously for the removal of oleic acid from OA-SPIONs provided a bare NP surface with surface hydroxyl groups and dispersibility in pH 8 solution, pH 2 SPIONs were subjected to the same conditions and reagents in order to attempt to provide the same stability in pH 8 solution. After this conditioning treatment, pH 2 SPIONs were found to be dispersible in pH 8 NaOH solution which was confirmed by their stability in suspension after >24 hours at ambient.

4.2.5 Synthesis of Silica Coated SPIONs (γFe_2O_3 and Fe_3O_4) by the sol-gel Stöber process

Silica coated SPIONs (SiO_2-SPIONs) were prepared following an adapted method by Lu *et al*.[36] Briefly, pH 8 dispersible SPIONs were added to a solution of DIW and ammonia and sonicated and stirred using an overhead mixer at a speed of 250 rpm for 20 minutes. After this time, the stirring speed was then increased to 720 rpm to help further break up any aggregates or clusters in the reaction mixture. To this, a solution of TEOS in propan-1-ol was added gradually to the reaction flask using syringe and pump at a flow rate of 79 cc min^{-1} and left under continuous stirring and sonication for 4 hours. After the coating procedure, NPs were transferred to water *via* dialysis in order to remove ammonia and propan-1-ol prior to characterisation. To prepare samples for biological studies, NPs were concentrated *via* rotary evaporation to remove two thirds of the water and a solution of sodium azide (0.01 %) was added to aqueous samples to prevent bacterial growth.

4.2.5.1 Preliminary Experiments

To decide on the amount of TEOS to use in the reaction for the preparation of SiO_2-SPIONs for stem cell labelling experiments, three different volumes of TEOS were used for separate experiments. The aim of this experimental setup was to synthesise SiO_2-SPIONs containing different shell thicknesses in addition to determine the optimal amount of TEOS for the silica coating procedure. The volumes of TEOS

used in each experiment were 150, 100 and 50 µL which were denoted as Experiments A, B and C respectively. For the experimental setup, pH 8 dispersible γFe_2O_3 SPIONs were used as the starting material for the coating reaction due to the abundance of material available when compared with Fe_3O_4 SPIONs. The SiO_2-SPIONs prepared in Experiments A to C were then assessed by visual inspection using TEM, **Figure 4.10**.

For the SiO_2-SPIONs prepared in Experiments A and B larger volumes of TEOS were used, 150 and 100 µL respectively, thicker silica shells on the surface of γFe_2O_3 SPIONs were observed through TEM, **Figure 4.10A and B** respectively. For Experiment A, 150 µL of TEOS was used in the reaction. Nucleation and formation of silica NPs were found in addition to clusters of SPIONs coated by silica. In Experiment B, where 100 µL of TEOS was used, fusion of NPs and silica coating surrounding a cluster of NPs were observed and large aggregates were found.

For Experiment C, a 50 µL volume of TEOS was used. Silica was observed to mainly coat individual SPIONs. In some cases, a coating surrounding a cluster of SPIONs was observed. It was difficult to tell how many cores per coated NP since the SPION cores used have an ill-defined shape. The TEM image shown in **Figure 4.10C** also demonstrated that some of the NPs appeared to be aggregated on the TEM grid, which could have been caused from the sample preparation of the TEM grid during the drying process. It is however likely that the few aggregates present are actually SiO_2-SPIONs which have fused together during the later stage of the coating process.

Silica coated γFe_2O_3 SPIONs synthesised using 50 µL of TEOS appeared to be the best volume of TEOS to work with since the sample showed synthesis of a thin silica shell surrounding the SPION core(s) and SPIONs appeared to be moderately uniform in size and distribution with very few aggregates observed.

4.2.5.2 Characterisation of Silica Coated γFe_2O_3 SPIONs

Characterisation by TEM of the silica coated γFe_2O_3 SPIONs synthesised using 50 µL of TEOS for the coating reaction gave a histogram with average (mean) diameter of 33 ± 15 nm, which was determined from >200 measurements using ImageJ

software, **Figure 4.11**. Since TEM core diameter measurements could not be obtained for the γFe_2O_3 SPIONs, the silica shell thickness could only be determined using the core diameter taken from PXRD of 8.4 nm which gave a calculated shell thickness of 11-12 nm.

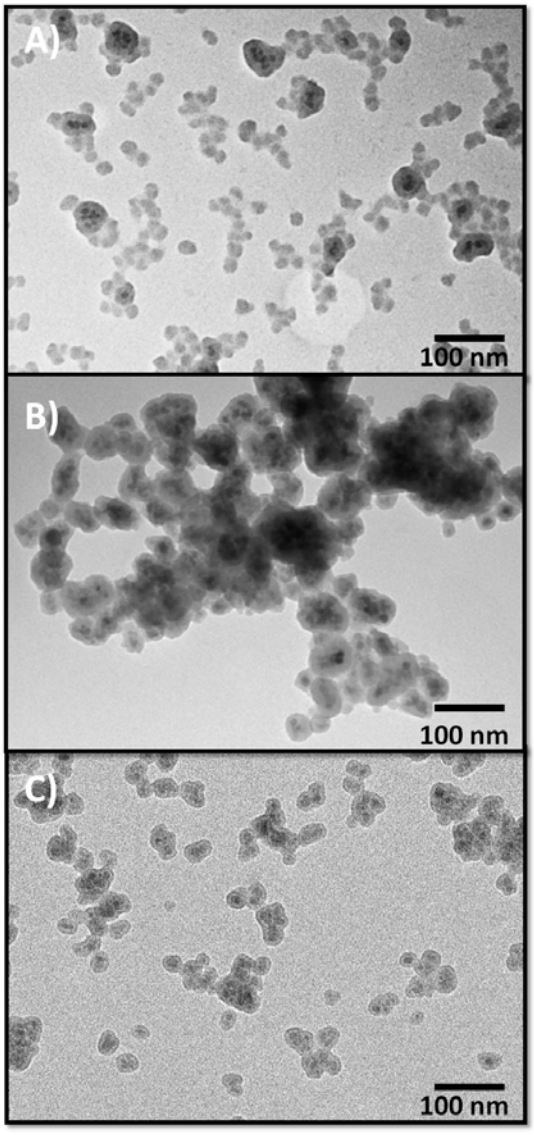

Figure 4.10. TEM images of silica coated γFe_2O_3 SPIONs using TEOS aliquots of A) 150 µL, B) 100 µL and C) 50 µL in the reaction. Image A) shows presence of silica NPs formed and A) and B) showing increased numbers of multiple SPION cores surrounds by a silica coating.

A sample of the silica coated γFe_2O_3 SPIONs, **Figure 4.10C**, was diluted and briefly sonicated for TEM analysis in order to determine whether or not aggregation was caused from the sample preparation of the TEM grid during the drying process, **Figure 4.12B**.

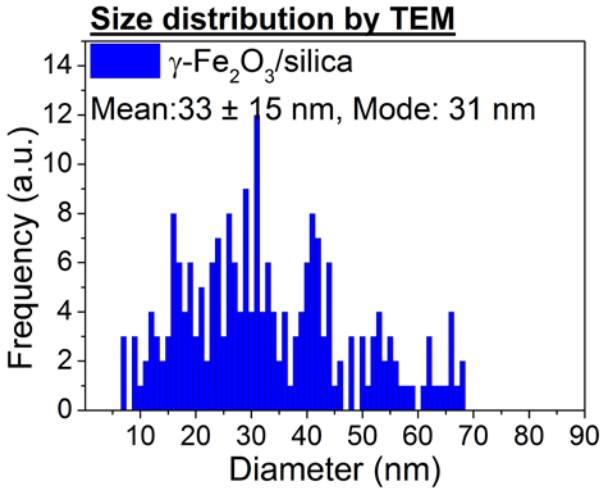

Figure 4.11. Size distribution of silica coated γFe_2O_3 SPIONs by TEM. Average diameter 33 ± 15 nm taken from >200 measurements.

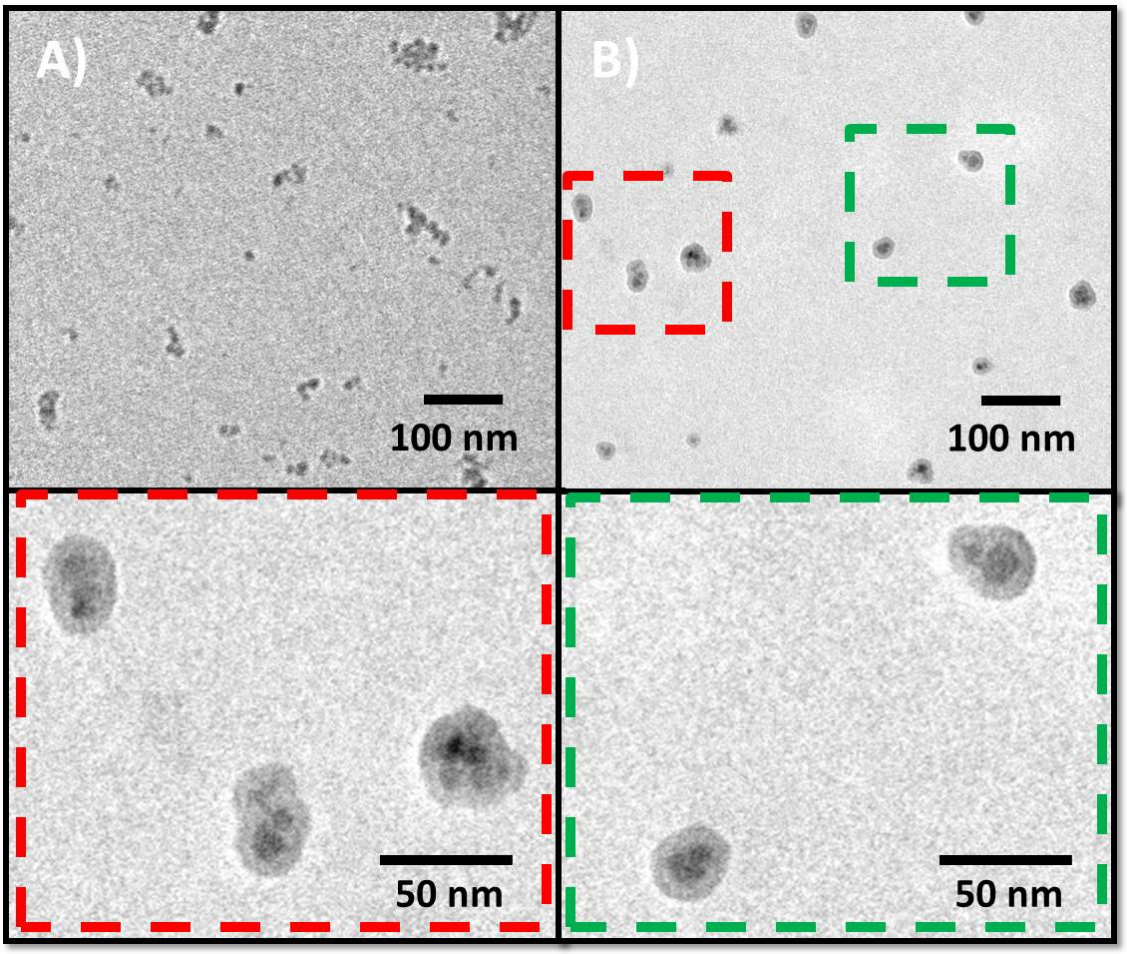

Figure 4.12. TEM images of A) γFe_2O_3 SPION starting material and B) silica coated γFe_2O_3 SPIONs using TEOS aliquot of 50 µL with zoomed in areas highlighted in red and green inset.

From the TEM image (**Figure 4.12B**), NPs showed better dispersion. The small aggregates that had been previously seen in **Figure 4.10C** were also not found. A closer look at the NPs (red and green dashed boxes) provided visualisation of the silica shell and iron oxide core(s) and again confirmed that the iron oxide cores were not spherical and are more globular shaped.

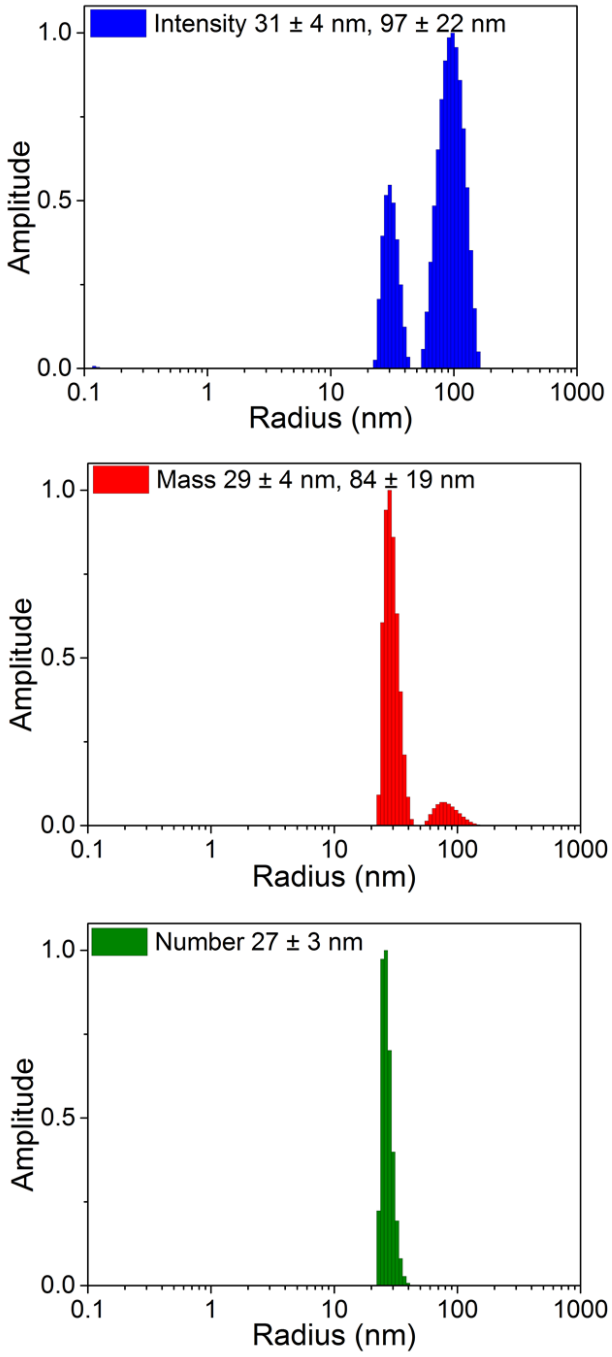

Figure 4.13. DLS hydrodynamic radius peak height measurements of silica coated maghemite SPIONs.

Some silica coated NPs showed more than one core present but it is difficult to visualise how many in each composite NP since the contrast of the cores compared to the shell in some silica coated NPs are found to be hazy and unclear. A rough measurement of the shell thickness measured by TEM using silica coated composite NPs which do have a good contrast compared to the cores gave a thickness of 5 - 7 nm. The size of SiO_2-γFe_2O_3 SPIONs was assessed by DLS in DIW pH 8 showed two hydrodynamic radius peak height populations found in both the intensity and mass weighted distributions: $R_{h,\ intensity}$ = 31 ± 14 nm and 97 ± 22 nm, $R_{h,\ mass}$ = 29 ± 4 nm and 84 ± 19 nm and $R_{h,\ number}$ = 27 ± 3 nm, **Figure 4.19**.

FT-IR spectroscopy measurements of pH 8 dispersible γFe_2O_3 SPIONs before and after coating with TEOS were carried out to investigate the NP surface chemistry, **Figure 4.14A and B**.

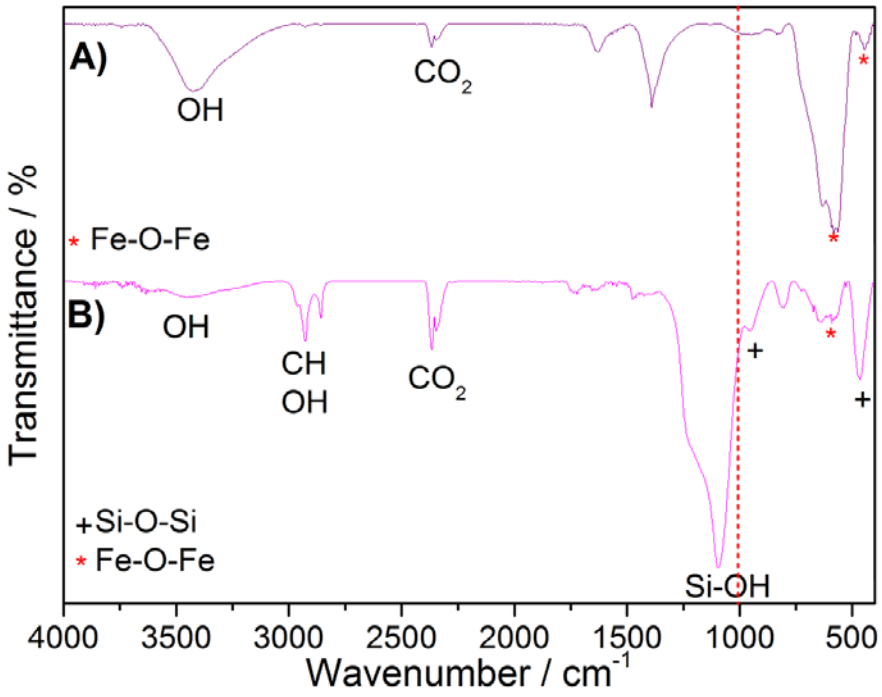

Figure 4.14. FT-IR spectra of A) pH 8 dispersible γFe_2O_3 SPIONs (before coating procedure) and B) silica coated γFe_2O_3 SPIONs (after coating procedure). The red dashed line represents the start of the fingerprint region to identify iron oxide composition using **Figure 4.16.**

Table 4.2. Infrared bands of iron oxides.

Iron Oxide	Bands found at wavenumber / cm^{-1}
Magnetite	590
Maghemite	450, 570, 590, 630
Hematite	470, 540

From FT-IR spectrum B, a strong Si-O-H stretching band at 1100 cm^{-1} was observed in addition to bands assigned to Si-O-Si vibration at 990 cm^{-1} and Si-O-Si asymmetric bending at 450 cm^{-1} were found which confirmed the presence of silica in the sample. Bands assigned to Si-O-Fe are expected in the region of 800 to 400 cm^{-1}.[37] Bands for CO_2 were seen for both samples around 2300 cm^{-1}. The OH groups observed for FT-IR spectrum A and B around 3400 cm^{-1} (and 3000 cm^{-1} for B) confirm the surface hydroxyl groups present on the surface of uncoated and SiO_2 coated γFe_2O_3 SPIONs respectively. The CH band found around 3000 cm^{-1} in FT-IR spectrum B for SiO_2 coated γFe_2O_3 SPIONs are likely to be C-H bonds from un-hydrolysed TEOS on the outer surface of the SPION.

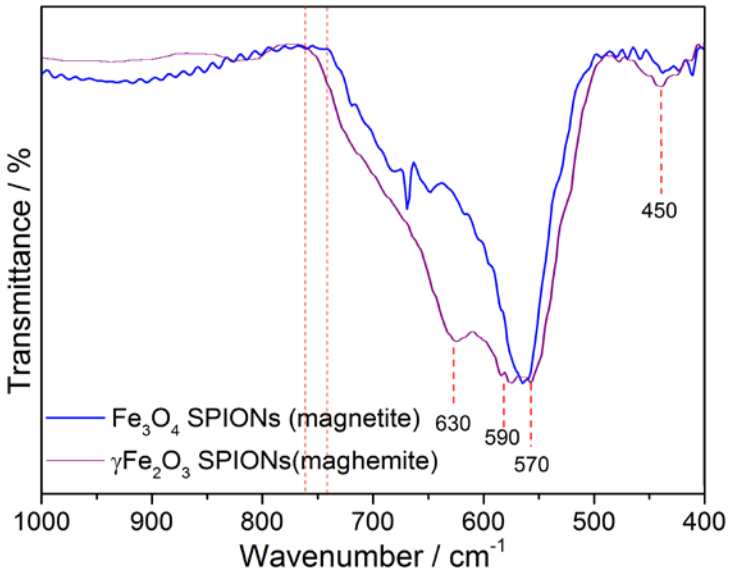

Figure 4.15. FT-IR spectra fingerprint region of **Figure 4.14A** against **Figure 4.20A**. Peaks picked using reported wavenumbers for maghemite, **Table 4.2**. Red dash lines show the wavenumbers for when the broad peaks plateau with the baseline.

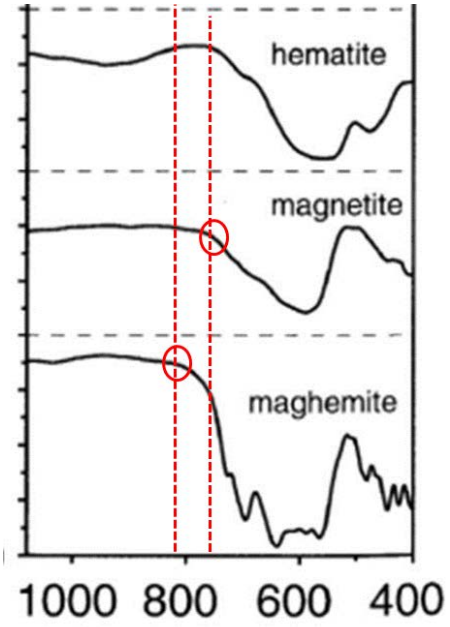

Figure 4.16. FT-IR spectra of iron oxides showing the fingerprint region of the FT-IR spectrum of iron oxides. Image taken from reference.[38] Red lines added to figure to highlight the wavenumbers for when the broad peaks plateau with the baseline.

FT-IR spectroscopy was used to determine the composition of the iron oxide NPs synthesised by looking at the band pattern in the fingerprint region reported, **Table 4.2** and **Figure 4.16**.[38] Magnetite has a smooth broad peak with a characteristic left hand slope at 590 cm^{-1}. The fingerprint peak pattern for Maghemite however is broader than magnetite and has a characteristic jagged tooth shaped foot to its peak due to four peaks found from 450 to 630 cm^{-1}, **Table 4.2**. Another characteristic sign of magnetite compared to maghemite is the point at which the peak for magnetite joins the baseline. Magnetite reaches the baseline at a lower wavenumber compared to maghemite which joins the base line at a higher wavenumber due to being broader, **Figure 4.16**. A closer look at the fingerprint region of pH 8 dispersible γFe_2O_3 SPIONs before coating with TEOS, **Figure 4.15** taken from **Figure 4.14A,** showed a peak with a broad jagged tooth foot shape and wavenumbers characteristic of maghemite as highlighted by peaks picked. Zeta potential measurements carried out on the SiO_2- γFe_2O_3 SPIONs in DIW pH 8 gave a high negative zeta potential value of -61.6 ± 7.5 mV. The high zeta potential value and the observation of excellent colloidal stability of the NPs in water indicate these NPs achieved colloidal stability through an electrostatic repulsion/stabilisation mechanism.

4.2.5.3 Synthesis and Characterisation of Silica Coated Fe_3O_4 SPIONs

Using the same reaction conditions as described previously, pH 8 dispersible Fe_3O_4 SPIONs were reacted using a TEOS volume of 50 µL. Silica coated Fe_3O_4 SPIONs were successfully prepared as confirmed by TEM, **Figure 4.18B**. Here, the silica coated particles are evenly dispersed on the grid with most silica coated NPs containing only one SPION core. There are also other composite NPs which show two or three SPION cores fused together during the silica coating procedure, **Figure 4.18**. A closer look at the NPs (**Figure 4.18B** red dashed box) provided visualisation of a uniform silica shell and the iron oxide core. The size by TEM was measured as average (mean) diameter of 25 ± 12 nm and mode diameter as 21 nm. Using the core diameter determined by TEM of 10 nm, a shell thickness of 6 – 8 nm was deduced. Using the core diameter as determined by PXRD of 9 nm, a shell thickness of 6 - 8 nm was calculated.

A frequency histogram using TEM images taken from >100 measurements of silica coated composite NPs, **Figure 4.18**, showed that over 60 % of silica coated particles contained one SPION core with around 25 % and 10 % for silica coated particles contain two and three SPION cores respectively.

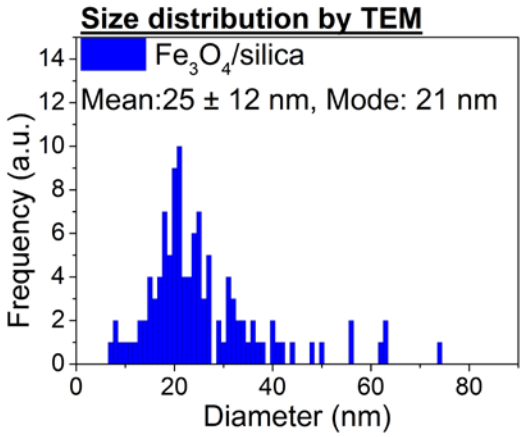

Figure 4.17. Size distribution of silica coated γFe_2O_3 SPIONs by TEM. Average diameter of 25 ± 12 nm taken from >100 measurements.

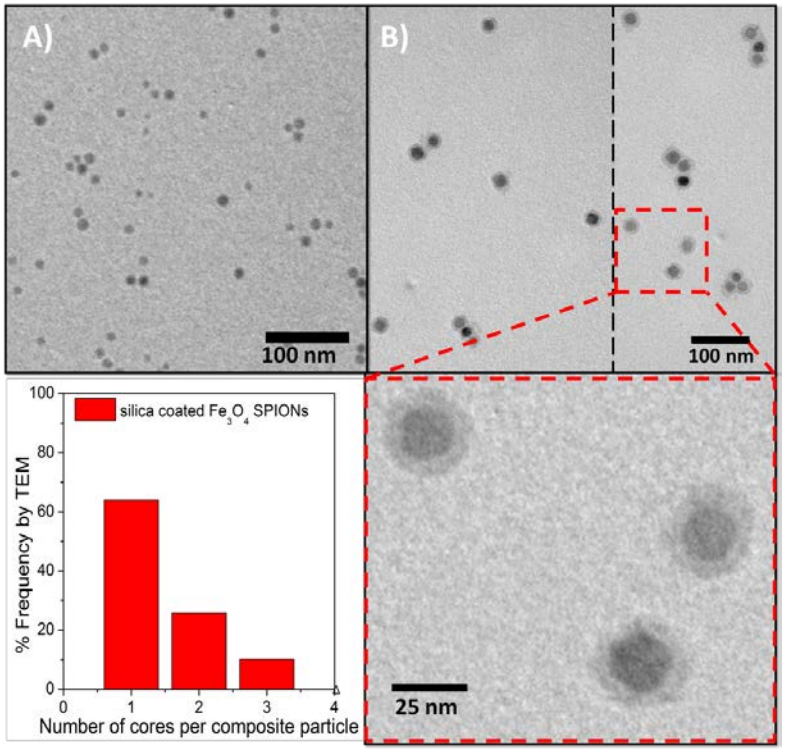

Figure 4.18. TEM images of A) oleic acid coated Fe_3O_4 SPION starting material and B) silica coated Fe_3O_4 SPIONs using TEOS aliquot of 50 µL with zoomed in area highlighted in red inset. Bottom left shows a frequency histogram for the number of SPION cores counted per silica coated composite particle.

The size of SiO_2-Fe_3O_4 SPIONs was assessed by DLS in DIW pH 8 showed two hydrodynamic radius peak height populations found in both the intensity and mass weighted distributions: $R_{h,\ intensity}$ = 32 ± 4 nm and 137 ± 35 nm, $R_{h,\ mass}$ = 31 ± 4 nm and 114 ± 28 nm and $R_{h,\ number}$ = 28 ± 3 nm, **Figure 4.19**. The bimodal distribution observed by DLS confirms the presence of silica SPIONs with single and multiple cores. When comparing to size measurements obtained by TEM, the DLS hydrodynamic radius peak height measurements are much bigger by a diameter difference of 31 to 39 nm which will include contribution from the hydrodynamic/solvation layers on the surface of SiO_2- Fe_3O_4 SPIONs in addition to size contribution from the fusion of two or more silica coated SPION NPs together.[39]

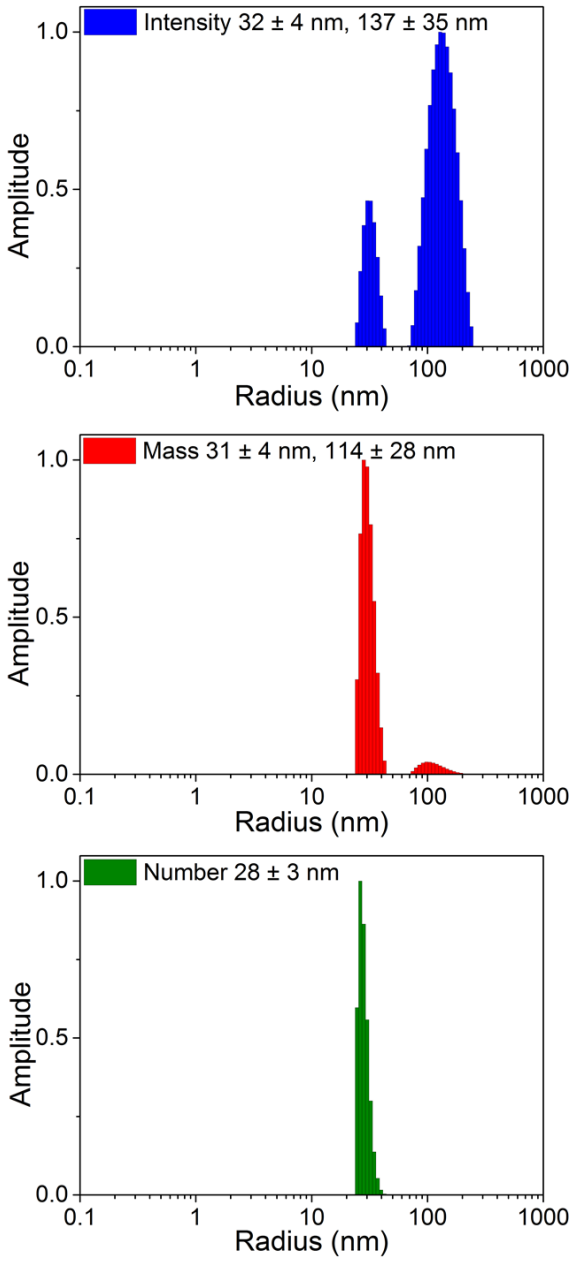

Figure 4.19. DLS hydrodynamic radius peak height measurements of silica coated magnetite Fe_3O_4 SPIONs.

FT-IR spectroscopy measurements of pH 8 dispersible γFe_2O_3 SPIONs before and after coating with TEOS were carried out to investigate the NP surface chemistry, **Figure 4.20**.

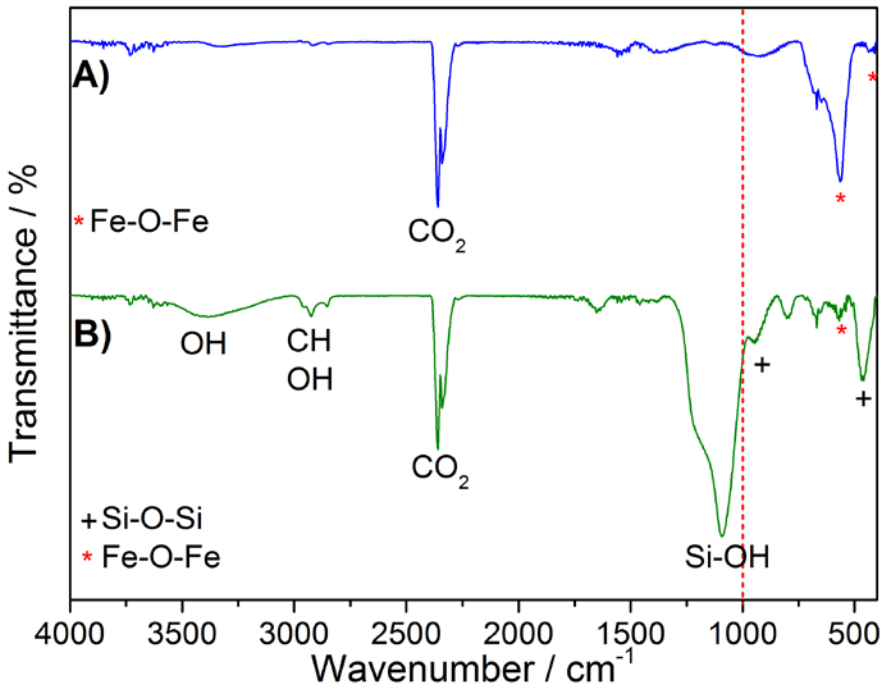

Figure 4.20. FT-IR spectra of A) pH 8 dispersible Fe_3O_4 SPIONs (before coating procedure) and B) silica coated Fe_3O_4 SPIONs (after coating procedure). The red dashed line represents the start of the fingerprint region to identify iron oxide composition using **Figure 4.16.**

The FT-IR spectrum for silica coated γFe_2O_3 SPIONs showed similar surface chemistry to that found in the FT-IR spectrum for silica coated Fe_3O_4 SPIONs and therefore similar bands were observed. From FT-IR spectrum B, a strong Si-O-H stretching band at 1100 cm^{-1} was observed in addition to bands assigned to Si-O-Si vibration at 990 cm^{-1} and Si-O-Si asymmetric bending at 450 cm^{-1} were found which confirmed the presence of silica in the sample. Bands assigned to Si-O-Fe are expected in the region of 800 to 400 cm^{-1}.[37]

Carbon dioxide for both samples were observed around 2300 cm^{-1}. Again, the CH band found around 3000 cm^{-1} in FT-IR spectrum B for SiO_2 coated γFe_2O_3 SPIONs is likely to come from un-hydrolysed TEOS on the surface of the coated NPs. The iron oxide composition of pH 8 dispersible Fe_3O_4 SPIONs was associated with magnetite, **Figure 4.15** taken from **Figure 4.21A** compared to **Figure 4.16** and **Table 4.2**, as observed by a single broad peak with a characteristic left hand slope shape found around 590 cm^{-1}.

The zeta potential of SiO_2-Fe_3O_4 SPIONs in DIW pH 8 was found to be -58.8 ± 10.5 mV. As observed from SiO_2-γFe_2O_3 SPIONs, a highly negative zeta potential value is an indication of excellent colloidal stability of the NPs in water through a electrostatic repulsion/stabilisation mechanism.

4.2.5.4 Properties of Silica Coated SPIONs (γFe_2O_3 and Fe_3O_4)

SiO_2-SPIONs were tested for cytotoxicity *via* a colorimetric assay using cell counting kit-8 (CCK-8) for the quantification for the number of viable cells after a period of 24 hours.

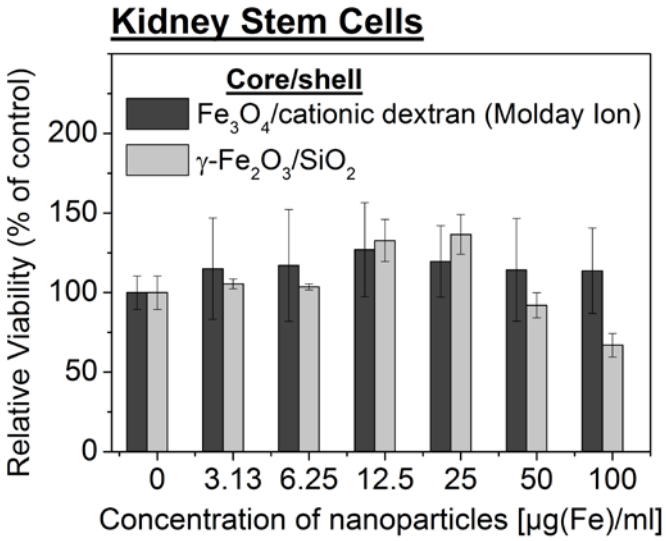

Figure 4.22. Relative viability of KSCs exposed to a range of concentrations of SiO_2-SPIONs (γFe_2O_3 SPION core) or Molday Ions. The cells were incubated in culture medium containing the NPs for 24 hours followed by viability measurement with CCK-8 reagent. Results are plotted as the relative viability as a function of NP concentration and error bars represent the standard deviation from three replicates. Cell viability with SiO_2-SPIONs (Fe_3O_4 SPION core) was not measured.

A kidney-derived murine stem cell (KSC) line[40] was used and exposed to cell culture medium containing concentrations of NPs ranging up to 100 μg Fe mL^{-1} for 24 hours after which cell viability was then determined. After 24 hour exposure for cells exposed to NP concentrations up to and including 50 μg Fe mL^{-1}, the cell viability of KSCs exposed to SiO_2-SPIONs was maintained ≥100 % and was found to be the same with error and within the percentage limits compared to the Molday Ion control. At 100 μg Fe mL^{-1}, cell viability decreased to ~70 % and was found outside the percentage error limits of the Molday Ion control. KSC viability exposed to the

Molday Ion control was found to be maintained ≥100 % and was the same within error, **Figure 4.22**. Overall, the cell viability results support the selection of silica as a biocompatible surface coating for bio-application.

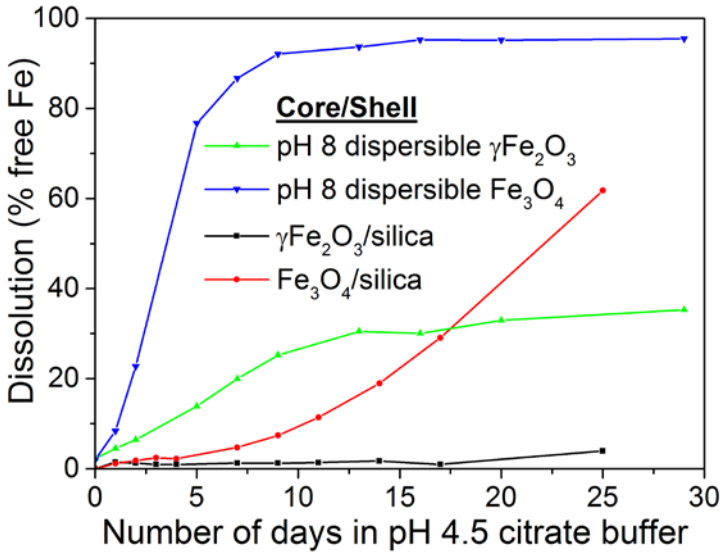

Figure 4.23. Dissolution assay of uncoated SPIONs (pH 8 and pH 2 dispersible) vs. silica coated-SPIONs in pH 4.5 citrate buffer solution at 37 °C.

Silica SPIONs were tested for their stability in pH 4.5 citrate buffer solution at 37 °C over a period of at least 25 days. This was carried out to assess whether SiO_2-SPIONs would be suitable for long term stem cell tracking. Here, the stability of SiO_2-SPION samples containing Fe_3O_4 and γFe_2O_3 cores was investigated. For this study, the dissolution behaviour of pH 8 dispersible SPIONs (Fe_3O_4 and γFe_2O_3 cores) with a bare surface was also investigated as a comparison to see if the silica surface coating affected stability and rate of dissolution when compared to uncoated SPIONs. Firstly, the dissolution results for uncoated SPIONs from the dissolution assay, **Figure 4.23**, showed that uncoated Fe_3O_4 SPIONs dissolved at a high rate and achieved 77 % dissolution by day 5. When compared to uncoated γFe_2O_3 SPIONs, the dissolution rate was found to be much lower with around 30 % dissolution observed after 12 days, which then was found to plateau around 35 %. The dissolution trend for uncoated SPIONs is in agreement with the data found for the dissolution of iron oxides as reported, **Figure 4.1**.[15]

For dissolution data regarding SiO_2-SPION samples, a significant decrease in SPION dissolution rate was observed when compared to the uncoated SPION cores. Specifically, for SiO_2-SPIONs containing magnetite Fe_3O_4 core, a very low rate of dissolution was found where at 5 days only 5 % dissolution had been reached. After this point, the dissolution rate began to increase which suggests there is an induction period and could be due to diffusion of acidic protons through the silica porous coating to reach the SPION core. In addition, dissolved Fe ions may take time to diffuse through the shell into the citrate solution. This would explain why the dissolution rate speeds up past 7-10 day. At 14 days, the dissolution reached 20 % and at 25 days, the dissolution reached 60 % thus confirming that silica coating provided Fe_3O_4 SPIONs with protection from dissolution in pH 4.5 citrate buffer solution at 37 °C. For SiO_2-SPIONs containing maghemite γFe_2O_3, the results showed very little dissolution of the iron oxide core over the period of 25 days with only 5 % dissolution found at the final time point. Again, this confirms the suitability of silica as a NP surface coating with regards to providing protection and stability in the lysosomal environment of a stem cell. The difference in chemical stability of Fe_3O_4 SPION versus γFe_2O_3 (uncoated and silica coated) further supports the reported chemical stability results of iron oxides with different composition, **Figure 4.1**and **Figure 4.2**.[15,16]

4.2.5.5 Magnetic Measurements

Magnetisation saturation (M_s) values for SiO_2-SPIONs samples and their uncoated SPION cores were measured using SQUID. For SiO_2-SPIONs containing magnetite Fe_3O_4, **Figure 4.24A**, an M_s of 52.9 emu g^{-1} Fe_3O_4 was measured which was similar to the M_s value measured for oleic acid coated SPIONs of 51.6 emu g^{-1} Fe_3O_4. No changes to the magnetisation of the iron oxide cores were therefore observed after reaction with TEOS. For SiO_2-SPIONs containing maghemite γFe_2O_3, **Figure 4.24B**, a M_s value of 85.8 emu g^{-1} γFe_2O_3 was obtained and higher than that measured for SiO_2-SPIONs containing magnetite Fe_3O_4 . An M_s value of 73.7 emu g^{-1} γFe_2O_3 was measured for the γFe_2O_3 starting material which is lower than that found for SiO_2-SPIONs containing maghemite γFe_2O_3.

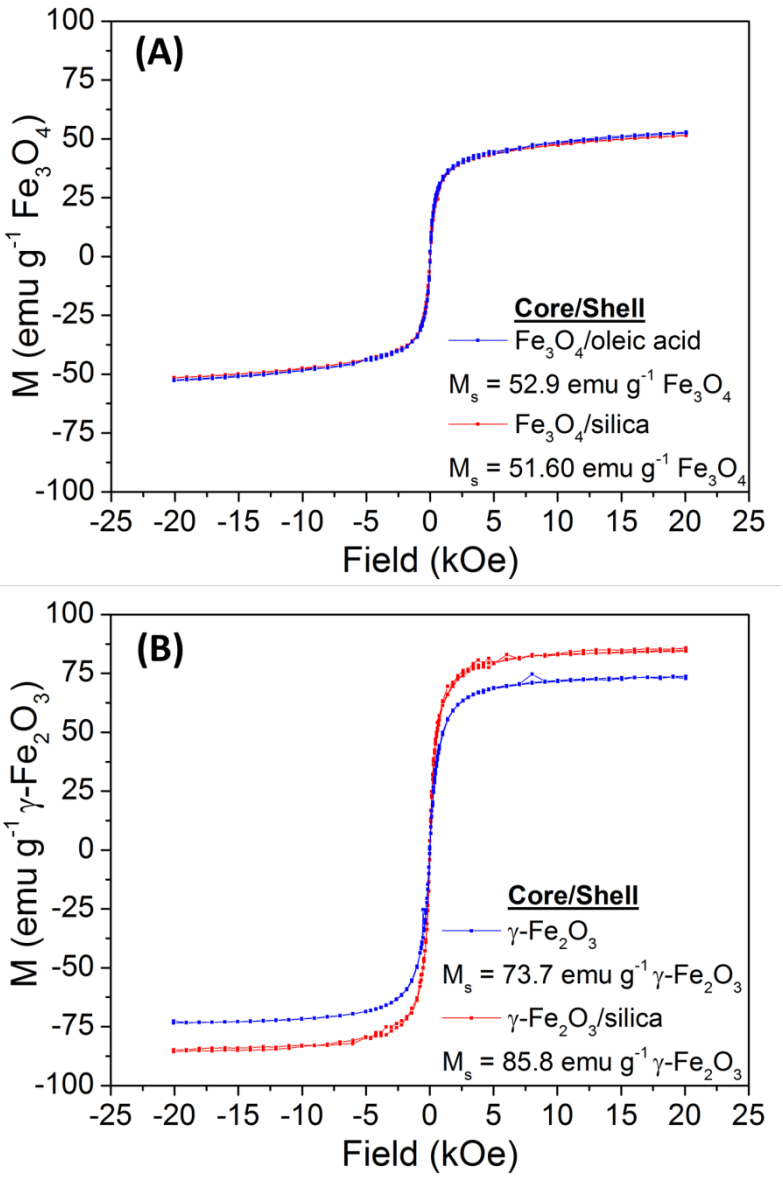

Figure 4.24. Magnetisation-field magnetic hysteresis curves for uncoated SPIONs vs. silica coated-SPIONs at 300K. The results show samples containing A) Fe_3O_4 and B) γFe_2O_3 cores.

An explanation for the increased M_s value for the silica coated SPION compared to the starting material could stem from the fact that the M_s value is measured by per gram of iron oxide. Because of this, excess unreacted/unco-preciptated free Fe ions are likely to be present in the starting material sample. This could have been caused by i) insufficient nucleation and reaction of all the Fe ions present during the reaction or ii) some dissolution of the SPION cores which may have been caused by the pH 2 environment in the sample or iii) *via* the Oswald ripening process. Overall, the SQUID measurements show SiO_2-SPIONs have high M_s values despite reaction of the iron oxide surface with TEOS.

SiO_2-SPION samples, containing Fe_3O_4 and γFe_2O_3 cores, were evaluated for their potential for use as an MRI contrast agent, **Figure 4.25**. SiO_2-SPION samples with concentrations ranging from 0 to 1.0 mM Fe fixed in 1 % agarose were analysed by MRI to measure their R_2 relaxivity. The R_2 relaxivity for SiO_2-SPION samples containing Fe_3O_4 and γFe_2O_3 cores were found at 140 and 163 $mMFe^{-1}\ s^{-1}$ respectively. The high R_2 relaxivity values observed confirms there is good diffusion of hydrogen nuclei from water molecules through the porous silica shell framework to the iron oxide surface and therefore confirms silica as a suitable surface coating for SPIONs as a MRI contrast agent.

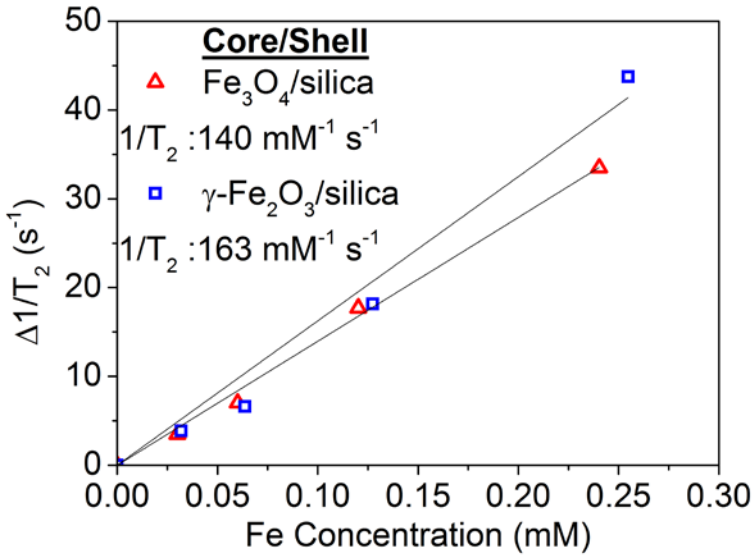

Figure 4.25. R_2 ($1/T_2$) Relaxivity data for SiO_2-SPION samples containing Fe_3O_4 and γFe_2O_3 cores.

4.3 Conclusion

To conclude, silica was investigated as a surface coating for SPIONs see whether it would provide protection and stability of the iron oxide core to dissolution in conditions mimicking those found in the lysosomal environment of a stem cell. SiO_2-SPION samples containing Fe_3O_4 and γFe_2O_3 cores were first synthesised using core size of 9 and 8 nm (by PXRD) respectively. The amount of TEOS optimised for the silica coating reaction was determined as 50 µl which gave an average silica shell thickness of 5-8 nm and 11-12 nm for SiO_2-SPION samples containing Fe_3O_4 and γFe_2O_3 cores respectively (as determined by TEM). For the coating procedure of SiO_2-SPION samples containing Fe_3O_4 cores, SPIONs were found to be evenly and

uniformly coated (as observed by TEM). SiO_2-SPIONs containing two or more SPION cores were also found to be coated during the silica coating reaction; however 60 % of the distribution of SiO_2-SPIONs contained a single core. Prior to pre-biological studies, the biocompatibility of silica as a NP surface coating was first evaluated by cytotoxicity assay using KSCs. The cell viability remained high throughout exposure to all NP concentrations apart from kidney stem cells exposed to 50 and 100 µg Fe mL^{-1} which showed a decrease in viability (90 % and 70 % respectively). The results from the dissolution assay confirmed the silica coating provided a significant decrease in dissolution rate over a period of 25 days when compared with uncoated SPIONs. Pre-biological studies of SiO_2-SPION samples containing Fe_3O_4 and γFe_2O_3 cores were found to have high R_2 relaxivity values of 140 and 163 mM^{-1} s^{-1} respectively which confirmed their suitability as a contrast agent for MRI imaging. The magnetisation of SiO_2-SPION samples containing Fe_3O_4 and γFe_2O_3 cores were measured using SQUID and gave M_s values of 51.6 emu g^{-1} $Fe_3O_4^{-1}$ and 85.8 emu g^{-1} $\gamma Fe_2O_3^{-1}$ respectively. The high M_s values confirmed the suitability of silica as a surface coating since the interaction of silica onto the surface of iron oxide did not affect the M_s value after coating reaction.

Overall, the suitability of silica as a surface coating for SPIONs used as a contrast-labelling agent for long term stem cell tracking has been studied. The biological studies for SiO_2-SPION samples containing Fe_3O_4 and γFe_2O_3 cores have been investigated and are discussed in the stem cell biology Chapter 6.

4.4 References

1. A. K. Gupta, R. R. Naregalkar, V. D. Vaidya, *et al.*, *Nanomedicine*, 2007, **2**, 23-39.
2. R. Ghosh Chaudhuri and S. Paria, *Chem. Rev.*, 2012, **112**, 2373-2433.
3. C. Jin, Y. Wang, H. Wei, *et al.*, *J. Mater. Chem. A*, 2014, **2**, 11202-11208.
4. I. Y. Goon, L. M. H. Lai, M. Lim, *et al.*, *Chem. Mater.*, 2009, **21**, 673-681.
5. R. Alwi, S. Telenkov, A. Mandelis, *et al.*, *Biomed. Opt. Express*, 2012, **3**, 2500-2509.
6. L. Li, W. Jiang, K. Luo, *et al.*, *Theranostics*, 2013, **3**, 595-615.
7. N. Erathodiyil and J. Y. Ying, *Acc. Chem. Res.*, 2011, **44**, 925-935.
8. S. Laurent, D. Forge, M. Port, *et al.*, *Chem. Rev.*, 2008, **108**, 2064-2110.

9. Y. Sun, L. Duan, Z. Guo, *et al.*, *J. Magn. Magn. Mater.*, 2005, **285**, 65-70.
10. R. Souda, *Surf. Sci.*, 2011, **605**, 1257-1262.
11. A. Ulman, *Chem. Rev.*, 1996, **96**, 1533-1554.
12. P. M. Paulus, H. Bönnemann, A. M. van der Kraan, *et al.*, *Eur. Phys. J. D*, 1999, **9**, 501-504.
13. E. D. Smolensky, H.-Y. E. Park, T. S. Berquó, *et al.*, *Contrast Media Mol. Imaging*, 2011, **6**, 189-199.
14. D. A. van Leeuwen, J. M. van Ruitenbeek, L. J. de Jongh, *et al.*, *Phys. Rev. Lett.*, 1994, **73**, 1432-1435.
15. R. M. Cornell and U. Schwertmann, *The Iron Oxides*, Wiley-VCH Verlag GmbH & Co. KGaA, 2004, 297-344.
16. M. Auffan, J. Rose, M. R. Wiesner, *et al.*, *Environ. Pollut.*, 2009, **157**, 1127-1133.
17. M. Auffan, W. Achouak, J. Rose, *et al.*, *Environ. Sci. Technol.*, 2008, **42**, 6730-6735.
18. W. Stöber, A. Fink and E. Bohn, *J. Colloid Interface Sci.*, 1968, **26**, 62-69.
19. Y. Lu, Y. Yin, B. T. Mayers, *et al.*, *Nano Lett.*, 2002, **2**, 183-186.
20. P. Tartaj and C. J. Serna, *Chem. Mater.*, 2002, **14**, 4396-4402.
21. J. E. Smith, L. Wang and W. Tan, *TrAC, Trends Anal. Chem.*, 2006, **25**, 848-855.
22. D. K. Yi, S. S. Lee, G. C. Papaefthymiou, *et al.*, *Chem. Mater.*, 2006, **18**, 614-619.
23. S. Santra, R. Tapec, N. Theodoropoulou, *et al.*, *Langmuir*, 2001, **17**, 2900-2906.
24. X. Liu, Z. Ma, J. Xing, *et al.*, *J. Magn. Magn. Mater.*, 2004, **270**, 1-6.
25. M. D. Butterworth, S. A. Bell, S. P. Armes, *et al.*, *J. Colloid Interface Sci.*, 1996, **183**, 91-99.
26. X. Liu, J. Xing, Y. Guan, *et al.*, *Colloids Surf., A*, 2004, **238**, 127-131.
27. J. Park, K. An, Y. Hwang, *et al.*, *Nat Mater*, 2004, **3**, 891-895.
28. R. Massart, *IEEE Trans. Magn.*, 1981, **17**, 1247-1248.
29. E. Valero, S. Tambalo, P. Marzola, *et al.*, *J. Am. Chem. Soc.*, 2011, **133**, 4889-4895.
30. A. H. Lu, E. L. Salabas and F. Schüth, *Angew. Chem. Int. Ed.*, 2007, **46**, 1222-1244.

31. W. Wu, Q. He and C. Jiang, *Nanoscale Res. Lett.*, 2008, **3**, 397-415.
32. N. Kohler, G. E. Fryxell and M. Zhang, *J. Am. Chem. Soc.*, 2004, **126**, 7206-7211.
33. W. Zhou, K. Tang, S. Zeng, *et al.*, *Nanotechnology*, 2008, **19**, 065602.
34. Y. Dong, R. Ma, M. Hu, *et al.*, *PCCP*, 2013, **15**, 7174-7181.
35. R. M. Cornell and U. Schwertmann, *The Iron Oxides*, Wiley-VCH Verlag GmbH & Co. KGaA, 2004, xxi-xxxix.
36. Y. Lu, Y. Yin, B. T. Mayers, *et al.*, *Nano Lett.*, 2002, **2**, 183-186.
37. R. L. Frost, J. T. Kloprogge and Z. Ding, *Spectrochim. Acta, Part A*, 2002, **58**, 1657-1668.
38. R. M. Cornell and U. Schwertmann, *The Iron Oxides*, Wiley-VCH Verlag GmbH & Co. KGaA, 2004, 139-183.
39. J. B. Hall, M. A. Dobrovolskaia, A. K. Patri, *et al.*, *Nanomedicine*, 2007, **2**, 789-803.
40. A. S. Arbab, L. B. Wilson, P. Ashari, *et al.*, *NMR Biomed.*, 2005, **18**, 383-389.

5

Synthesis of Gold Coated SPIONs: The Development of SPIONs Stable to the Conditions of a Lysosomal Environment

For experimental details related to this Chapter, see Chapter 2.

List of Figures

Figure 5.1. A reaction scheme for the synthesis of core@shell iron oxide@gold nanoparticles and TEM images of A) silica coated iron oxide nanoparticles, B) APTMS functionalised silica coated iron oxide nanoparticles with gold seeds attached to the surface and C) core@shell iron oxide@gold nanoparticles. Image taken from reference.[17] 179

Figure 5.2. FT-IR spectra for A-SPIONs. 182

Figure 5.3. TGA spectra for A-SPIONs. The dotted line represents the isotherm at temperature of 120 °C for the removal of adsorbed solvent. 182

Figure 5.4. $pMPC_{135}$ coated Au-SPIONs showing dispersibility and colloidal stability in PBS..... 186

Figure 5.5. HR-TEM images for Au-SPIONs. Images were carried out by Dr Tobias Heil at the University of Liverpool. 186

Figure 5.6. Characterisation data for Au-SPIONs showing A) DLS hydrodynamic radius peak height measurements (by intensity, mass and number), B) size distribution by TEM, C) PXRD and D) SPR absorbance at 540 nm by UV-Vis..... 187

Figure 5.7. A theoretical diagram representing an iron oxide core with amino silane and gold coatings/shells. 190

Figure 5.8. TGA spectra for $pMPC_{135}$ coated Au-SPIONs. The dotted line represents the isotherm at 120 °C for the removal of adsorbed water..... 191

Figure 5.9. $pMPC_{135}$ coated Au-SPIONs - 1 mg(Fe) ml^{-1} sample in PBS..... 191

Figure 5.10. Relative viability of KSCs exposed to a range of concentrations of $pMPC_{135}$ coated Au-SPIONs or Molday Ion nanoparticles. The cells were incubated in culture medium containing the nanoparticles for 24 hours followed by viability measurement with CCK-8 reagent. Results are plotted as the relative viability as a function of nanoparticle concentration and error bars represent the standard deviation from three replicates..... 192

Figure 5.11. Dissolution assay of uncoated Fe_3O_4 SPIONs and Au-SPIONs in pH 4.5 citrate buffer solution at 37 °C..... 195

Figure 5.12. Magnetisation-field magnetic hysteresis curves for OA-SPION and Au-SPIONs at 300K. The 2 T magnetisation for OA-SPION is 49.80 emu g^{-1} Fe_3O_4 and Au-SPION 47.80 emu g^{-1} Fe_3O_4. 196

Figure 5.13. Relaxivity data for Au-SPIONs showing R_2 ($1/T_2$) as 123.0 mM^{-1} s^{-1}196

Figure 5.14. Characterisation data for OA-SPIONs used for the second generation Au-SPIONs showing A) DLS solvodynamic radius peak height measurements (by intensity, mass and number), B) TEM image C) size distribution by TEM and D) PXRD.... 198
Figure 5.15. TGA spectra for A-SPIONs used in the second generation Au-SPIONs. The dotted line represents the isotherm at temperature of 120 °C for the removal of adsorbed solvent. 199
Figure 5.16. Au-SPIONs uncoated in DIW. 201
Figure 5.17. Characterisation data for second generation Au-SPIONs showing A) DLS of pMPC coated Au-SPIONs hydrodynamic radius peak height measurements (by intensity, mass and number), B) PXRD and D) SPR absorbance at 525 - 530 nm by UV-Vis. 202
Figure 5.18. HR-TEM of second generation Au-SPIONs. Images were captured by Dr Tobias Heil at the University of Liverpool. 203
Figure 5.19. Magnetic separation study of $pMPC_{81}$ coated Au-SPIONs. 204
Figure 5.20. FT-IR of second generation Au-SPIONs. 204
Figure 5.21. Retention experiment: 24 hour labelling with MICB or Au-SPIONs for 24 hours, wash and then measurement 0 hours, 24 hours or 48 hours after labelling. Bar charts show A) cell count, B) total cell count (0 and 24 hours: 500 µl, 48 hours: 1000 µl) and C) growth ratio over 48 hour period. 207
Figure 5.22. Dissolution assay of uncoated Fe_3O_4 SPIONs, A-SPIONs, Au-SPIONs (no polymer) and a 1:1 mix of A-SPIONs with Au NPs in pH 4.5 citrate buffer solution at 37 °C. 209
Figure 5.23. Dissolution assay of A-SPIONs subjected to conditioning in $HAuCl_4$ solution (red line) and pH 1.8 solution (green line) in pH 4.5 citrate buffer solution at 37 °C. 210
Figure 5.24. TEM images taken of Au-SPIONs (no polymer) which were subjected to dissolution assay conditions(pH 4.5 citrate buffer solution at 37 °C). 211
Figure 5.25. PXRD spectra for Au-SPIONs, Au NPs, mix of A-SPIONs/Au NPs and A-SPIONs treated with $HAuCl_4$ solution. 212
Figure 5.26. PXRD spectra for A-SPIONs treated with $HAuCl_4$ solution. 212
Figure 5.27. Shows TEM image of a) hollow gold nanoshells and b) the appearance of the gold nanoshells containing AgCl cores . The PXRD spectra (bottom) shows the pattern obtained for hollow gold nanoshells. Image taken from reference.[29] 213

Figure 5.28. Magnetisation-field magnetic hysteresis curves for OA-SPION and Au-SPIONs at 300K. The 2 T magnetisation for A-SPION 50.9 emu g^{-1} Fe_3O_4 and Au-SPION 49.2 emu g^{-1} Fe_3O_4. 214

Figure 5.29. Room temperature magnetisation curves of (a) A-SPIONs, (b) Au-SPIONs (2^{nd} generation) measured using SQUID magnetometry. Values of the total and magnetic radius as deduced from log-weighted Langevin expression are indicated for each particle, respectively. 215

Figure 5.30. Relaxivity data for second generation Au-SPIONs showing R_2 ($1/T_2$) relaxivity as 194 mM^{-1} s^{-1} 216

Figure 5.31. A) OA-SPION starting material observed by conventional TEM, Au-SPIONs imaged by B) STEM-HAADF bright field, C) STEM-HAADF dark field. Images were carried out by Dr Tobias Heil at the University of Liverpool. 217

Figure 5.32. Shows from left to right TEM Au-SPIONs under bright field (black and white image), Fe map by HAADF-EELS (green and black), high energy view under dark field with highest atomic number appearing brightest (red and black) and finally an overlay of the Fe map with the high energy dark field image. Images were carried out by Dr Tobias Heil at the University of Liverpool. Scale bar :100 nm. 217

Figure 5.33. Showing a) TEM image of gold coated iron oxide NP, b) EDX intensity profile for Au and Fe and C) the EDX plot, d), e) and f) show an overalay and individual elemental maps using EELS over a TEM image of NPs for the distribution of Fe (purple) and gold (red). Image taken from reference.[31] 218

List of Tables

Table 5.1. GPC and ^{1}H-NMR results for S-pMPC polymers. GPC: PBS solution pH 7.4 eluent, 50 °C, set of polyethylene oxide (PEO) calibration standards with M_p values of 125,8, 909.5, 442.8, 116.3, 62.1, 23.5, 12.1, 12, 3.9, 1.5 kDa, differential refractive index (DRI) detector used. 185

Table 5.2. Elemental analysis results obtained from ICP measurements for Au-SPION sample. 188

Table 5.3. Volume fractions deduced from percentage mass and density of the material. 189

Table 5.4. Sphere volume for 9.2 nm iron oxide and the deduced sphere volumes for amino silane only and gold only using the volume fraction deduced from 189
Table 5.5. Shell thicknesses calculated from the total volumes of each material by re-arranging the volume of a sphere equation to give radius. 190
Table 5.6. Elemental analysis results obtained from ICP measurements for Au-SPION sample. 205
Table 5.7. Volume fractions deduced from percentage mass and density of the material 205
Table 5.8. Sphere volume for 7.4 nm iron oxide and the deduced sphere volumes for amino silane and gold using volume fraction deduced from **Table 5.7.** 206
Table 5.9. Shell thicknesses calculated from the total volumes of each material by re-arranging the volume of a sphere equation to give radius. 206
Table 5.10. Best fit parameters extracted from ambient temperature magnetisation curves presented in **Figure 5.29**. Where D_t is the total SPION core diameter and D_m is the magnetic core diameter..... 215

List of Schemes

Scheme 5.1. disulphide-poly 2-methacryloyloxyethyl phosphorylcholine (SS-2pMPC) cleavage..... 184
Scheme 5.2. Stabilisation of Au-SPIONs with thiol functionalised-pMPC polymer. 185

5.1 Introduction

In Chapter 4, silica as a nanoparticle (NP) surface coating was investigated for chemical resistance and stability in acidic conditions which mimicked those found in a lysosome which was assessed by monitioring the rate of dissolution of the superparamagnetic iron oxide NP (SPION) core over a period of 25 days. In this Chapter, the investigations continue by looking at gold as an alternative NP surface coating to compare the chemical stability and dissolution rate of the SPION core to silica. As mentioned in the introduction (Chapter 1) to this project, gold NPs possess many qualities as a material suitable for a NP cell labelling agent such as excellent biocompatibility, chemical stability,[1] optical properties from its surface plasmon resonance (SPR)[2] and high affinity

for conjugation of gold with amine and thiol groups present in organic molecules (such as polymers and other steric stabilisers) to the surface of the NP which allows for benefits to colloidal stability in aqueous and bio-active media.[3] The properties of gold as a surface coating for SPIONs are therefore benefical and can allow for the creation of a versatile and robust cell labelling magnetic resonance imaging (MRI) contrast agent with multimodal imaging capabilities through optical, photothermal, optoacoustic and MR imaging which is interesting for magnetic, optical and biomedical applications.[4-6] The disadvantages to the use of gold as a surface coating for SPIONs include demagnetisation (thus decreasing the magnetisation saturation value (M_s)) which is caused by direct reaction and reduction of gold onto the iron oxide surface which thus produces a magnetic dead layer.[7-9] Direct contact of gold with the iron oxide surface would also prevent the relaxation of water protons which can thus lead to a reduction of the R_2 relaxivity value.[10]

For the preparation of gold coatings for NP surfaces, there are two commonly used gold chemical reagents which are auric chloride and gold acetate. Auric chloride ($HAuCl_4.3H_2O$) is the most commonly used reagent reported which is mainly due to its solubility in water and hence versatility during chemical reactions.[7, 11, 12] Gold acetate however is only soluble in non-polar solvents and reactions require NPs with hydrophobic surfaces such as oleic acid coated SPIONs (OA-SPIONs) to achieve uniform coatings.[13, 14]

To avoid the direct reaction and reduction of gold with the iron oxide NP surface, a barrier coating is typically used. Such barriers include silica or silanes and polymers containing functional groups for the attachment and reduction of gold. Examples of such gold coatings include: Wu *et al.*[15] who reported the synthesis of gold coated SPIONs through a sonication approach whereby amino silane functionalised SPIONs (A-SPIONs) in ethanol were mixed with a 1 % solution (w/v) of $HAuCl_4$. Sodium citrate is then added under sonication until the mixture turns from yellow to black. Magnetic separation of the resulting material and centrifugation provided a purple NP suspension in ethanol. A slight reduction of the M_s value was also observed. Bell *et al.*[16] used the same principles reported by Wu *et al.* and reported the synthesis of a single iron oxide core containing a five layered nanostructure whereby two individual layers consisted of gold. The overall diameter obtained was reported as 60 nm.

A similar approach was carried out by Ji *et al.*[17] who synthesised iron oxide/gold core/shell nanoparticles with overall average size of 82 nm with a gold shell thickness found at 8 nm. For the synthesis procedure, **Figure 5.1**, 10 nm iron oxide NPs were first reacted with tetraethylorthosilicate (TEOS) to form a silica shell with thickness ~28 nm.

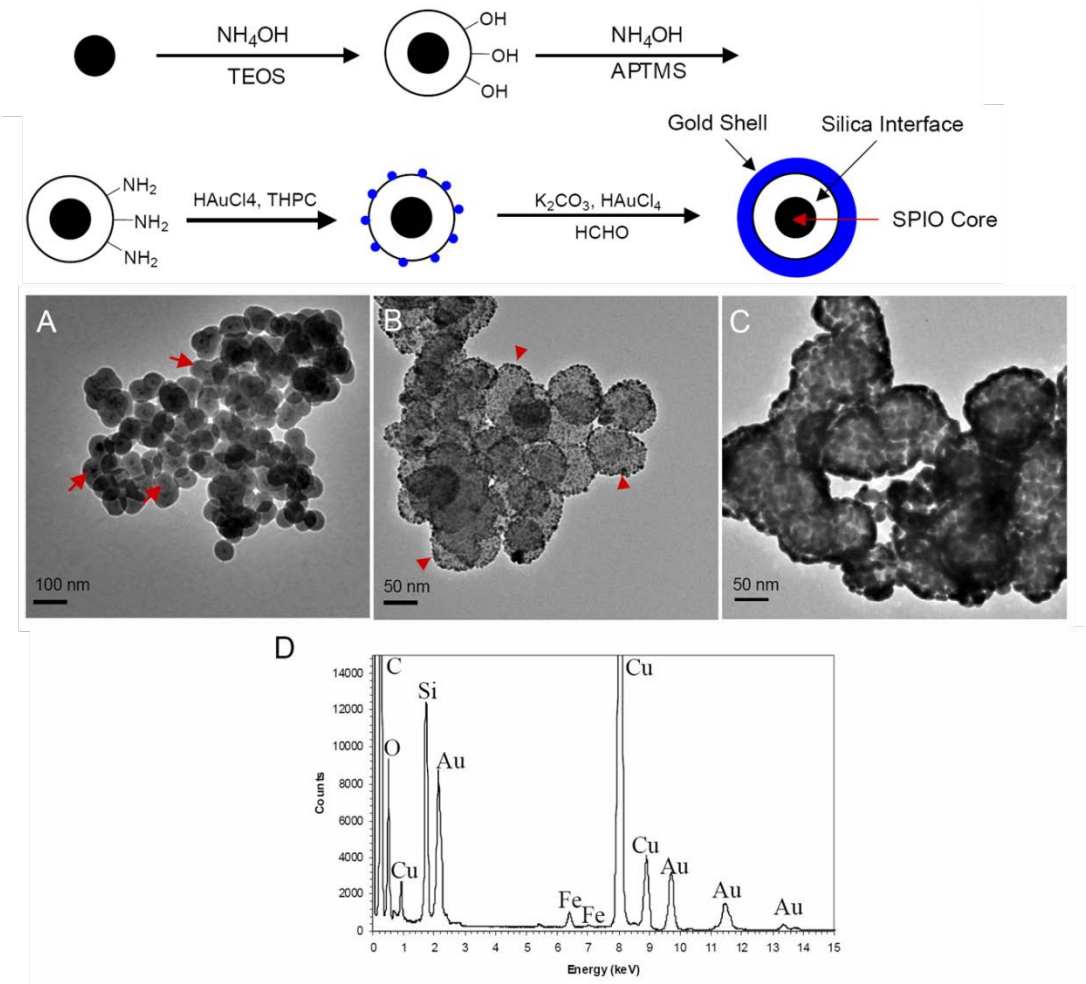

Figure 5.1. A reaction scheme for the synthesis of core@shell iron oxide@gold nanoparticles and TEM images of A) silica coated iron oxide nanoparticles, B) APTMS functionalised silica coated iron oxide nanoparticles with gold seeds attached to the surface and C) core@shell iron oxide@gold nanoparticles. Image taken from reference.[17]

The silica coated SPIONs were then subjected to reaction with 3-aminopropyl trimethoxysilane (APTMS). The gold nanoshell was synthesised through the co-ordination of gold seeds with diameter of 2-3 nm to the amino silane NP surface. The shell was then grown by the addition of auric chloride solution in the presence of potassium carbonate and tetrakis(hydroxymethyl) phosphonium chloride (THPC). The transmission electron microscope (TEM) images in **Figure 5.1** show A) silica coated

SPIONs, B) APTMS functionalised silica coated SPIONs with gold seeds on the surface and C) the overall core shell iron oxide gold NPs. The EDX characterisation D) also shows presence of Au and Fe in the sample. M_s values and R_2 MRI relaxivity values were also observed for the gold coated NPs.

5.2 Results and Discussion: First Generation Gold Coated SPIONs (Au-SPIONs)

For the preparation of Au-SPIONs, the method reported by Wu *et al.*[15] was followed which involves the co-ordination of amines present on the surface of SPIONs with Au^{3+} ions which are then subjected to reduction by sodium citrate to form Au^0 and hence a gold shell/coating. Since A-SPIONs had successfully been prepared and characterised in **Chapter 3**, A-SPIONs were used as the starting material for the gold coating procedure. Sonication was used during the co-ordination and reduction steps as reported to ensure sufficient co-ordination and reduction of gold surrounding individual SPIONs. Here, the amino silane layer is likely to provide a barrier inbetween the iron oxide surface and the gold coating thus preventing any unwanted chemical interactions between gold and the iron oxide surface which may reduce the M_s value of the SPION core and the R_2 relaxivity value through the formation of a magnetic dead layer.[7, 9]

5.2.1 Synthesis and Characterisation of OA-SPIONs

Prior to the preparation of A-SPIONs for the gold deposition reaction, monodisperse OA-SPIONs were prepared following the thermal decomposition method reported by Hyeon and co-workers.[18] The SPIONs used here were the same for those used in **Chapter 4**. The characterisation data can therefore be found in **Chapter 4 Section 4.2.1**.

5.2.2 Synthesis and Characterisation of A-SPIONs

A-SPIONs were prepared as mentioned in Chapter 3 using (3-amino)propyl trimethoxysilane (APTMS) as the ligand to provide a hydrophilic surface in addition to providing a stable covalently bound ligand to the SPION surface.

The presence of amine groups on the surface of A-SPIONs was confirmed by zeta potential, which was found at +28.5 ± 4.8 mV in deionised water (DIW) pH 8. Fourier

transform infrared (FT-IR) spectroscopy also confirmed the presence of primary amine groups at ~3450 $cm^{-1}$and around 1500 cm^{-1}. Bands were also found at wavenumbers of 1200 cm^{-1} and lower which confirmed the presence of silane bonds, **Figure 5.2**.

Measurements of the A-SPIONs by thermal gavimetric analysis (TGA) determined the weight contribution of adsorbed solvent as 5.25 % which was the percentage weight loss calculated from ambient to 120 °C. The total organic weight loss for the A-SPIONs by TGA was found to be 35.32 %, **Figure 5.3**. As described and discussed in Chapter 3, the composition of the amino silane coating of an A-SPION prepared could be determined using the elemental analysis measured for A-SPIONs which was found as C: 22.52 %, H: 3.91 %, N: 4.95 % and TGA results (see appendix). In summary, the theoretical number of amine ligands for one mono-layer on the surface of a 9.2 nm diameter nanoparticle (as determined by powder X-ray diffraction (PXRD) using the Scherrer equation) was calculated as 3635 ± 149 amine ligands.

Using the percentage mass values for the contribution of Fe_3O_4 versus the contribution of the ligand shell, the molar composition of A-SPION with one monolayer of reacted APTMS could be written as $(Fe_3O_4)_1(C_3H_8NSiO_3)_{0.7.}$

The theoretical percentage mass for one monolayer of reacted amino silane ligands around a 9.2 nm Fe_3O_4 core was found as 27.82 %. This percentage mass value includes the percentage mass contribution from the inorganic silane, which is not thermal decomposed during TGA. The theoretical percentage mass contribution of the silane (SiO_2) was therefore deducted to give a predicted TGA percentage for one monolayer of reacted APTMS as 12.05 %. The theoretical percentage mass contribution from C, H and N was also used to predict the elemental analysis. The predicted results were deduced as C: 7.47 % , H: 1.67 % and N: 2.90 %. The actual measured results obtained from the elemental and TGA were used to determine the actual composition of A-SPION. The actual results could then be used to predict the actual average number of APTMS ligands reacted with the SPION surface with diameter of 9.2 nm and thus determine the average number of monolayer(s) of amino silane.

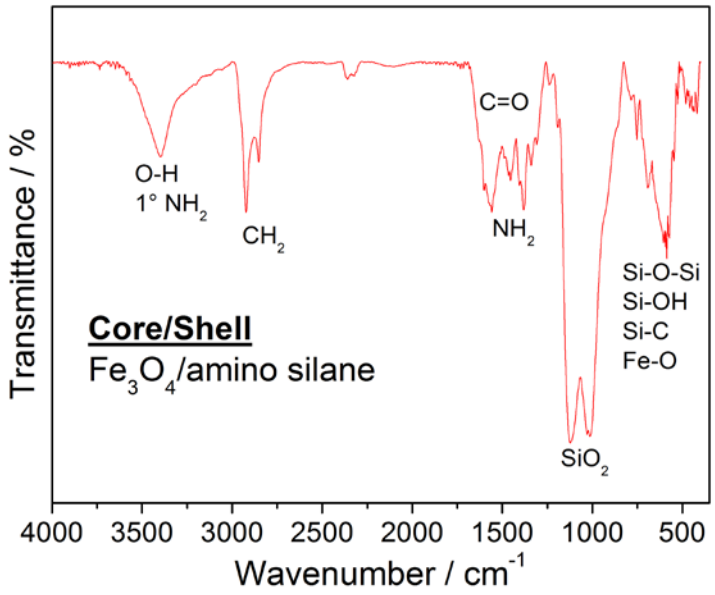

Figure 5.2. FT-IR spectra for A-SPIONs.

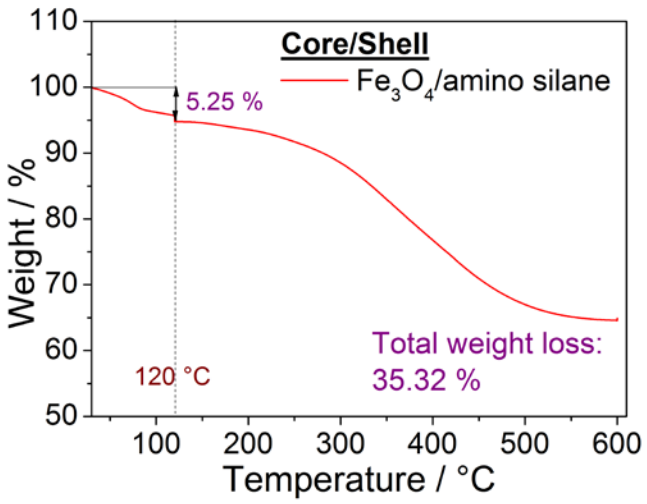

Figure 5.3. TGA spectra for A-SPIONs. The dotted line represents the isotherm at temperature of 120 °C for the removal of adsorbed solvent.

From the experimental procedure, the nitrogen content of the A-SPION product could only be attributed to APTMS ligands reacted onto the surface. Using the weight percentage measured for nitrogen, it was possible to calculate the carbon and hydrogen contribution for APTMS. It was deduced from the elemental analysis data that an excess of carbon and hydrogen was observed compared to the expected values for a pure APTMS coverage. The weight composition of A-SPION was determined as Fe_3O_4:

37.80 %, APTMS: 47.41 %, oleic acid: 9.54 % and solvent: 5.25 %. The molar composition of A-SPION was determined as $(Fe_3O_4)_1$ $(C_3H_8NSiO_3)_{2.2}$ $(C_{18}H_{34}O_2)_{0.2}$ $(C_6H_8O_1)_{0.3}$. The amount of APTMS on the A-SPION (with residual organic contaminate removed) corresponded to 2.94 equivalents of the value calculated earlier for a monolayer so the number of APTMS ligands on the surface (L_{exp}) was estimated at 10698 (5.55 % N).

5.2.3 Sonochemical Synthesis and Characterisation of Gold Coated SPIONs

In **Chapter 3**, A-SPIONs were found to only be dispersible in alcohols but were found not to be stable when added to water or phosphate buffered saline (PBS). Following the gold deposition method by Wu *et al.*[15], ethanol was used to pre-disperse A-SPIONs prior to a deposition reaction with auric chloride solution. Ethanol was also the solvent of choice in **Chapter 3** to disperse A-SPIONs prior to amidation reaction since it was found to be the best solvent to disperse A-SPIONs. To ensure the amino silane layer surrounding the NP core co-ordinates with sufficient Au^{3+} ions in solution and thus achieve a full coating/shell of gold, A-SPIONs were firstly pre-sonicated before the addition of 1 % $HAuCl_4$ solution to the vial. The mixture was then further sonicated to allow for the co-ordination of Au^{3+} with the amine groups on the SPION surface. At the same time, the amines on the surface of A-SPIONs surface will protonate which helps break up small aggregates in the suspension. Protonation of the amines on the SPION surface has been observed through increased colloidal stability and clarity of the reaction mixture. The addition of 1 % $HAuCl_4$ solution significantly lowers the pH of the reaction mixture (from pH 8 to pH 1.8) which at this pH would dissolve the SPION core, if left to sonicate or stand for a long period of time (as seen by the dissolution of uncoated Fe_3O_4 in **Chapter 4**). A solution of sodium citrate (20 mM) was then added dropwise into the reaction vial under sonication until the colour of the reaction mixture turned from yellow to black at which point the addition of sodium citrate to the reaction vial was stopped. Using a NdFeB rare earth magnet, the magnetic NPs were separated and washed twice with ethanol using sonication during the washing steps. The sample was then finally re-suspended using sonication and stored in ethanol. The colour of the final suspension was purple. To make Au-SPIONs dispersible and colloidally stable in water/PBS, thiol functionalised pMPC polymer (S-pMPC) was used with DP_n of 135

(see appendix for characterisation data), **Scheme 5.1** and **Table 5.1**. To obtain thiol functionalised pMPC, cleavage of disulphide-poly(2-methacryloyloxyethyl phosphorylcholine) (SS-2pMPC)) disulphide bond using tris(2-carboxyethyl)phosphine (TCEP)was required. The bifunctional disulphide SS-2pMPC polymers were prepared by Dr. Solène Cauët by atom transfer radical polymerisation (ATRP) using bis[2-(2'-bromoisobutyryloxy) ethyl] disulfide (BriBOEDS) initiator. The polymerisation of thiol functional pMPC with DP_n of 100 and 135 were targeted. Here, DP_ns higher than pMPC polymers used in **Chapter 3** were prepared in order to stabilise gold containing NPs with higher density and larger size.

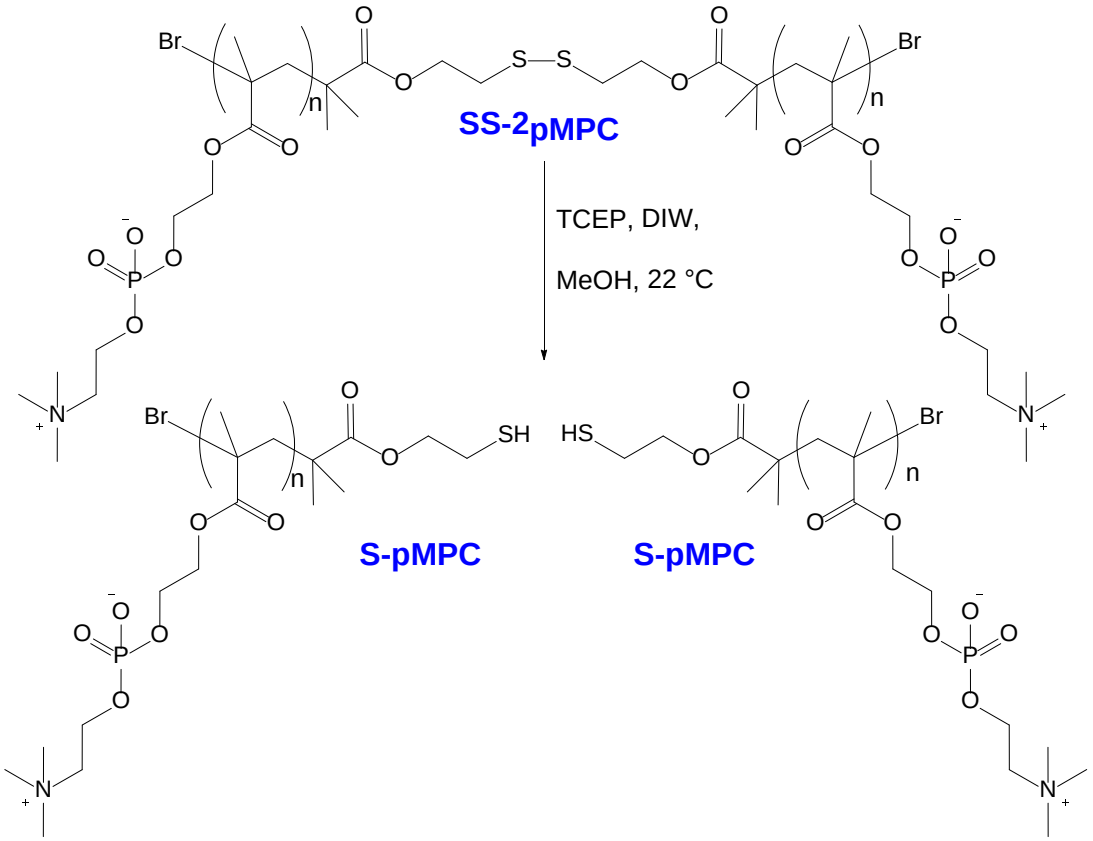

Scheme 5.1. disulphide-poly 2-methacryloyloxyethyl phosphorylcholine (SS-2pMPC) cleavage.

The DP_n of S-pMPC polymers measured by gel permeation chromatography (GPC) with target DP_n of 100 and 135 were found as 120 and 145 with Đ of 1.44 and 1.54 respectively, **Table 5.1**. The dispersity (Đ) of both S-pMPC polymers were found to be broader than expected for ATRP, however this may have been caused by the reformation of the disulphide bond from S-pMPC to SS-2pMPC thus causing a broader distribution of polymer chains present, **Scheme 5.1**. By proton nuclear magnetic

resonance (^{1}H-NMR) ,the DP_n of S-pMPC with target DP_n of 100 and 135 were found as 81 and 135 respectively.

Table 5.1. GPC and ^{1}H-NMR results for S-pMPC polymers. GPC: PBS solution pH 7.4 eluent, 50 °C, set of polyethylene oxide (PEO) calibration standards with M_p values of 125,8, 909.5, 442.8, 116.3, 62.1, 23.5, 12.1, 12, 3.9, 1.5 kDa, differential refractive index (DRI) detector used.

Target polymer	^{1}H-NMR		GPC		
	DP_n	M_n / g mol^{-1}	DP_n	M_n / g mol^{-1}	Đ
$(S\text{-}pMPC_{100})_2$	81	24,000	120	35,500	1.44
$(S\text{-}pMPC_{135})_2$	135	40,000	145	42,100	1.54

To attach S-pMPC polymers to the gold NP coating of Au-SPIONs through gold-thiol coupling, cleavage of the disulphide bond of SS-2pMPC using TCEP was first carried out in water and added to Au-SPIONs pre-dispersed in ethanol *via* sonication, **Scheme 5.2**.

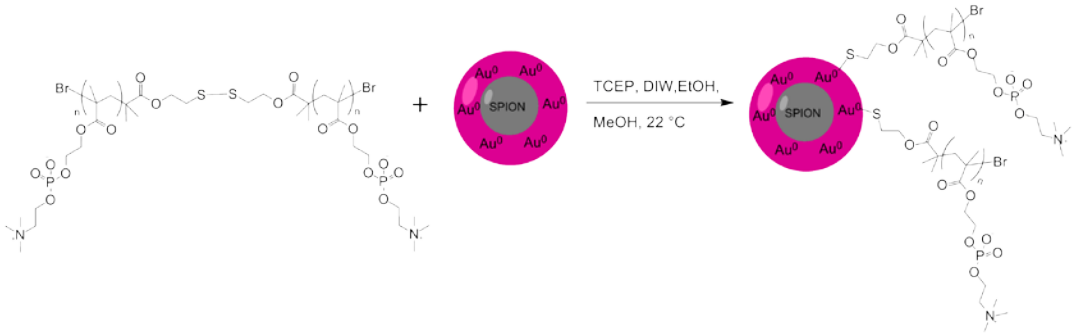

Scheme 5.2. Stabilisation of Au-SPIONs with thiol functionalised-pMPC polymer.

After cleavage of the bifunctional initiator disulphide bond (**Scheme 5.1**), S-pMPC in water was added to Au-SPIONs under sonication. The reaction was then left to further sonicate for an hour at 22 °C and then placed on the rotary mixer for 15 hours at 22 °C. Removal ethanol and unbound polymer was carried out by dialysis and using a Sephadex G100 gel filtration chromatography column in PBS pH 7.4. The $pMPC_{135}$ coated Au-SPIONs in PBS were colloidally stable and purple in colour, **Figure 5.4**.

Figure 5.4. $pMPC_{135}$ coated Au-SPIONs showing dispersibility and colloidal stability in PBS.

To determine size and morphology of Au-SPIONs, high resolution transmission electron microscopy (HR-TEM) was used, **Figure 5.5**. The TEM images showed nanoparticles with a range of sizes and shapes indicating poor control over shell thickness and morphology.

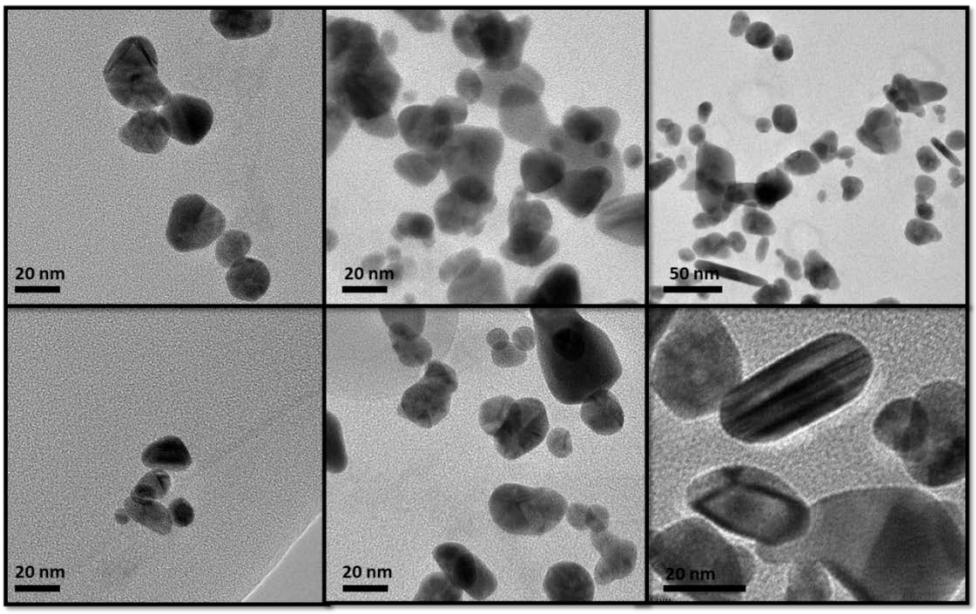

Figure 5.5. HR-TEM images for Au-SPIONs. Images were carried out by Dr Tobias Heil at the University of Liverpool.

DLS size measurements of the $pMPC_{135}$ coated Au-SPIONs in water gave hydrodynamic radius peak height measurements by intensity, mass and number of: $R_{s,\ intensity}$ = 16 ± 1 nm and 81 ± 13 nm, $R_{s,\ mass}$ = 16± 1 nm and 75 ± 12 and $R_{s,\ number}$ = 15 ± 1 nm (**Figure 5.6A**). From the HR-TEM images, NPs have defined contrast and shape, a size distribution from over 100 measurements was therefore obtained using ImageJ software. The average diameter of the composite NPs was measured at 18 ± 9 nm and

the mode found at 20 nm, **Figure 5.6B**. PXRD was also used to characterise the Au-SPIONS. The PXRD pattern obtained showed good agreement for gold and indicated the material was crystalline, **Figure 5.6C**. However, no magnetite peaks were observed since they were hidden by high intensity of the peaks obtained for gold. The average particle size diameter measured was 11 nm. A surface plasmon resonance of the $pMPC_{135}$ coated Au-SPIONs in water was observed using UV-Visible spectroscopy an absorbance with maximum wavelength (λ_{max}) of 540 nm which indicated the gold shell was overall 60 nm in diameter, **Figure 5.6D**.[19]

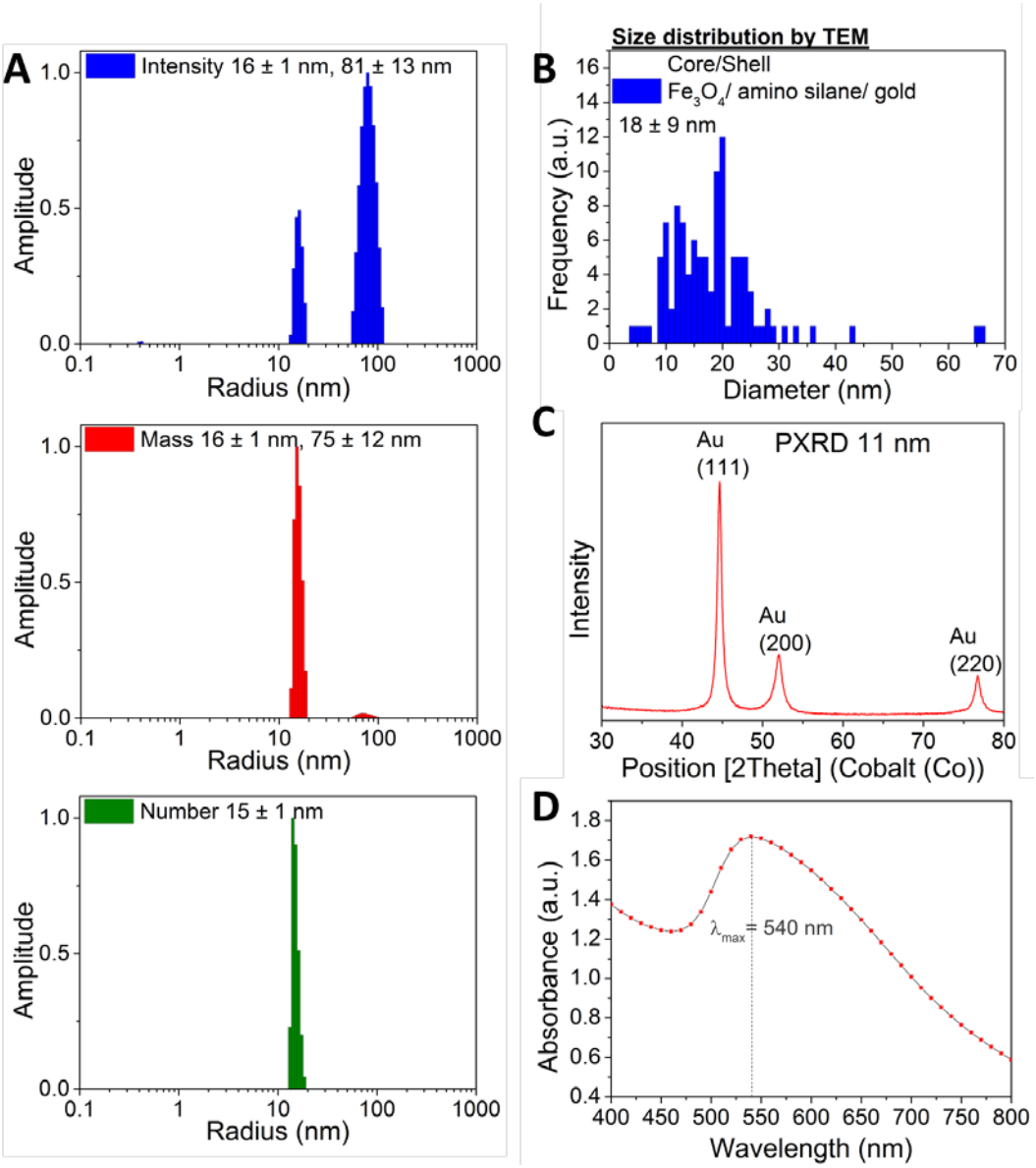

Figure 5.6. Characterisation data for Au-SPIONs showing A) DLS hydrodynamic radius peak height measurements (by intensity, mass and number), B) size distribution by TEM, C) PXRD and D) SPR absorbance at 540 nm by UV-Vis.

The amount of Au, Fe and Si present in the sample was measured by inductively coupled plasma optical emission spectrometry (ICP-OES) *via* the digestion of the material in aqua regia prior to analysis, **Table 5.2**. The material was found to contain Fe 0.15 µg mL^{-1} or ppm, Si 0.03 µg mL^{-1} or ppm and Au 5.0 µg mL^{-1} or ppm. Using the ICP data for the Au-SPION sample (**Table 5.2**), the mass for iron oxide (Fe_3O_4) and amino silane could be deduced using percentage elemental analysis of each compound.The percentage mass values of iron oxide (Fe_3O_4), Au and amino silane (reacted to the surface ($C_3H_8NO_2Si$)) were thus determined as: iron oxide: 3.89 %, Au: 93.22 % and amino silane: 2.89 % using elemental analysis results, **Table 5.2**. Since the density of gold, iron oxide (Fe_3O_4) and amino silane is 19.30 g cm^{-3}, 5.17 g cm^{-3} and 1.68 g cm^{-3} respectively, the percentage volume of each material can be deduced using the percentage mass obtained, **Table 5.3**. The volume of iron oxide can be calculated using the diameter measured for the SPION core as 9.2 nm. Using the volume fractions calculated in **Table 5.3** the volume of amino silane and gold could then be calculated based on the volume calculated for iron oxide (406.39 nm^3) as 929.13 nm^3 and 2608.78 nm^3 respectively, **Table 5.4**.

Table 5.2. Elemental analysis results obtained from ICP measurements for Au-SPION sample.

Element	**Mass (µg mL^{-1} or ppm)**	**Material**	**Mass (µg mL^{-1} or ppm)**	**% Mass**
Fe	0.149	**Iron oxide (Fe_3O_4)**	0.209	3.89
Si	0.032	**Amino silane ($C_3H_8NO_2Si$)**	0.155	2.89
Au	5.005	**Gold**	5.005	93.22

Using the volume calculated for each material, the shell thickness of each layer can be calculated from the total volume of iron oxide and amino silane together. This is done by rearranging the equation for the volume of a sphere to give the radius and thus deducting the radius of iron oxide only (4.60 nm) from the radius obtained from the total volume of iron oxide and amino silane ($V_{t(\ V1+V2)}$) together where V_1 is the volume of iron oxide only and V_2 is the volume of amino silane only. This is repeated to obtain the shell thickness for gold from the total volumes of all three materials ($V_{t(\ V1+V2+V3)}$) where

V_3 is the volume of gold, this time deducting the total radius obtained for iron oxide and amino silane, **Table 5.5**.

Table 5.3. Volume fractions deduced from percentage mass and density of the material.

Material	% Mass	Density ($g\ cm^{-3}$)	Volume Fraction
Iron oxide	3.89	5.17	0.75
Amino silane	2.89	1.68	1.72
Gold	93.22	19.30	4.83

Table 5.4. Sphere volume for 9.2 nm iron oxide and the deduced sphere volumes for amino silane only and gold only using the volume fraction deduced from

Using the volume calculated for each material, the shell thickness of each layer can be calculated from the total volume of iron oxide and amino silane together. This is done by rearranging the equation for the volume of a sphere to give the radius and thus deducting the radius of iron oxide only (4.60 nm) from the radius obtained from the total volume of iron oxide and amino silane ($Vt_{(V1+V2)}$) together where V1 is the volume of iron oxide only and V2 is the volume of amino silane only. This is repeated to obtain the shell thickness for gold from the total volumes of all three materials ($Vt_{(V1+V2+V3)}$) where V3 is the volume of gold, this time deducting the total radius obtained for iron oxide and amino silane, **Table 5.5.**

Table 5.3.

Material	Sphere volume (nm^3) based on iron oxide as 9.2 nm	Diameter of sphere (nm)
Iron oxide	406.39	9.2
Amino silane	929.13	12.1 (amino silane only)
Gold	2608.78	17.1 (gold only)

A theoretical diagram representing an iron oxide core with amino silane and gold coatings/shells is found in **Figure 5.7**.

The shell thicknesses obtained from each coating were calculated as the following: amino silane 2.2 nm and gold 3.0 nm. The overall diameter for Au-SPION was

calculated as 19.6 nm. The A-SPION was calculated to have an overall diameter of 13.7 nm. Since the percentage mass of iron oxide is 3.89 % (or 2.81 % of Fe), the amount of sample to make up a concentration of 1 mg Fe ml^{-1} in 1 mL for biological studies is 35.59 mg of Au-SPION sample calculated as the amount required. This is not considering the mass of polymer required for stability in aqueous solution. The amount of sample required containing polymer would therefore be much greater.

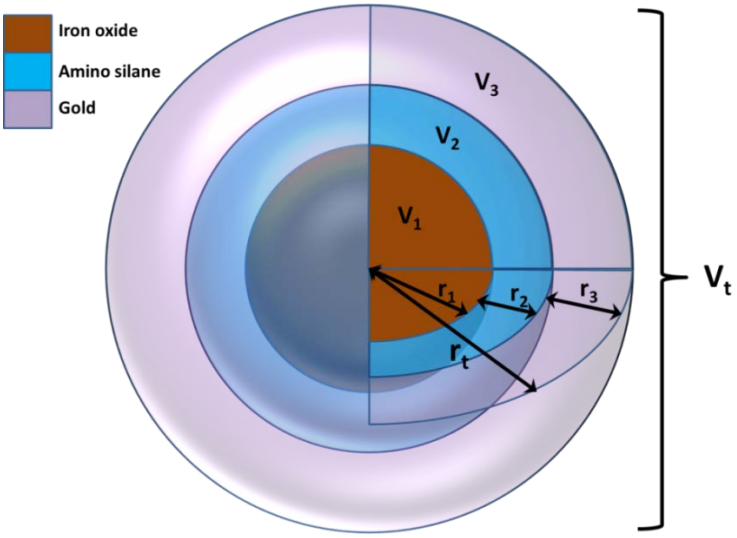

Figure 5.7. A theoretical diagram representing an iron oxide core with amino silane and gold coatings/shells.

Table 5.5. Shell thicknesses calculated from the total volumes of each material by re-arranging the volume of a sphere equation to give radius.

Material	Volume ID	Volume (nm^3)	Radius (nm)	Shell thickness (nm)	Diameter (nm)
Iron oxide	V_1	406.39	4.6		9.2
Amino silane	V_2	929.13		2.2	
	$V_{t(\ V1+V2)}$	1335.52	6.8		13.7
Gold	V_3	2608.78		3.0	
	$V_{t(\ V1+V2+V3)}$	3944.30	9.8		19.6

By TGA, **Figure 5.8**, the percentage mass contribution for pMPC (with the percentage adsorbed water content (9.97 %) removed and mass of pMPC-Au-SPION from TGA rescaled to 100 %) was determined as 88.09 % and the inorganic Au-SPION as 11.91 % (0.33 % Fe). Therefore for a 1 mg Fe ml^{-1} concentration in a 1 mL sample, 299 mg is

required. The large amount of sample required very little water to make a 1 mL volume sample and hence the sample became very viscous, **Figure 5.9**.

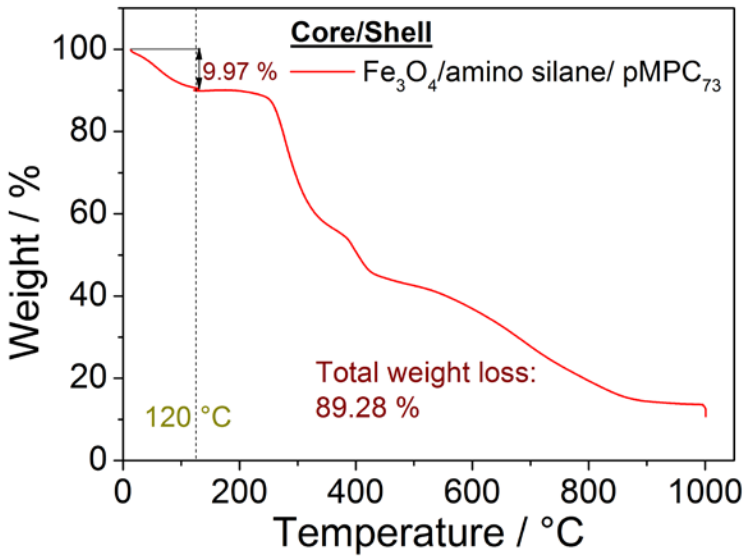

Figure 5.8. TGA spectra for $pMPC_{135}$ coated Au-SPIONs. The dotted line represents the isotherm at 120 °C for the removal of adsorbed water.

Figure 5.9. $pMPC_{135}$ coated Au-SPIONs - 1 mg(Fe) ml^{-1} sample in PBS.

5.2.3.1 First Generation Au-SPIONs: Cytotoxicity

$pMPC_{135}$ coated Au-SPIONs were tested for cytotoxicity *via* a colorimetric assay using cell counting kit-8 (CCK-8) for the quantification for the number of viable cells after a period of 24 hours. A kidney-derived murine stem cell (KSC) line [20] was used and exposed to cell culture medium containing concentrations of NPs ranging up to 100 µg Fe mL^{-1} for 24 hours after which cell viability was then determined. KSCs exposed to $pMPC_{135}$ coated Au-SPIONs showed no cytotoxicity at concentrations up to 25 µg Fe mL^{-1} .In fact cell viability was found to be above 100% within the limits of the Molday

Ion control at NP concentrations up to 25 µg Fe mL^{-1}. At a NP concentration of 25 µg Fe mL^{-1}, the cell viability was above the percentage error limits for the control and was observed around 170 %. The increase in cell viability is likely to have been caused by interference with the CCK-8 reading at 450 nm from $pMPC_{135}$ coated Au-SPIONs which have a maxium peak absorbance at 540 nm. The cell viability for Molday Ions was found to be ≥100 % for KSCs exposed to all NP concentrations used. At NP concentrations above 25 µg Fe mL^{-1} (50 and 100 µg Fe mL^{-1}), the $pMPC_{135}$ coated Au-SPIONs sample became difficult to pipette due to the high viscosity liquid sample and the amount of sample required to add to stem cells to achieve the required Fe concentration. The exposure of KSCs with a high viscous sample resulted in complete cytotoxicity of all cells. The safe NP concentration limit to label KSCs with $pMPC_{135}$ coated Au-SPIONs therefore lies at 25 µg Fe mL^{-1}, **Figure 5.10**.

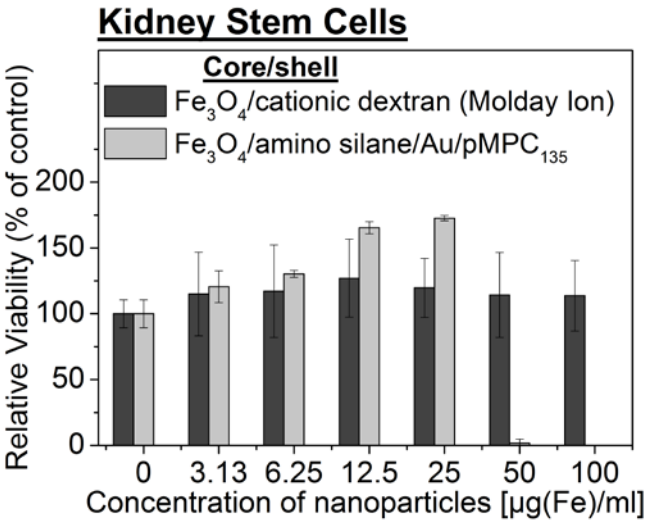

Figure 5.10. Relative viability of KSCs exposed to a range of concentrations of $pMPC_{135}$ coated Au-SPIONs or Molday Ion nanoparticles. The cells were incubated in culture medium containing the nanoparticles for 24 hours followed by viability measurement with CCK-8 reagent. Results are plotted as the relative viability as a function of nanoparticle concentration and error bars represent the standard deviation from three replicates.

5.2.3.2 First Generation Au-SPIONs: Chemical Stability

Au-SPIONs coated with S-$pMPC_{135}$ were tested for their stability in pH 4.5 citrate buffer solution at 37 °C over a period of 25 days. This was carried out to assess whether they would be suitable for long term stem cell tracking. For this study, the dissolution behaviour of pH 8 stable SPIONs (Fe_3O_4) with a bare surface containing only surface

hydroxyl groups were included as a comparison to check if the gold coating affected stability and rate of dissolution compared to uncoated SPIONs, **Figure 5.11A**. from the dissolution assay, a significant decrease in SPION dissolution rate was observed for $pMPC_{135}$ coated Au-SPIONs. At 25 days the dissolution of Fe had reached <5 % when compared to the uncoated SPION cores which reached an Fe dissolution of just over 75 % at 5 days and just over 95 % at 8 days was observed. The significant increase in chemical stability observed for the Au-SPIONs indicated a good coating of gold surrounding SPION cores had been achieved. This confirms the suitability of gold as a NP surface coating with regards to providing protection and stability in the lysosomal environment of a stem cell.

One factor during the dissolution assay process that was observed was that the Au-SPIONs had a maximum absorbance of 540 nm which overlapped with the maximum absorbance of Prussian blue at 590 nm used to quantify the amount Fe of in the sample.

A calibration curve was prepared to check if the absorbance from Au-SPIONs effected the accuracy of the Prussian blue assay (containing FerroZine) used to determine Fe concentration. The calibration curve consisted of a series of Fe standards prepared by serial dilution in pH 4.5 citrate buffer including a blank. To each standard and blank, an liquot containing 5 µg Fe mL^{-1} $pMPC_{135}$ coated Au-SPIONs was added. The absorbance value obtained from the blank containing 5 µg Fe mL^{-1} $pMPC_{135}$ coated Au-SPIONs was deducted from the absorbance value obtained for each Fe standard containing 5 µg Fe mL^{-1} $pMPC_{135}$ coated Au-SPIONs and plotted to make a calibration curve, **Figure 5.11B.** The calibration curve provided an R^2 value of 0.999 and thus confirmed the absorbance of $pMPC_{135}$ coated Au-SPIONs did not interefere with the absorbance measurements used to quantify Fe by the Prussian blue dissolution assay.

5.2.3.3 First Generation Au-SPIONs:Magnetisation Saturation Measurements

The M_s values for OA-SPION starting material and Au-SPIONs after the gold deposition reaction were measured using SQUID magnetometry to assess if their were any chemical interations with auric chloride during the gold deposition reaction/coating procedure with the iron oxide surface and thus affecting the magnetisation. For OA-SPIONs the M_s value obtained was found at 49.8 emu g^{-1} Fe_3O_4 and for Au-SPIONs the

M_s value obtained was found at 47.8 emu g^{-1} Fe_3O_4, **Figure 5.12**. From this, it can be deduced that very little change to the M_s value was observed after reaction with auric chloride solution which confirms there were no interactions of the Au^{3+} ions with the iron oxide surface. This synthesis procedure for the deposition of gold is therefore suitable with regards to preventing the formation of a magnetic dead layer which has been seen in the literature for procedures involving the deposition of a gold directly onto the SPION surface. [9, 21-23]

5.2.3.4 First Generation Au-SPIONs: Relaxivity Measurements

Au-SPIONs coated with thiol functionalised $pMPC_{135}$ were evaluated for their potential for use as an MRI contrast agent, **Figure 5.13**. $pMPC_{135}$-Au-SPIONs with concentrations ranging from 0 to 1.0 mM Fe fixed in 1 % agarose were analysed by MRI to measure their R_2-relaxivity. The R_2-relaxivity for $pMPC_{135}$-Au-SPIONs were found at 123.0 $mMFe^{-1}$ s^{-1}. The high R_2-relaxivity value observed confirms there is good diffusion of water protons through the porous silica shell framework to the iron oxide surface and therefore supports the use of gold as a suitable surface coating for SPIONs as a MRI contrast agent.[10, 24]

5.2.4 Outlook: First Generation Au-SPIONs

The chemical stability results for the first generation Au-SPIONs in pH 4.5 citrate buffer over a period of 25 days showed less than 5 % dissolution. However, due to the issues surrounding the amount of sample required to obtain a 1 mg Fe mL^{-1} solution and the difficulty found after working with a sample with high viscosity thus leading to pipetting problems during the preparation of solutions at concentrations of 100 and 50 µg Fe mL^{-1} required an improvement in the sample so that it may be easier to use for cell labelling experiments. The proposed solution to this problem was to reduce the amount of gold in the sample since its density is much higher than silica or iron oxide and therefore contributes to much of the overall sample mass. This way, the percentage mass of Fe in the sample would be greater and thus the overall amount of sample required would be lower.

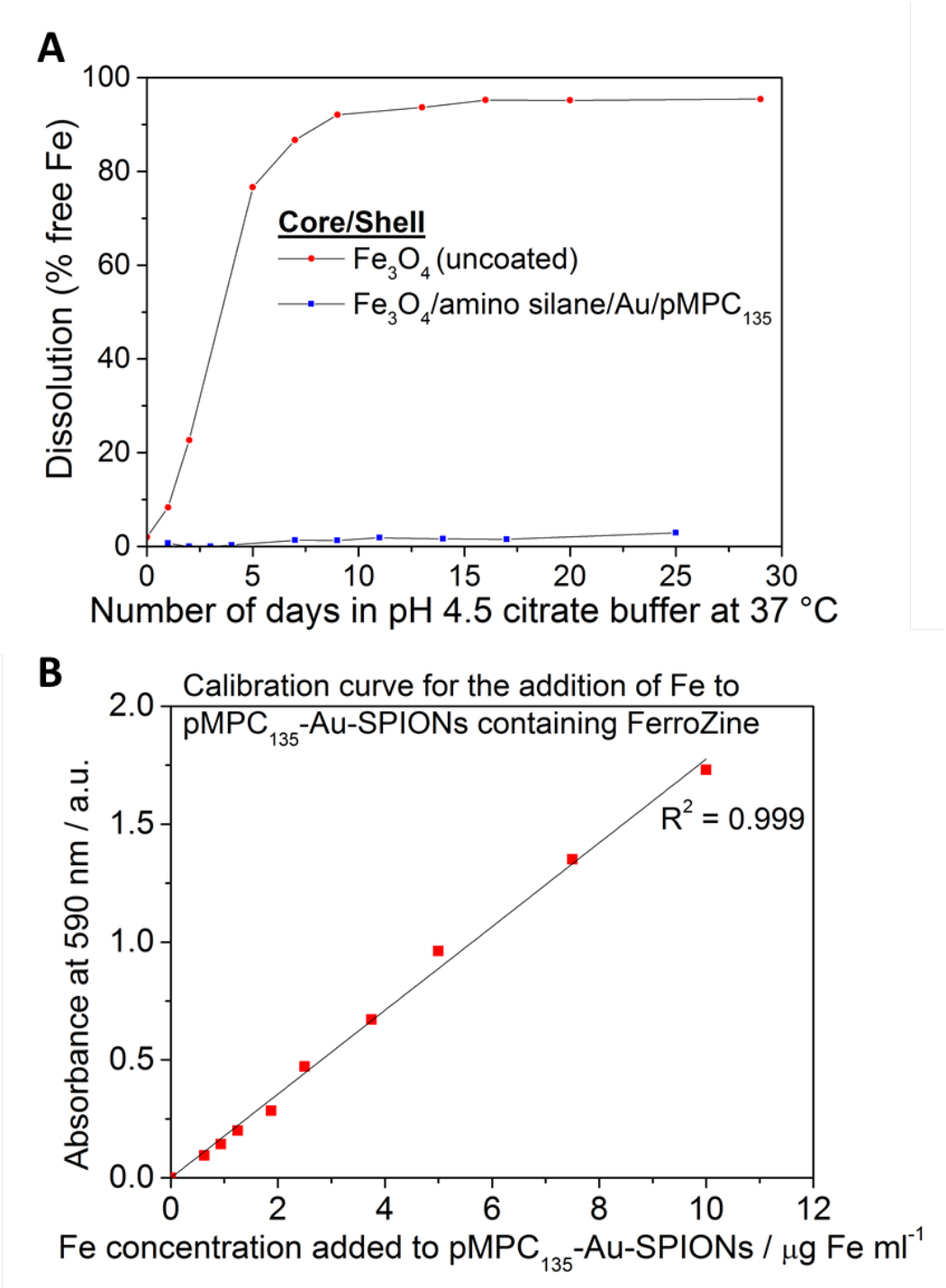

Figure 5.11. Dissolution assay of uncoated Fe_3O_4 SPIONs and Au-SPIONs in pH 4.5 citrate buffer solution at 37 °C.

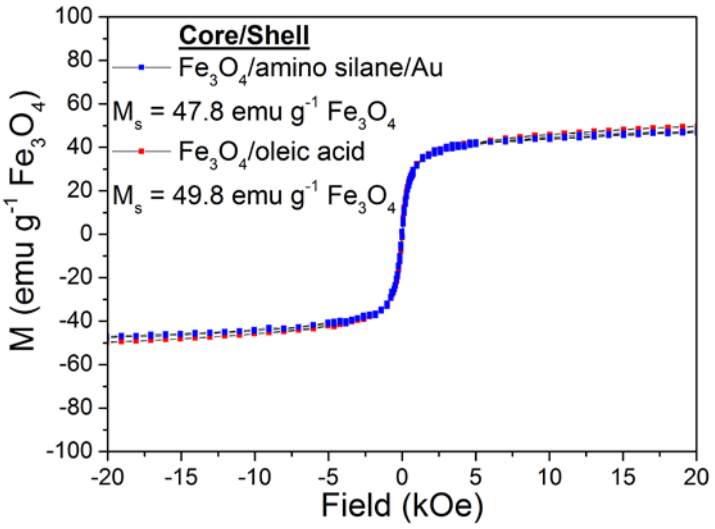

Figure 5.12. Magnetisation-field magnetic hysteresis curves for OA-SPION and Au-SPIONs at 300K. The 2 T magnetisation for OA-SPION is 49.80 emu g^{-1} Fe_3O_4 and Au-SPION 47.80 emu g^{-1} Fe_3O_4.

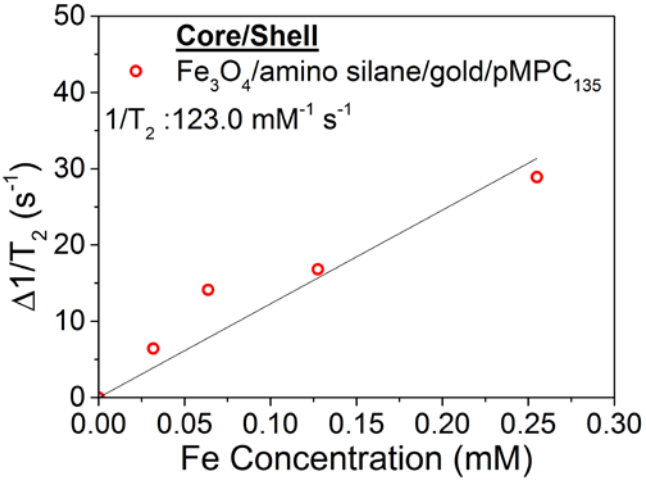

Figure 5.13. Relaxivity data for Au-SPIONs showing R_2 ($1/T_2$) as 123.0 mM^{-1} s^{-1}

5.3 Results and Discussion: Second Generation Au-SPIONs

In this section of the Chapter, a modification to the gold deposition reaction on the surface of A-SPIONs was carried out to attempt to increase the percentage Fe mass in the sample and thus reduce the overall amount of sample required to make a 1 mg mL^{-1} solution for cell labelling experiments. At the same time, trying to reduce the shell thickness of the gold shell and control the size and the morphology of the gold coating on the surface of A-SPIONs.

5.3.1 Synthesis and Characterisation of OA-SPIONs

A different batch of OA-SPIONs was used for the second generation Au-SPIONs prior to the preparation of A-SPIONs. Again, monodisperse OA-SPIONs were prepared following the thermal decomposition method reported by Hyeon and co-workers.[18] Dynamic light scatting (DLS) size measurements of the OA-SPIONs in tetrahydrofuran (THF) gave solvodynamic radius peak height measurements by intensity, mass and number of: $R_{s,\ intensity}$ = 8 ± 2 nm and 28 ± 8 nm, $R_{s,\ mass}$ = 7 ± 1 nm and 22 ± 7 nm, $R_{s,\ number}$ = 6 ± 1 nm (**Figure 5.14A**). TEM showed OA-SPIONs were spherical in shape. From the TEM image, a size distribution from over 400 measurements was obtained using ImageJ software. The average diameter of the cores was measured at 8 ± 4 nm, **Figure 5.14B and C**. PXRD was also used to characterise the SPIONS and the PXRD pattern obtained for the OA-SPIONs showed good agreement with the reference pattern for magnetite (ICDD no. 01-088-0315) and indicated the material was crystalline, **Figure 5.14D**. The average particle size diameter measured was 7.4 nm as derived from the Scherrer equation.

5.3.2 Synthesis and Characterisation of A-SPIONs

A-SPIONs were prepared as mentioned in Chapter 3 using (3-amino)propyl trimethoxysilane (APTMS) as the ligand to provide a hydrophilic surface in addition to providing a stable covalently bound ligand to the SPION surface.

The presence of amine groups on the surface of A-SPIONs was confirmed by zeta potential, which was found at + 22.8 ± 3.68 mV in deionised water (DIW) pH 8. Fourier transform infrared (FT-IR) spectroscopy also confirmed the presence of primary amine groups at ~3450 cm^{-1}. Bands found at wavenumbers of 1200 cm^{-1} and lower also confirmed the presence of silane bonds,

From thermal gravimetric analysis (TGA), the weight contribution of adsorbed solvent was determined as 4.98 % which was the percentage weight loss calculated from ambient to 120 °C. The total organic weight loss for the A-SPIONs by TGA was found to be 35.47 %,**Figure 5.15**.

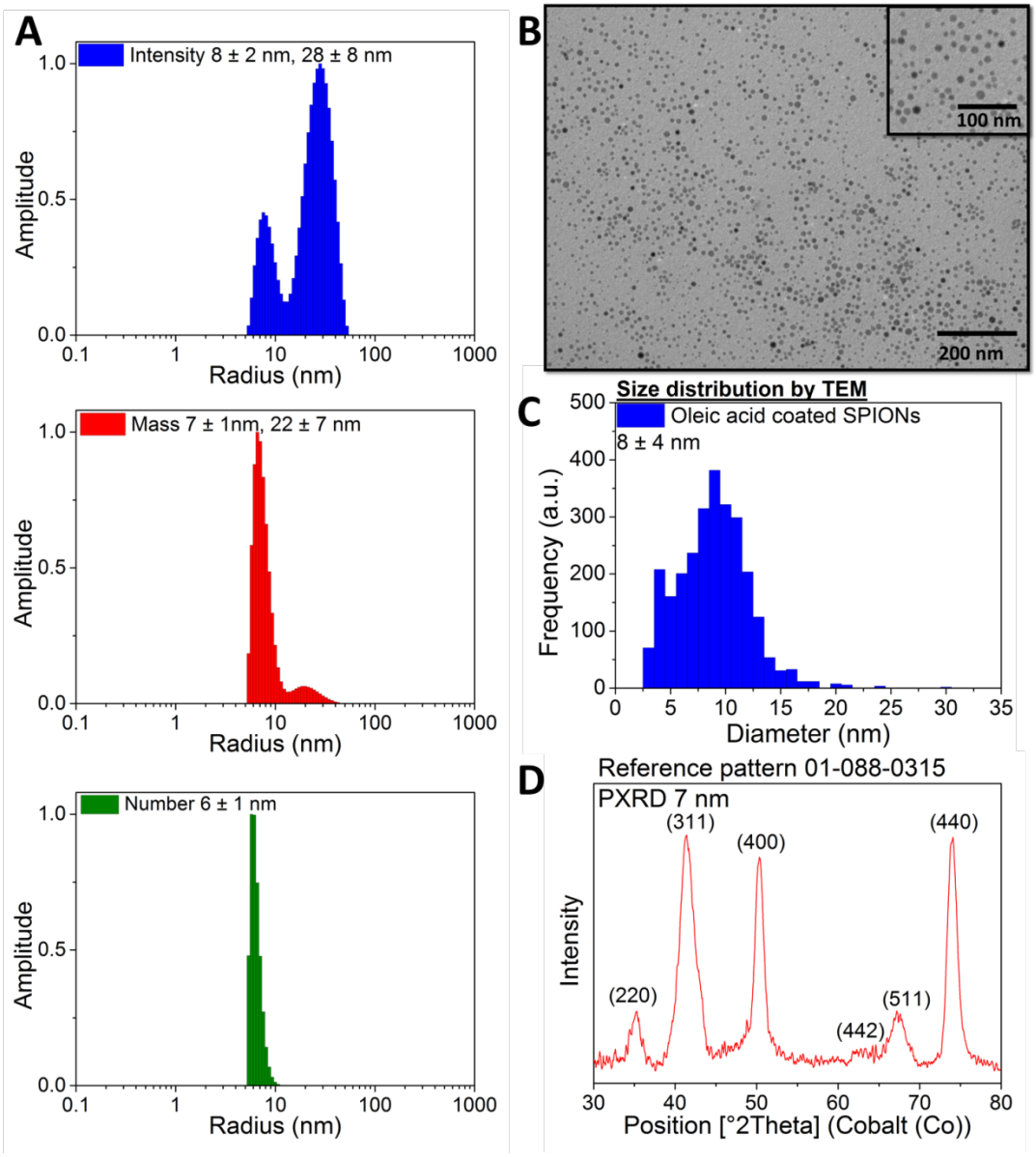

Figure 5.14. Characterisation data for OA-SPIONs used for the second generation Au-SPIONs showing A) DLS solvodynamic radius peak height measurements (by intensity, mass and number), B) TEM image C) size distribution by TEM and D) PXRD.

As described and discussed in **Chapter 3**, the composition of the amino silane coating of A-SPION prepared could be determined using the elemental analysis measured for A-SPIONs which was found as C:22.55 %, H: 3.87 %, N: 4.12 % and TGA results (see appendix A). In summary, the theoretical number of amine ligands for one mono-layer on the surface of a 7.4 nm diameter nanoparticle (as determined by PXRD using the Scherrer equation) was calculated as 2338 ± 229 amine ligands.

Using the percentage mass values for the contribution of Fe_3O_4 versus the contribution of the ligand shell, the molar composition of A-SPION with one monolayer of reacted APTMS could be written as $(Fe_3O_4)_1(C_3H_8NSiO_3)_{0.8}$.

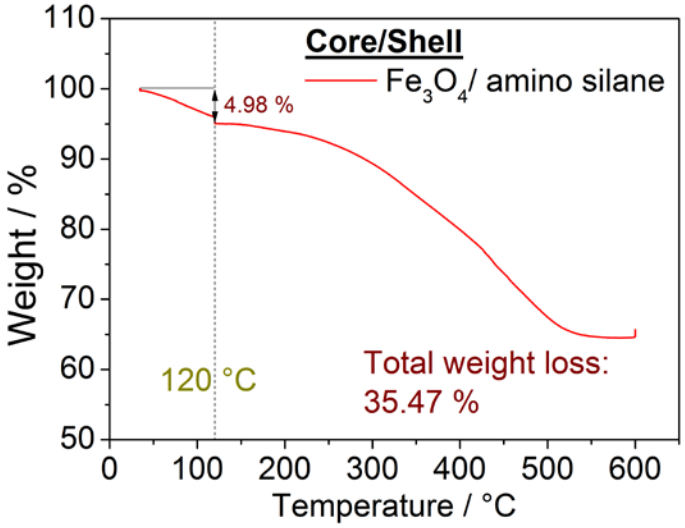

Figure 5.15. TGA spectra for A-SPIONs used in the second generation Au-SPIONs. The dotted line represents the isotherm at temperature of 120 °C for the removal of adsorbed solvent.

The theoretical percentage mass for one monolayer of reacted amino silane ligands around a 7.4 nm Fe_3O_4 core was found as 32.46 %. This percentage mass value includes the percentage mass contribution from the inorganic silane, which is not thermal decomposed during the TGA. The theoretical percentage mass contribution of the silane (SiO_2) was therefore deducted to give a predicted TGA percentage for one monolayer of reacted APTMS as 14.06 %. The theoretical percentage mass contribution from C, H and N was also used to predict the elemental analysis. The theoretical percentage mass contribution from C, H and N was also used to predict the elemental analysis. The predicted results were C: 8.72 %, H: 1.95 % and N: 3.39 %.

The actual measured results obtained from the elemental analysis and TGA were used to determine the actual composition of A-SPION. The actual results could then be used to predict the actual average number of APTMS ligands reacted with the SPION surface with diameter of 7.4 nm and thus determine the average number of monolayer(s) of amino silane. From the experimental procedure, the nitrogen content of the A-SPION product could only be attributed to APTMS ligands reacted onto the surface. Using the weight percentage measured for nitrogen, it was possible to calculate the carbon and

hydrogen contribution for APTMS. It was deduced from the elemental analysis data that an excess of carbon and hydrogen was observed compared to the expected values for a pure APTMS coverage. The weight composition of A-SPION was determined as Fe_3O_4 42.15 %, APTMS 39.46 %, oleic acid 13.40 % and solvent 4.98 %. The molar composition of A-SPION was determined as $(Fe_3O_4)_1$ $(C_3H_8NSiO_3)_{1.6}$ $(C_{18}H_{34}O_2)_{0.3}$ $(C_6H_8O_1)_{0.3}$. The amount of APTMS on the A-SPION (with residual organic contaminate removed) corresponded to 1.74 equivalents of the value calculated earlier for a monolayer so the number of APTMS ligands on the surface (L_{exp}) was estimated at 4074 (4.76 % N).

5.3.3 Sonochemical Synthesis and Characterisation of Gold Coated SPIONs

For the preparation of Au-SPIONs containing a lower percentage mass of gold, the gold deposition reaction on the surface of A-SPIONs was modified. Here the gold deposition method by Wu *et al.*[15] was again followed. Instead of following the procedure as reported in Section 5.2.3 and adding a solution of sodium citrate (20 mM) drop wise, the yellow supernatant containing uncoordinated Au^{3+} ($HAuCl_4$ solution) was instead removed by centrifugation at 5,000 rpm for 2 minutes and the A-SPIONs reacted with Au^{3+} ions were re-dispersed into ethanol under sonication. Sodium citrate (20 mM) was then added drop wise under sonication until a colour change from brown to black was observed. The reaction solution was then centrifuged at 5,000 rpm for 2 minutes. The supernatant was decanted and particles were re-suspended through sonication 1:1 (v/v) solvent mixture of ethanol and water. To this, a 1% $HAuCl_4.3H_2O$ solution was again added and further sonicated. During sonication, the colour of the solution turned red. The solution was again centrifuged at 5,000 rpm for 2 minutes and supernatant decanted. The nanoparticles were again re-suspended through sonication in a 1:1 (v/v) solvent mixture of ethanol and water. The NPs were further separated using a rare earth magnet and re-suspended *via* sonication into ethanol and water solvent mixture – the magnetic separation step was again repeated to yield a red stable suspension in ethanol/water, **Figure 5.16**.

Figure 5.16. Au-SPIONs uncoated in DIW.

To make Au-SPIONs dispersible and colloidally stable in water/PBS, S-pMPC (as prepared by Dr. Solène Cauët) was used with DP_n of 81 (see appendix for characterisation data). The polymer coating procedure was the same as that used for the first generation Au-SPIONs. DLS size measurements of the S-$pMPC_{81}$ coated Au-SPIONs in water gave hydrodynamic radius peak height measurements by intensity, mass and number of: $R_{s,\ intensity}$ = 9 ± 1 nm and 143 ± 20 nm, $R_{s,\ mass}$ = 9 ± 1 nm and $R_{s,\ number}$ = 9 ± 1 nm. PXRD was also used to characterise the Au-SPIONS. The PXRD pattern obtained showed good agreement for gold and lower intensity peaks found for iron oxide and indicated the material was crystalline, **Figure 5.17B** The presence of magnetite peaks indicate the magnetite NPs are exposed to the X-rays through the shell or are simply uncoated. The average particle size diameter measured was 11.4 nm using the Scherrer equation. An SPR of the Au-SPIONs in water was observed using UV-Visible spectroscopy an absorbance with maximum wavelength (λ_{max}) of 525-530 nm which indicated the gold shell or gold NPs were overall 25 to 40 nm in diameter, **Figure 5.17C**.[19]

A closer look at the second generation Au-SPIONs (uncoated with S-pMPC) by HR-TEM, **Figure 5.18**, show a population of two different types of NPs which consist of NPs containing a dark contrast and NPs containing a grey contrast. It appears that not all NPs have been coated with gold or simply that the coating procedure did not work at all and there are a population of gold NPs and a population of SPIONs.

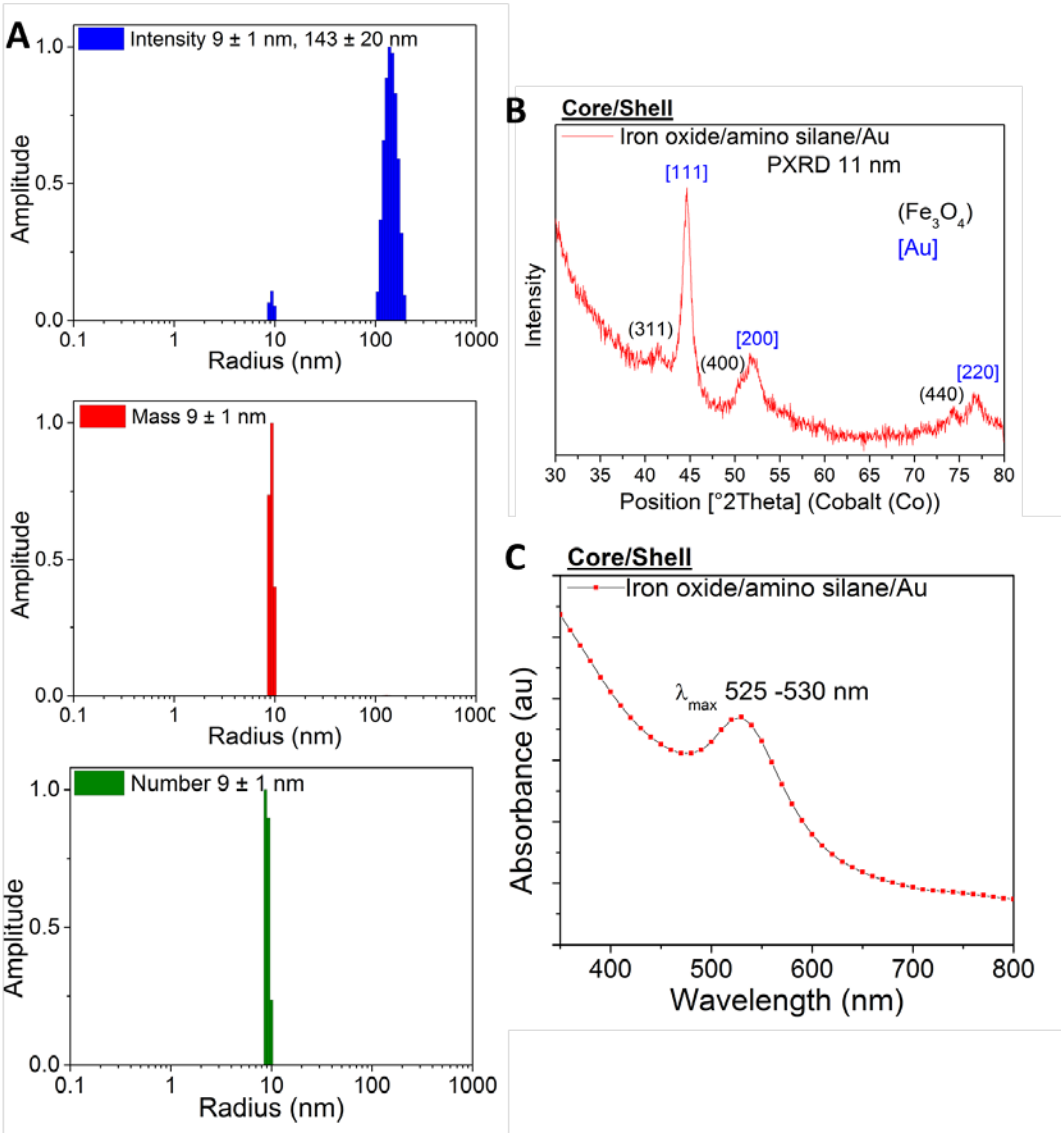

Figure 5.17. Characterisation data for second generation Au-SPIONs showing A) DLS of pMPC coated Au-SPIONs hydrodynamic radius peak height measurements (by intensity, mass and number), B) PXRD and D) SPR absorbance at 525 - 530 nm by UV-Vis.

The images show that the NPs are clumped together which may have been caused through sample preparation of the TEM grid during the sample application and drying step. The measurements by DLS indicate a narrow distribution in addition to the SPR absorbance at 525 nm which suggest no gold to gold NP interactions. To investigate whether there are gold NPs in the sample, Au-SPIONs coated with $pMPC_{81}$ were dispersed in PBS and the magnetic NPs were separated using magnetic separation over a period of 48 hours. The images of the magnetically separated $pMPC_{81}$ Au-SPION sample, **Figure 5.19**, show that by 48 hours, a clear colourless supernatant was observed with magnetic NPs drawn to one side of the glass vial. The fact that none or very few

gold NPs remained in the supernatant suggested there were no gold NPs present in the sample or that they were attached to the uncoated A-SPIONs in the sample through co-ordination with amine groups.

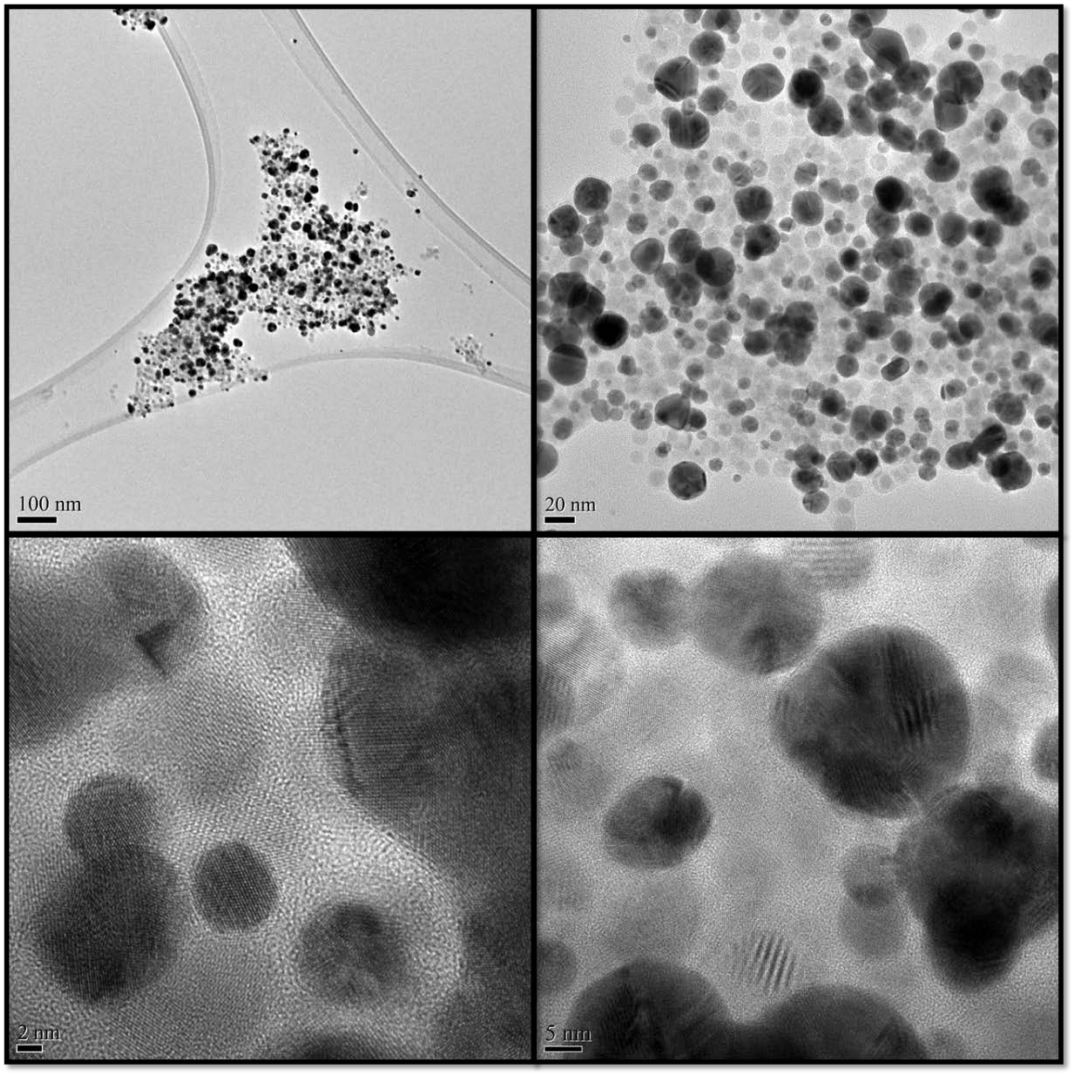

Figure 5.18. HR-TEM of second generation Au-SPIONs. Images were captured by Dr Tobias Heil at the University of Liverpool.

The zeta potential for Au-SPIONs without coating gave +24.3 ± 3.3 mV and for $pMPC_{81}$ coated Au-SPIONs a measurement of -15.03 ± 0.9 mV were found. The colloidal stability of uncoated Au-SPIONs at 37 °C for 48 hours was found to be stable in PBS and cell medium containing serum. However, in cell medium not containing serum, the uncoated Au-SPIONs precipitated within 24 hours.

FT-IR was carried out on the uncoated Au-SPIONs to investigate their surface chemistry. **Figure 5.20** shows bands for carbonyl groups and hydroxyl groups

associated around 1450 and 3200 cm^{-1} which are likely to be from the citrate stabilised onto the gold surface. A band was found for amine groups around 1600 cm^{-1} and silane band found around 1100 cm^{-1} which indicates that not all the A-SPIONs were coated with gold. The CH_2 groups around 2850 and 1150 cm^{-1} are likely to come from either citrate or the amino silane.

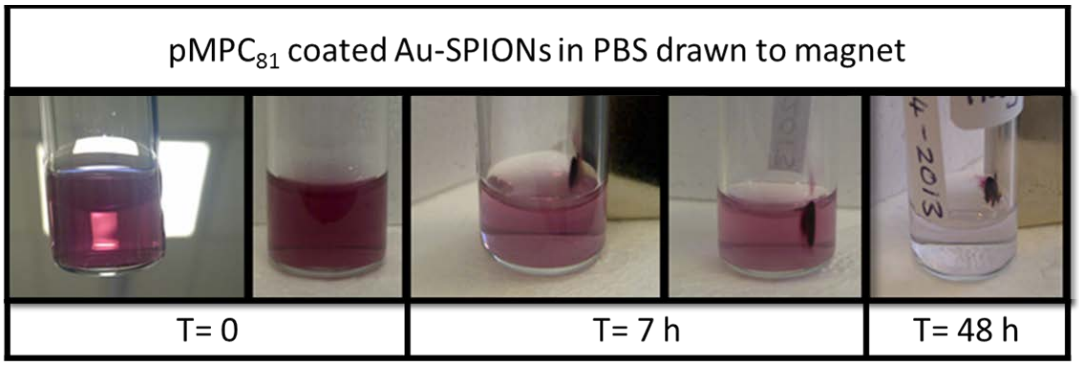

Figure 5.19. Magnetic separation study of $pMPC_{81}$ coated Au-SPIONs.

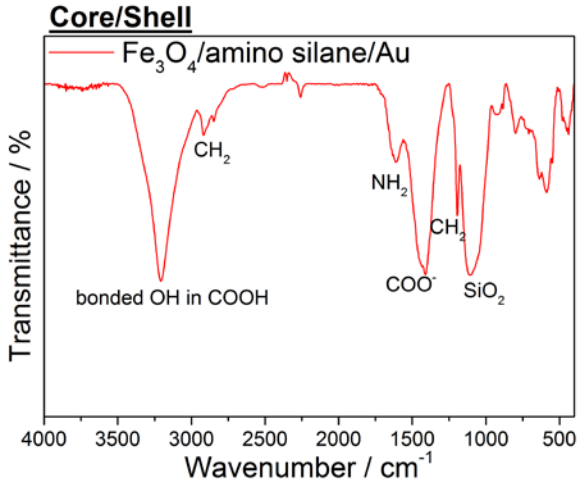

Figure 5.20. FT-IR of second generation Au-SPIONs.

Again, the amount of Au, Fe and Si present in the sample was measured by ICP *via* the digestion of the material in aqua regia prior to analysis. Using the ICP data for the Au-SPION sample (**Table 5.6**), the mass for iron oxide (Fe_3O_4) and amino silane could be deduced using percentage elemental analysis of each compound.

Table 5.6. Elemental analysis results obtained from ICP measurements for Au-SPION sample.

Element	Mass (µg/ml or ppm)	Material	Mass (µg/ml or ppm)	% Mass
Fe	9.009	**Iron oxide (Fe_3O_4)**	12.662	31.79
Si	1.663	**Amino silane ($C_3H_8NO_2Si$)**	7.946	19.95
Au	19.228	**Gold**	19.228	48.27

The percentage mass values of iron oxide (Fe_3O_4), Au and amino silane (reacted to the surface ($C_3H_8NO_2Si$)) were thus determined as: iron oxide: 31.79 %, Au: 48.27 % and amino silane: 19.95 % using elemental analysis obtained from **Table 5.6**.

The volume of iron oxide was calculated using the diameter measured for the SPION core as 9.2 nm. Using the volume fractions calculated in **Table 5.7**, the volume of amino silane and gold could then be calculated based on the volume calculated for iron oxide (209.60 nm^3) as 404.79 nm^3 and 85.26 nm^3 respectively, **Table 5.8**.

Table 5.7. Volume fractions deduced from percentage mass and density of the material

Material	% Mass	Density (g cm^{-3})	Volume Fraction
Iron oxide	31.79	5.17	6.15
Amino silane	19.95	1.68	11.88
Gold	48.27	19.30	2.50

Using the volume calculated for each material, the shell thickness of each layer was calculated from the total volume of iron oxide, amino silane and gold, **Table 5.9**.

The shell thicknesses obtained from each coating was calculated as the following: amino silane 1.59 nm and gold 0.23 nm. The overall diameter for Au-SPION was calculated as 11.01 nm. The A-SPION was calculated to have an overall diameter of 10.55 nm.

Since the percentage mass of iron oxide is 31.79 % (or 23.00 % of Fe), the amount of sample to make up a concentration of 1 mg Fe ml^{-1} in 1 mL for biological studies was

determined as 4.34 mg of Au-SPION sample. Compared to the first generation Au-SPIONs containing no pMPC coating, this is over 8 times less the amount of overall sample required to achieve the Fe concentration desired.

Table 5.8. Sphere volume for 7.4 nm iron oxide and the deduced sphere volumes for amino silane and gold using volume fraction deduced from **Table 5.7.**

Material	Sphere volume (nm^3) based on iron oxide as 7.4 nm	Diameter of sphere (nm)
Iron oxide	209.60	7.4
Amino silane	404.79	9.2 (amino silane only)
Gold	85.26	5.5 (gold only)

Table 5.9. Shell thicknesses calculated from the total volumes of each material by re-arranging the volume of a sphere equation to give radius.

Material	Volume ID	Volume (nm^3)	Radius (nm)	Shell thickness (nm)	Diameter (nm)
Iron oxide	V_1	209.6	3.7		7.4
Amino silane	V_2	404.8		1.6	
	$V_{t(V1+V2)}$	614.4	5.3		10.6
Gold	V_3	85.3		0.2	
	$V_{t(V1+V2+V3)}$	699.7	5.5		11.0

5.3.3.1 Second Generation Au-SPIONs: Cytotoxcity

To determine if Au-SPIONs were suitable for cell labelling studies, NPs were tested for cytotoxicity *via* a proliferation study whereby cells were counted over a 48 hour period and monitored for growth and increased cell numbers. This method was chosen to assess cytotoxicity rather than using the CCK-8 assay since the sample used contained 30 % ethanol and at high concentrations the cells died so the upper toxic limits of this sample could not be established. Ethanol could not be removed from the sample since it provided colloidal stability to the Au-SPIONs. Dialysis of the sample to remove ethanol

caused aggregation and sedimentation. A MSC line[20] was used and exposed to cell culture medium containing concentrations of NPs at 25 µg Fe mL^{-1} for 24 hours after which cell viability was then determined. The cell proliferation assay was carried out by Dr Arthur Taylor at the University of Liverpool, Institute of Translational Medicine.

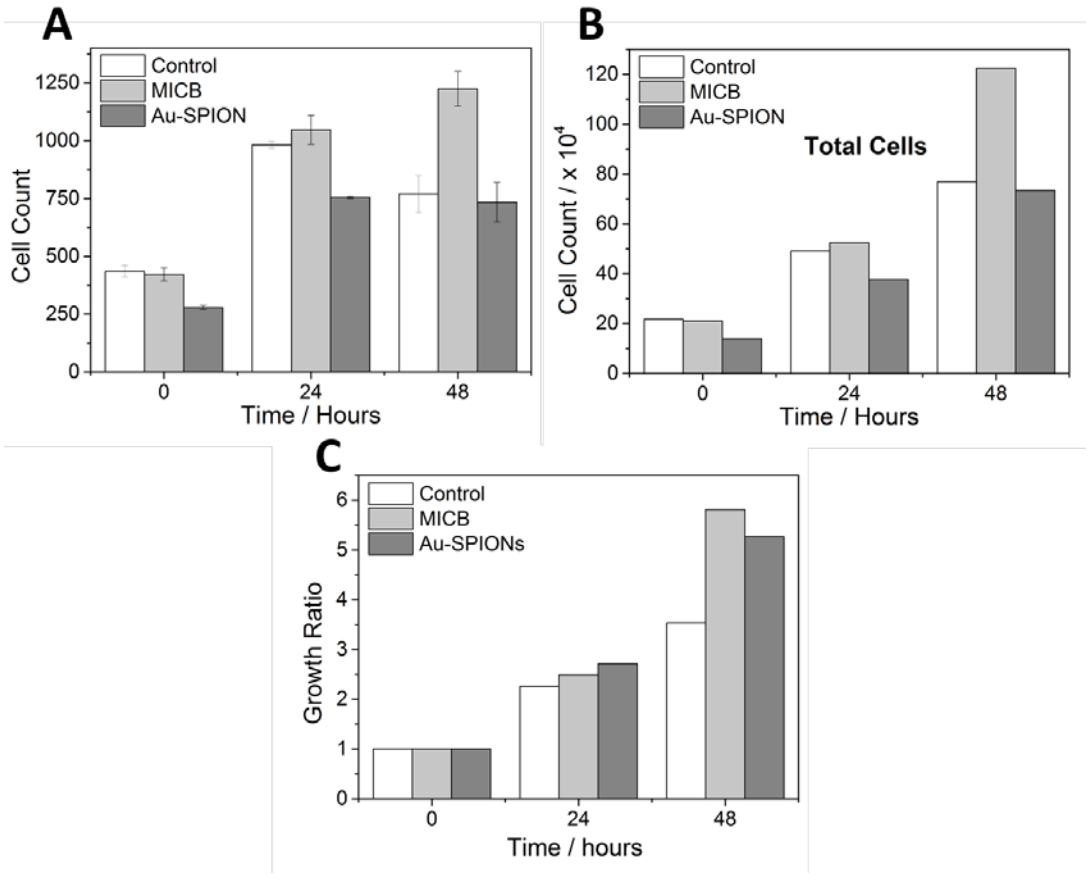

Figure 5.21. Retention experiment: 24 hour labelling with MICB or Au-SPIONs for 24 hours, wash and then measurement 0 hours, 24 hours or 48 hours after labelling. Bar charts show A) cell count, B) total cell count (0 and 24 hours: 500 µl, 48 hours: 1000 µl) and C) growth ratio over 48 hour period.

Comparing cell count over 48 hours, **Figure 5.21A and B**, at 0 hours MSCs exposed to Au-SPIONs showed less cell numbers compared to the blank control and Molday Ion Coumarin Blue (MICB) which suggested some cytotoxicity with cells. At 24 hours, MSC numbers exposed to Au-SPIONs had tripled indicating proliferation and cell viability but cell numbers were still around 25 % fewer compared with the blank control and MICB. At 48 hours, MSC numbers exposed to Au-SPIONs were similar to those measured at 24 hours and were within the error limits measured for the blank control. MSCs exposed to MICB however continued to proliferate.

From the results comparing cell growth ratios, **Figure 5.21C**, at time point 0 to 24 hours, the cell division for Au-SPIONs showed the highest growth ratio of 2.7 when compared to the blank control and MICB which had cell growth ratios of 2.3 and 2.5 respectively. From time point 0 to 48 hours the cell growth division for Au-SPIONs was 5.3 which was higher than that found for the control of 3.5 but slightly lower than that for MICB which was found at 5.8. Overall the data shows cells proliferate over 48 hours after exposure to Au-SPIONs which the cells survived and proliferated as much as the controls which indicated good biocompatibility.

5.3.3.2 Second Generation Au-SPIONs: Chemical Stability

Second generation Au-SPIONs (no polymer) were tested for their stability in pH 4.5 citrate buffer solution at 37 °C over a period of 40 days. This was carried out to assess whether they would be suitable for long term stem cell tracking. For this study, the dissolution behaviour of pH 8 stable SPIONs (Fe_3O_4) with a bare surface containing only surface hydroxyl groups were again included in addition to A-SPIONs (since the FT-IR and TEM characterisation data indicate the existence of two populations of NPs with one population likely to be uncoated A-SPIONs). The dissolution for the A-SPIONs and pH 8 stable SPIONs (Fe_3O_4) will be used as a comparison to determine whether gold coating was formed and thus determine whether the presence of gold NPs would affect chemical stability and rate of dissolution.

For dissolution data regarding Au-SPIONs without a polymer coating, **Figure 5.22**, a decrease in SPION dissolution rate was again observed however the dissolution was greater than that found for the first generation Au-SPIONs containing more gold. At 40 days the dissolution of the Au-SPION sample had reached a dissolution of around 40 % which is over 8 times the amount observed for the first generation Au-SPIONs containing more gold. When compared to the dissolution of A-SPIONs, at 40 days the percentage Fe dissolution reached ~ 82 % which is lower than that observed for uncoated SPION cores which reached an Fe dissolution of just over 75 % at 5 days and just over 95 % at 8 days. The fact that there is around 18 % of Fe in the A-SPION sample undissolved suggests that the amine groups may provide a protective layer. In Chapter 3, it was mentioned that amino silane groups co-ordinate with heavy metal ions in solution.[25-27] This co-ordination behaviour may be occurring with free Fe ions in solution which are not readily used to form the Prussian blue complex.[28] Dissolution

behaviour was also assessed for Au NPs (diameter of 15 nm) which had been premixed with A-SPIONs. The dissolution assay showed a similar dissolution trend to that found for uncoated pH 8 stable SPIONs (Fe_3O_4) which confirms that Au NPs do not provide sufficient protection and chemical stability to A-SPIONs.

To understand the dissolution behaviour (chemical stability and rate of dissolution) of the second generation Au-SPIONs further, different samples of A-SPIONs were subjected to the same conditions used for the gold deposition reaction. The first condition was to sonicate A-SPIONs with a 1 % solution of $HAuCl_4.3H_2O$ (simulating conditions used in the gold deposition reaction) which were then separated from the yellow supernatant and washed in a 1:1 mix of ethanol/water. The second condition was to sonicate A-SPIONs in a pH 1.8 solution of HCl.

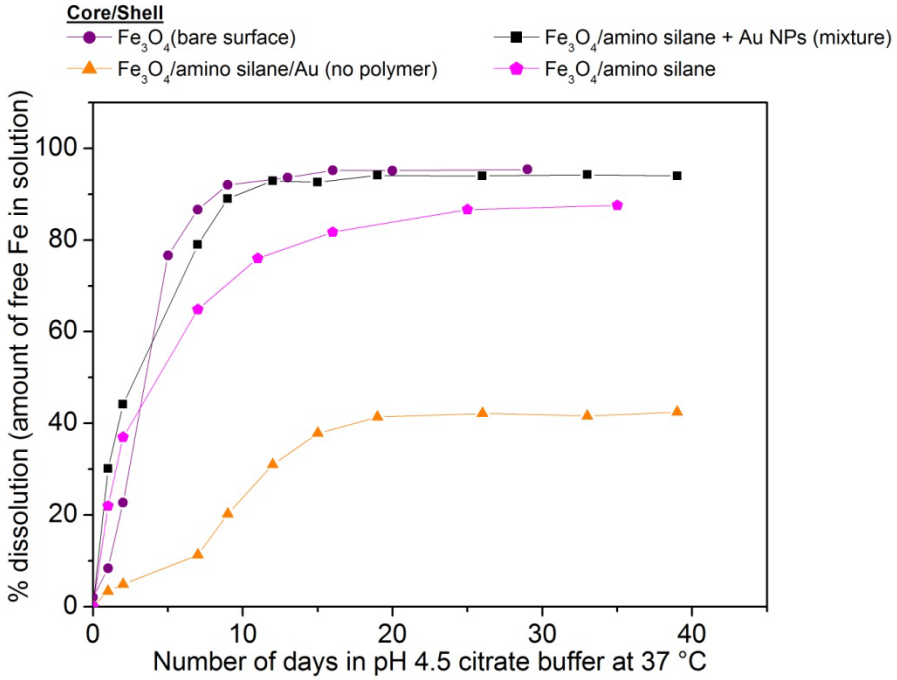

Figure 5.22. Dissolution assay of uncoated Fe_3O_4 SPIONs, A-SPIONs, Au-SPIONs (no polymer) and a 1:1 mix of A-SPIONs with Au NPs in pH 4.5 citrate buffer solution at 37 °C.

Since 1 % $HAuCl_4.3H_2O$ solution is pH 1.8, chemical modification of the amino silane layer might occur which could be providing protection and a degree of chemical stability. The dissolution data of these A-SPIONs, **Figure 5.23**, showed that conditioning in pH 1.8 HCl solution gave a dissolution trend similar to that obtained for A-SPIONs without treatment. For A-SPIONs subjected to 1% $HAuCl_4$, the dissolution was found to be slower. At 0 to 10 days the trend appears to be very similar to those

observed for the second generation Au-SPIONs without polymer. However, after this time point the dissolution rate increases and reaches 72 % dissolution at 34 days. This indicates that the co-ordination of Au^{3+} ions with surface amines provides some chemical stability of the SPION core.

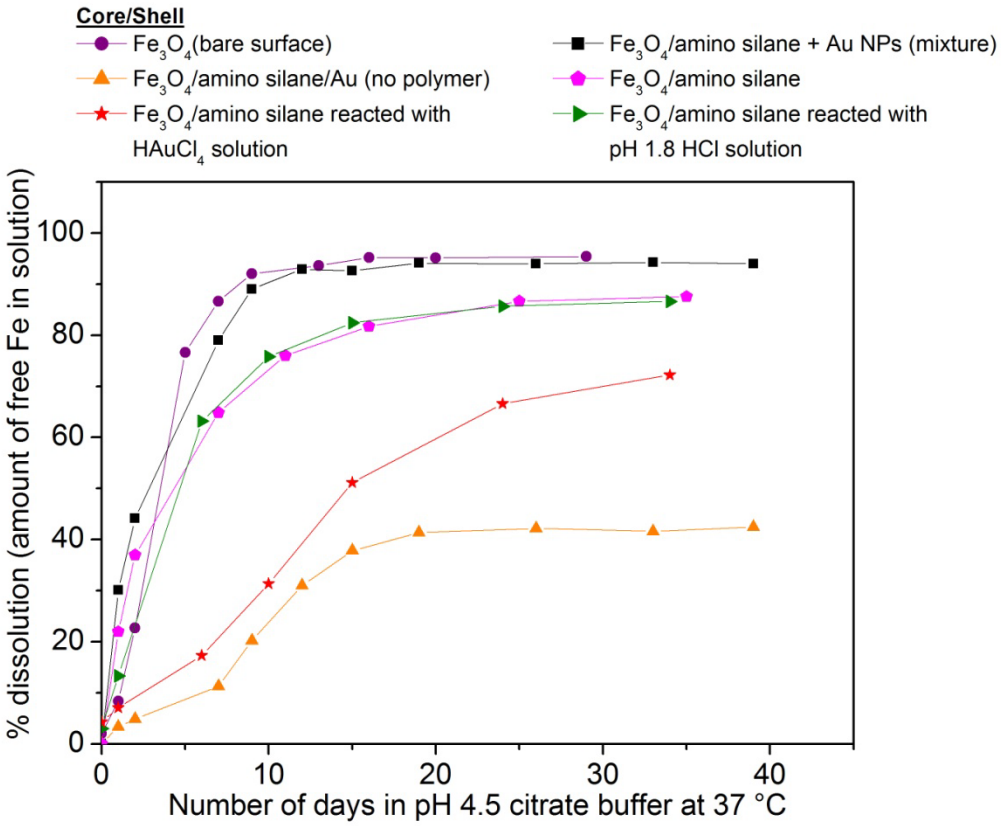

Figure 5.23. Dissolution assay of A-SPIONs subjected to conditioning in $HAuCl_4$ solution (red line) and pH 1.8 solution (green line) in pH 4.5 citrate buffer solution at 37 °C.

The chemical stability results from the dissolution assay for the second generation Au-SPIONs without polymer indicate that the co-ordination of Au^{3+} with amines contributes to its chemical stability. The low contrast NPs observed by HR-TEM, **Figure 5.18**, are therefore likely to consist of Au^{3+} co-ordinated A-SPIONs.

TEM images of Au-SPIONs without polymer were taken at 0 and 20 days which were subjected to the same conditions used for the dissolution assay. Samples were magnetically separated to image only magnetic NPs, **Figure 5.24**. From time 0 to day 20, a disappearance of most of the low contrast NPs was observed. A silica matrix surrounding the NPs was also seen which confirm the low contrast NPs were indeed A-SPIONs which were likely to contain Au^{3+} ions co-ordinated to amino silane layer.

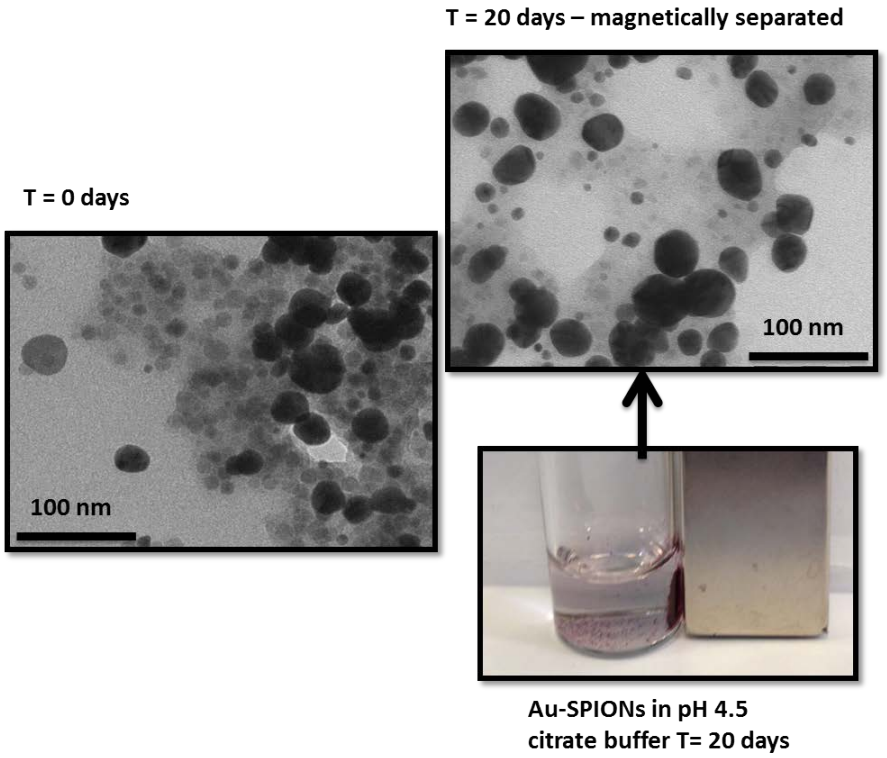

Figure 5.24. TEM images taken of Au-SPIONs (no polymer) which were subjected to dissolution assay conditions(pH 4.5 citrate buffer solution at 37 °C).

PXRD was carried out on all gold containing samples investigated by the dissolution assay study, **Figure 5.23**, in addition to Au NPs with diameter of 15 nm which were measured as a comparison. The spectra obtained for each sample was normalised by relative intensity and were overlayed onto the same graph, **Figure 5.25**. The spectra obtained for A-SPIONs mixed with Au NPs was very closely related to the PXRD pattern obtained for Au-SPIONs (second generation, no polymer) which suggests the composition of Au-SPIONs are gold NPs mixed with A-SPIONs. Interestingly, for A-SPIONs treated with $HAuCl_4$, a PXRD pattern for Au was only observed. A closer look at the baseline of the PXRD pattern, **Figure 5.26**, shows the high intensity peaks for Au are hiding peaks for iron oxide which has a much lower intensity. The Scherrer equation for peaks matching gold give a crystal size of 71 nm which maybe the reduction of Au^{3+} ions to Au^0 upon drying of the sample.

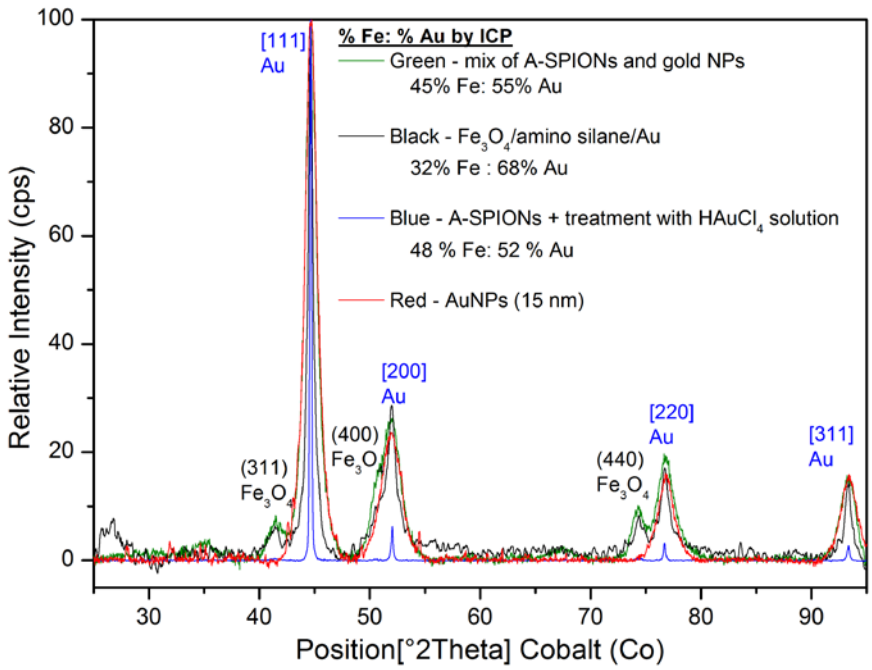

Figure 5.25. PXRD spectra for Au-SPIONs, Au NPs, mix of A-SPIONs/Au NPs and A-SPIONs treated with $HAuCl_4$ solution.

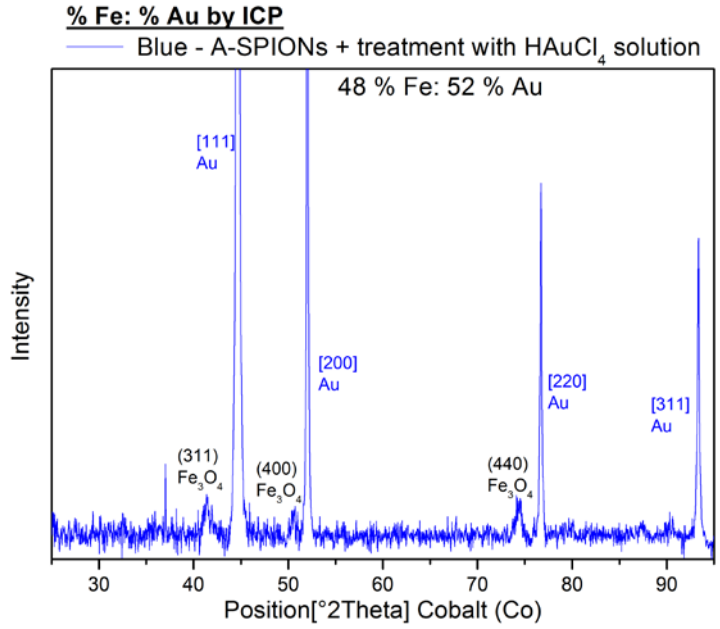

Figure 5.26. PXRD spectra for A-SPIONs treated with $HAuCl_4$ solution.

Kumar *et al.*[29] synthesised hollow gold nanoshells and demonstrated the appearance of these by TEM, **Figure 5.27A**. Here, transparent shells showing a dark rim are observed which thus confirmed the success of the synthesis. Hollow gold nanoshells containing

AgCl cores **Figure 5.27B** were also imaged and the presence the gold shell could not be distinguished from the core. PXRD was carried out on the hollow gold nanoshells and the pattern obtained follows a similar trend to those observed for solid Au NPs. Therefore this data indicates that gold nanoshells provide a similar PXRD pattern to that of solid gold NPs which thus supports that a Au coated SPION could be obtained.

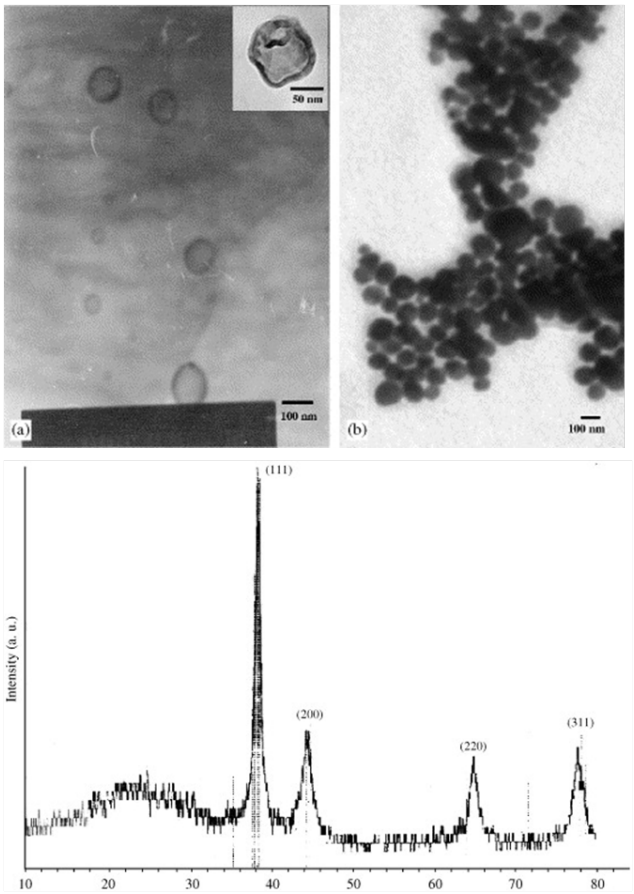

Figure 5.27. Shows TEM image of a) hollow gold nanoshells and b) the appearance of the gold nanoshells containing AgCl cores . The PXRD spectra (bottom) shows the pattern obtained for hollow gold nanoshells. Image taken from reference.[29]

5.3.3.3 Second Generation Au-SPIONs: Magnetisation Saturation Measurements

The M_s values measured from A-SPIONs gave 50.9 emu g^{-1} Fe_3O_4 and for Au-SPIONs 49.2 emu g^{-1} Fe_3O_4, **Figure 5.28** . As observed with the first generation Au-SPIONs, very little change to the M_s value was observed after reaction with auric chloride solution confirming no interactions of the Au^{3+} ions with the iron oxide surface. [7, 9, 30]

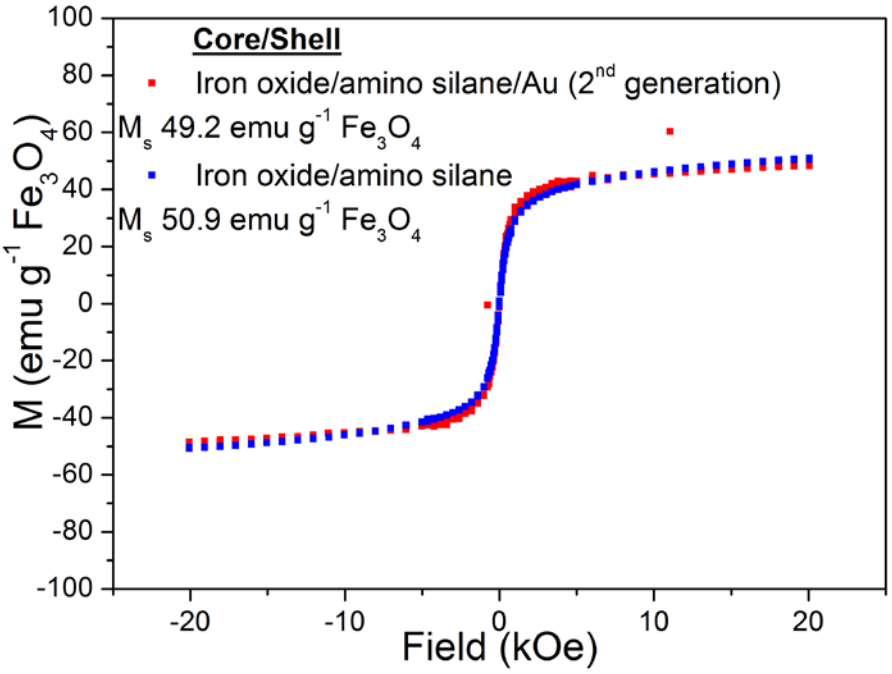

Figure 5.28. Magnetisation-field magnetic hysteresis curves for OA-SPION and Au-SPIONs at 300K. The 2 T magnetisation for A-SPION 50.9 emu g^{-1} Fe_3O_4 and Au-SPION 49.2 emu g^{-1} Fe_3O_4.

Dr. Lara Bogart at the University of Liverpool, Institute of Integrative Biology determined the magnetic SPION cores sizes using SQUID magnetometry curves obtained from measurements taken for A-SPIONs, Au-SPIONs and Molday Ion Rhodamine B, **Figure 5.29**. The sizes were determined using a simple Langevin expression modified by the log-normal polydispersity function, where D_t is the total SPION core diameter and D_m is the magnetic core diameter. For the A-SPIONs, a total core diameter of 10.0 ± 0.11 nm was deduced which contained a magnetic core diameter of 8.2 ± 0.11 nm. For the second generation Au-SPIONs, a total core diameter of 9.5 ± 0.12 nm was deduced which contained a magnetic core diameter of 7.5 ± 0.12 nm. On average, there is around a 2 nm difference in size (or a 1 nm thick shell dead layer) for both SPION samples.

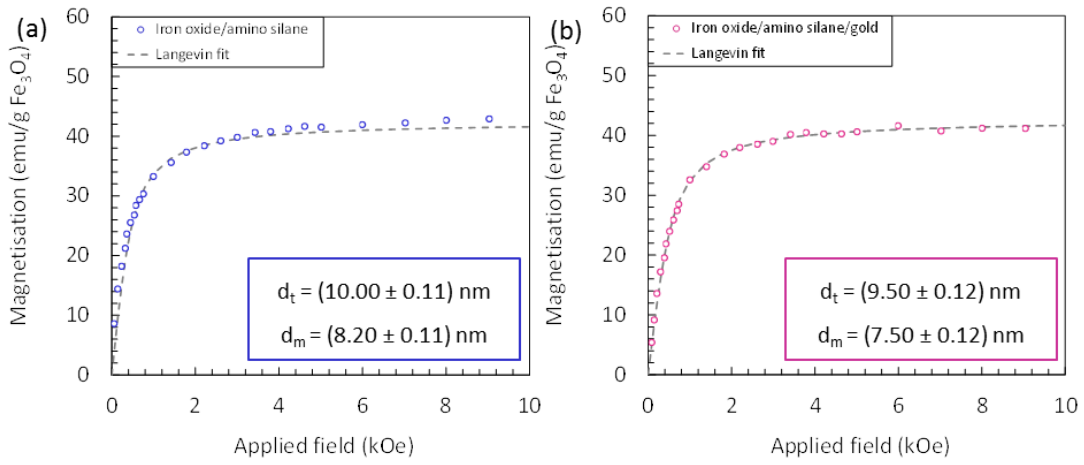

Figure 5.29. Room temperature magnetisation curves of (a) A-SPIONs, (b) Au-SPIONs (2nd generation) measured using SQUID magnetometry. Values of the total and magnetic radius as deduced from log-weighted Langevin expression are indicated for each particle, respectively.

Table 5.10. Best fit parameters extracted from ambient temperature magnetisation curves presented in **Figure 5.29**. Where D_t is the total SPION core diameter and D_m is the magnetic core diameter.

Sample	D_t (nm)	D_m (nm)	Standard deviation	Comment
A-SPIONs	10.0	8.2	0.11	Powdered sample
Au-SPIONs (2nd gen)	9.5	7.5	0.12	

5.3.3.4 Second Generation Au-SPIONs: Relaxivity Measurements

Au-SPIONs were evaluated for their potential for use as an MRI contrast agent, **Figure 5.30**. Au-SPIONs with concentrations ranging from 0 to 1.0 mM Fe fixed in 1 % agarose were analysed by MRI to measure their R_2 relaxivity. The R_2 relaxivity for Au-SPIONs was found at 194 $mMFe^{-1}$ s^{-1}. The high R_2 relaxivity value observed confirmed there was good diffusion of water protons to the iron oxide surface and therefore supports the use of gold as a suitable surface coating for SPIONs as an MRI contrast agent.[10, 24]

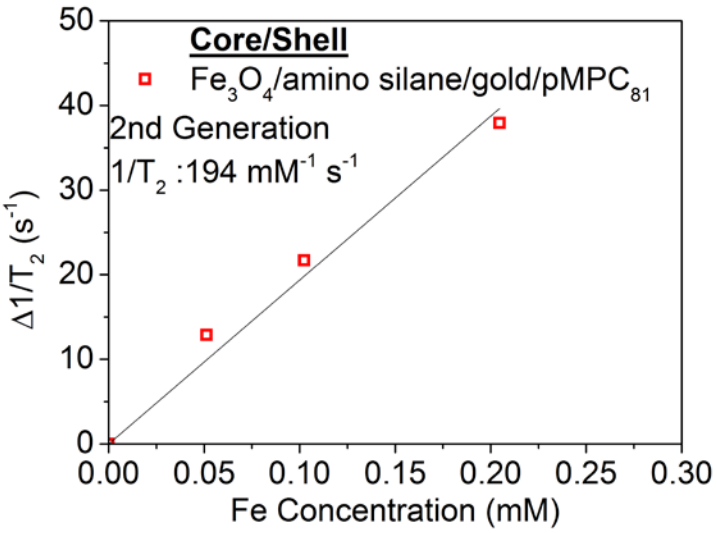

Figure 5.30. Relaxivity data for second generation Au-SPIONs showing R_2 ($1/T_2$) relaxivity as 194 mM^{-1} s^{-1} .

5.3.3.5 Second Generation Au-SPIONs: Elemental Mapping Measurements

Elemental mapping of Au-SPIONs was carried out using scanning transmission electron microscopy-high angle annular dark field (STEM-HAADF) and bright field imaging, **Figure 5.31**. Here elements with the highest atomic number appear brighter than those containing lower atomic number. From the dark field image, two separate populations of NPs exist which is likely to be gold NPs and iron oxide NPs. For a core shell NP containing a core with low atomic number and shell containing higher atomic number, a dark core is expected with a lighter shell on the dark field image. Here, this is not observed which indicates the bright NPs are likely to be solid gold NPs. Elemental mapping was also carried out using HAADF-electron energy loss spectroscopy (EELS) which is a technique complimentary to energy dispersive X-ray (EDX) spectroscopy, **Figure 5.32**. A map of Fe is scanned over Au-SPIONs during TEM. Unfortunately Au could not be mapped over the Au-SPIONs due to limitations of the instrument from low signal intensity for Au. Instead, a HAADF image was used to highlight areas for Au. The image for the Fe map show strong signals for NPs which have low contrast under conventional TEM. For the dark contrast NPs, weak Fe signal is observed which may be an artefact from the instrument.

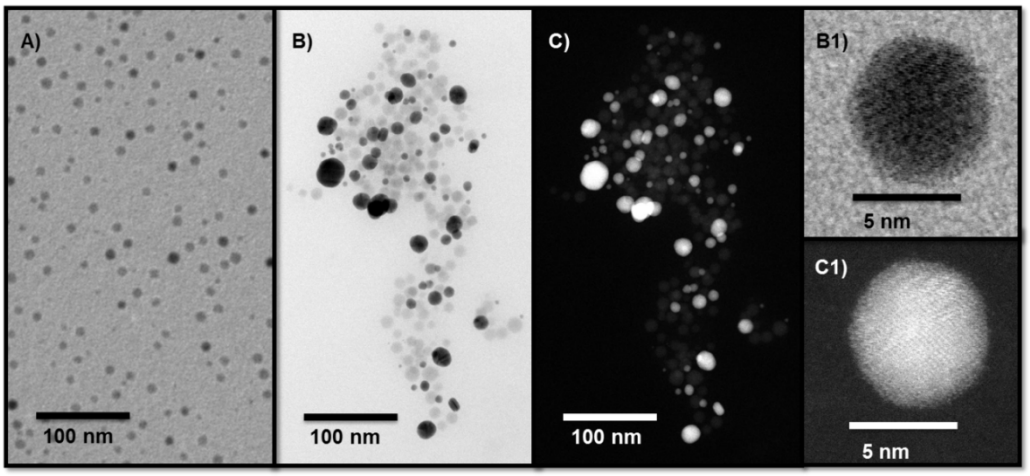

Figure 5.31. A) OA-SPION starting material observed by conventional TEM, Au-SPIONs imaged by B) STEM-HAADF bright field, C) STEM-HAADF dark field. Images were carried out by Dr Tobias Heil at the University of Liverpool.

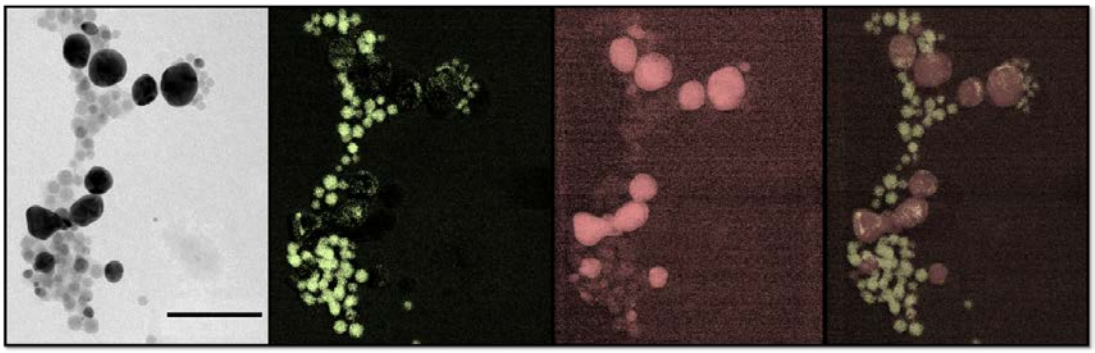

Figure 5.32. Shows from left to right TEM Au-SPIONs under bright field (black and white image), Fe map by HAADF-EELS (green and black), high energy view under dark field with highest atomic number appearing brightest (red and black) and finally an overlay of the Fe map with the high energy dark field image. Images were carried out by Dr Tobias Heil at the University of Liverpool. Scale bar :100 nm.

Core shell iron oxide gold nanoparticles synthesised by Sharma *et al.*[31] were analysed by TEM- EELS, **Figure 5.33**. Here, the signal intensity level measured for Fe was also found to be low over the NPs found in the TEM image of core/shell iron oxide/gold NPs. This Fe mapping thus provides a view to whether core/shell of iron oxide/gold can be adequately characterised through EELS mapping.

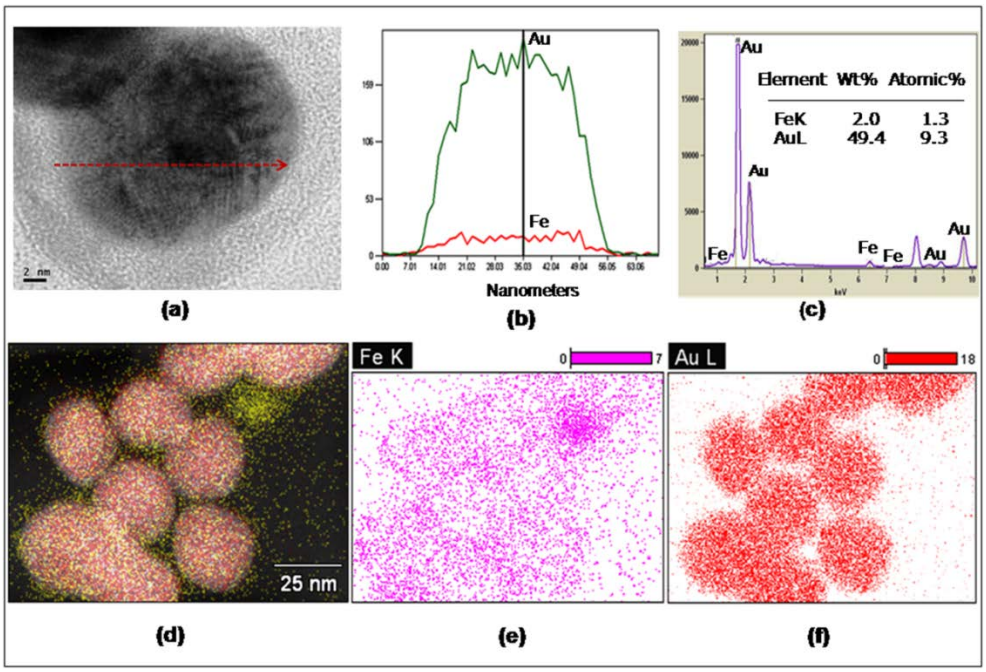

Figure 5.33. Showing a) TEM image of gold coated iron oxide NP, b) EDX intensity profile for Au and Fe and C) the EDX plot, d), e) and f) show an overalay and individual elemental maps using EELS over a TEM image of NPs for the distribution of Fe (purple) and gold (red). Image taken from reference.[31]

5.4 Conclusions

To conclude, in this Chapter gold was investigated as a NP surface coating to see if improvements to the chemical stability and protection of the SPION core to dissolution in conditions mimicking those found in the lysosomal environment of a stem cell. The initial stage of the work in this Chapter involved the use of A-SPIONs as a surface to co-ordination with Au^{3+} ions and reduction to Au^{0} to form a gold shell/coating. SPIONs containing a core diameter of 9.2 nm (by PXRD) were used. TEM images indicated the gold deposition process was uncontrolled as confirmed by the morphology of different shapes obtained. Au-SPIONs were found to have average crystal diameter of 10.8 nm by PXRD. The first generation Au-SPIONs were found to be purple in colour after the reaction procedure and an SPR with maxium absorbance of 540 nm was observed by UV-Vis spectroscopy. The SPR absorbance of known spherical Au NPs indicate at this wavelength an average size of 60 nm gold NPs is expected. By TEM, an average diameter of 18 ± 9 nm was measured and a total shell thickness of around 4 nm containing silane and gold was obtained. ICP analysis showed 2.81 % percentage mass of Fe was present in the sample. A large amount of Au was also present. To prepare a 1 mg Fe mL^{-1} concentrated sample for cell labelling experiments, a mass of 35.6 mg of

overall sample was required per 1 mL. Thiol functionalised pMPC polymer was required to stabilise Au-SPIONs in PBS or water. From TGA results, 88 % polymer weight contribution was found and which thus significantly reduced the Fe weight percent to 0.33 % in the overall sample. Thus, 299 mg of $pMPC_{135}$-Au-SPION sample was now required in 1 mL to prepare a 1 mg Fe mL^{-1} concentrated sample. The large amount of sample required lead to a high viscosity sample which was difficult to pipette and dispense into cell culture petri dishes. Cytotoxicity results at cell labelling concentrations of 100 and 50 µ Fe mL^{-1} were found to be cytotoxic with cells which was likely to have been caused by the excessive mass of sample present in the petri dish. The dissolution assay data for $pMPC_{135}$ coated Au-SPIONs provided significant chemical stability and protection of the iron oxide core to dissolution over a period of 25 days in pH 4.5 citrate buffer at 37 °C which confirms the suitability of gold as a surface coating for the protection of the SPION core. The magnetic properties were found to be retained which was confirmed by the M_s value which was measured at 47.8 emu g^{-1} Fe_3O_4 and by the R_2 relaxivity value of 123 mM^{-1} s^{-1} which again, further supports the suitability of gold as a surface coating.

In the second stage of this Chapter, the gold deposition reaction was modified in order to try and reduce the amount of gold present in the sample and thus reduce the amount of sample required to make a 1 mg Fe mL^{-1} sample for cell labelling studies and thus reduce viscosity of the sample and the cytotoxic effects observed with stem cells. A-SPIONs containing 7.4 nm SPION cores (by PXRD) were used for the gold deposition reaction. The second generation Au-SPIONs were found to be red in colour after the reaction procedure and an SPR was observed by UV-Vis spectroscopy whereby the maxium absorbance was found at 525-530 nm.The SPR absorbance for known spherical Au NPs indicate at this wavelength an average size of 25 to 40 nm gold NPs is expected. ICP analysis of the sample indicated a percentage mass of Fe as 23 % with the amount of sample required to make a 1 mg Fe mL^{-1} solution as 4.3 mg which was an 8 fold reduction compared to the first generation Au-SPIONs. Cytotoxity was assessed by cell proliferation over a period of 48 hours and cells showed better growth rates compared to the control which confirmed their biocompatibility. The dissolution assay data for the second generation Au-SPIONs provided a degree of chemical stability and protection of the iron oxide core to 40 % dissolution at 40 days in pH 4.5 citrate buffer at 37 °C. By TEM, two populations of NPs were observed which showed darker NPs containing Au

as confirmed by HAADF imaging and lighter contrast NPs which were determined to be uncoated A-SPIONs or A-SPIONs containing Au^{3+} ions co-ordinated to surface amine groups which was confirmed by EELS and taking a TEM image at 20 days during conditions simulated for the dissolution assay. The interaction of Au^{3+} ions with surface amine groups were found to contribute to the chemical stability results, however a full mechanism to the chemical stability for the second generation Au-SPIONs has not been determined. It is likely that the dark contrast NPs observed by conventional TEM are solid gold NPs and that a gold shell was not produced during the gold deposition reaction which was confirmed by HAADF. The magnetic properties were again found to be retained which was confirmed by the M_s value which was measured at 49.2 emu g^{-1} Fe_3O_4 and by the MRI R_2 relaxivity value of 194 mM^{-1} s^{-1} which again, further support the suitability of the use of gold to provide chemical stability to SPIONs.

Overall, the suitability of the use of gold for SPIONs used as a contrast-labelling agent for long term stem cell tracking has been studied. The biological studies for Au-SPION samples have been investigated and are discussed in the stem cell biology Chapter 6.

5.5 References

1. I. Y. Goon, L. M. H. Lai, M. Lim, *et al.*, *Chem. Mater.*, 2009, **21**, 673-681.
2. Z. Shuwen, Y. Ken-Tye, I. Roy, *et al.*, *Plasmonics*, 2011, **6**, 491-506.
3. P. D. Jadzinsky, G. Calero, C. J. Ackerson, *et al.*, *Science* 2007, **318**, 430-433.
4. L. Dykman and N. Khlebtsov, *Chem. Soc. Rev.*, 2012, **41**, 2256-2282.
5. A. Liu and B. Ye, *Clin. Lab.*, 2013, **59**, 23-36.
6. A. Taylor, K. M. Wilson, P. Murray, *et al.*, *Chem. Soc. Rev.*, 2012, **41**, 2707-2717.
7. U. Tamer, Y. Gündoğdu, İ. H. Boyacı, *et al.*, *J. Nanopart. Res.*, 2010, **12**, 1187-1196.
8. Z. Xu, Y. Hou and S. Sun, *J. Am. Chem. Soc.*, 2007, **129**, 8698-8699.
9. D. A. van Leeuwen, J. M. van Ruitenbeek, L. J. de Jongh, *et al.*, *Phys. Rev. Lett.*, 1994, **73**, 1432-1435.
10. B. Doan, S. Meme and J. Beloeil, *The Chemistry of Contrast Agents in Medical Magnetic Resonance Imaging*, John Wiley & Sons Ltd, 2013, 1-23.
11. G. Liang, S. Cai, P. Zhang, *et al.*, *Anal. Chim. Acta*, 2011, **689**, 243-249.
12. C. K. Lo, D. Xiao and M. M. F. Choi, *J. Mater. Chem.*, 2007, **17**, 2418-2427.

13. J. Gallo, I. Garcia, D. Padro, *et al.*, *J. Mater. Chem.*, 2010, **20**, 10010-10020.
14. I. Robinson, D. Tung le, S. Maenosono, *et al.*, *Nanoscale*, 2010, **2**, 2624-2630.
15. W. Wu, Q. He, H. Chen, *et al.*, *Nanotechnology*, 2007, **18**, 145609.
16. C. S. Bell, S. S. Yu and T. D. Giorgio, *Small*, 2011, **7**, 1158-1162.
17. X. Ji, R. Shao, A. M. Elliott, *et al.*, *J. Phys. Chem. C*, 2007, **111**, 6245-6251.
18. J. Park, K. An, Y. Hwang, *et al.*, *Nat Mater*, 2004, **3**, 891-895.
19. http://www.sigmaaldrich.com/materials-science/nanomaterials/gold-nanoparticles.html
20. A. S. Arbab, L. B. Wilson, P. Ashari, *et al.*, *NMR Biomed.*, 2005, **18**, 383-389.
21. P. M. Paulus, H. Bönnemann, A. M. van der Kraan, *et al.*, *Eur. Phys. J. D*, 1999, **9**, 501-504.
22. B. Issa, I. M. Obaidat, B. A. Albiss, *et al.*, *Int. J. Mol. Sci.*, 2013, **14**, 21266-21305.
23. E. D. Smolensky, H.-Y. E. Park, T. S. Berquó, *et al.*, *Contrast Media Mol. Imaging*, 2011, **6**, 189-199.
24. S. R. Veith, E. Hughes, G. Vuataz, *et al.*, *J. Colloid Interface Sci.*, 2004, 216-228.
25. A. Megia-Fernandez, M. Ortega-Muñoz, J. Lopez-Jaramillo, *et al.*, *Adv. Synth. Catal.*, 2010, **352**, 3306-3320.
26. Y. Hao, C. Man and Z. Hu, *J. Hazard. Mater.*, 2010, **184**, 392-399.
27. J. Wang, S. Zheng, Y. Shao, *et al.*, *J. Colloid Interface Sci.*, 2010, **349**, 293-299.
28. L. L. Stookey, *Anal. Chem.*, 1970, **42**, 779-781.
29. R. Kumar, A. N. Maitra, P. K. Patanjali, *et al.*, *Biomaterials*, 2005, **26**, 6743-6753.
30. L. Wang, J. Luo, Q. Fan, *et al.*, *J. Phys. Chem. B*, 2005, **109**, 21593-21601.
31. P. Sharma, V. Bhalla, E. S. Prasad, *et al.*, *Sci. Rep.*, 2012, **2**, 877.

PAGE LEFT INTENTIONALLY BLANK

6

Stem Cell Labelling Studies

For experimental details related to this Chapter, see Chapter 2.

List of Figures

Figure 6.1. Showing various endocytotic pathways and their appearance under a transmission electron microscope (TEM). Image taken from reference.[1] 228

Figure 6.2. Velocity histogram (left) and mean intracellular iron (right) of MSCs following a 24 hour exposure period to 25 µg Fe mL^{-1} of three different Molday Ion SPIONs as measured by single cell magnetophoresis. For each condition, the magnetic velocity was measured for cells suspended in 30% glycerol. A minimum of 300 cells were tracked over at least 3 image acquisitions. 231

Figure 6.3: Particle uptake study using a KSC line exposed to NP concentrations of 5 µg Fe mL^{-1} of A) MIRB, B) $pMPC_{29}$-SPIONs and 50 µg Fe mL^{-1} C) MIRB and D) $pMPC_{29}$-SPIONs incubated for 24 hours. Cells were stained with the Iron Stain Kit (Sigma Aldrich), which consists of a Prussian Blue staining for iron deposits and a Pararosaniline counterstain (pink). 233

Figure 6.4: KSC line exposed to re-constituted $pMPC_{29}$-SPIONs (after freeze drying) at 50 µg Fe mL^{-1} incubated for 24 hours. Cells were stained with the Iron Stain Kit (Sigma Aldrich), which consists of a Prussian Blue staining for iron deposits and a Pararosaniline counterstain (pink). 234

Figure 6.5. TEM images of stained KSCs incubated with 5 µg Fe mL^{-1} MIRB for 24 hours. Images A, B, C are captured at different magnification whereby the red area highlighted in the square of A represents the image presented in B. The orange area highlighted in the square of A represents the image presented in C. The yellow outlines found on the right hand side set of images are highlighted versions of the same set of images represented on the left and represent areas within the endosome where $pMPC_{29}$-SPIONs appear to be contained. 235

Figure 6.6. TEM images of areas of KSC and MSC lines exposed to 25 µg Fe mL^{-1} of $pMPC_{29}$-SPIONs for 24 hours. Images A) to F) shows areas of KSCs captured at different magnification where A, C, D, E and F show different magnifications of endosomes within the cell.Image B shows the membrane of the cell. Images G) to L) show areas of MSCs captured at different magnification of endosomes within the cell. Image G shows the membrane of the cell. 236

Figure 6.7. Photothermal images of KSCs labelled with $pMPC_{29}$-SPIONs compared to KSCs labelled with MIRB. Cell images in the green and red boxes show cells after

24 hour exposure to 5 μg Fe mL^{-1} and 25 μg Fe mL^{-1} of SPIONs respectively. Scale bar 62 μm. 237
Figure 6.8. CTV trajectory plots of KSCs exposed to $pMPC_{29}$-SPIONs and MIRB after 24 hours incubation. Cells were suspended in 30 % glycerol. 238
Figure 6.9. Magnetic velocity histogram (right) and total mass of Fe per cell histogram (left) comparing intracellular content of KSCs exposed to $p(MPC)_{29}$-SPIONs and MIRB SPIONs for 24 hours as measured by single cell magnetophoresis. For each condition, a minimum of 400 cells were tracked over at least 3 acquisitions. 239
Figure 6.10. Comparison of (a) magnetic velocity and (b) mean m_{Fe} per KSC exposed to MIRB SPIONs and (c) magnetic velocity and (d) mean m_{Fe} per KSC exposed to $p(MPC)_{29}$-SPIONs. Cells were initially exposed to a NP concentration of 10 μg Fe mL^{-1} of the respective magnetic NPs and left in NP free medium for a further 1, 3, 6 and 14 days. Cells were suspended in 30% glycerol for magnetophoresis measurements. The mean magnetic velocity, mean m_{Fe} per cell and cell numbers for each condition are indicated in **Table 6.1**. 241
Figure 6.11. Optical microscopy images of stem cell lines which have undertaken 24 hour exposure of 25 μg Fe mL^{-1} of B) MICB with Prussian blue stain and C) SiO_2 coated γFe_2O_3 SPIONs with Prussian blue stain. A) Shows stem cells not exposed to NPs. Scale bar 100 μm. Cells were stained with the Iron Stain Kit (Sigma Aldrich), which consists of a Prussian Blue staining for iron deposits. 245
Figure 6.12. Magnetic velocity histograms (top left and bottom left) and mean m_{Fe} per MSC (top right and bottom right) exposed to (a) 5 μg Fe mL^{-1} and (b) 25 μg Fe mL^{-1} of SiO_2 coated γFe_2O_3, SiO_2 coated Fe_3O_4 and MICB SPIONs as measured by single cell magnetophoresis in 30% glycerol. The mean and standard deviation of each condition is indicated. For each condition, a minimum of 300 cells were imaged over a minimum of 3 different image acquisitions. 246
Figure 6.13. Comparison of the mean m_{Fe} per KSC and MSC exposed to 5μg Fe mL^{-1} of MICB SPIONs to SiO_2-γFe_2O_3 and SiO_2-Fe_3O_4 SPIONs. For each condition, the magnetic velocity of at least 800 cells were imaged over at least 3 different acquisitions. Error bars correspond to standard deviation of the population. 247
Figure 6.14. Magnetic velocity (υ_m) histograms (top left and bottom left) and mean m_{Fe} (top right and bottom right) for (a) KSCs and (b) MSCs exposed to 5 μg Fe mL^{-1}

[1] of SiO_2 coated γFe_2O_3, SiO_2 coated Fe_3O_4 and MICB SPIONs as measured by single cell magnetophoresis in 30% glycerol. The mean and standard deviation of each condition is indicated. For each condition, a minimum of 300 cells were imaged over a minimum of 3 different image acquisitions. 247

Figure 6.15. Photograph of cell culture dishes containing cell lines exposed to 25 µg Fe mL^{-1} $pMPC_{135}$ coated Au-SPIONs with no staining. Exposure for 24 hour at 37 °C. 250

Figure 6.16. Optical microscopy images of stem cell lines. Images 1 are KSCs and images 2 are MSCs. A) Stem cells not exposed to NPs. B) to D) cell lines exposed for 24 hours to 25 µg Fe mL^{-1} of B) MICB stained with Prussian blue, C) and D) first generation $pMPC_{135}$ coated Au-SPIONs stained with Prussian blue and silver respectively. Scale bar 100 µm. 251

Figure 6.17. Optical microscopy *via* phase contrast images of MSCs. A) MSCs not exposed to NPs. MSCs exposed for 24 hours to 25 µg Fe mL^{-1} of B) MICB and C) second generation Au-SPIONs. 252

Figure 6.18. Example bright field microscopy images of MSCs exposed to 25 µg Fe mL^{-1} of Au-SPIONs for 24 hours captured using a Thor Labs colour CCD camera. Scale bar left 50 µm, scale bar right 25 µm. 253

Figure 6.19. Example TEM images of MSCs exposed to second generation Au-SPIONs. 254

Figure 6.20. Comparison of bright field imaging (A-D), fluorescent stain of nuclei (DAPI) (E-H), fluorescent stain of lysosomes (I-L), photothermal microscopy (M-P) and overlays (Q-T) of MSCs only and cells exposed to 25 µg Fe mL^{-1} of MICB and Au-SPIONs for 24 hours. All fluorescence and photothermal images are presented in false colours using the same brightness and contrast settings apart from images D, H, L, P and T which used lower brightness and contrast settings to demonstrate fluorescence quenching within lysosomes. 256

Figure 6.21. Magnetic velocity (υ_m) histogram (left) and mean intracellular iron (right) of MSCs following a 24 hour exposure period to three different NP concentrations (25, 50 and 100 µg Fe mL^{-1}) of Au-SPIONs as measured by single cell magnetophoresis. For each condition, the magnetic velocity was measured for cells suspended in 30% glycerol. A minimum of 400 cells were imaged over a minimum of 3 different image acquisitions. 257

List of Tables

Table 6.1. Summary of the cell count, mean magnetic velocity and mean m_{Fe} per cell of KSCs exposed to an initial NP concentration of 10 μg Fe mL^{-1} in the culture medium and left to grow in particle free medium. In deducing the mean m_{Fe} per cell, it has been assumed that the mean magnetic and total radius does not decrease due to degradation within the acidic environment of the lysosomes. *** indicates KSCs in 40 % glycerol solution.** 242

Table 6.2. Summary of average magnetic velocities of KSCs exposed to $pMPC_{29}$SPIONs compared with MIRB. 243

Table 6.3. Average magnetic velocities of MSCs exposed to 25 μg Fe mL^{-1} silica coated SPIONs compared with Molday Ion samples. 246

Table 6.4. Summary of average magnetic velocities of stem cell lines exposed to silica coated SPIONs compared with Molday Ion samples. 249

Table 6.5. Summary of average magnetic velocities of MSCs exposed to Au-SPIONs compared with Molday Ion samples. 258

Table 6.6. Summary of average magnetic velocities of stem cell lines exposed to all SPIONs covered in this Chapter. 259

6.1 Introduction

The intracellular fate of nanoparticles (NPs) is largely dependent on their endocytotic pathway type. Depending on the type(s) of endocytotic pathway present in the cell membrane of a particular cell (see **Figure 6.1**),[1, 2] extracellular material can be selectively internalised depending on its properties. This selectivity can allow different cell types containing one or more endocytotic pathway type to internalise material at different rates.[3] The design and development of nanomaterial and their surface coating is therefore important in obtaining good internalisation of material for cell labelling and tracking capability and knowledge of the endocytotic pathway(s) present in the targeted cell for labelling is beneficial. Properties of materials that can influence selectivity and rate of internalisation include size, shape/morphology, and surface charge/chemistry.[4, 5] For example, electrostatic

interactions with the membrane of a cell are known to occur with NPs which possess a surface charge since the membrane of a cell is known to have an overall net negative charge.[6] Positively charged NPs are therefore likely to have high affinity for a negatively charged cellular membrane and can thus encourage a faster rate of NP internalisation.[7] Negatively charged particles are likely to be electrostatically attracted to positively charged proteins present in the membrane of the cell but due to an overall electrostatic repulsion with the overall net negative charge of the cell membrane, the rate of internalisation by endocytosis is likely to be lower than that seen for NPs with a positively charged surface.[8] A neutral surface present on NPs coated with hydrophilic ligands does not show a preference for a specific endocytotic pathway and their uptake is typically labelled as non-specific but interaction with the cell membrane is still likely to occur through hydrogen bonding.[9]

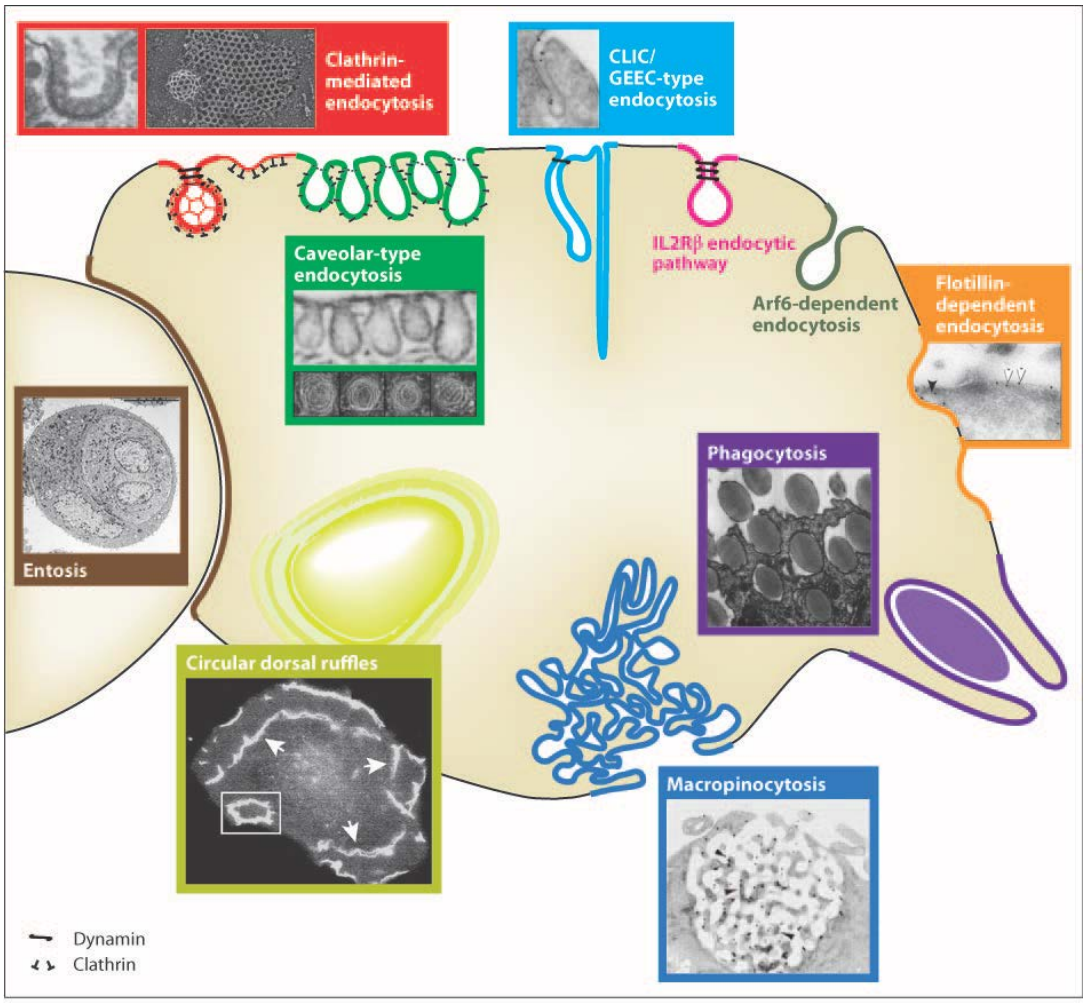

Figure 6.1. Showing various endocytotic pathways and their appearance under a transmission electron microscope (TEM). Image taken from reference.[1]

The administration and internalisation of NPs with stem cells in this project is carried out *in vitro* whereby stem cells are cultured in a petri dish and are exposed to cell culture medium containing NPs for a period of 24 to 48 hours to allow for the internalisation of NPs to take place. In Chapters 3-5, the chemical stability and dissolution of NPs prepared in this Thesis were assessed using a citrate buffer assay which was carried out at pH as low as 4.5 in order to mimic the conditions of an acidic lysosomal environment within a stem cell.

In this Chapter, magnetically labelled stem cells were studied by a technique known as cell tracking velocimetry (CTV), a concept similar to flow cytometry, whereby the magnetic velocity of each cell was measured.[10] Using magnetic velocity and the magnetic saturation (M_s) value obtained by SQUID for the magnetic NP sample internalised, the cell uptake of SPIONs for each cell could be quantified using Equation 9 of Chapter 2, Section 2.2.17.

The biological studies in this Chapter are discussed by the author, who did not carry out any of the biological experiments/studies or process any of the data. The author provided nanomaterials to the collaborating cell biologist (Dr Arthur Taylor) and biophysist (Dr Lara Bogart), who were funded on this EPSRC project. The nanomaterials prepared in this Thesis were submitted for cell labelling studies to understand the behaviour and suitability of the prepared materials as potential contrast agents for long term stem cell labelling/tracking. Cell labelling studies involved the use of murine derived kidney stem cells (KSCs) and mesenchymal stem cells (MSCs). The KSC lines used for cell labelling studies were isolated by the laboratories at the University of Liverpool Institute of Translational Medicine and their use was not commonly reported in the literature. The reason for using KSC lines in this project was that earlier work from the laboratory showed its potential use to help regenerate damaged kidneys which was the main area of research for this group.[11] All experiments in this Chapter involving KSC H6 were performed with cells between passage number of 10 and 30. Experiments using MSC D1 were performed with cells between passage number of 8 and 25. Cells were cryopreserved at their earliest passage number (10, 8), thus no cells at an earlier passage were used. At the later passage number (30, 25), these cells were known to preserve their stem

cell like characteristics and had not undergone any phenotypic changes as a consequence of prolonged culture.

Dr Arthur Taylor performed stem cell labelling experiments and prepared and took images of stem cells by optical and transmission electron microscopy (TEM) for the determination of cell uptake and intracellular localisation of NPs. In addition, Dr Lara Bogart used labelled stem cells prepared by Dr Arthur Taylor for CTV measurements for the determination of NP cell uptake and retention of NPs over a period of time. Photothermal imaging was also carried out by Dr Lara Bogart for the determination of NP cell uptake and for the determination of intracellular localisation of NPs. Alongside the nanomaterials prepared in this project; Molday Ion Rhodamine B (MIRB) and Molday Ion Coumarin Blue (MICB) commercially available contrast agents were used as controls to compare NP cell uptake and retention.

6.2 Results and Discussion

The uptake protocol for the following studies can be found in the experimental section of this Thesis Chapter 2 sections 2.2.17 and 2.3.2.2 and describes the process conditions used to prepare cells for optical, photothermal and CTV imaging.

6.2.1 Molday Ion Contrast Agents

To compare uptake of NPs prepared in this Thesis against commercially available contrast agents, the uptake/performance of the different Molday Ion contrast agents used was first determined. MSCs were exposed to a Molday Ion NP concentration of 25 μg Fe mL^{-1} for a period of 24 hours. To quantify the level of uptake, the magnetic velocities of MSCs exposed to MIRB, MICB and Molday Ion Evergreen (MIEG) contrast agents were measured by single cell magnetophoresis using CTV, **Figure 6.2**.[10] Average magnetic velocity measurements were found for MIRB, MICB and MIEG as 145 ± 80 μm s^{-1}, 270 ± 200 μm s^{-1} and 130 ± 60 μm s^{-1} respectively with mean intercellular iron content determined as 5.0 ± 3.0 pg, 8.7 ± 6.4 pg and 4.1 ± 2.0 pg respectively. MIRB and MIEG were found to have very similar levels of uptake compared with MICB which showed a higher level of uptake by a factor of two. For MICB, the standard deviation for the magnetic velocity measurements was found to

be much higher than that seen for MIRB and MIEG at ± 200 µm s^{-1}, which suggests a heterogeneous level of uptake behaviour measured from cell to cell. MSCs are perhaps selective at internalising MICB unlike MSC samples exposed to MIRB and MIEG which show a more homogeneous level of uptake behaviour. All three Molday Ion contrast agents have an average 8 nm diameter SPION core and cationic dextran proprietary shell with average zeta potential of ~+31 mV.[12] The only difference between each contrast agent is the fluorescent tag. The higher level of uptake for MICB must be considered when using this contrast agent when comparing against NPs prepared in this Thesis.

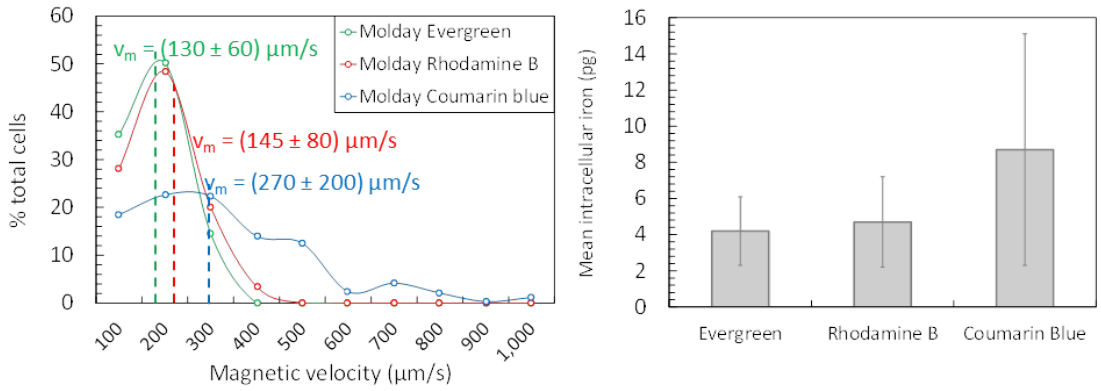

Figure 6.2. Velocity histogram (left) and mean intracellular iron (right) of MSCs following a 24 hour exposure period to 25 µg Fe mL^{-1} of three different Molday Ion SPIONs as measured by single cell magnetophoresis. For each condition, the magnetic velocity was measured for cells suspended in 30% glycerol. A minimum of 300 cells were tracked over at least 3 image acquisitions.

6.2.2 Stem cell labelling studies using poly[2-(methacryroyloxy)ethylphosphorylcholine] (pMPC) coated SPIONs

In Chapter 3, pMPC coated SPIONs were prepared and their suitability as a contrast labelling agent for bioapplication was assessed prior to cell uptake studies. In this Chapter, the cell uptake of $pMPC_{29}$-SPIONs with MSCs and KSC lines were investigated. In addition, the chemical stability of $pMPC_{29}$-SPIONs was investigated through a retention study with KSCs over a period of 14 days and is compared against the dissolution assay results obtained from Chapter 3 which were also used to assess the chemical stability of $pMPC_{29}$-SPIONs over time.

For cell uptake studies, KSCs were exposed to cell culture medium containing $pMPC_{29}$-SPIONs and MIRB NP concentrations of 1-50 µg Fe mL^{-1} and incubated for a period of 24 hours.[11] MIRB was initially selected due to having a similar core size to $pMPC_{29}$-SPIONs and containing a polymeric shell (dextran). The only difference was their average zeta potential value ($pMPC_{29}$-SPIONs in DIW pH 7 was near to neutral at +3.0 ± 0.3 mV compared to Molday Ion contrast agents which have an average zeta potential value of +31 mV). After this period, cells were washed, fixed and the iron oxide cores were stained using Prussian blue to form a complex with iron for imaging of SPIONs. Pararosaniline counterstain was used to visualise and image KSCs using bright field optical microscopy. For KSCs exposed to SPION concentrations of 5 µg Fe mL^{-1} of MIRB and $pMPC_{29}$-SPIONs (**Figure 6.3A and B** respectively), the Prussian blue staining appeared to be more intense with KSCs exposed to MIRB when compared to $pMPC_{29}$-SPIONs and thus indicated higher levels of uptake were obtained with MIRB. At higher labelling concentrations of 50 µg Fe mL^{-1}, the Prussian blue staining intensity for KSCs exposed to MIRB and $pMPC_{29}$-SPIONs (**Figure 6.3C and D** respectively) appeared even and thus suggested an even level of uptake was obtained in both cases. The even levels of Prussian blue staining could also indicate KSCs had become saturated at this labelling concentration.

At cell labelling concentrations of 5 µg Fe mL^{-1}, the lower level of uptake of $pMPC_{29}$-SPIONs suggests the pMPC surface coating is 'stealthy' and provides non-specific uptake as observed from the lower levels of Prussian blue staining, **Figure 6.3**, when compared with MIRB.[13] MIRB showed higher levels of uptake at lower NP concentrations. This is likely due to its cationic dextran surface coating, which results in a positive surface charge as measured by zeta potential of ~+31 mV when compared with the neutral $pMPC_{29}$-SPIONs ($pMPC_{29}$-SPIONs in DIW pH 7 was +3.0 ± 0.3 mV).[14] The optical microscopy images, **Figure 6.3**, also show heterogeneous uptake of $pMPC_{29}$-SPIONs at low NP concentrations within the KSC sample as observed from varying intensity of Prussian blue staining from cell to cell. This is thought to be due to the presence of more than one KSC type present in this population whereby cells have become more specialised than others and are therefore more selective in terms of the level of uptake.[11]

KSCs were also exposed to re-constituted $pMPC_{29}$-SPIONs (freeze dried and re-dissolved in PBS pH 7.4 solution) at a NP concentration of 50 µg Fe mL^{-1} for 24 hours, **Figure 6.4**. Here, a lower intensity of Prussian blue staining was observed within KSCs and thus suggested a lower level of uptake was achieved when compared to non-reconstituted $pMPC_{29}$-SPIONs (**Figure 6.3D**). In addition, adhesion of reconstituted $pMPC_{29}$-SPIONs to the outer cell membrane occurred as observed from the presence of blue staining around the outside of the cells. This may have been caused due to a number of reasons: 1) the reconstituted $pMPC_{29}$-SPIONs required a longer period of time to fully hydrate the pMPC shell coating, 2) the reconstituted $pMPC_{29}$-SPIONs were not fully dissolved and dispersed into the PBS solution or 3) the surface of the pMPC shell had been modified by the lyophilisation process thus changing the surface chemistry and hence changing the NP interaction with KSCs.

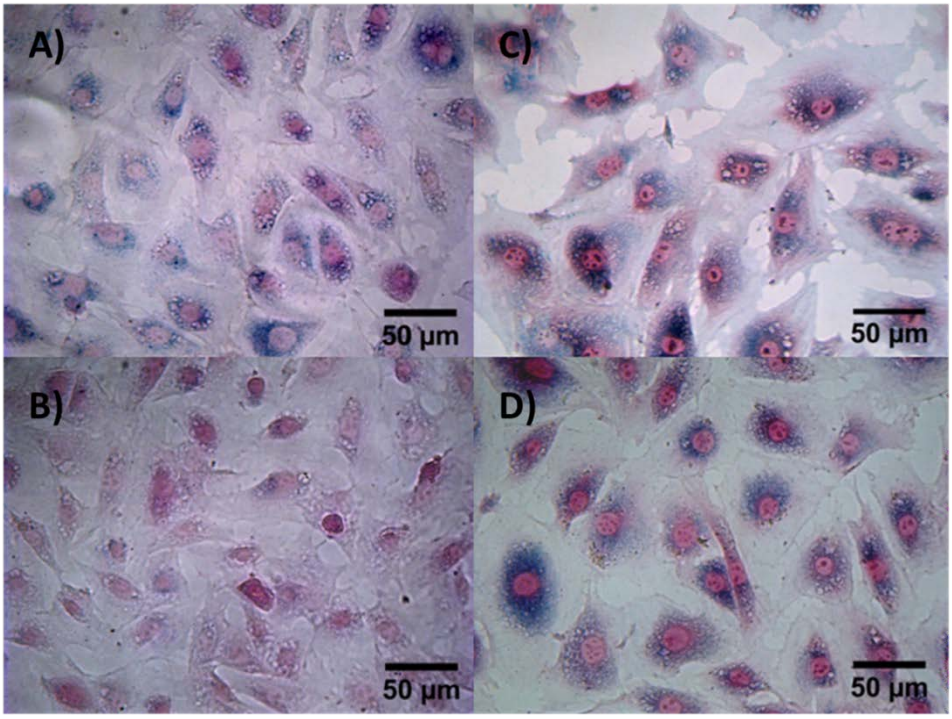

Figure 6.3: Particle uptake study using a KSC line exposed to NP concentrations of 5 µg Fe mL^{-1} of A) MIRB, B) $pMPC_{29}$-SPIONs and 50 µg Fe mL^{-1} C) MIRB and D) $pMPC_{29}$-SPIONs incubated for 24 hours. Cells were stained with the Iron Stain Kit (Sigma Aldrich), which consists of a Prussian Blue staining for iron deposits and a Pararosaniline counterstain (pink).

Overall the results show $pMPC_{29}$-SPIONs provided non-specific cell uptake at lower NP concentrations and indicate that the pMPC surface coating may require further

development in order to obtain a coating which can provide higher levels of uptake within cells if requiring the use of less nanomaterial for future cell labelling studies.

To determine the intracellular location of $pMPC_{29}$-SPIONs and MIRB within MSCs and KSCs, TEM was used, **Figure 6.5** and **Figure 6.6** respectively. For both cell lines, TEM images showed the intracellular internalisation route for $pMPC_{29}$-SPIONs and MIRB into stem cells had been *via* the endosome of the cell through endocytosis. From the TEM images, the endocytotic pathway is not clear but to speculate by looking at the shape of the endosomes and the way the cell plasma membrane forms a vesicle through invagination it is likely to be *via* clathrin or caveolae mediated endocytosis.[1] For the visualisation of organelles within cells by TEM, cells were stained using 5% uranyl acetate and 2 % lead citrate, **Figure 6.5**.

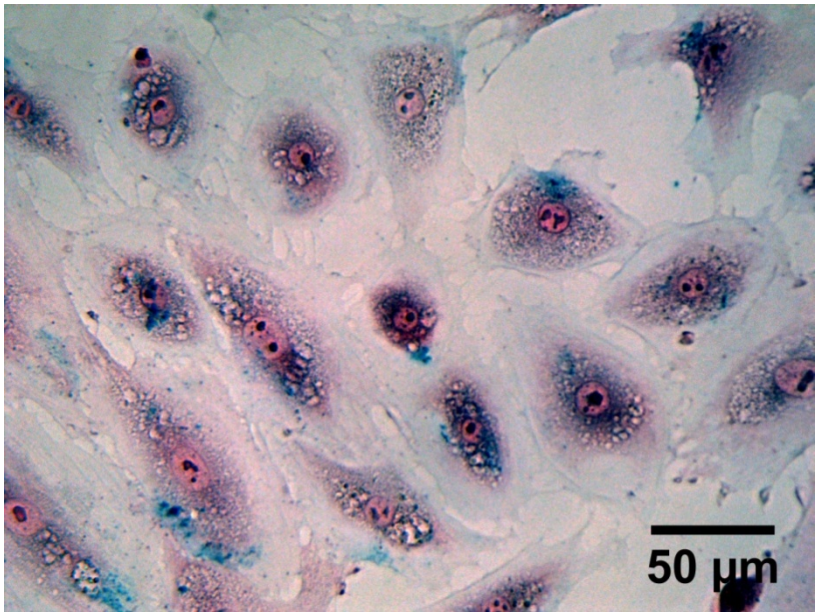

Figure 6.4: KSC line exposed to re-constituted $pMPC_{29}$-SPIONs (after freeze drying) at 50 µg Fe mL^{-1} incubated for 24 hours. Cells were stained with the Iron Stain Kit (Sigma Aldrich), which consists of a Prussian Blue staining for iron deposits and a Pararosaniline counterstain (pink).

Here, endosomes appear darker compared to the endosomes observed in TEM images found in **Figure 6.6** which show unstained KSCs and MSCs exposed to $pMPC_{29}$-SPIONs. Not staining KSCs and MSCs allows a clearer visualisation of the location of $pMPC_{29}$-SPIONs where they are clearly seen within the endosomes of the stem cell and are thus not confused with other stained material and organelles within the cell. Areas within the endosome that contain SPIONs are highlighted in yellow

on the TEM images (right hand side set of TEM images **Figure 6.5A to C**). Here, the yellow outlines highlight jagged and broken shaped areas where NPs are contained within the stained endosomes and highlights that $pMPC_{29}$-SPIONs are not fully occupying all the space within the endosomes of the cell. $pMPC_{29}$-SPIONs also do not occupy all of the space within the endosomes and are more clearly observed without a stain.

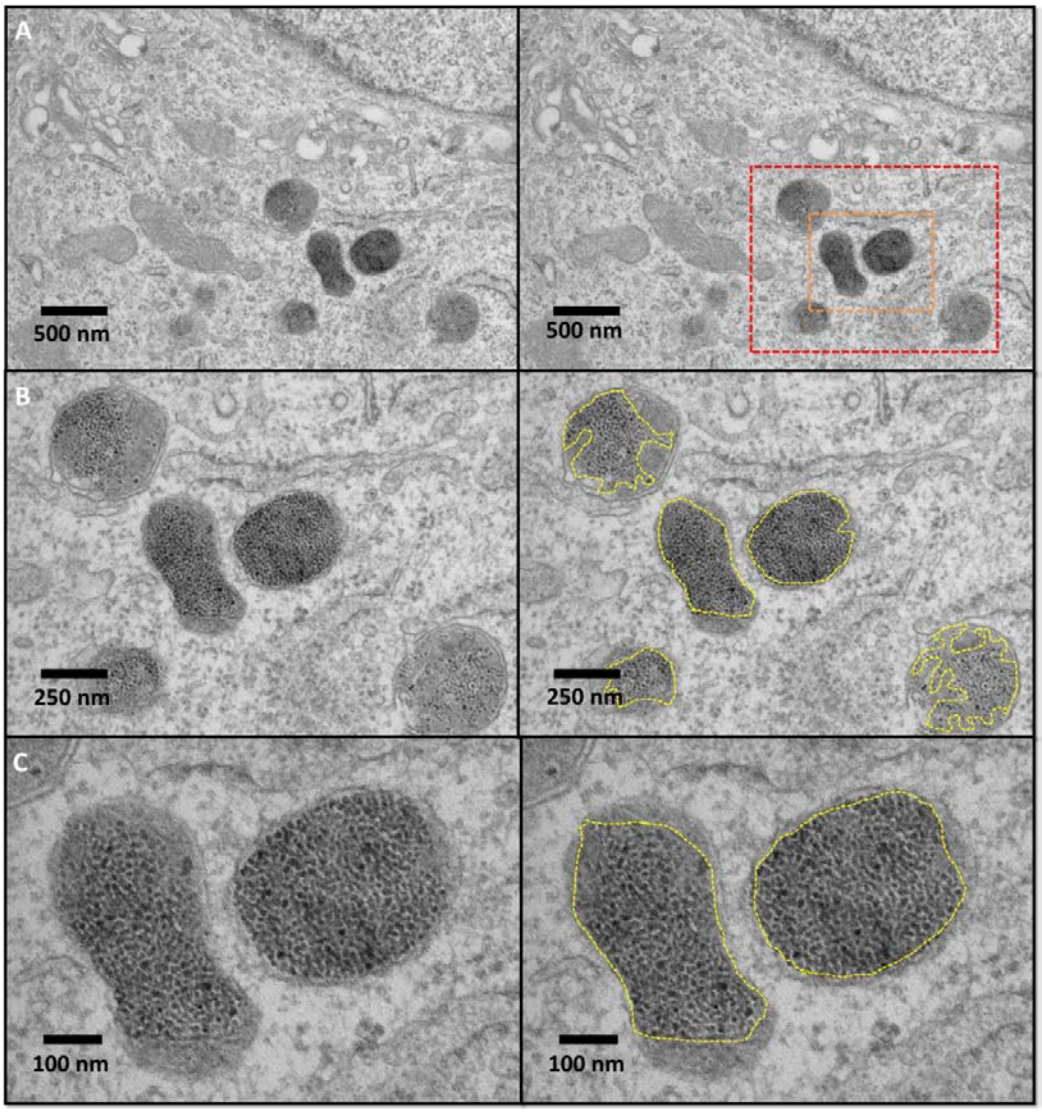

Figure 6.5. TEM images of stained KSCs incubated with 5 µg Fe mL^{-1} MIRB for 24 hours. Images A, B, C are captured at different magnification whereby the red area highlighted in the square of A represents the image presented in B. The orange area highlighted in the square of A represents the image presented in C. The yellow outlines found on the right hand side set of images are highlighted versions of the same set of images represented on the left and represent areas within the endosome where $pMPC_{29}$-SPIONs appear to be contained.

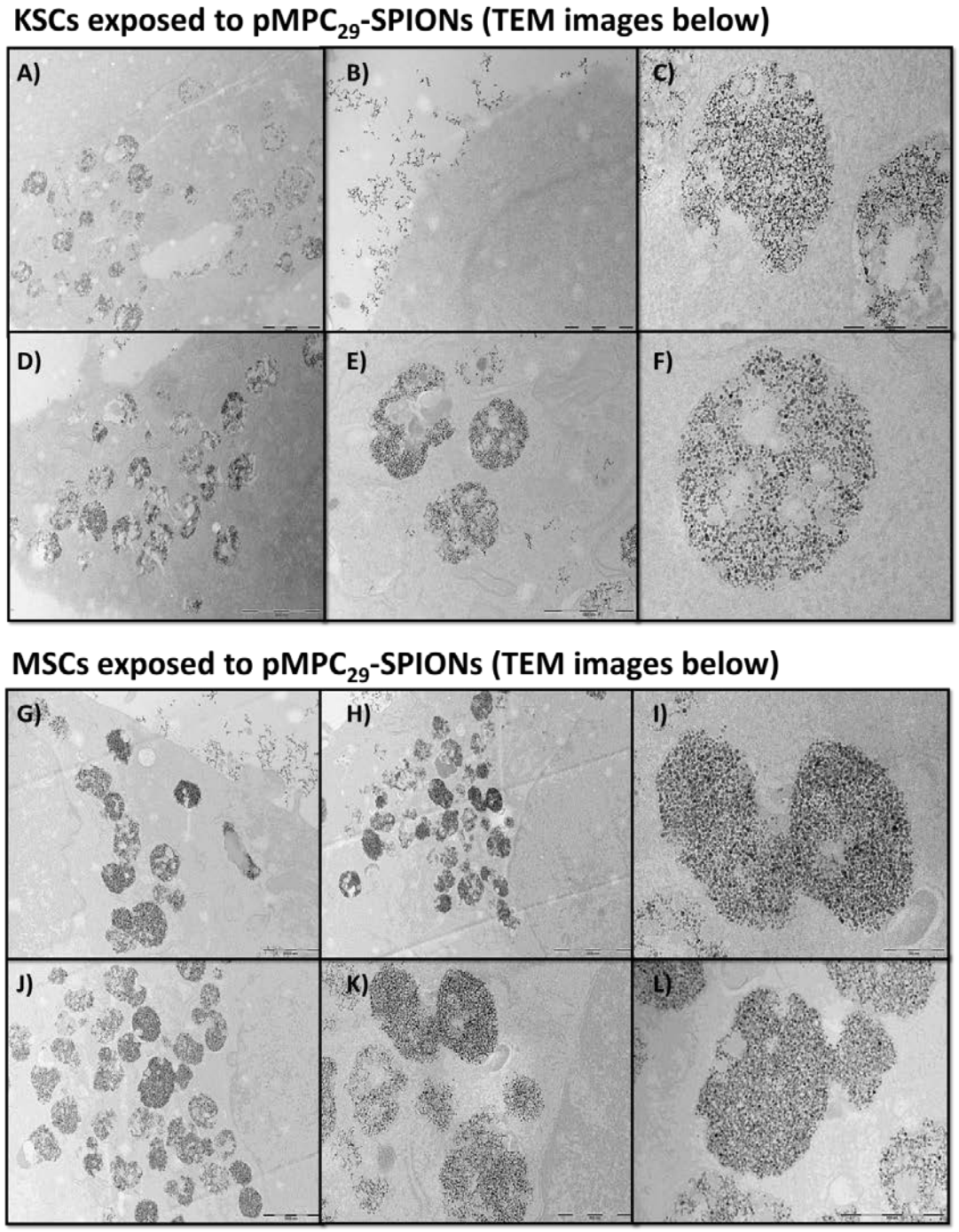

Figure 6.6. TEM images of areas of KSC and MSC lines exposed to 25 μg Fe mL^{-1} of $pMPC_{29}$-SPIONs for 24 hours. Images A) to F) shows areas of KSCs captured at different magnification where A, C, D, E and F show different magnifications of endosomes within the cell.Image B shows the membrane of the cell. Images G) to L) show areas of MSCs captured at different magnification of endosomes within the cell. Image G shows the membrane of the cell.

Photothermal imaging was used to investigate the intracellular localisation of $pMPC_{29}$-SPIONs *vs.* MIRB in KSCs. Cells were exposed to two different NP

concentrations of 5 and 25 µg Fe mL^{-1} for 24 hours and were then washed to remove free NPs from the cell dish before imaging. The photothermal images produced, **Figure 6.7**, confirmed a lower level of intracellular uptake of $pMPC_{29}$-SPIONs at the NP concentration of 5 µg Fe mL^{-1} when compared with MIRB. This was observed by the difference of photothermal intensity/contrast between the two sample images where lighter areas showed higher concentrations of NP uptake compared to darker areas which indicated lower levels of NP uptake. For the exposure of stem cells to NP concentrations of 25 µg Fe mL^{-1}, the level of intensity for $pMPC_{29}$-SPIONs again seemed to be lower compared to stem cells exposed to MIRB at both 5 and 25 µg Fe mL^{-1}. A small increase in the level of intensity for $pMPC_{29}$-SPIONs at 25 µg Fe mL^{-1} was noticed compared to 5 µg Fe mL^{-1} but was not significant when compared to the cell uptake images of cells taken under optical microscopy using Prussian Blue staining, **Figure 6.3**.

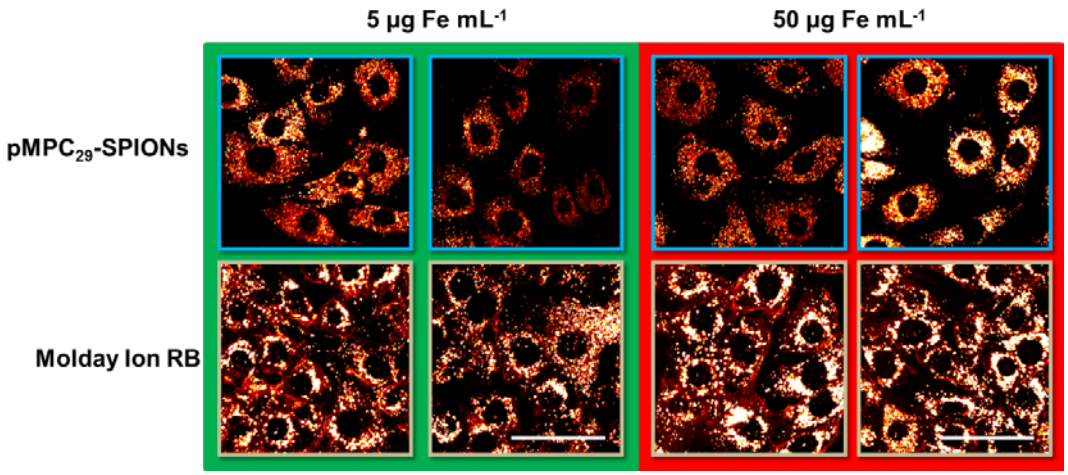

Figure 6.7. Photothermal images of KSCs labelled with $pMPC_{29}$-SPIONs compared to KSCs labelled with MIRB. Cell images in the green and red boxes show cells after 24 hour exposure to 5 µg Fe mL^{-1} and 25 µg Fe mL^{-1} of SPIONs respectively. Scale bar 62 µm.

Overall from **Figure 6.7**, the intracellular location for both SPION samples appear to be different. At both concentrations used, $pMPC_{29}$-SPIONs appear to have a uniform distribution within the cells, whereas the photothermal images of stem cells exposed to MIRB showed granular areas which are likely to suggest the endosomes inside the cell are highly compacted with NPs. In addition, the stem cell membranes of cells exposed to MIRB were visualised by photothermal microscopy which may suggest there are attractions/adhesion of MIRB to the outer cell membrane which might have

been caused by an electrostatic attraction of the cationic dextran surface coating to the overall negatively charged cell membrane. For cells exposed to $pMPC_{29}$-SPIONs, cell membranes were not visualised; again suggesting the pMPC surface coating is stealthy and that non-specific uptake is likely.

Labelled KSCs were further investigated by CTV to determine the average number of SPIONs internalised per cell and thus quantify the average amount of iron oxide per cell. This was measured from the magnetic velocity (υ_m) of each cell which was obtained from the horizontal component of the trajectory plots drawn of the velocity of cells moving through a capillary under a uniform magnetic field gradient (single cell magnetophoresis).[10] **Figure 6.8** shows CTV trajectory plots of KSCs exposed to SPION concentrations of 1 and 5 μg Fe mL^{-1} for 24 hours and **Figure 6.9** shows the complementary υ_m and mass histograms for MIRB and $pMPC_{29}$-SPIONs.

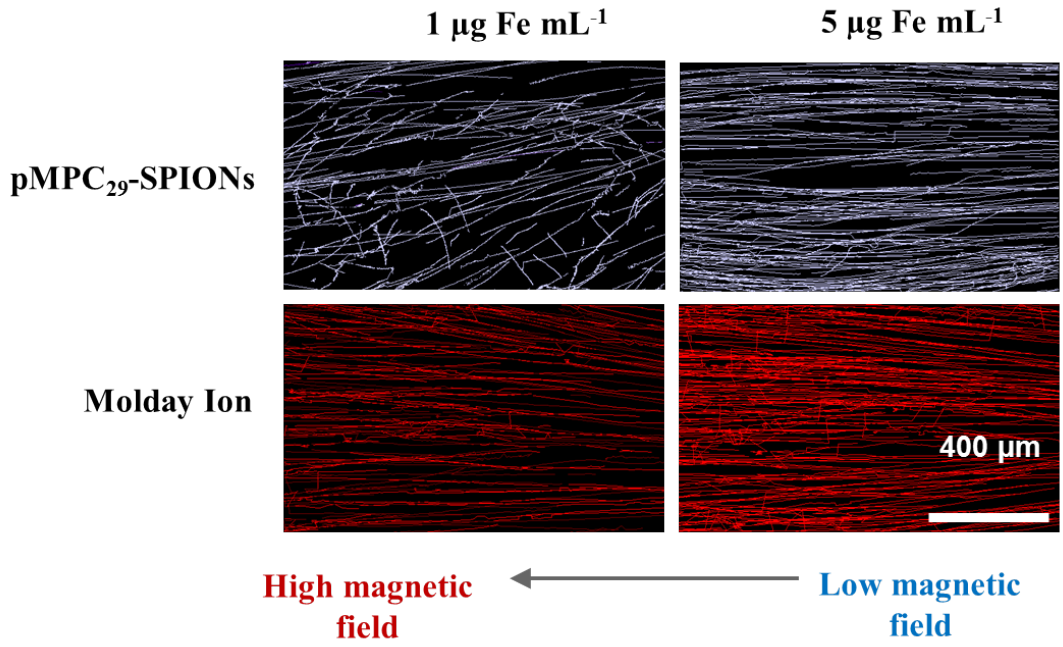

Figure 6.8. CTV trajectory plots of KSCs exposed to $pMPC_{29}$-SPIONs and MIRB after 24 hours incubation. Cells were suspended in 30 % glycerol.

At the lowest NP concentration of 1 μg Fe mL^{-1}, the trajectory plots for MIRB were found to have unbroken horizontal tracks, which indicate a sufficient level of NP uptake was obtained to ensure cells could travel through the capillary under a uniform magnetic field gradient. For cells exposed to 1 μg Fe mL^{-1} of $pMPC_{29}$-SPIONs, broken trajectory plots were observed and therefore suggest a

lower level of uptake since cells were not able to travel a full length through the capillary under a uniform magnetic field gradient. The average υ_m for KSCs exposed to 1 and 5 µg Fe mL^{-1} of $pMPC_{29}$-SPIONs was found at 12 ± 6 µm s^{-1} and 56 ± 35 µm s^{-1} respectively compared with average υ_m of KSCs exposed to 1 µg Fe mL^{-1} of MIRB which was found at 43 ± 25 µm s^{-1}, which is a factor of 3.6 times higher average υ_m.

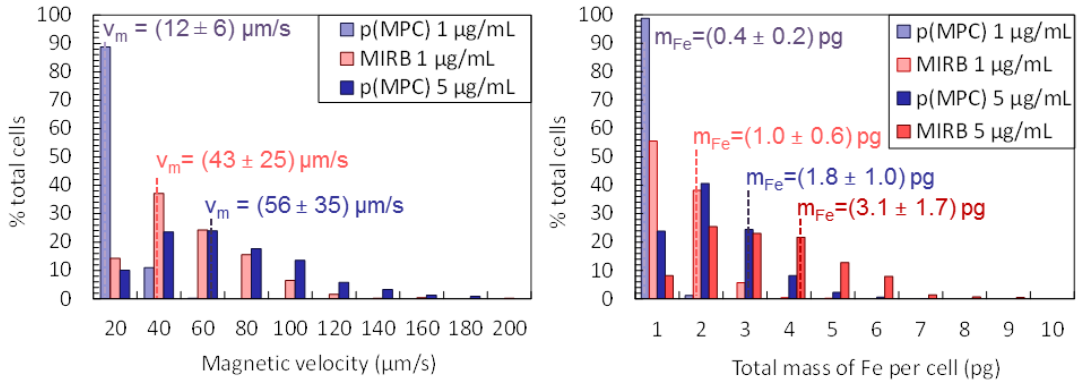

Figure 6.9. Magnetic velocity histogram (right) and total mass of Fe per cell histogram (left) comparing intracellular content of KSCs exposed to $p(MPC)_{29}$-SPIONs and MIRB SPIONs for 24 hours as measured by single cell magnetophoresis. For each condition, a minimum of 400 cells were tracked over at least 3 acquisitions.

In terms of mass of iron per cell (m_{Fe}) or intracellular iron, the mean m_{Fe} per KSC for $pMPC_{29}$-SPIONs exposed to 5 µg Fe mL^{-1} compared with MIRB was found to be 1.8 ± 1.0 pg and 3.1 ± 1.7 pg respectively. This shows that there was twice the level of uptake of MIRB as compared to $pMPC_{29}$-SPIONs, **Figure 6.9**. However at lower NP concentration of 1 µg Fe mL^{-1}, the mean m_{Fe} per KSC for $pMPC_{29}$-SPIONs compared with MIRB was found at 0.4 ± 0.2 pg and 1.0 ± 0.6 pg respectively which shows there was two and a half times the level of uptake of MIRB. The CTV results overall confirm higher levels of uptake for KSCs exposed to MIRB compared to $pMPC_{29}$-SPIONs.

6.2.2.1 Stem Cell Retention of $pMPC_{29}$-SPIONs

In Chapter 3, the chemical stability of the $pMPC_{29}$-SPION core was assessed by a dissolution assay which measured the amount of iron oxide dissolved in an acidic citrate buffer solution overtime. This was to mimic the endosomal and lysosomal environments inside a stem cell (see Chapter 2 for Experimental).[15, 16] The

dissolution assay showed that $pMPC_{29}$-SPION cores were rapidly digested at pH 4.5 within a period of 5 days with dissolution at 70 %. The rapid rate in dissolution showed that $pMPC_{29}$-SPIONs would not be a suitable candidate for long-term stem cell tracking using Magnetic Resonance Imaging (MRI).

Before completely ruling out the suitability of $pMPC_{29}$-SPIONs for long term application, the chemical stability of $pMPC_{29}$-SPIONs was further investigated, this time by exposing $pMPC_{29}$-SPIONs with stem cells and measuring/monitoring their initial uptake and retention over time using CTV. By measuring the magnetic velocity per labelled stem cell and determining the mean magnetic m_{Fe} per cell over a period of 14 days, the chemical stability of $pMPC_{29}$-SPIONs could be more realistically determined.

To determine the mean m_{Fe} per cell, it was assumed that the mean magnetic and total radius does not decrease due to degradation within the acidic environment of the lysosomes. Firstly, KSCs were exposed to a NP concentration of 10 μg Fe mL^{-1} of MIRB SPIONs and $pMPC_{29}$-SPIONs for 24 hours, after which the cell culture medium was rinsed three times and replaced with SPION free cell culture medium. KSCs were then left to proliferate for an additional 14 days and the magnetic velocity was measured on day 1, 3, 6 and 14 following initial exposure to magnetic NPs. **Figure 6.10** compares the magnetic velocity and mean m_{Fe} per KSC exposed to a NP concentration of 10 μg Fe mL^{-1} of MIRB (top) and $pMPC_{29}$-SPIONs (bottom) measured in 30 % glycerol. Cell proliferation is taken into account by counting the number cells prior to measuring the mean magnetic velocity and mean m_{Fe} per cell, **Table 6.1.** KSCs exposed to MIRB showed an initial decrease in numbers after which they increased by a factor of approximately 3.5 after 14 days, whilst the mean m_{Fe} per cell decreased by a factor of approximately 6. For cells exposed to the $pMPC_{29}$-SPIONs, a similar initial decrease in cell numbers was observed after which they increased by a factor of 2 and after 14 days. Over this time period, the mean m_{Fe} per cell decreased by a factor of 3. The magnetophoresis measurements suggest that the $pMPC_{29}$-SPION retention was comparable to that of MIRB, suggesting that material was diluted during cell division and not degraded and that the $pMPC_{29}$ shell was offering good protection and preventing degradation of the iron oxide core.

In summary, the retention study using KSCs shows that $pMPC_{29}$-SPIONs cores do not degrade as fast as initially predicted by the dissolution assay carried out in Chapter 3. The chemical stability results of $pMPC_{29}$-SPIONs found from the retention study show $pMPC_{29}$-SPIONs cores last for at least 14 days as confirmed by magnetic velocity measurements found on day 14, **Table 6.1**.

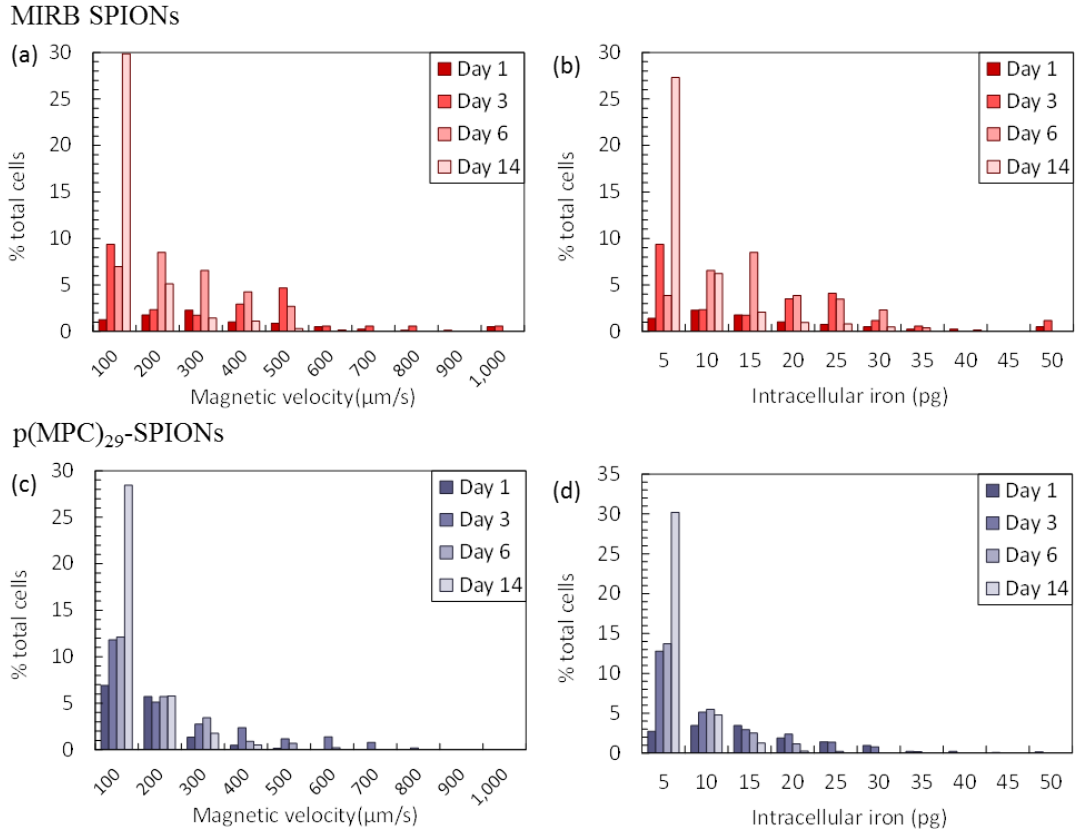

Figure 6.10. Comparison of (a) magnetic velocity and (b) mean m_{Fe} per KSC exposed to MIRB SPIONs and (c) magnetic velocity and (d) mean m_{Fe} per KSC exposed to $p(MPC)_{29}$-SPIONs. Cells were initially exposed to a NP concentration of 10 μg Fe mL^{-1} of the respective magnetic NPs and left in NP free medium for a further 1, 3, 6 and 14 days. Cells were suspended in 30% glycerol for magnetophoresis measurements. The mean magnetic velocity, mean m_{Fe} per cell and cell numbers for each condition are indicated in **Table 6.1**.

These findings show that the conditions used in the dissolution assay are harsh and do not realistically simulate the true conditions found with the endosome/lysosome of the cell.[17, 18] In addition, pH in the endosome/lysosome naturally reduces with time. This is a condition that is not simulated in the dissolution assay but occurs naturally in the retention study. This would help to account for the extended

dissolution period observed for MIRB and $pMPC_{29}$-SPIONs by the retention study. Improvements to the dissolution assay to account for this would be needed to closely represent conditions within the endosome/lysosome. Work carried out by Lévy *et al.*[19] and Soenen *et al.*[17] report findings of a correlation between dissolution rate of iron oxide NPs and citrate concentration. Iron is readily transported out of the endosome into the cytoplasm after chelating with ligands such as citrate.

Table 6.1. Summary of the cell count, mean magnetic velocity and mean m_{Fe} per cell of KSCs exposed to an initial NP concentration of 10 μg Fe mL^{-1} in the culture medium and left to grow in particle free medium. In deducing the mean m_{Fe} per cell, it has been assumed that the mean magnetic and total radius does not decrease due to degradation within the acidic environment of the lysosomes. *** indicates KSCs in 40 % glycerol solution.**

Sample	Time after exposure (days)	Cell count ($x10^3$)	Mean magnetic velocity (μm s^{-1})	Mean m_{Fe} (pg)
MIRB	0	35	-	-
	1	30	420 ± 440	20.5 ± 21.2
	3	80	270 ± 260	13.5 ± 12.7
	6	96	205 ± 120	9.9 ± 5.9
	14	120	70 ± 90	3.3 ± 4.3
$p(MPC)_{29}$-SPIONs	0	49	-	-
	1	**40**	**120 ± 85***	12.9 ± 9.2
	3	70	180 ± 180	11.6 ± 11.6
	6	63	114 ± 115	7.4 ± 7.5
	14	100	65 ± 71	4.2 ± 4.5

The reports suggests that NP dissolution is controlled by the availablility and affintity of chelates (such as citrate) produced intracellularly. The concentration of chelates present in the endsome/lysosome of the stem cell are unlikely to be known and to vary depending on active biological mechanisms with the cell. The dissolution assay developed by Arbab *et al.*[16] which has been used in this Thesis to model the conditions of the endosome/lysosome of a stem cell uses a sodium citrate concentration of 20 mM in PBS whereas above this concentration (50 mM) the dissolution rate accelerates. A question therefore remains to what citrate concentration would represent that found within the cell.

The retention study results compared to results from the dissolution assay to assess chemical stability in the long term highlights that there are likely to be mechanisms

at play within the cell which decrease the rate of SPION core degradation. Such mechanisms are likely to be caused by the compacted environment of the SPIONs within the endosome/lysosome. Here, there is likely to be a decrease in surface area for acidic protons to reach all of the compacted SPIONs in the centre of the endosome/lysosome. Another mechanism could be that extra layers of polymer around the compacted SPIONs may be created from SPIONs which have degraded on the outer surface within the endosome leaving only the polymer shell. In addition, any proteins present within the endosomes containing SPIONs may become protonated with acidic protons thus acting as a buffer or scavenger and slowing down the drop in pH environment.

6.2.3 Conclusions: pMPC coated SPIONs

Cell uptake of $pMPC_{29}$-SPIONs was achieved as confirmed by Prussian blue staining within KSCs as visualised by optical microscopy. The level of uptake of KSCs exposed to MIRB compared to $pMPC_{29}$-SPIONs was noticeably higher which was observed by the intensity levels of blue staining. The level of uptake was also confirmed by CTV magnetophoresis measurements of labelled cells and determining the amount of intracellular iron content. A summary of all the CTV measurements are outlined in **Table 6.1** which highlights the level of NP uptake of cells exposed to MIRB was around twice as high compared to cells exposed to $pMPC_{29}$-SPIONs.

Table 6.2. Summary of average magnetic velocities of KSCs exposed to $pMPC_{29}$SPIONs compared with MIRB.

Sample	Stem Cell Line	NP Concentration (μg Fe mL^{-1})	Average Magnetic Velocity (μm s^{-1})	Mean m_{Fe} (pg)
MIRB	KSC	1	43 ± 25	1.0 ± 0.6
$pMPC_{29}$-SPIONs	KSC	1	12 ± 6	0.4 ± 0.2
MIRB	KSC	5	93 ± 50	3.1 ± 1.7
$pMPC_{29}$-SPIONs	KSC	5	56 ± 35	1.8 ± 1.0

Photothermal images of both SPION samples also showed differences in the level of intensity which again confirmed a difference in the level of uptake. TEM images of stem cells exposed to $pMPC_{29}$-SPIONs confirmed the internalisation NPs *via* the

endosome through endocytosis. The chemical stability of $pMPC_{29}$-SPIONs was investigated by a retention study with KSCs over a period of 14 days. The results showed that $pMPC_{29}$-SPIONs cores did not degrade as fast as initially predicted by the dissolution assay carried out in Chapter 3 and that the chemical stability results of $pMPC_{29}$-SPIONs found from the retention study show $pMPC_{29}$-SPIONs cores last for at least 14 days.

6.2.4 Stem cell labelling studies using silica coated γFe_2O_3 and Fe_3O_4 SPIONs

In Chapter 4, silica coated γFe_2O_3 and silica coated Fe_3O_4 SPIONs were prepared and their suitability as a contrast labelling agent for bioapplication was studied and evaluated prior to cell uptake studies with MSC and KSC lines. To prepare silica coated γFe_2O_3 and silica coated Fe_3O_4 SPIONs for cell uptake, KSCs and MSCs were exposed to cell culture medium containing NP concentrations of 5 and 25 μg Fe mL^{-1} and incubated for a period of 24 hours.[11] After this period, cells were washed and fixed.

Optical microscopy images were captured of MSCs and KSCs exposed to SiO_2 coated γFe_2O_3 SPIONs at NP labelling concentration of 25 μg Fe mL^{-1}, **Figure 6.11C**. For the visualisation uptake of SPIONs within cells, iron oxide cores within cells were stained using Prussian blue. From the images, compared to cells labelled with MICB, no staining of the iron oxide cores was found for cells exposed to SiO_2 coated γFe_2O_3 SPIONs as indicated by the lack of Prussian blue staining and thus suggested either a very low uptake was obtained or that the silica shell may have protected the Prussian blue reaching the iron oxide core.

To determine whether a very low uptake of SiO_2 coated SPIONs with MSCs exposed to NP concentration of 25 μg Fe mL^{-1} was obtained, CTV measurements were carried out. CTV measurements were also carried out on MSCs exposed to SiO_2 coated SPIONs with a NP concentration of 5 μg Fe mL^{-1}, **Figure 6.12**. The CTV results showed that the intracellular iron uptake of SiO_2 coated γFe_2O_3 and SiO_2 coated Fe_3O_4 SPIONs exposed to 5 and 25 μg Fe mL^{-1} were 0.9 ± 0.8 pg to 5.4 ± 3.1 pg and 1.6 ± 1.6 pg to 5.2 ± 3.0 pg respectively, **Figure 6.12**. At cell labelling concentrations of 5 and 25 μg Fe mL^{-1}, the CTV results showed a 6 fold increase in

uptake for SiO_2 coated γFe_2O_3 SPIONs and a 3 fold increase in uptake for SiO_2 coated Fe_3O_4 SPIONs compared to MICB, the intracellular iron uptake was found at 5.7 ± 3.6 pg to 8.7 ± 6.4 pg, which gave a 1.5 fold increase in uptake.

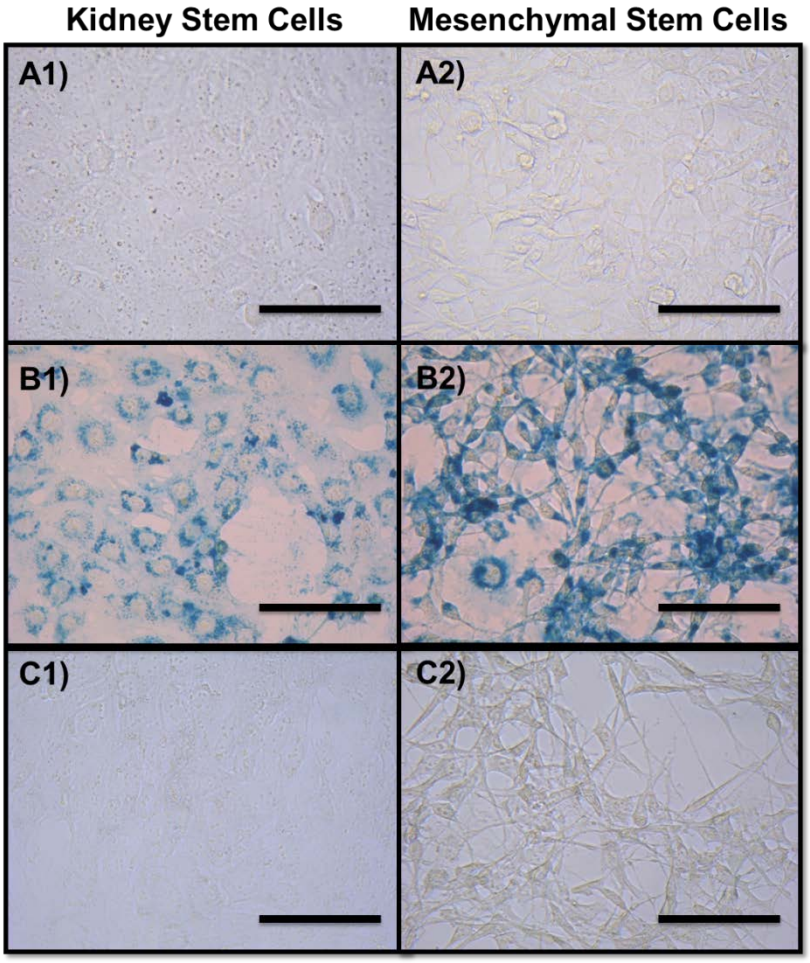

Figure 6.11. Optical microscopy images of stem cell lines which have undertaken 24 hour exposure of 25 μg Fe mL^{-1} of B) MICB with Prussian blue stain and C) SiO_2 coated γFe_2O_3 SPIONs with Prussian blue stain. A) Shows stem cells not exposed to NPs. Scale bar 100 μm. Cells were stained with the Iron Stain Kit (Sigma Aldrich), which consists of a Prussian Blue staining for iron deposits.

Earlier in the Chapter, MICB was found to give higher levels of uptake compared to MIRB which was used as a control for cell labelling studies using $pMPC_{29}$-SPIONs. As a reminder, for the uptake of MSCs exposed to a NP concentration of MIRB of 25 μg Fe mL^{-1}, an average intracellular iron uptake of 5.0 ± 3.0 pg was obtained. Compared to SiO_2 coated γFe_2O_3 and SiO_2 coated Fe_3O_4, SPIONs exposed to the same NP concentration of 25 μg Fe mL^{-1}, the intracellular iron uptake results are slightly higher and thus confirms that the silica shell prevented Prussian blue staining

of the SPION cores which is used to visualise cell uptake by optical microscopy, **Table 6.3** and **Figure 6.11C**.

Table 6.3. Average magnetic velocities of MSCs exposed to 25 µg Fe mL^{-1} silica coated SPIONs compared with Molday Ion samples.

Sample	Stem Cell Line	NP Concentration (µg Fe mL^{-1})	Average Magnetic Velocity (µm s^{-1})	Mean m_{Fe} (pg)
MIRB	MSC	25	145 ± 80	5.0 ± 3.0
MICB	MSC	25	270 ± 200	8.7 ± 6.4
MIEG	MSC	25	130 ± 60	4.1 ± 2.0
SiO_2-Fe_3O_4	MSC	25	130 ± 75	5.2 ± 3.0
SiO_2-γFe_2O_3	MSC	25	101 ± 60	5.4 ± 3.1

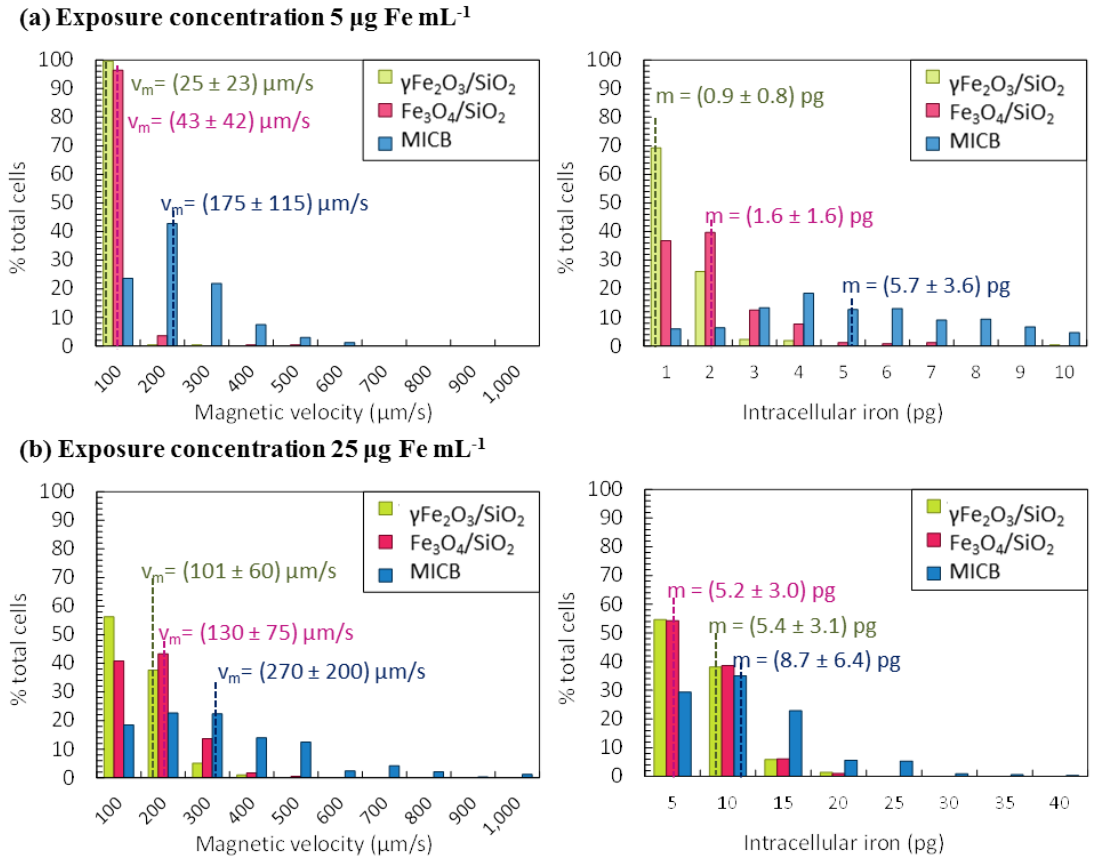

Figure 6.12. Magnetic velocity histograms (top left and bottom left) and mean m_{Fe} per MSC (top right and bottom right) exposed to (a) 5 µg Fe mL^{-1} and (b) 25 µg Fe mL^{-1} of SiO_2 coated γFe_2O_3, SiO_2 coated Fe_3O_4 and MICB SPIONs as measured by single cell magnetophoresis in 30% glycerol. The mean and standard deviation of each condition is indicated. For each condition, a minimum of 300 cells were imaged over a minimum of 3 different image acquisitions.

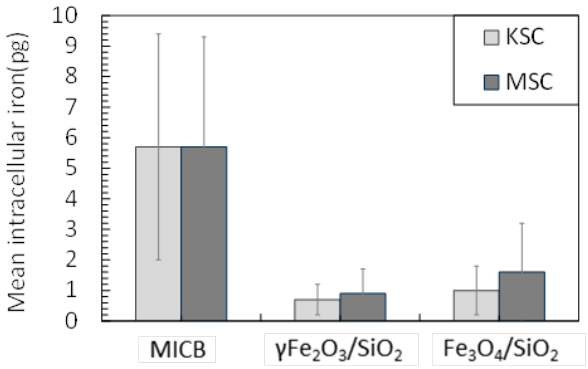

Figure 6.13. Comparison of the mean m_{Fe} per KSC and MSC exposed to 5µg Fe mL^{-1} of MICB SPIONs to SiO_2-γFe_2O_3 and SiO_2-Fe_3O_4 SPIONs. For each condition, the magnetic velocity of at least 800 cells were imaged over at least 3 different acquisitions. Error bars correspond to standard deviation of the population.

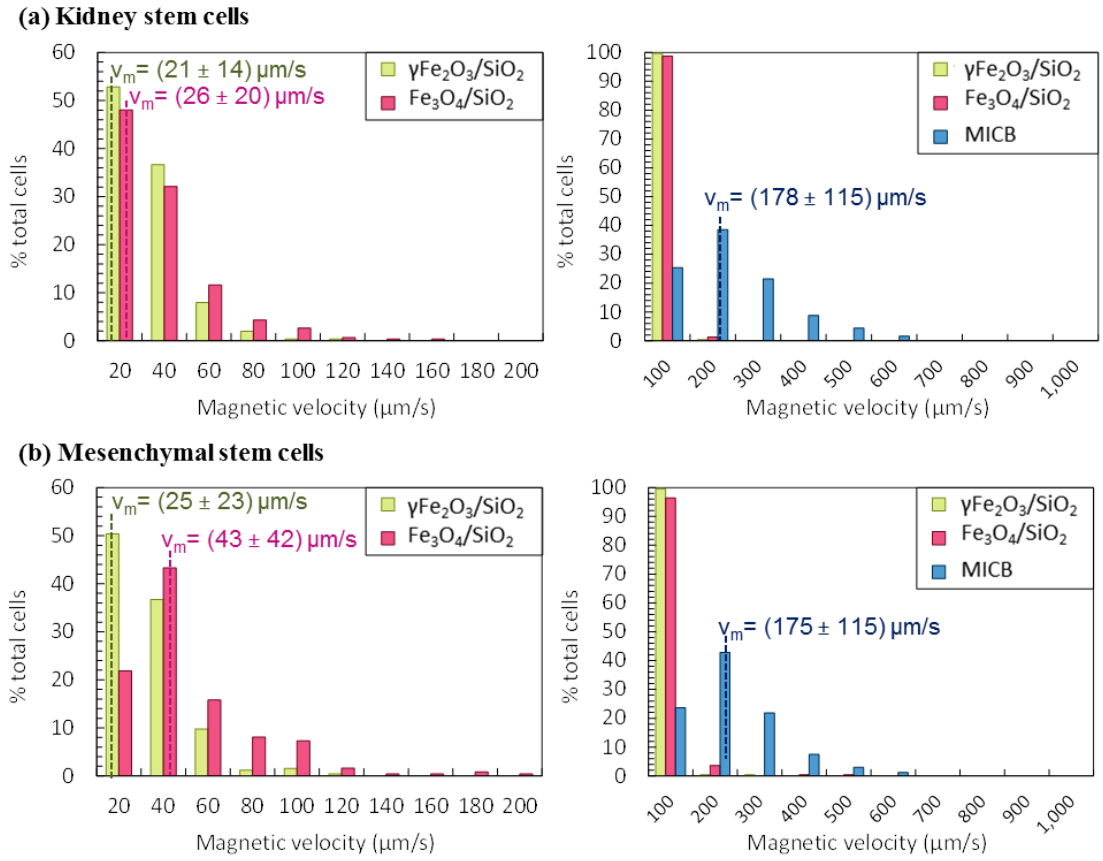

Figure 6.14. Magnetic velocity (υ_m) histograms (top left and bottom left) and mean m_{Fe} (top right and bottom right) for (a) KSCs and (b) MSCs exposed to 5 µg Fe mL^{-1} of SiO_2 coated γFe_2O_3, SiO_2 coated Fe_3O_4 and MICB SPIONs as measured by single cell magnetophoresis in 30% glycerol. The mean and standard deviation of each condition is indicated. For each condition, a minimum of 300 cells were imaged over a minimum of 3 different image acquisitions.

This means that optical microscopy would not be a reliable technique to assess cells for uptake with silica coated SPIONs and that other microscopy methods such as TEM and photo thermal microscopy would be required. To see if there were any differences in uptake between MSCs and KSCs**,** CTV measurements were carried out on MSCs and KSCs exposed to 5 μg Fe mL^{-1} of SiO_2 coated γFe_2O_3, SiO_2 coated Fe_3O_4 and MICB SPIONs, **Figure 6.13** and **Figure 6.14**.

The CTV results determined the intracellular iron uptake of SiO_2 coated γFe_2O_3 and SiO_2 coated Fe_3O_4 SPIONs exposed to MSCs and KSCs at a NP concentration of 5 μg Fe mL^{-1} and showed that with MSCs the uptake was slightly higher than that observed with KSCs however the level of uptake with MSCs and KSCs was significantly lower than MSCs and KSCs exposed to MICB. The differences in uptake were also highlighted by the average magnetic velocity measurements from which the mean intracellular iron content was calculated, **Figure 6.14**.

6.2.5 Conclusions: Silica coated γFe_2O_3 and Fe_3O_4 SPIONs

Optical microscopy images of MSCs exposed to silica coated γFe_2O_3 SPIONs at NP cell labelling concentration of 25 μg Fe mL^{-1} showed no Prussian blue staining which from CTV measurements, confirmed uptake had actually occurred and that staining with Prussian blue was unsuccessful. This finding suggested the SPION cores were shielded by the silica coating and prevented them from being stained.

MSCs and KSCs exposed to silica coated γFe_2O_3 and Fe_3O_4 SPIONs at cell labelling concentrations of 5 μg Fe mL^{-1} showed very low levels of NP cell uptake which was confirmed by magnetic velocity measurements from CTV when compared to MICB. However, upon increase of the NP cell labelling concentration to 25 μg Fe mL^{-1} a 6 fold increase in uptake for silica coated γFe_2O_3 SPIONs and a 3 fold increase in uptake for silica coated Fe_3O_4 SPIONs was observed when compared with MSCs exposed to MICB which showed a 1.5 fold increase in NP cell uptake. A summary of all the CTV measurements are outlined in **Table 6.4** which highlights that MSCs and KSCs exposed to silica coated γFe_2O_3 and Fe_3O_4 SPIONs at cell labelling concentrations of 25 μg Fe mL^{-1} provide slightly higher levels of uptake when compared to MSCs exposed to MIRB at the same labelling concentration.

Table 6.4. Summary of average magnetic velocities of stem cell lines exposed to silica coated SPIONs compared with Molday Ion samples.

Sample	Stem Cell Line	NP Concentration (μg Fe mL^{-1})	Average Magnetic Velocity (μm s^{-1})	Mean m_{Fe} (pg)
MIRB	KSC	5	93 ± 50	3.1 ± 1.7
MICB	KSC	5	178 ± 115	5.6 ± 4.0
SiO_2-Fe_3O_4	KSC	5	26 ± 20	1.2 ± 0.5
SiO_2-γFe_2O_3	KSC	5	21 ± 14	0.5 ± 0.6
MICB	MSC	5	175 ± 115	5.7 ± 3.6
SiO_2-Fe_3O_4	MSC	5	43 ± 42	1.6 ± 1.6
SiO_2-γFe_2O_3	MSC	5	25 ± 23	0.9 ± 0.8
MIRB	MSC	25	145 ± 80	5.0 ± 3.0
MICB	MSC	25	270 ± 200	8.7 ± 6.4
MIEG	MSC	25	130 ± 60	4.1 ± 2.0
SiO_2-Fe_3O_4	MSC	25	130 ± 75	5.2 ± 3.0
SiO_2-γFe_2O_3	MSC	25	101 ± 60	5.4 ± 3.1

Overall, at low cell labelling concentrations used, a low NP uptake of silica coated SPIONs was observed. This could be due to silica's highly negative surface charge as confirmed by zeta potential measurement for SiO_2-Fe_2O_3 and SiO_2-Fe_3O_4 SPIONs which may have reduced NP interactions with the membrane of the cell. This is likely to occur through electrostatic repulsion with the membrane of the cell which has an overall net negative surface charge.[7]

6.2.6 Stem Cell Labelling Studies using Gold SPIONs

In Chapter 5, gold reacted amino silane functionalised SPIONs (Au-SPIONs) were prepared and their suitability as a contrast labelling agent for bioapplication was studied and evaluated prior to cell uptake studies with MSCs and KSC lines. Two generations of Au-SPIONs were prepared containing two different amounts of reacted gold in order to simplify the sample preparation of a 1 mg Fe mL^{-1} stock solution for use in biological studies.

6.2.6.1 First Generation Gold SPIONs

To prepare $pMPC_{135}$-Au-SPIONs for cell uptake, KSCs and MSCs were exposed to cell culture medium containing a NP concentration of 25 µg Fe mL^{-1} and incubated for a period of 24 hours.[11] After this period, cells were washed, fixed and the uptake was assessed by optical microscopy, **Figure 6.16**. Prussian blue and silver staining was used to stain iron oxide and gold respectively, **Figure 6.16C and D**.

Due to the nature of the purple colour of the Au-SPION sample, the Prussian blue staining used to highlight uncoated residual iron oxide was difficult to distinguish from the purple colour obtained from the gold in the sample. The silver stain used on stem cells compared to stem cells stained with Prussian blue appeared darker in colour and therefore confirmed the presence of gold within the cells surrounding cell nuclei. Overall, both staining methods confirmed uptake of Au-SPIONs within cells.

A photograph of KSCs and MSCs in their culture dishes after exposure to 25 µg Fe mL^{-1} of $pMPC_{135}$ coated Au-SPIONs (no staining used), **Figure 6.15**, show that uptake could clearly be seen after washing cells due to the nature of the purple colour from Au-SPIONs.

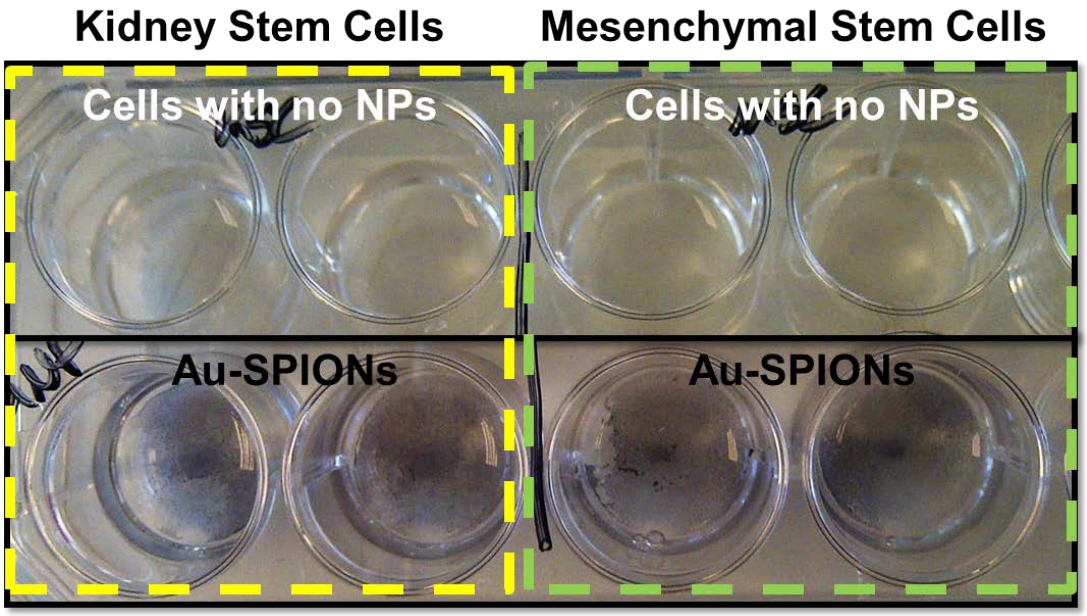

Figure 6.15. Photograph of cell culture dishes containing cell lines exposed to 25 µg Fe mL^{-1} $pMPC_{135}$ coated Au-SPIONs with no staining. Exposure for 24 hour at 37 °C.

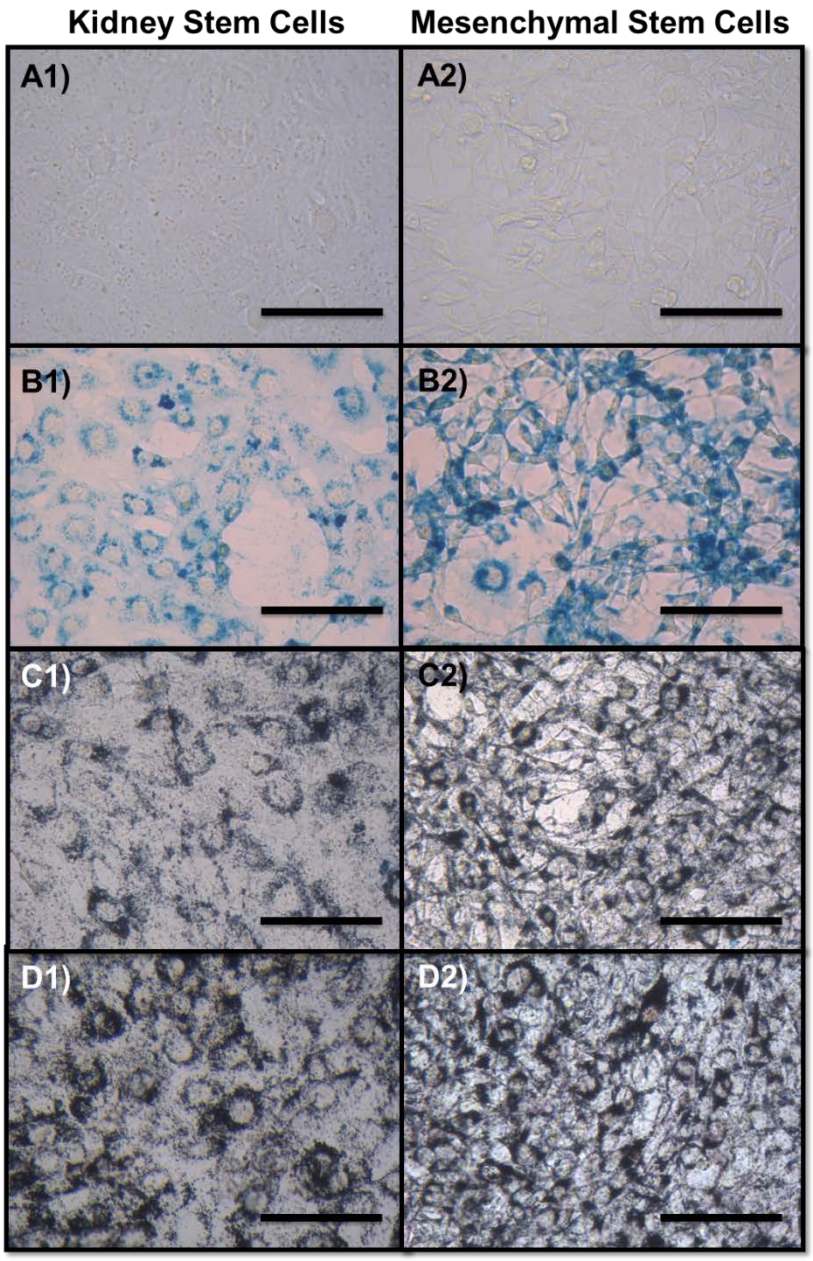

Figure 6.16. Optical microscopy images of stem cell lines. Images 1 are KSCs and images 2 are MSCs. A) Stem cells not exposed to NPs. B) to D) cell lines exposed for 24 hours to 25 µg Fe mL^{-1} of B) MICB stained with Prussian blue, C) and D) first generation $pMPC_{135}$ coated Au-SPIONs stained with Prussian blue and silver respectively. Scale bar 100 µm.

6.2.6.2 Second generation gold SPIONs

In the second half of Chapter 5, a second generation of gold SPIONs was prepared in order to produce Au-SPIONs that contained less gold and thus simplify the sample preparation of a 1 mg Fe mL^{-1} stock solution for stem cell labelling experiments. The second generation Au-SPIONs did not require thiol functionalised pMPC polymer

for colloidal stabilisation upon storage since the second generation Au-SPIONs were found to be stable in a 30 % ethanol solution. To prepare Au-SPIONs for cell uptake, MSCs were exposed to cell culture medium containing a NP concentration of 25 µg Fe mL^{-1} and incubated for a period of 24 hours.[11] After this period, cells were washed, fixed and NP uptake was assessed and visualised *via* phase contrast optical microscopy and compared to MSCs exposed to MICB, **Figure 6.17**.

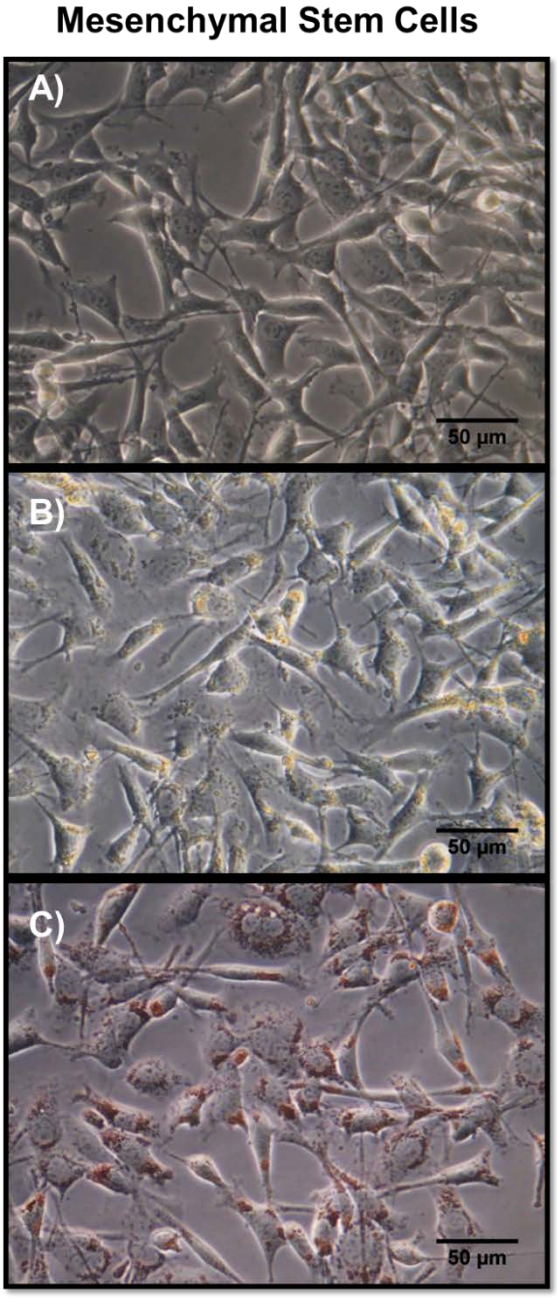

Figure 6.17. Optical microscopy *via* phase contrast images of MSCs. A) MSCs not exposed to NPs. MSCs exposed for 24 hours to 25 µg Fe mL^{-1} of B) MICB and C) second generation Au-SPIONs.

Optical microscopy *via* phase contrast images allowed the visualisation of dead cells as observed by the lighter spherical MSCs when compared against living MSCs not exposed to NPs, **Figure 6.17A**. **Figure 6.17B and C** show MSCs exposed to MICB and second generation Au-SPIONs respectively. For MSCs exposed to MICB, image B, orange areas found within MSCs highlight the intracellular uptake and localisation of MICB SPIONs. For MSCs exposed to second generation Au-SPIONs, image C, red areas were found within MSCs were clearly observed and confirmed uptake of the Au-SPION sample within stem cells.

Images of MSCs which were not stained captured by bright field optical microscopy prior to photothermal imaging also show clearly pink areas contained within the cells which is characteristic of the colour of the Au-SPIONs, **Figure 6.18**. Comparing the phase contrast image of MSCs with those under bright field, **Figure 6.17** and **Figure 6.18** respectively, it appears that cells have a different shape and this is simply due to the type of imaging method used. Phase contrast shows many more cellular structures and features that cannot be observed *via* bright field optical microscopy. In addition, the images taken under bright field view show less features at double the magnification. The nuclei and Au-SPIONs (pink areas) can be seen very well under bright field however the cytoplasm is not clearly observed. The cell in the top of the left image of **Figure 6.18** shows a shape that is comparable to those observed *via* phase contrast. Cells were fixed prior to imaging and thus were not biologically active so could not have changed shape/feature between imaging techniques.

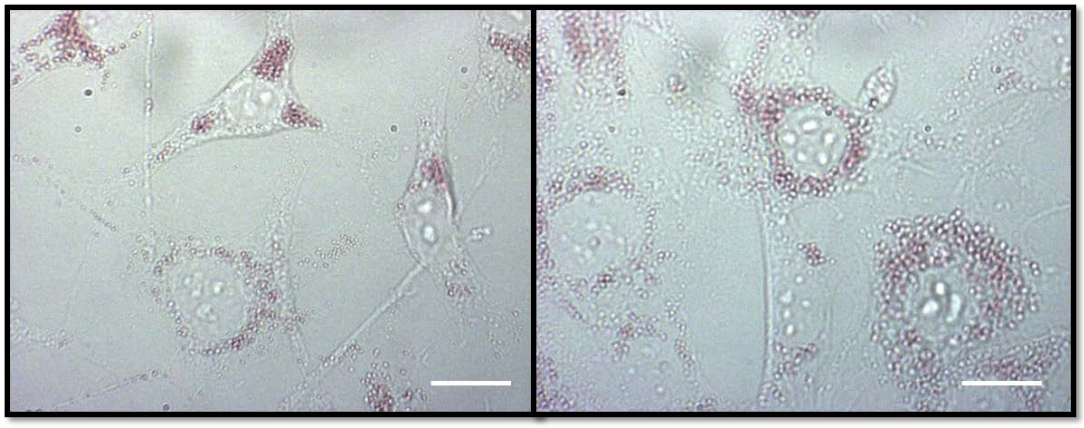

Figure 6.18. Example bright field microscopy images of MSCs exposed to 25 µg Fe mL^{-1} of Au-SPIONs for 24 hours captured using a Thor Labs colour CCD camera. Scale bar left 50 µm, scale bar right 25 µm.

Unstained TEM images, **Figure 6.19**, confirmed uptake of Au-SPIONs by endocytosis. Au-SPIONs were found to be contained within endosomes of the MSC as indicated by the clustered areas of dark and light NPs. Darker NPs were likely to be NPs containing gold, and lighter NPs were likely to be unreacted amino silane coated SPIONs (A-SPIONs) not containing any gold. As observed previously in this Chapter for the unstained TEM images seen for pMPC-SPION labelled cells, the TEM images labelled with Au-SPIONs **Figure 6.19** (top left picture) show broken areas of NP clusters. The endosomes for cells labelled with Au-SPIONs compared to pMPC-SPIONs appear to be severely broken which may be due to an increase in contrast under the TEM by visualising gold when compared with iron oxide which is less electron dense. The severely broken areas could also suggest Au-SPIONs are present in the cytoplasm of the cell and caused by endosomal escape.[20] Another possibility could be that the level of uptake is lower than that observed with pMPC-SPION labelled cells.

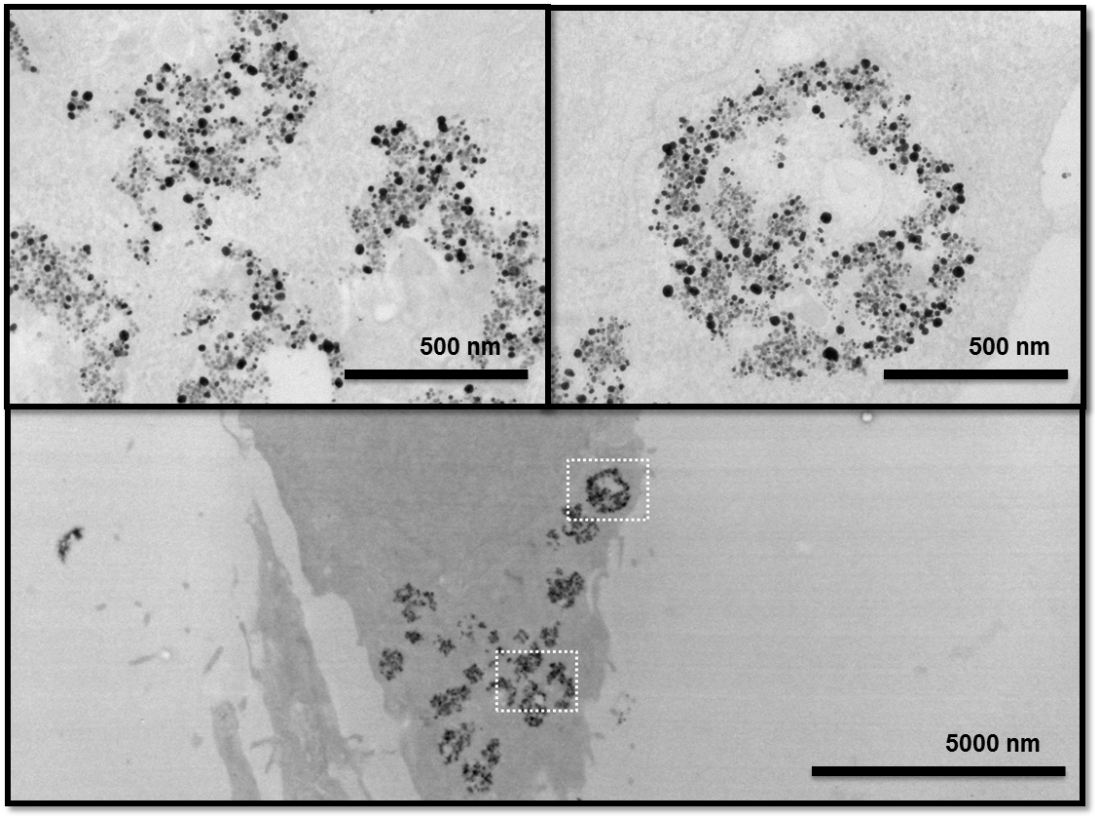

Figure 6.19. Example TEM images of MSCs exposed to second generation Au-SPIONs.

Uptake of Au-SPIONs *via* endocytosis within MSCs was also confirmed using bright field optical, fluorescence and photothermal microscopy, **Figure 6.20**, where the

same area was imaged and overlaid to understand areas of uptake within the cell. Fluorescent dyes were used to highlight cell nuclei (blue, stained with DAPI) and lysosomes (green). By overlaying the green fluorescent image (indicating lysosomes contained within the cells, **Figure 6.20 K and L**) with the red photothermal image (location of Au-SPIONs, **Figure 6.20 O and P**), **Figure 6.20 S and T**, uptake and localisation of Au-SPIONs within lysosomes was confirmed by overlap of the coloured images. The brightness and contrast settings were lowered, **images L, P and T Figure 6.20**, to demonstrate quenching/ photo bleaching of the dye as observed by low intensity green fluorescence seen in image K. By lowering the brightness and contrast settings, an increased intensity of green fluorescence was observed in image L which demonstrated quenching/photo bleaching had occurred in image K. Photo bleaching of the fluorescence signal after photothermal scanning is

due to the proximity of peak excitation wavelength of the fluorophore to the heating laser (555 nm and 523 nm respectively, see Photothermal experimental details in Chapter 2). The reason why this was observed for images containing Au-SPIONs and not for those containing MICB is due to interference with Au-SPIONs within the lysosomes, since the peak absorbance wavelength of Au-SPIONs measured by UV-Vis was found at 525-530 nm.

Magnetic velocity measurements were carried out to assess the level uptake of Au-SPIONs with MSCs. Here, MSCs were exposed to three different Au-SPION concentrations of 25, 50 and 100 µg Fe mL^{-1}, **Figure 6.21**. The results showed MSCs exposed to Au-SPION concentrations of 50 µg Fe mL^{-1} provided the highest mean magnetic velocity of 170 ± 90 µm s^{-1} with a mean intracellular iron content of 5.6 ± 3.7 pg and thus indicated the highest level of uptake at this NP concentration. At a higher NP concentration of 100 µg Fe mL^{-1}, a mean magnetic velocity of 155 ± 82 µm s^{-1} was obtained with a mean intracellular iron content of 5.1 ± 3.5 pg, suggesting MSCs are saturated with Au-SPIONs past a NP concentration of 50 µg Fe mL^{-1}. At lower Au-SPION concentration, a lower mean magnetic velocity of 120 ± 70 µm s^{-1} was obtained with a mean intracellular iron content of 4.0 ± 3.0 pg as expected since MSCs were exposed to a lower Au-SPION concentration.

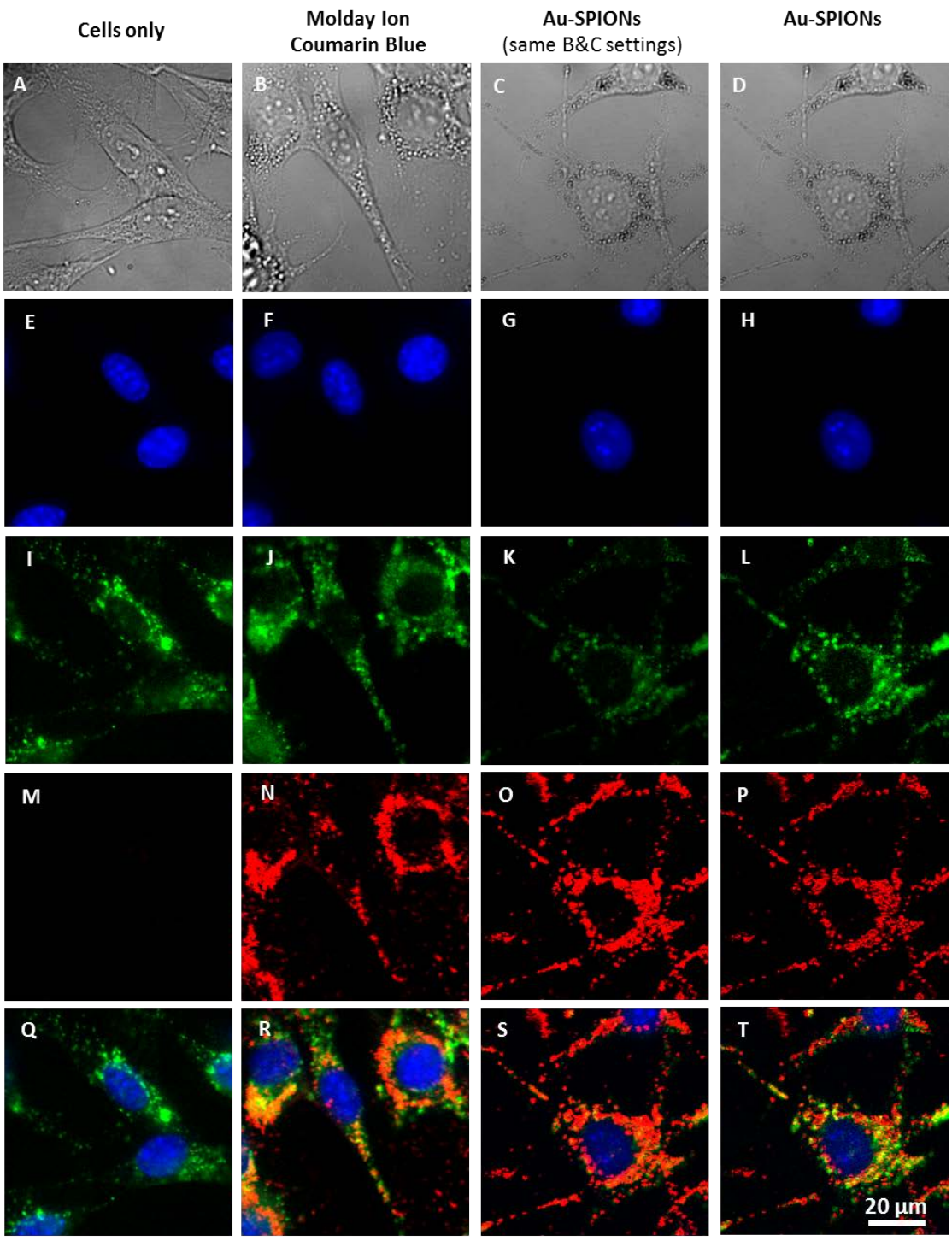

Figure 6.20. Comparison of bright field imaging (A-D), fluorescent stain of nuclei (DAPI) (E-H), fluorescent stain of lysosomes (I-L), photothermal microscopy (M-P) and overlays (Q-T) of MSCs only and cells exposed to 25 µg Fe mL^{-1} of MICB and Au-SPIONs for 24 hours. All fluorescence and photothermal images are presented in false colours using the same brightness and contrast settings apart from images D, H, L, P and T which used lower brightness and contrast settings to demonstrate fluorescence quenching within lysosomes.

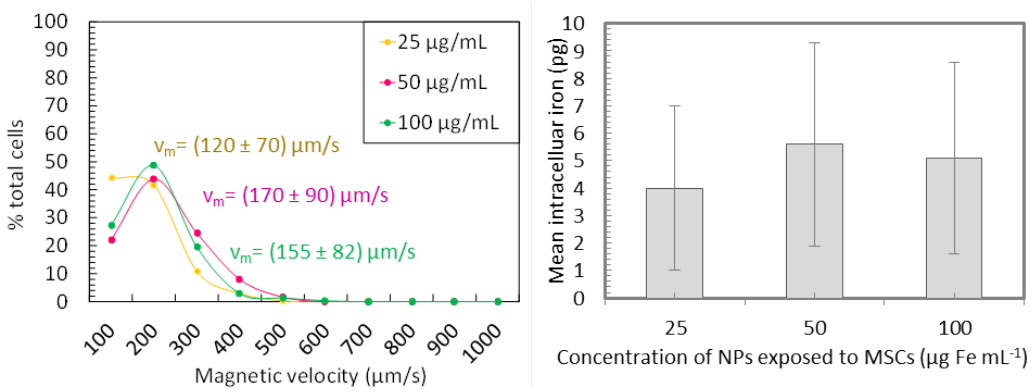

Figure 6.21. Magnetic velocity (υ_m) histogram (left) and mean intracellular iron (right) of MSCs following a 24 hour exposure period to three different NP concentrations (25, 50 and 100 µg Fe mL^{-1}) of Au-SPIONs as measured by single cell magnetophoresis. For each condition, the magnetic velocity was measured for cells suspended in 30% glycerol. A minimum of 400 cells were imaged over a minimum of 3 different image acquisitions.

6.3 Conclusions: Au-SPIONs

Optical microscopy images under bright field view of MSCs exposed to first generation Au-SPIONs at NP cell labelling concentration of 25 µg Fe mL^{-1} confirmed uptake using Prussian blue and silver staining methods. Optical microscopy images *via* phase contrast of MSCs exposed to second generation Au-SPIONs at NP cell labelling concentration of 25 µg Fe mL^{-1} allowed the visualisation of uptake without the use of a stain and confirmed uptake of second generation Au-SPIONs within cells. Uptake of second generation Au-SPIONs could also be clearly observed under bright field optical microscopy as shown by pink areas within cells. TEM confirmed the internalisation route into MSCs occurred *via* the endosome through endocytosis and was also confirmed by photothermal and fluorescent imaging by overlaying fluorescent stained lysosome images with photothermal images. CTV showed the intracellular iron uptake level of second generation Au-SPIONs with MSCs at NP concentration of 25 µg Fe mL^{-1} to be comparable with those found using MIEG. The CTV data has been summarised in **Table 6.5**. The CTV results show that a NP labelling concentration of 50 µg Fe mL^{-1} provides the highest intracellular iron content before the MSC is likely to become saturated.

Table 6.5. Summary of average magnetic velocities of MSCs exposed to Au-SPIONs compared with Molday Ion samples.

Sample	Stem Cell Line	NP Concentration (μg Fe mL^{-1})	Average Magnetic Velocity (μm s^{-1})	Mean m_{Fe} (pg)
MIRB	MSC	25	145 ± 80	5.0 ± 3.0
MICB	MSC	25	270 ± 200	8.7 ± 6.4
MIEG	MSC	25	130 ± 60	4.1 ± 2.0
Au-SPIONs (2nd Gen)	MSC	25	120 ± 70	4.0 ± 3.0
Au-SPIONs (2nd Gen)	MSC	50	170 ± 90	5.6 ± 3.7
Au-SPIONs (2nd Gen)	MSC	100	155 ± 82	5.1 ± 3.5

6.4 Conclusions: Overall

The overall outlook of the project and whether the goal of long-term stem cell labelling can be achieved will be discussed in depth in the Conclusions, Chapter 7. In summary here, subtle differences in cell uptake have been best observed at low cell labelling concentrations (1- 5 μg Fe mL^{-1}) and provided information on the surface interactions of NP coatings prepared in this thesis with the membrane of the stem cell, **Table 6.6**. At higher cell labelling concentrations (25 - 100 μg Fe mL^{-1}) the intracellular iron content appears comparable to commercial contrast agents MIRB and MIEG with the exception of MICB which provides higher uptake, **Table 6.6**. TEM and photothermal microscopy confirm the internalisation route of most NPs used in this Thesis *via* the endosome through endocytosis. The retention study has shown that the chemical based dissolution assay used to test NPs for long term chemical stability does not provide a realistic modal of conditions found within the endosome and lysosome of the stem cell. Improvements to such dissolution assay are required if a realistic result is to be obtained and so the retention study using cells at present seems to be the best way to measure this. The dissolution assay however can be one way to easily measure differences in chemical stability if developing a 'bullet proof' chemically stable coating.

Table 6.6. Summary of average magnetic velocities of stem cell lines exposed to all SPIONs covered in this Chapter.

Sample	Stem Cell Line	NP Concentration (μg Fe mL^{-1})	Average Magnetic Velocity (μm s^{-1})	Mean m_{Fe} (pg)
MIRB	KSC	1	43 ± 25	1.0 ± 0.6
$pMPC_{29}$-SPIONs	KSC	1	12 ± 6	0.4 ± 0.2
$pMPC_{29}$-SPIONs	KSC	5	56 ± 35	1.8 ± 1.0
MIRB	KSC	5	93 ± 50	3.1 ± 1.7
MICB	KSC	5	178 ± 115	5.6 ± 4.0
SiO_2-Fe_3O_4	KSC	5	26 ± 20	1.2 ± 0.5
SiO_2-γFe_2O_3	KSC	5	21 ± 14	0.5 ± 0.6
MICB	MSC	5	175 ± 115	5.7 ± 3.6
SiO_2-Fe_3O_4	MSC	5	43 ± 42	1.6 ± 1.6
SiO_2-γFe_2O_3	MSC	5	25 ± 23	0.9 ± 0.8
MIRB	MSC	25	145 ± 80	5.0 ± 3.0
MICB	MSC	25	270 ± 200	8.7 ± 6.4
MIEG	MSC	25	130 ± 60	4.1 ± 2.0
SiO_2-Fe_3O_4	MSC	25	130 ± 75	5.2 ± 3.0
SiO_2-γFe_2O_3	MSC	25	101 ± 60	5.4 ± 3.1
Au-SPIONs (2nd Gen)	MSC	25	120 ± 70	4.0 ± 3.0
Au-SPIONs (2nd Gen)	MSC	50	170 ± 90	5.6 ± 3.7
Au-SPIONs (2nd Gen)	MSC	100	155 ± 82	5.1 ± 3.5

6.5 References

1. G. J. Doherty and H. T. McMahon, *Annu. Rev. Biochem.*, 2009, **78**, 857-902.
2. S. D. Conner and S. L. Schmid, *Nature*, 2003, **422**, 37-44.
3. M. R. Lorenz, V. Holzapfel, A. Musyanovych, *et al.*, *Biomaterials*, 2006, **27**, 2820-2828.
4. B. D. Chithrani, A. A. Ghazani and W. C. W. Chan, *Nano Lett.*, 2006, **6**, 662-668.
5. W. L. Langston Suen and Y. Chau, *J. Pharm. Pharmacol.*, 2014, **66**, 564-573.

6. S. A. Coulman, A. Anstey, C. Gateley, *et al.*, *Int. J. Pharm.*, 2009, **366**, 190-200.
7. Y. Ge, Y. Zhang, J. Xia, *et al.*, *Colloids Surf. B.*, 2009, **73**, 294-301.
8. T. Yeung, G. E. Gilbert, J. Shi, *et al.*, *Science*, 2008, **319**, 210-213.
9. T. F. Vandamme and L. Brobeck, *J. Control Release*, 2005, **102**, 23-38.
10. J. J. Chalmers, Y. Zhao, M. Nakamura, *et al.*, *J. Magn. Magn. Mater.*, 1999, **194**, 231-241.
11. C. F. Mora, E. Ranghini, S. Bruno, *et al.*, *Stem Cells Dev*, 2012, **21**, 296-307.
12. http://www.biopal.com/molday-ion.htm
13. S. Li and L. Huang, *J. Control. Release*, 2010, **145**, 178-181.
14. http://www.biopal.com/pdf-downloads/price-list/mri-price-list.pdf
15. T. Skotland, P. C. Sontum and I. Oulie, *J Pharmaceut Biomed*, 2002, **28**, 323-329.
16. A. S. Arbab, L. B. Wilson, P. Ashari, *et al.*, *NMR Biomed.*, 2005, **18**, 383-389.
17. S. J. H. Soenen, U. Himmelreich, N. Nuytten, *et al.*, *Small*, 2010, **6**, 2136–2145.
18. L. Michael, L. Florence, M. Valentin-Adrian, *et al.*, *Nanotechnology*, 2010, **21**, 395103.
19. M. Lévy, F. Lagarde, V. Maraloiu, *et al.*, *Nanotechnology*, 2010, **21**, 395103.
20. Ž. Krpetić, P. Nativo, V. Sée, *et al.*, *Nano Lett.*, 2010, **10**, 4549-4554.

7

Conclusions and Outlook

List of Figures

Figure 7.1. Dissolution assay comparing all SPIONs prepared in this Thesis exposed to pH 4.5 citrate buffer solution at 37 °C. 270

List of Tables

Table 7.1. Summary of relaxivity for all SPIONs prepared in this Thesis in addition to commercial contrast agents Endorem and MIRB. 269
Table 7.2. Summary of average magnetic velocities and the mean intracellular iron content of stem cell lines exposed to all SPIONs covered in this Chapter. 269

7.1 Conclusions

The aim of this project was to develop iron oxide based superparamagnetic magnetic resonance imaging (MRI) contrast agents with a biocompatible surface coating to allow easy stem cell labelling capability *in vitro*. The location of stem cells administered *in vivo* to patients would be closely monitored/tracked *via* MRI in order to help understand the fate and behaviour of stem cells long-term and ensure patients remain healthy and safe during the course of the stem cell therapy treatment. Throughout the development process of bionanomaterials prepared in this Thesis, several obstacles have arisen. The main obstacle has been achieving good chemical stability of coatings developed onto the surface of superparamgnetic iron oxide nanoparticle (SPION) cores that readily dissolve and degrade in acidic environments typically found within the endosome/lysosome of a stem cell. Without the SPIONs, there is no MRI contrast signal to image stem cells long-term. The importance of obtaining a chemically stable SPION surface coating was first highlighted in the initial stages of this project (Chapter 3) whereby polymer coatings were first prepared and screened.

7.1.1 Chapter 3

In Chapter 3, well-defined biocompatible poly (2-methyacryloyloxyethyl phosphorylcholine) (pMPC) homopolymers were prepared by atom transfer radical

polymerisation (ATRP) and screened for the colloidal stabilisation of amino silane functional superparamagnetic iron oxide nanoparticles (A-SPIONs) in physiological buffer solution at 25 and 37 °C. Well defined *N*-succinimidyl functional pMPC homopolymers with a degree of polymerisation (DP_n) 29 or M_n ~9,000 g mol^{-1} was found to be a suitable polymer for the covalent grafting to A-SPIONs and provided good colloidal stability in PBS at 37 °C for more than 48 hours and up to 7 days with cell labelling concentrations of 187 μg Fe mL^{-1} and 53 μg Fe mL^{-1} respectively. PolyMPC$_{29}$ coated SPIONs (pMPC$_{29}$-SPIONs) showed good biocompatibility and low cytotoxicity with stem cells which confirmed the suitability of pMPC as a surface coating for SPIONs for potential cell labelling. Further pre-biological studies showed pMPC$_{29}$-SPIONs had a good relaxivity (R_2) which was found to be higher than the commercially available contrast agent Molday Ion Rhodamine B (MIRB).

PolyMPC$_{29}$-SPIONs provided a good magnetisation saturation value (M_s). The chemical stability of polyMPC$_{29}$-SPIONs were measured in citrate buffers at pH 7.4 to 4.5 incubated at 37 °C in order to mimic the endosomal and lysosomal environments inside a stem cell. The dissolution assay showed that the SPION cores rapidly digested at pH 4.5 within a period of 5 days. The rapid dissolution of the SPION core of pMPC$_{29}$-SPIONs thus indicates that the MRI signal will rapidly be lost with time and therefore indicates that further improvements of the SPION coating is required in order to achieve SPIONs for long term stem cell labelling.

7.1.2 Chapter 4

In Chapter 4, silica was investigated as a SPION surface coating to see if improvements could be made to the chemical stability and protection of the SPION core to dissolution in conditions modelling those found in the lysosome of a stem cell. Silica coated SPION (SiO_2-SPION) samples containing Fe_3O_4 and γFe_2O_3 cores were synthesised. The amount of tetra ethyl orthosilicate (TEOS) optimised for the silica coating reaction was determined as 50 μl which gave an average silica shell thickness of 5.2 -7.7 nm and 11.3-12 nm for SiO_2-SPION samples containing Fe_3O_4 and γFe_2O_3 cores respectively. For the coating procedure of SiO_2-SPION samples containing Fe_3O_4 cores, SPIONs were evenly and uniformly coated. Prior to cell uptake studies, the biocompatibility of silica as a nanoparticle (NP) surface coating was evaluated. The cell viability remained high throughout exposure to all NP

concentrations apart from kidney stem cells (KSCs) exposed to 50 and 100 µg Fe mL^{-1} which showed a decrease in viability (90 % and 70 % respectively). The results from the dissolution assay confirmed the silica coating provided a significant decrease in dissolution rate over a period of 25 days when compared with uncoated SPIONs. SiO_2-SPION samples containing Fe_3O_4 and γFe_2O_3 cores were found to have high R_2 relaxivity values which confirmed their suitability as a contrast agent for MRI. The magnetisation of SiO_2-SPION samples containing Fe_3O_4 and γFe_2O_3 cores were measured using SQUID and were found to give high M_s values which confirmed the suitability of silica as a surface coating since the interaction of silica onto the surface of iron oxide did not affect the M_s value after coating reaction.

7.1.3 Chapter 5

In Chapter 5, gold was investigated as a SPION surface coating to see if improvements could be made to the chemical stability and protection of the SPION core to dissolution in conditions modelling those found in the lysosome of a stem cell. Amino silane coated SPIONs (A-SPIONs) were used to provide a surface for the co-ordination of Au^{3+} ions and reduction to Au^0 for the formation of a gold shell/coating. Transmission electron microscopy (TEM) images indicated the deposition process was uncontrolled which was confirmed by the morphology of different shapes obtained. The first generation of gold reacted amino silane SPIONs (Au-SPIONs) were purple in colour after the reaction procedure and a surface plasmon resonance (SPR) at 540 nm was observed. The SPR for known spherical Au nanoparticles (NPs) indicate that at this wavelength an average diameter of 60 nm was expected. By TEM, an average diameter of 18 ± 9.2 nm was measured which indicated a total shell thickness of around 4 nm containing silane and gold was obtained. It was found that a total overall mass of 299 mg of $pMPC_{135}$-Au-SPION sample was required in 1 mL in order to prepare a 1 mg Fe mL^{-1} concentrated sample for cell labelling experiments. The large quantity of sample required lead to a sample with high viscosity and thus provided a difficult solution to pipette and dispense into cell culture petri dishes. At cell labelling concentrations of 100 and 50 µg Fe mL^{-1}, cytotoxic results were observed and was likely caused by the excessive mass of sample present in the petri dish. The dissolution assay data for $pMPC_{135}$ coated Au-SPIONs provided significant chemical stability and protection of the iron oxide

core to dissolution over a period of 25 days in pH 4.5 citrate buffer at 37 °C which confirms the suitability of gold as a surface coating for the protection of the SPION core. The magnetic properties were found to be retained which was confirmed by the M_s value which was measured at 47.8 emu g^{-1} Fe_3O_4 and by the MRI R_2 relaxivity value of 123 mM^{-1} s^{-1} which again, further supports the suitability of gold as a surface coating.

In the second half of Chapter 5, a second generation of Au-SPIONs were prepared by modifying the gold deposition reaction in order to reduce the amount of gold present in the sample. Through this, the amount of sample required to prepare a 1 mg Fe mL^{-1} was reduced and thus the viscosity of the sample was suitable for cell labelling studies thus avoiding any cytotoxic effects observed with stem cells at high cell labelling concentrations.

The amount of sample required to make a 1 mg Fe mL^{-1} solution was determined as 4.3 mg using elemental analysis which was an 8 fold reduction compared to the first generation Au-SPIONs. The colour of the second generation Au-SPIONs were found to be red and had a SPR at 525-530 nm. Cytotoxicity was assessed by cell proliferation over a period of 48 hours and cells showed better growth rates compared to the control which confirmed their biocompatibility. The dissolution assay data for the second generation Au-SPIONs provided a degree of chemical stability and protection of the iron oxide core to 40 % dissolution at 40 days in pH 4.5 citrate buffer at 37 °C. By TEM, two populations of NPs were observed which showed darker NPs containing Au as confirmed by high-angle annular dark-field (HAADF) imaging. Lighter contrast NPs were determined to be uncoated A-SPIONs or A-SPIONs containing Au^{3+} ions co-ordinated to surface amine groups as confirmed by electron energy loss spectroscopy (EELS) and by observations using TEM at 20 days during conditions simulated for the dissolution assay. The interaction of Au^{3+} ions with surface amine groups were found to contribute to the chemical stability results, however a full mechanism to the chemical stability for the second generation Au-SPIONs was not determined. It is likely that the dark contrast NPs observed by conventional TEM are solid gold NPs and that a gold shell was not produced during the gold deposition reaction which was confirmed by HAADF. The magnetic properties were again found to be retained which was confirmed by the M_s

value and MRI R_2 relaxivity value which again, further support the suitability of the use of gold to provide chemically stable SPIONs.

7.1.4 Chapter 6

In Chapter 6, stem cell labelling studies were carried out with NPs prepared throughout this Thesis. Firstly, cell uptake of $pMPC_{29}$-SPIONs was achieved as confirmed by Prussian blue staining within KSCs as visualised by optical microscopy. The level of uptake of KSCs exposed to MIRB compared to $pMPC_{29}$-SPIONs was noticeably higher which was observed by the intensity levels of blue staining. The level of uptake was also confirmed by cell tracking velocimetry (CTV) magnetophoresis measurements of labelled cells and determining the amount of intracellular iron content. A summary of all the CTV measurements are outlined in **Table 7.2** which highlights the level of NP uptake of cells exposed to MIRB was around twice as high compared to cells exposed to $pMPC_{29}$-SPIONs.

Photothermal images of both SPION samples also showed differences in the level of intensity which again confirmed a difference in the level of uptake. TEM images of stem cells exposed to $pMPC_{29}$-SPIONs confirmed the internalisation NPs *via* the endosome through endocytosis. The chemical stability of $pMPC_{29}$-SPIONs was investigated by a retention study with KSCs over a period of 14 days. The results showed that $pMPC_{29}$-SPIONs cores did not degrade as fast as initially predicted by the dissolution assay carried out in Chapter 3 and that the chemical stability results of $pMPC_{29}$-SPIONs found from the retention study show $pMPC_{29}$-SPIONs cores last for at least 14 days.

Optical microscopy images of mesenchymal stem cells (MSCs) exposed to silica coated γFe_2O_3 SPIONs at NP cell labelling concentration of 25 μg Fe mL^{-1} showed no Prussian blue staining which from CTV measurements, confirmed uptake had actually occurred and that staining with Prussian blue was unsuccessful. This finding suggested the SPION cores were shielded by the silica coating and prevented them from being stained.

MSCs and KSCs exposed to silica coated γFe_2O_3 and Fe_3O_4 SPIONs at cell labelling concentrations of 5 μg Fe mL^{-1} showed very low levels of NP cell uptake which was

confirmed by magnetic velocity measurements from CTV when compared to Molday Ion Coumarin Blue (MICB). However, upon increase of the NP cell labelling concentration to 25 µg Fe mL^{-1} a 6 fold increase in uptake for silica coated γFe_2O_3 SPIONs and a 3 fold increase in uptake for silica coated Fe_3O_4 SPIONs was observed when compared with MSCs exposed to MICB which showed a 1.5 fold increase in NP cell uptake. A summary of all the CTV measurements are outlined in **Table 7.2** which highlights that MSCs and KSCs exposed to silica coated γFe_2O_3 and Fe_3O_4 SPIONs at cell labelling concentrations of 25 µg Fe mL^{-1} provide slightly higher levels of uptake when compared to MSCs exposed to MIRB at the same labelling concentration.

Optical microscopy images under bright field view of MSCs exposed to first generation Au-SPIONs at NP cell labelling concentration of 25 µg Fe mL^{-1} confirmed uptake using Prussian blue and silver staining methods. Optical microscopy images *via* phase contrast of MSCs exposed to second generation Au-SPIONs at NP cell labelling concentration of 25 µg Fe mL^{-1} allowed the visualisation of uptake without the use of a stain and confirmed uptake of second generation Au-SPIONs within cells. Uptake of second generation Au-SPIONs could also be clearly observed under bright field optical microscopy as shown by pink areas within cells. TEM confirmed the internalisation route into MSCs occurred *via* the endosome through endocytosis and was also confirmed by photothermal and fluorescent imaging by overlaying fluorescent stained lysosome images with photothermal images. CTV showed the intracellular iron uptake level of second generation Au-SPIONs with MSCs at NP concentration of 25 µg Fe mL^{-1} to be comparable with those found using Molday Ion EverGreen (MIEG). The CTV data has been summarised in **Table 7.2**. The CTV results show that a NP labelling concentration of 50 µg Fe mL^{-1} provides the highest intracellular iron content before the MSC is likely to become saturated.

7.1.5 Overall Conclusions

Based on all results obtained throughout this Thesis which include chemical stability (**Figure 7.1**), relaxivity (**Table 7.1**) and cell uptake by intracellular iron content (**Table 7.2**) of all nanomaterials prepared, the most promising nanomaterials for use as potential contrast agents for long-term stem cell tracking are silica coated γFe_2O_3 SPIONs, silica coated Fe_3O_4 SPIONs and second generation Au-SPIONs. The main conclusions from the results are:

1. Inorganic coatings provide greater chemical stability compared to hydrophilic polymer coatings, which has been observed using silica and gold compared to pMPC and dextran (Molday Ion), **Figure 7.1**.

2. The dissolution/degradation rate of $pMPC_{29}$-SPIONs measured by the retention study was slower when compared to the dissolution assay. The dissolution assay therefore showed that it did not truly represent a model of the conditions found within the endosome of a stem cell. This was likely due to the amount of time it would take for the endosome of a stem cell to decrease in pH in addition to mechanisms of degradation, which exist inside the endosome containing compacted NPs, which were not considered by the dissolution assay. The results therefore show that all nanomaterials prepared in this Thesis have a slower dissolution/degradation rate than initially predicted by the dissolution assay.

3. The composition of the iron oxide core is an important parameter in providing greater chemical stability in acidic conditions modelling those of an endosome/lysosome of a stem cell. Maghemite (γFe_2O_3) provided greater chemical stability compared to magnetite (Fe_3O_4), **Figure 7.1**.

4. All nanomaterials prepared in this Thesis have an R_2 relaxivity value above the commercial contrast agent MIRB. In addition, silica coated γFe_2O_3 SPIONs, and second generation Au-SPIONs show an R_2 relaxivity value above that measured for the commercial contrast agent Endorem, **Table 7.1**.

Table 7.1. Summary of relaxivity for all SPIONs prepared in this Thesis in addition to commercial contrast agents Endorem and MIRB.

SPION (core/shell)	Relaxivity R_2 (mM^{-1} s^{-1})
Fe_3O_4/amino silane/$pMPC_{29}$	127
Fe_3O_4/amino silane/$pMPC_{29}$ reconstituted	112
Fe_3O_4/silica	140
γFe_2O_3/silica	163
Fe_3O_4/amino silane/Au/$pMPC_{135}$ (1st gen)	123
Fe_3O_4/amino silane/Au/$pMPC_{81}$ (2nd gen)	194
Endorem	159
MIRB	77

Table 7.2. Summary of average magnetic velocities and the mean intracellular iron content of stem cell lines exposed to all SPIONs covered in this Chapter.

Sample	Stem Cell Line	NP Concentration (μg Fe mL^{-1})	Average Magnetic Velocity (μm s^{-1})	Mean m_{Fe} (pg)
MIRB	KSC	1	43 ± 25	1.0 ± 0.6
$pMPC_{29}$-SPIONs	KSC	1	12 ± 6	0.4 ± 0.2
$pMPC_{29}$-SPIONs	KSC	5	56 ± 35	1.8 ± 1.0
MIRB	KSC	5	93 ± 50	3.1 ± 1.7
MICB	KSC	5	178 ± 115	5.6 ± 4.0
SiO_2-Fe_3O_4	KSC	5	26 ± 20	1.2 ± 0.5
SiO_2-γFe_2O_3	KSC	5	21 ± 14	0.5 ± 0.6
MICB	MSC	5	175 ± 115	5.7 ± 3.6
SiO_2-Fe_3O_4	MSC	5	43 ± 42	1.6 ± 1.6
SiO_2-γFe_2O_3	MSC	5	25 ± 23	0.9 ± 0.8
MIRB	MSC	25	145 ± 80	5.0 ± 3.0
MICB	MSC	25	270 ± 200	8.7 ± 6.4
MIEG	MSC	25	130 ± 60	4.1 ± 2.0
SiO_2-Fe_3O_4	MSC	25	130 ± 75	5.2 ± 3.0
SiO_2-γFe_2O_3	MSC	25	101 ± 60	5.4 ± 3.1
Au-SPIONs (2nd Gen)	MSC	25	120 ± 70	4.0 ± 3.0
Au-SPIONs (2nd Gen)	MSC	50	170 ± 90	5.6 ± 3.7
Au-SPIONs (2nd Gen)	MSC	100	155 ± 82	5.1 ± 3.5

5. Subtle differences in cell uptake have been best observed at low cell labelling concentrations (1- 5 µg Fe mL^{-1}) and provided information on the surface interactions of NP coatings prepared in this Thesis with the membrane of the stem cell, **Table 7.2**.

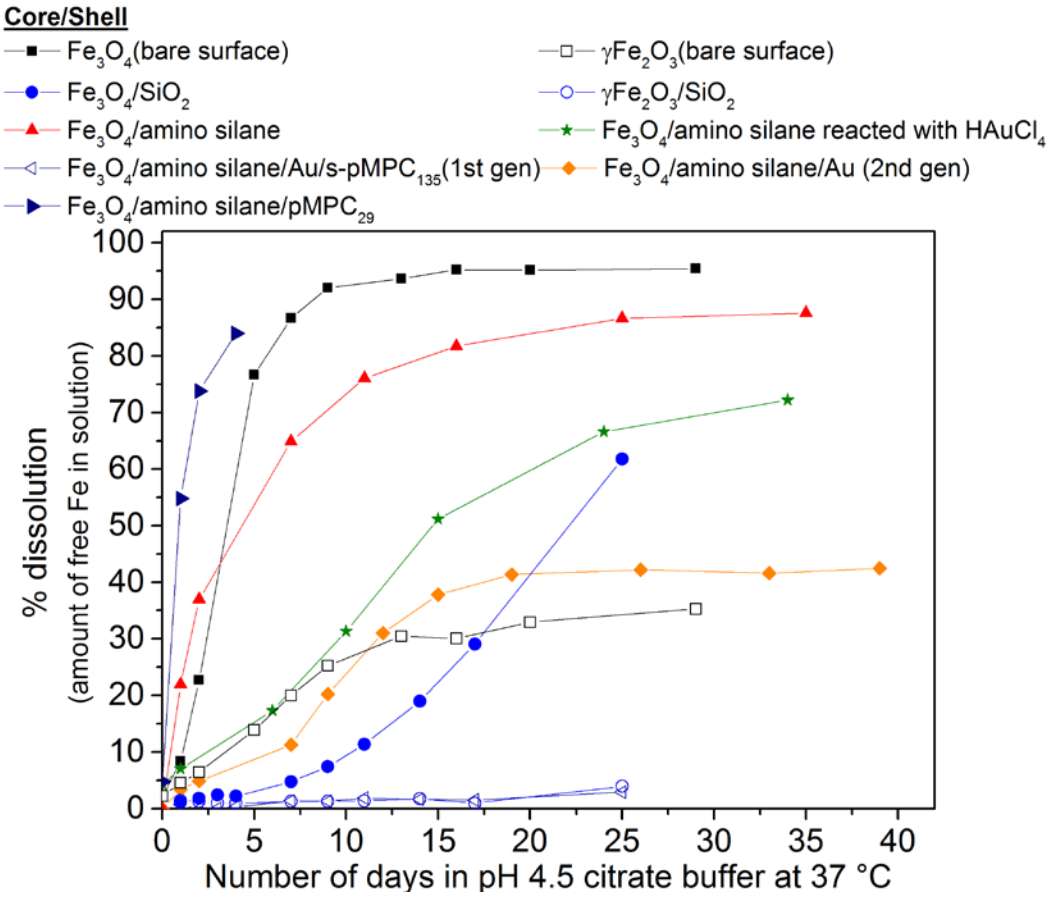

Figure 7.1. Dissolution assay comparing all SPIONs prepared in this Thesis exposed to pH 4.5 citrate buffer solution at 37 °C.

At higher cell labelling concentrations (25 - 100 µg Fe mL^{-1}) the intracellular iron content appears comparable to commercial contrast agents MIRB and MIEG with the exception of MICB which provides higher uptake, **Table 7.2**. TEM and photothermal microscopy confirm the internalisation route of most NPs used in this Thesis *via* the endosome through endocytosis. The retention study has shown that the chemical based dissolution assay used to test NPs for long term chemical stability does not provide a realistic modal of conditions found within the endosome and lysosome of the stem cell. Improvements to such dissolution assay are required if a realistic result is to be obtained and so the retention study using cells at present seems to be the best way to measure

this. The dissolution assay however can be one way to easily measure differences in chemical stability if developing a 'bullet proof' chemically stable coating.

7.2 Future Outlook - Can Long-Term Stem Cell Labelling be Achieved?

At present, the goal of achieving long-term stem cell labelling is still quite a way off but the goal is getting closer. As observed with this project, many obstacles exist. The biggest obstacle in obtaining this goal will be maintaining a strong relaxivity signal required to monitor and track stem cells long-term *in vivo*. The R_2 relaxivity signal diminishes with time through the dilution of NPs *via* natural proliferation of active stem cells. The best solution to ensure the concentration of internalised NPs is kept constant thus preventing a decline in contrast signal long-term would be to develop a contrast agent which contains aggregated NPs or clustered NPs created by micellisation or induced aggregation.[1] Here the MRI contrast would remain strong and diffuse long-term in the area administered compared to the uptake of individual SPIONs where the signal would become weakened and diluted by proliferation of stem cells. There are unanswered questions about whether stem cells would readily uptake such large sized aggregates of NPs and be happy to retain them long-term. Would there be any affect to the overall function of the stem cells long-term?

The R_2 relaxivity signal can also diminish long-term through the loss of NPs initially internalised into stem cells *in vitro*. The long-term intracellular fate of nanomaterials is still unclear. Reports currently show that some of the endocytosed intracellular NPs eventually become exocytosed out of the stem cell or escape out of the endosome into the cytoplasm of the cell through endosomal escape.[2-4]

Cationic or positively charged NPs can escape endosomes into the cytoplasm of the cell by the 'proton-sponge' effect whereby surface groups (such as low pKa amines) are able to buffer the acidic endosomal vesicle environment thus leading to endosomal swelling through a build-up of osmotic pressure and finally lysis.[4, 5] In this Thesis, Au-SPIONs (2^{nd} generation) and Molday Ion contrast agents used have a cationic surface charge as measured by zeta potential of +24.3 ± 3.3 mV and + 31

mV respectively. It is possible that these nanomaterials may have or would have eventually escaped the endosome into the cytoplasm of the cell by the 'proton-sponge' effect.

Facilitating endosomal escape could be one way to retain NPs long-term and prevent dissolution. Entrapment of SPIONs by the endosome has been shown to significantly reduce R_2 relaxivity compared to those dispersed freely.[6] It has been hypothesised that by releasing SPIONs into the cytoplasm *via* endosomal escape or other mechanism, R_2 relaxivity will significantly improve compared to SPIONs trapped in the endosome.[4]

Other methods used to facilitate endosomal escape include ion-pair formation, membrane-destabilising macromolecules and hydrophobic modifications of cationic polymers, pH sensitive degradable vectors.[7] Further work would be required to understand whether this would be beneficial or if it would change/disrupt the overall function of the cell. Cytotoxic effects have been observed with NPs possessing a highly positive surface charge (through the use of a transfection agent such as poly(lysine)) *via* adhesion of NPs with the cell plasma membrane.[8]

Externalised SPIONs *via* exocytosis (a cell mechanism which removes endocytosed intracellular NPs out of the stem cell *via* reverse endocytosis) can migrate to other neighbouring stem cells or untargeted host cells in tissues/organs. Externalised SPIONs can be transported around the body *via* the blood system, lymphatic system, digestive system, urinary system etc. SPIONs could be reabsorbed by neighbouring stem cells by cell death and entosis.[9] Not only does this reduce the R_2 relaxivity signal but also the location of labelled stem cells administered can become unclear long-term through a creation of false positives. Multimodal imaging is currently used as a way to ensure the location of original targeted labelled stem cells are tracked correctly long-term.[10] Contrast agents would require multimodal imaging capabilities in order to be successful at reaching the goal of long-term tracking.

7.3 Future Work

To continue with this project, the following proposed future work would be carried out in order to further improve the development of contrast agents for long-term stem cell tracking:

- Synthesis of spherical monodisperse γFe_2O_3 SPIONs.
    - The dissolution assay has shown γFe_2O_3 is more chemically resistant than Fe_3O_4. The synthesis route used in this Thesis by co-precipitation produces SPIONs with undefined shape and morphology. By producing spherical monodisperse γFe_2O_3 SPIONs, the surface density of reacted polymers or functional end groups can be measured and calculated as carried out in Chapter 3. It would be interesting to investigate the chemical stability of pMPC coated γFe_2O_3 SPIONs compared to pMPC coated Fe_3O_4 SPIONs prepared in Chapter 3.
- Synthesis of a range of SPIONs with different core diameters.
    - To determine if the dissolution rate and relaxivity is affected.
- Further biological studies investigating the intracellular fate of SPIONs prepared in this Thesis.
    - Are SPIONs exocytosed back out of the cell? Do any nanomaterials escape the endosome into the cytoplasm of the cell? Does the surface coating make a difference in either scenario and does it affect the cell functionality? Do any NPs remain long-term?

Possible deviations from the design used in this Thesis to improve the development of contrast agents for long-term stem cell tracking:

- Using an alternative superparamagnetic material which provides a stronger contrast signal and maintains low cytotoxicity with cells such as FePt, $MnFe_2O_4$, FeCo.[11, 12]

7.4 References

1. K. Letchford and H. Burt, *Eur. J. Pharm. Biopharm.*, 2007, **65**, 259-269.
2. N. Oh and J. Park, *Int. J. Nanomed.*, 2014, **9**, 51-63.

3. S. Salatin, S. Maleki Dizaj and A. Yari Khosroushahi, *Cell Biol. Int.*, 2015, **39**, 881-890.
4. C. Schweiger, P. Gil, W. Parak, *et al.*, *J. Con. Rel.*, 2010, **148**, e67-e68.
5. H. Duan and S. Nie, *J. Am. Chem. Soc.*, 2007, **129**, 3333-3338.
6. A. Taylor, A. Herrmann, D. Moss, *et al.*, *PLoS ONE*, 2014, **9**, e100259.
7. S. Guo and L. Huang, *J. Nanomater.*, 2011, **2011**, 12.
8. M. R. Lorenz, V. Holzapfel, A. Musyanovych, *et al.*, *Biomaterials*, 2006, **27**, 2820-2828.
9. D. De Stefano, R. Carnuccio and M. C. Maiuri, *J. Drug Deliv.*, 2012, **2012**, 14.
10. A. Tennstaedt, M. Aswendt, J. Adamczak, *et al.*, *Imaging and Tracking Stem Cells*, ed. K. Turksen, Humana Press, 2013, vol. 1052, ch. 14, 153-166.
11. N. Venkatesha, S. M. Pudakalakatti, Y. Qurishi, *et al.*, *RSC Adv.*, 2015, **5**, 97807-97815.
12. Y. K. Gun'ko and D. F. Brougham, *Magnetic Nanomaterials as MRI Contrast Agents*, WILEY-VCH Verlag GmbH & Co. KGaA, Weinheim, 2009, ch. 4, 119-164.

Appendix A

List of Figures

Figure A.1. ^{1}H-NMR of thiol-pMPC polymer. DP_n 81 where the 4 H end group protons are at ~3 ppm. 282
Figure A.2. Disulphide-pMPC polymers. Where n is the degree of polymerisation (DP_n). 282

List of Tables

Table A.1. Predicted elemental percentage weight and TGA weight loss values for one monolayer of amino silane ligands surrounding a 9.2 nm SPION. 278
Table A.2. Experimental and calculated elemental analysis and TGA weight loss values for dried A-SPION. Shaded areas show actual experimental values. 280
Table A.3. Predicted elemental percentage weight and TGA weight loss values for one monolayer of amino silane ligands surrounding a 7.4 nm SPION. 285
Table A.4. Experimental and calculated elemental analysis and TGA weight loss values for dried A-SPION. Shaded areas show actual experimental values. 286

List of Schemes

Scheme A.1. Synthesis of Bis[2-(2'-bromoisobutyryloxy) ethyl] disulfide (BriBOEDS) ATRP initiator. 281

First generation Au-SPIONs: Quantification of amine groups reacted to the SPION surface

The number of amino silane ligands available on the surface of iron oxide nanoparticles was predicted using both the thermal gravimetric analysis (TGA) and the N value obtained from elemental analysis measured. Using the surface area of the footprint from the tridentate amino silane ligand as 0.073 nm^2,[1] The theoretical number of amine ligands for one mono-layer on the surface of a 9.2 nm diameter nanoparticle (as determined by PXRD using the Scherrer equation) was calculated as 3635 amine ligands. This was determined by the following:

The surface area (SA) of a 9.2 nm SPION:

$$SA_{SPION} = 4\pi r^2$$

SA_{SPION} = 265 ± 11 nm^2

Predicted number of reacted APTMS ligands that can fit as one monolayer on a 9.2 nm SPION (L_{pred}):

$$L_{pred} = \frac{SA_{SPION}}{Footprint_{APTMS}}$$

L_{pred} = 3635 ± 149 ligands

Predicted elemental and thermalgravimetric analysis (TGA) percentage weight values for one monolayer of amino silane around a 9.2 nm SPION could also be calculated and compared with actual results.

$$Mass\ of\ one\ SPION = \rho_{Fe_3O_4} x \left(\left[\frac{4}{3}\pi r^3\right] x 10^{-21}\right)$$

$Mass\ of\ one\ SPION$ = 2.10 x 10^{-18} ± 1.27 x 10^{-19} g

$$Mass\ of\ ligand\ monolayer\ per\ SPION = \left[\frac{L_{pred}}{N_A} x MW_{reacted\ amino\ silane\ ligand}\right]$$

$Mass\ of\ ligand\ monolayer\ per\ SPION$ = 8.10 x 10^{-19} ± 3.3 x 10^{-20} g

Therefore, the total mass of one A-SPION

$Mass\ of\ 1\ SPION + Mass\ of\ ligand\ monolayer\ per\ SPION$= 2.9 x 10^{-18} ± 1.6 x 10^{-19} g

$$\%\ mass\ of\ Fe_3O_4 = \frac{Mass\ of\ one\ SPION}{Total\ mass\ of\ one\ ligand\ coated\ SPION}\ x\ 100$$

$\%\ mass\ of\ Fe_3O_4$ = 72.18 %

$$\%\ mass\ of\ ligand\ shell = \frac{Mass\ of\ ligand\ monolayer\ per\ SPION}{Total\ mass\ of\ one\ ligand\ coated\ SPION}\ x\ 100$$

$\%\ mass\ of\ ligand\ shell$ = 27.82 %

Using the percentage mass values for the contribution of Fe_3O_4 versus the contribution of the ligand shell, the molar composition of A-SPION with one monolayer of reacted APTMS could be written as $(Fe_3O_4)_1(C_3H_8NSiO_3)_{0.7}$.

The theoretical percentage mass for one monolayer of reacted amino silane ligands around a 9.2 nm Fe_3O_4 core was found as 27.82 %. This percentage mass value includes the percentage mass contribution from the inorganic silane, which is not thermal decomposed during the TGA. The theoretical percentage mass contribution of the silane (SiO_2) was therefore deducted to give a predicted TGA percentage for one monolayer of reacted APTMS as 12.05 %. The theoretical percentage mass contribution from C, H and N was also used to predict the elemental analysis. The theoretical percentage mass contribution from C, H and N was also used to predict the elemental analysis. The predicted results are highlighted in **Table A.1** as C: 7.47 % , H: 1.67 % and N: 2.90 %.

Table A.1. Predicted elemental percentage weight and TGA weight loss values for one monolayer of amino silane ligands surrounding a 9.2 nm SPION.

Element	**% mass for reacted amino silane ligand**	**% mass for reacted amino silane ligand (scaled to 27.82 %)**
C	26.85	7.47
H	6.01	1.67
N	10.44	2.90
O	35.77	9.95
Si	20.93	5.82
Predicted TGA weight loss	43.30	12.05
Total % mass	100	27.82

The actual measured results obtained from the elemental and TGA were used to determine the actual composition of A-SPION, **Table A.2**. The actual results could then be used to predict the actual average number of APTMS ligands reacted with the SPION surface with diameter of 9.2 nm and thus determine the average number of monolayer(s) of amino silane. **Table A.2** summarises experimental elemental analysis results, TGA weight loss and calculations of weight contributions from APTMS, residual oleic acid, adsorbed solvent and SPION core. From the experimental procedure, the nitrogen content of the A-SPION product could only be

attributed to APTMS ligands reacted onto the surface. Using the weight percentage measured for nitrogen, it was possible to calculate the carbon and hydrogen contribution for APTMS.

Table A.2 deduces from the elemental analysis data that an excess of carbon and hydrogen was observed compared to the expected values for a pure APTMS coverage. From the TGA, there was 5.25 % weight loss taken from ambient to 120 °C which was considered to be residual solvent (ethanol and toluene). The excess contaminant carbon and hydrogen values left over of 9.54 % were considered residual oleic acid, the theoretical percentage C, H and O has been predicted in **Table A.2**. The weight composition of A-SPION was determined as (Fe_3O_4), 37.80 %, (APTMS), 47.41 % (oleic acid), 9.54 % and (solvent), 5.25 %. The molar composition of A-SPION was determined as $(Fe_3O_4)_1(C_3H_8NSiO_3)_{2.2}$ $(C_{18}H_{34}O_2)_{0.2}$ $(C_6H_8O_1)_{0.3}$. The amount of APTMS on the A-SPION (with residual organic contaminate removed) corresponded to 2.94 equivalents of the value calculated earlier for a monolayer so the number of APTMS ligands on the surface (L_{exp}) was estimated at 10698 (5.55 % N).

Table A.2. Experimental and calculated elemental analysis and TGA weight loss values for dried A-SPION. Shaded areas show actual experimental values.

		Actual experimental values	Calculated from Nitrogen content	Calculated from TGA weight loss			
			APTMS	Residual Oleic Acid	Residual solvent	Total values	SPION (as Fe_3O_4)
Elemental analysis	C	22.52	12.73	7.30	2.49	22.52	
	H	3.91	2.85	1.16	-0.10	3.91	
	N	4.95	4.95			4.95	
	O		16.96	1.08	*2.86*	20.90	10.82
	Si		9.92			9.92	
	Fe						26.97
	Total weight %	31.38	47.41	9.54	5.25	62.20	37.80
TGA	Weight loss	35.32	20.53	9.54	5.25	35.32	

Synthesis of disulphide ATRP initator bis[2-(2'-bromoisobutyryloxy) ethyl] disulfide (BriBOEDS)

Bis[2-(2'-bromoisobutyryloxy) ethyl] disulfide (BriBOEDS) was prepared by Dr *Solène Cauët* at the University of Liverpool, Department of Chemistry. Following the method as reported by Tsarevsky and Matyjaszewski.[2] Bis(2-hydroxyethyl) disulfide (12.84 g, 0.08 mol) was dissolved in 200 mL of dry THF, excess triethylamine (35.0 mL, 0.25 mol) was added under a nitrogen atmosphere, and this solution was cooled in an ice bath. 2-Bromoisobutyryl bromide (25 mL, 46.5 g, 0.20 mol) was added dropwise from a dropping funnel over a 1 h period and the reaction solution turned reddish brown. The solution was allowed to warm up to ambient temperature and stir for 24 h. **Scheme A.1** outlines the synthesis procedure.

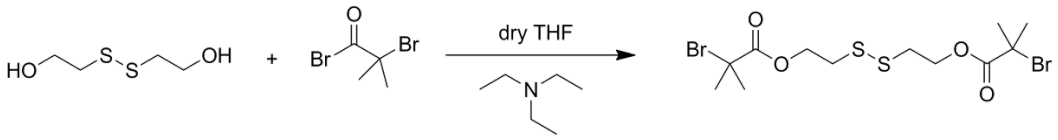

Scheme A.1. Synthesis of Bis[2-(2'-bromoisobutyryloxy) ethyl] disulfide (BriBOEDS) ATRP initiator.

The insoluble triethylammonium bromide salt was removed by filtration and the resulting yellowish solution was concentrated under vacuum. The concentrated solution was stirred with 100 mL 0.10 M aqueous Na_2CO_3. The crude product was then extracted three times with 100 mL dichloromethane using a separating funnel. The combined dichloromethane extracts were first dried with anhydrous magnesium sulfate and then concentrated to afford a reddish brown oil (24.6 g; yield 68%). The crude product was purified by dissolution in dichloromethane, followed by passage through a basic alumina column to yield a yellow liquid which was stored in the freezer.

^{1}H NMR ($CDCl_3$, 400 MHz) δ (ppm) 4.43 (t, 2H, -CH_2OOC-), 2.97 (t, 2H, -CH_2S-), and 1.93 (s, 6H, $(CH_3)_2$C-). ^{13}C NMR ($CDCl_3$, 100.6 MHz) δ (ppm) 171.49 (-OOC-), 63.56 (-CH_2O-), 55.54(-C-$(CH_3)_2$), 36.81 (-CH_2S-) and 30.76 (CH_3). FTIR (ATR cell) 2975, 1731, 1267, 1152 and 1104 cm^{-1}. Micromass LCT mass spectrometry expected (found): 452.22 g mol^{-1} (451.91 g mol^{-1}). Elemental Analysis: expected C 31.87 %, H 4.46 %, S 14.18 %, actual C 31.90 %, H 4.45 %, S 13.81 %.

Characterisation data for thiol functionalised pMPC polymers used to stabilise Au-SPIONs

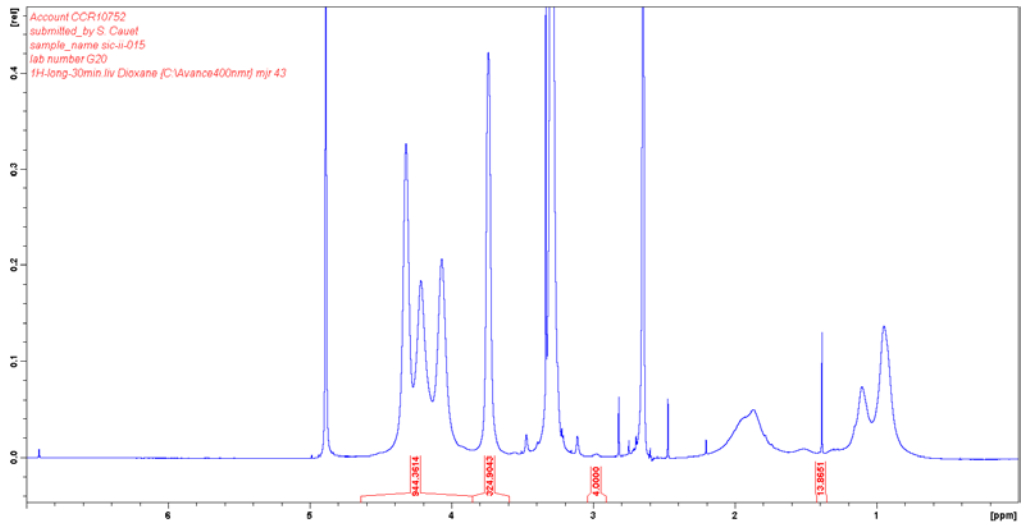

Figure A.1. ^{1}H-NMR of thiol-pMPC polymer. DP_n 81 where the 4 H end group protons are at ~3 ppm.

GPC data (**Figure A.2**) M_n 35,500 g mol^{-1}, M_w 50,900 g mol^{-1}, M_w/M_n 1.44 DP_nGPC 120. GPC data (**Figure A.2**) M_n 42,100 g mol^{-1}, M_w 65,000 g mol^{-1}, M_w/M_n 1.54 DP_nGPC 145.

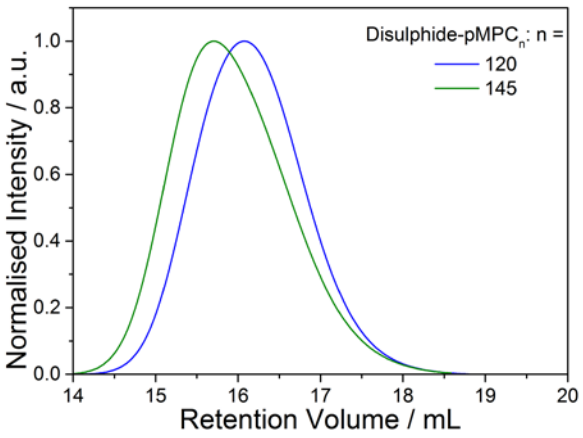

Figure A.2. Disulphide-pMPC polymers. Where n is the degree of polymerisation (DP_n).

Second Generation Au-SPIONs: Quantification of Amine Groups Reacted to the SPION Surface

The number of amino silane ligands available on the surface of iron oxide nanoparticles was predicted using both the thermal gravimetric analysis (TGA) and the N value obtained from elemental analysis measured. Using the surface area of the footprint from the tridentate amino silane ligand as 0.073 nm^2,[1] The theoretical number of amine ligands for one mono-layer on the surface of a 7.4 nm diameter nanoparticle (as determined by PXRD using the Scherrer equation) was calculated as 2338 amine ligands. This was determined by the following:

The surface area (SA) of a 7.4 nm SPION:

$$SA_{SPION} = 4\pi r^2$$

SA_{SPION} = 171 ± 17 nm^2

Predicted number of reacted APTMS ligands that can fit as one monolayer on a 7.4nm SPION (L_{pred}):

$$L_{pred} = \frac{SA_{SPION}}{Footprint_{APTMS}}$$

L_{pred} = 2338 ± 229 ligands

Predicted elemental and thermal gravimetric analysis (TGA) percentage weight values for one monolayer of amino silane around a 7.4 nm SPION could also be calculated and compared with actual results.

$$Mass\ of\ one\ SPION = \rho_{Fe_3O_4} x \left(\left[\frac{4}{3}\pi r^3\right] x10^{-21}\right)$$

$Mass\ of\ one\ SPION$ = 1.08 x 10^{-18} ± 1.51 x 10^{-19} g

$$Mass\ of\ ligand\ monolayer\ per\ SPION = \left[\frac{L_{pred}}{N_A} x MW_{reacted\ amino\ silane\ ligand}\right]$$

$Mass\ of\ ligand\ monolayer\ per\ SPION$ = 5.21 x 10^{-19} ± 5.11 x 10^{-20} g

Therefore, the total mass of one A-SPION

$$Mass\ of\ 1\ SPION + \ Mass\ of\ ligand\ monolayer\ per\ SPION = 1.6 \times 10^{-18} \pm 2.0 \times 10^{-19}\ g$$

$$\%\ mass\ of\ Fe_3O_4 = \frac{Mass\ of\ one\ SPION}{Total\ mass\ of\ one\ ligand\ coated\ SPION}\ x\ 100$$

$$\%\ mass\ of\ Fe_3O_4 = 67.54\ \%$$

$$\%\ mass\ of\ ligand\ shell = \frac{Mass\ of\ ligand\ monolayer\ per\ SPION}{Total\ mass\ of\ one\ ligand\ coated\ SPION}\ x\ 100$$

$$\%\ mass\ of\ ligand\ shell = 32.46\ \%$$

Using the percentage mass values for the contribution of Fe_3O_4 versus the contribution of the ligand shell, the molar composition of A-SPION with one monolayer of reacted APTMS could be written as $(Fe_3O_4)_1(C_3H_8NSiO_3)_{0.8}$.

The theoretical percentage mass for one monolayer of reacted amino silane ligands around a 7.4 nm Fe_3O_4 core was found as 32.46 %. This percentage mass value includes the percentage mass contribution from the inorganic silane, which is not thermal decomposed during the TGA. The theoretical percentage mass contribution of the silane (SiO_2) was therefore deducted to give a predicted TGA percentage for one monolayer of reacted APTMS as 14.06 %. The theoretical percentage mass contribution from C, H and N was also used to predict the elemental analysis. The theoretical percentage mass contribution from C, H and N was also used to predict the elemental analysis. The predicted results are highlighted in **Table A.3** as C: 8.72 % , H: 1.95 % and N: 3.39 %. The actual measured results obtained from the elemental and TGA were used to determine the actual composition of A-SPION,**Table A.4**. The actual results could then be used to predict the actual average number of APTMS ligands reacted with the SPION surface with diameter of 7.4 nm and thus determine the average number of monolayer(s) of amino silane. **Table A.4** summarises experimental elemental analysis results, TGA weight loss and calculations of weight contributions from APTMS, residual oleic acid, adsorbed solvent and SPION core. From the experimental procedure, the nitrogen content of the A-SPION product could only be attributed to APTMS ligands reacted onto the surface. Using the weight percentage measured for nitrogen, it was possible to calculate the carbon and hydrogen contribution for APTMS.

Table A.3. Predicted elemental percentage weight and TGA weight loss values for one monolayer of amino silane ligands surrounding a 7.4 nm SPION.

Element	% mass for reacted amino silane ligand	% mass for reacted amino silane ligand (scaled to 27.82 %)
C	26.85	8.72
H	6.01	1.95
N	10.44	3.39
O	35.77	11.61
Si	20.93	6.80
Predicted TGA weight loss	43.30	14.06
Total % mass	100	32.46

Table A.2 deduces from the elemental analysis data that an excess of carbon and hydrogen was observed compared to the expected values for a pure APTMS coverage. From the TGA, there was 4.98 % weight loss taken from ambient to 120 °C which was considered to be residual solvent (ethanol and toluene)**.** The excess contaminant carbon and hydrogen values left over of 13.40 % were considered residual oleic acid, the theoretical percentage C, H and O has been predicted in **Table A.4**. The weight composition of A-SPION was determined as Fe_3O_4 42.15 %, APTMS 39.46 %, oleic acid 13.40 % and solvent 4.98 %. The molar composition of A-SPION was determined as $(Fe_3O_4)_1(C_3H_8NSiO_3)_{1.6}$ $(C_{18}H_{34}O_2)_{0.3}(C_6H_8O_1)_{0.3}$. The amount of APTMS on the A-SPION (with residual organic contaminate removed) corresponded to 1.74 equivalents of the value calculated earlier for a monolayer so the number of APTMS ligands on the surface (L_{exp}) was estimated at 4074 (4.76 % N).

Table A.4. Experimental and calculated elemental analysis and TGA weight loss values for dried A-SPION. Shaded areas show actual experimental values.

		Actual experimental values	Calculated from Nitrogen content	Calculated from TGA weight loss			
			APTMS	Residual Oleic Acid	Residual solvent	Total values	SPION (as Fe_3O_4)
Elemental analysis	C	22.55	10.60	10.26	1.70	22.55	
	H	3.87	2.37	1.63	-0.13	3.87	
	N	4.12	4.12			4.12	
	O		14.12	1.52	*3.41*	19.04	12.07
	Si		8.26			8.26	
	Fe						30.09
	Total weight %	30.54	39.46	13.40	4.98	57.84	42.15
TGA	Weight loss	35.47	17.09	13.40	4.98	35.47	

References

1. L. Bouffier, H. H. P. Yiu and M. J. Rosseinsky, *Langmuir*, 2011, **27**, 6185-6192.
2. N. V. Tsarevsky and K. Matyjaszewski, *Macromolecules*, 2002, **35**, 9009-9014.

Appendix B

Studies using Polyethylene glycol (PEG)

Screening Polymer Coatings for SPIONs

At the very start of this Ph.D project, polyethylyene glycol methacrylate (PEGMA) with M_n of 300 and 1100 g mol^{-1} were the first monomers of choice to polymerise by atom transfer radical polymerisation (ATRP) due to known bio-compatibility of polyethylene glycol (PEG).[1-3] In addition, PEG(monomethyl ether)succinic acid ester (PEG-COOH) was prepared in order to compare the stabilisation of superparamagnetic nanoparticles (SPIONs) using linear *vs* branched polymers, **Scheme AB.1**.

Preparation of PEG(monomethyl ether)succinic acid ester (PEG-COOH)

PEG-COOH was prepared by Dr *Solène Cauët* at the University of Liverpool, Department of Chemistry. Following the method by Parrish *et al*.[4] PEG(monomethyl ether) 5 kDa (5.0g, 1 eq), succinic anhydride (0.18g, 2 eq), and 4-(dimethylamino)pydrine (DMAP) (25 mg, 0.2 eq) were dissolved in dichloromethane (85 mL) and heated to reflux for 48 h. **Scheme AB.1** outlines the synthesis procedure.

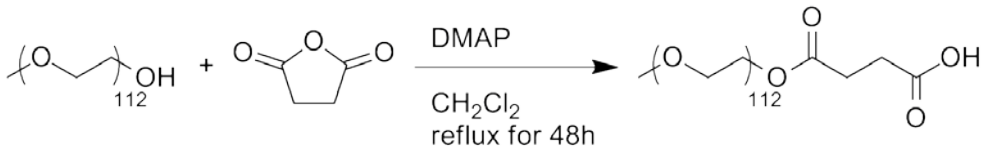

Scheme AB.1. Preparation of PEG(monomethyl ether)succinic acid ester (PEG-COOH).

The crude reaction mixture was washed with water several times. The organic phase was then dried over $MgSO_4$. The solvent was removed and the polymer obtained as a white powder from precipitation from THF in diethyl ether (yield 80%). ^{1}H NMR ($CDCl_3$, 400 MHz) δ (ppm) 2.72 (m, 4H, HOOC-C*H*$_2$-C*H*$_2$-COO), 3.37 (s, 3H, O-C*H*$_3$), 3.66 (br, 426 H, O-C*H*$_2$-C*H*$_2$-O), 4.28 (t, 2H, CH_2-C*H*$_2$-OCO-) ^{13}C NMR (CDCl3, 100.61 MHz) δ (ppm) 28.88 (OOC-CH_2-*C*H_2-COOH), 29.39 (OOC-*C*H_2-CH_2-COOH), 59.04 (*C*H_3-O-), 63.77 (O-CH_2-*C*H_2-OCO-), 68.97(O-*C*H_2-CH_2-OCO-), 70.54 (O-*C*H_2-*C*H_2-O), 71.90 (CH_3O-*C*H_2-, 172.16 (O-*C*O-CH_2-), 173.57 (-*C*OOH). FTIR (ATR cell) ν(C=O) 1733 cm^{-1}, **Figure AB.1**, **Figure AB.2** and **Figure AB. 3**.

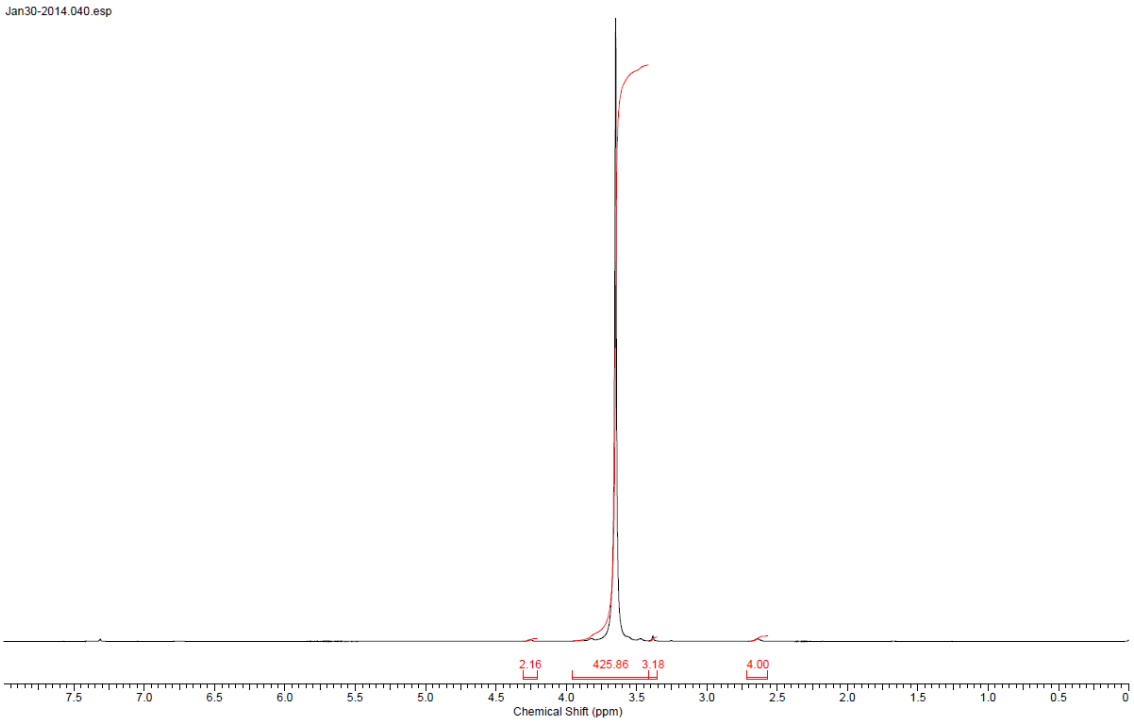

Figure AB.1. ^{1}H-NMR of PEG(monomethyl ether)succinic acid ester (PEG-COOH) 5kDa.

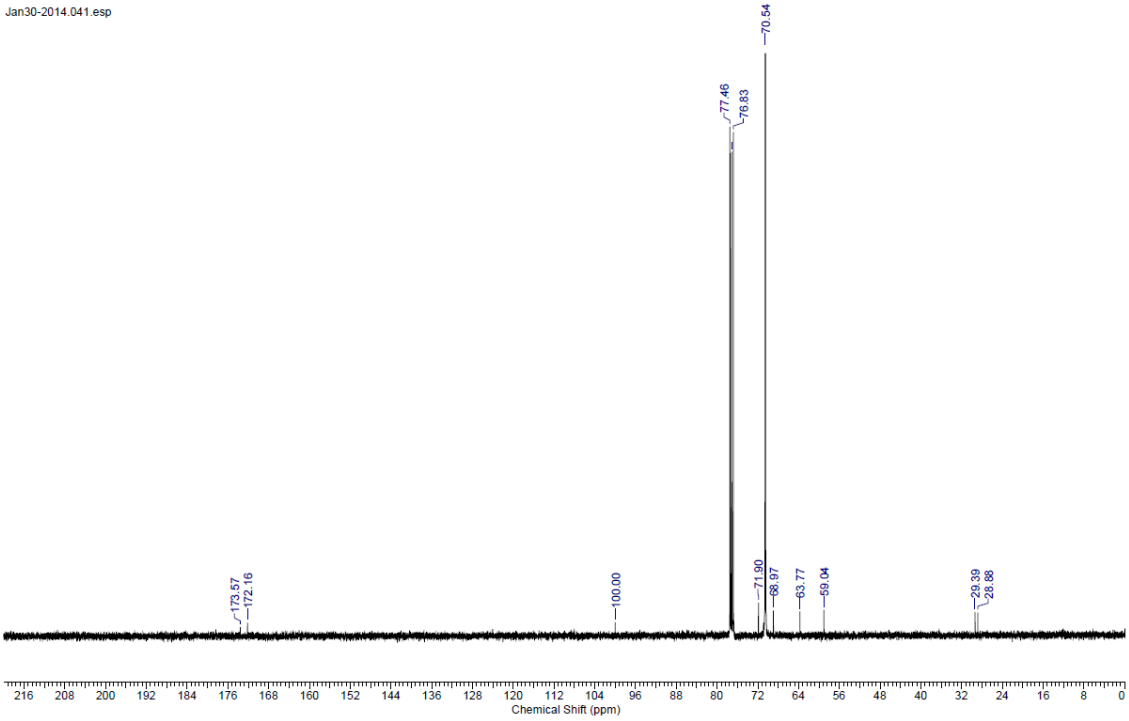

Figure AB.2. ^{13}C-NMR of PEG(monomethyl ether)succinic acid ester (PEG-COOH) 5kDa.

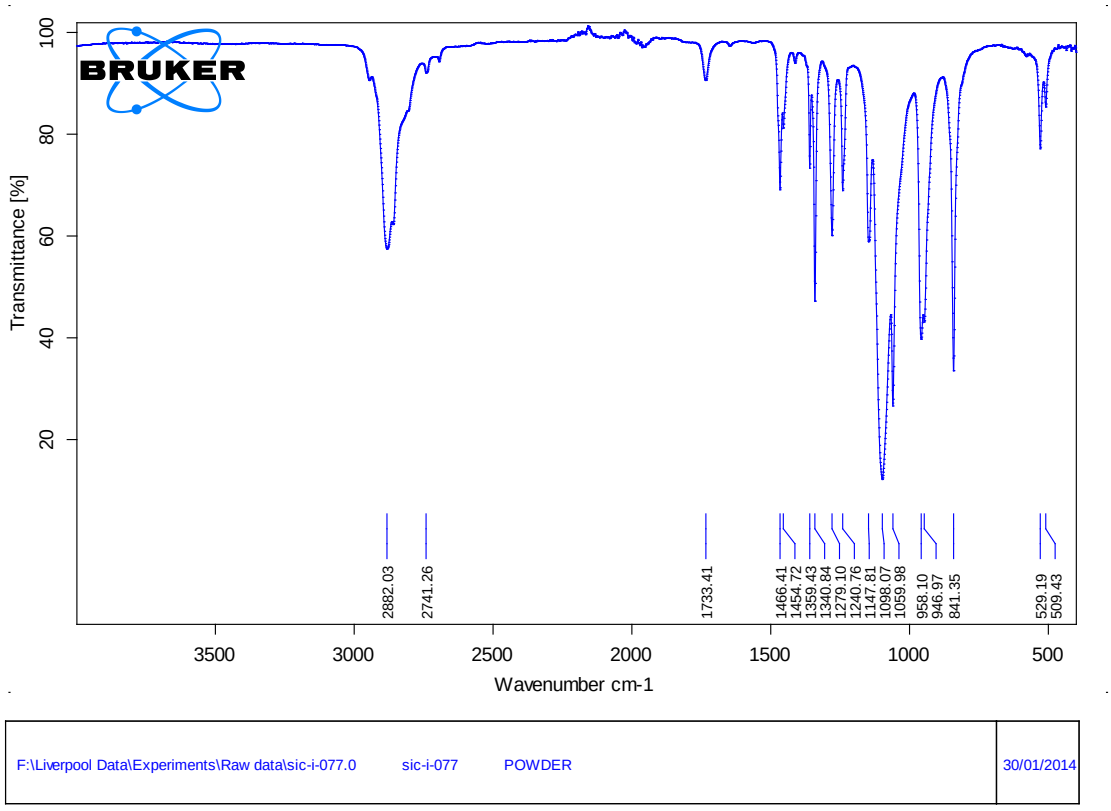

Figure AB. 3. FT-IR of PEG(monomethyl ether)succinic acid ester (PEG-COOH) 5kDa.

N-Succinimidyl Functionalisation of PEG-COOH and Amidation with A-SPIONs

In a 15 mL vial, PEG-COOH ((0.2 g, 5kDa) or (0.1 g, 2 kDa)) was added to methanol. To this, 1-ethyl-3-(3-dimethylaminopropyl)carbodiimide (EDC.HCl) (8 mg) and *N*-hydroxy succinimde (NHS) (4 mg) was added. The vial was sealed and left to rotary mix for 10 minutes. To this, DMAP (4 mg) and then A-SPIONs (pre-sonicated solution using an ultrasonic bath (Fisher Scientific, model FB15051, frequency = 30-40 kHz) in ethanol, 5 mL, 2 mg mL^{-1}) were added. The vial was resealed and sonicated for 1 hour in a sonication bath set to 22°C, **Scheme AB.2**. The sonication bath warmed up over the course of the 1 hour time period which reach a final temperature of 40°C. The reaction mixture was then left to rotary mix for 15 hours at 22 °C before dialysis into deionised water. The dialysis solution was changed with deionised water (4 L) five times over the course of a period of 8 hours. The dialysis bag was then left in the final change of deionised water (4 L) for 15 hours.

If polymer coated SPIONs were found to be colloidally stable in water for more than 24 hours, SPIONs were concentrated using a 50,000 MWCO Corning Spin-X UF centrifugal concentrator. The concentrated solution of polymer coated SPIONs were then passed through a Sephadex G25 gel filtration chromatography column in phosphate buffered saline (PBS) pH 7.4 to remove any unreacted polymer present. Samples as prepared were characterised by DLS, TEM and MRI. Samples were assessed for colloidal stability in PBS solution and for stability into citrate buffer solutions prior to biological studies. To determine polymer coverage, dry samples were prepared by dialysing polymer coated SPIONs back into deionised water to remove PBS salts prior to freeze drying. Samples were characterised by TGA, elemental analysis, SQUID, DLS and FT-IR.

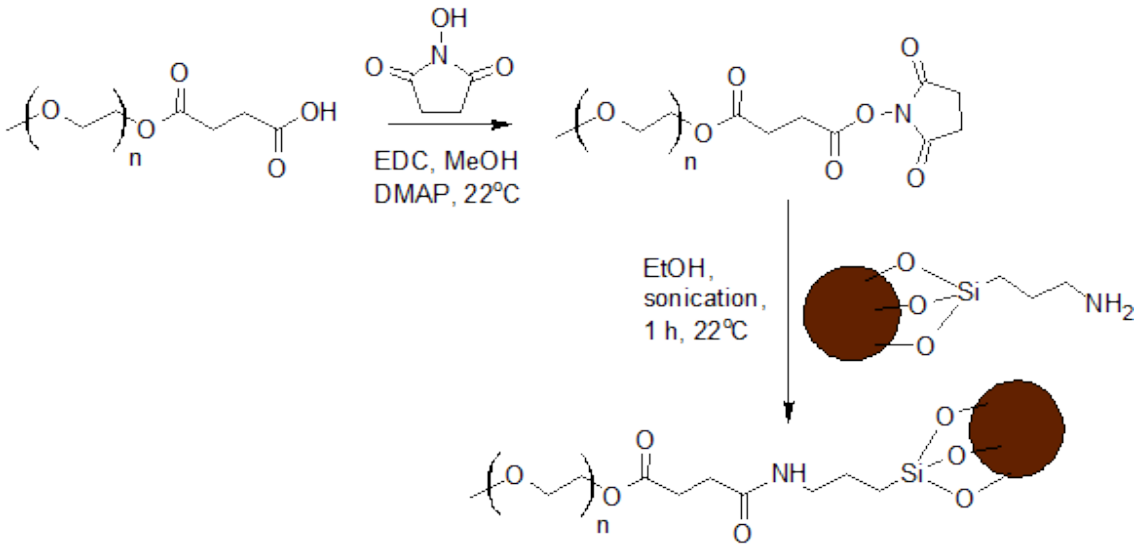

Scheme AB.2. mPEG-COOH coupling reaction with EDC/NHS and amidation with A-SPIONs.

Synthesis of benzyl-2-bromoisobutyrate (BzBriB) Initiator for ATRP

Benzyl-2-bromoisobutyrate (BzBriB) initiator was used as a control to demonstrate whether the amidation coupling reaction of *N*-succinimidyl functional polymers was successful and if there was any physisorption interaction of the polymers with the amino silane coated SPIONs (A-SPIONs) to cause colloidal stabilisation, **Scheme AB.3**.

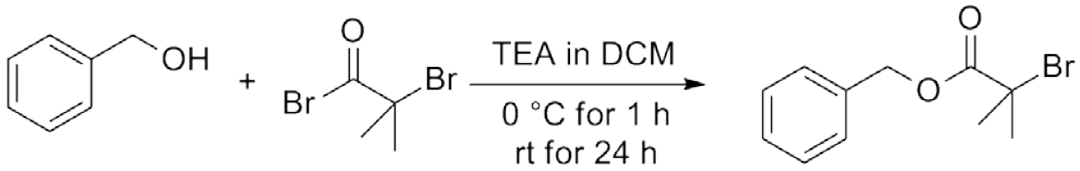

Scheme AB.3. Synthesis of benzyl-2-bromoisobutyrate (BzBriB) initiator.

In a 1 L round bottom flask, dry dichloromethane (DCM, 500 mL) was added and cooled to 0 °C under a nitrogen atmosphere. Under magnetic stirring, benzyl alcohol (BzOH, 5.20 mL, 50 mmol) and triethylamine (TEA, 14.0 mL, 100 mmol) were added. 2-bromoisobutyryl bromide (8.00 mL, 55 mmol) was then added to the mixture dropwise and the mixture was left to mix overnight and warm to room temperature. The TEA salts were filtered from the mixture and the remaining organic solution washed with 0.1 M HCl and 0.1 M Na_2CO_3 solutions. The DCM was then removed *via* rotary evaporation to leave a brown liquid which was then purified by vacuum distillation to yield a straw coloured liquid. The structure and purity of the final product was confirmed by ^{1}H-NMR, ^{13}C-NMR and mass spectrometry. Chemical purity (^{1}H-NMR) > 95 %. Chemical yield 9.98 g (78 %). ^{1}H-NMR (400 MHz, chloroform-*d*, ppm): δ 7.38-7.33 (m, 5 H, C_6H_5), 5.2 (s, 2 H, CH_2), 1.95 (s, 6 H, CH_3). ^{13}C-NMR (100 MHz, chloroform-*d*, ppm): δ 171.5, 135.4, 128.6, 128.3, 127.9, 67.6, 55.7, 30.8. Elemental Analysis: expected C 51.38 %, H 5.10 %, actual C 50.75 %, H 5.10 %. Micromass LCT mass spectrometry expected (found): 256.0 g mol^{-1} (256.0 g mol^{-1}).

2.1.1 Preparation of Hydrophillic Polymers by ATRP

The reagent amounts and conditions for the ATRP of the polymers synthesised for preliminary screening can be found in **Table AB.1**. Typically, ATRP reactions were carried out using molar ratios of [monomer]/[initiator]/[CuCl]/[bipy] = target DP_n:1:1:2.1 in a solvent or solvent mixture. In a dry 100 mL round bottom flask, monomer(s) (target DP_n equiv) was dissolved in degassed solvent (50 % of total solvent volume unless stated). In a separate flask, initiator (1 equiv) was dissolved in solvent (50 % of total solvent volume unless stated) with bipy ligand (2.1 equiv) and Cu(I)Cl (1 equiv). After purging both flasks with nitrogen for 30 min, the initiator/catalyst mixture was added to the stirred monomer(s) solution under

nitrogen at 22 °C. The reaction mixture was left for the required amount of time to ensure full conversion. Conversion was monitored by ^{1}H NMR analysis by observing the disappearance of vinyl signals at δ 5.5−6.0. On exposure to air, the reaction solution turned blue, indicating aerial oxidation of the Cu(I) catalyst. The resulting polymer was mixed with Dowex Marathon MSC ion-exchange resin to remove Cu(II)Cl. The ion-exchange resin was then removed by filtration and remaining solution was rotary evaporated to remove solvent and precipitated into diethylether. The precipitated polymer was then dried under vacuum and freeze dried. Sample was then stored in the fridge under an argon atmosphere with sealed drying tube attached. Characterisation of polymers prepared are summarised in **Table AB.2**.

Amidation Reaction of *N*-succinimidyl Functional Polymers with A-SPION

The amidation reaction was followed using the method found in Chapter 2, **Figure AB.4**.

Reactions were carried out in a 15 mL vial with *NS*-polymer or Bz-PEGMA (for amounts see **Table AB.3**) . Colloidal stability results are summarised in **Table AB.3**.

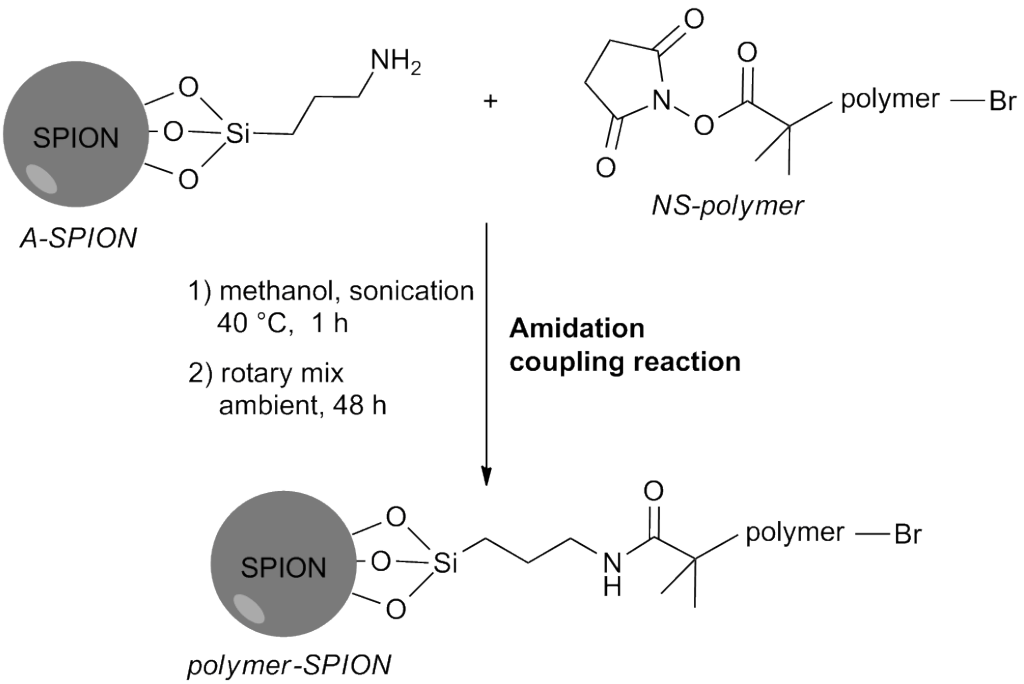

Figure AB.4. Amidation reaction of *NS*-polymer with A-SPIONs.

Stem Cell Labelling Studies using PEG_{112}-SPIONs

For cell uptake studies, kidney murine derived stem cells (KSCs) and mesenchymal stem cells (MSCs) were exposed to cell culture medium containing PEG_{112}-SPIONs and Molday Ion Coumarin Blue (MICB) NP concentrations of 5 µg Fe mL^{-1} and incubated for a period of 24 hours, **Figure AB. 5**.[5]

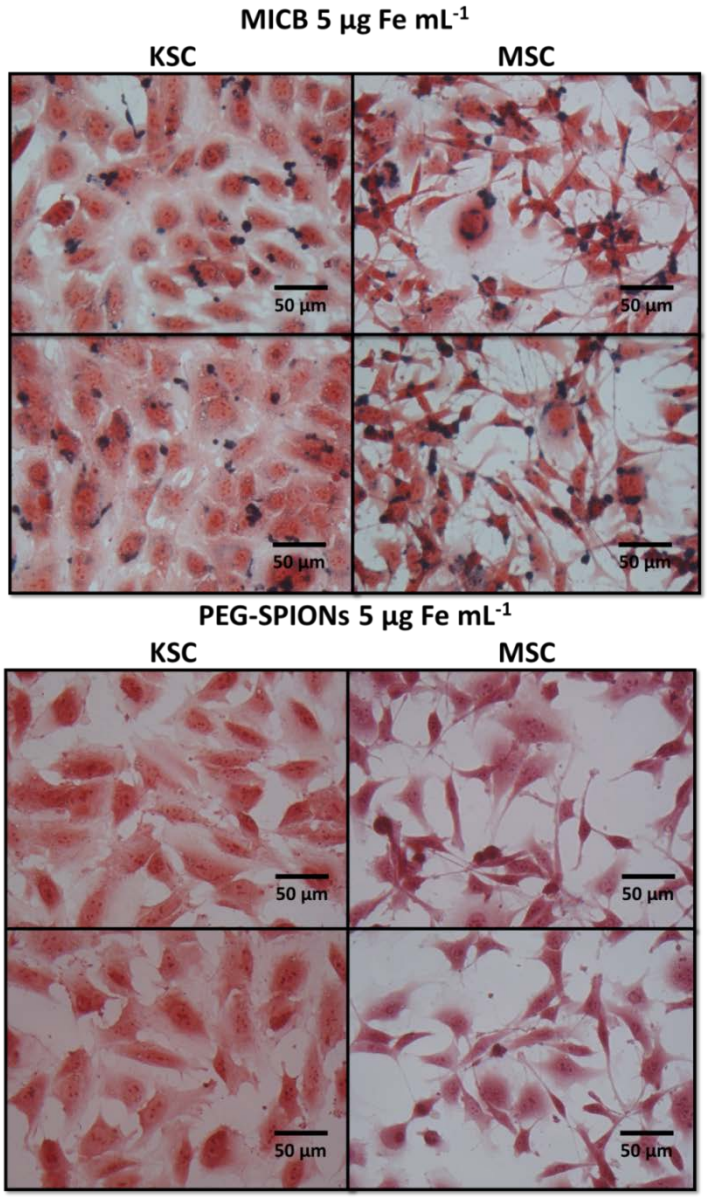

Figure AB. 5. Particle uptake study using a KSC and MSC line exposed to NP concentrations of 5 µg Fe mL^{-1} of MIRB and PEG_{112}-SPIONs incubated for 24 hours. Cells were stained with the Iron Stain Kit (Sigma Aldrich), which consists of a Prussian Blue staining for iron deposits and a Pararosaniline counterstain (pink).

After this period, cells were washed, fixed and the iron oxide cores were stained using Prussian blue to form a complex with iron for imaging of SPIONs. Pararosaniline counterstain was used to visualise and image stem cells using bright field optical microscopy. Lower uptake levels observed from very little Prussian blue staining for cells exposed to PEG_{112}-SPIONs confirms the PEG surface coating is 'stealthy' and provides non-specific uptake. MICB however showed much higher levels of uptake as expected from previous cell uptake results observed throughout this Thesis.

Table AB.1. Summary of polymers synthesised by ATRP (to be used for amidation coupling reaction) and their respective reaction parameters. Where *NS* and *Bz* are *N*-Succinimidyl and benzyl functional initiators used respectively.

ID	Polymer synthesised (*I*-(monomer)$_n$	Target Polymer DP$_n$	Target polymer Mw (K g mol^{-1})	Initiator (*I*) weight (mg)	Monomer weight used (g)	Solvent (added to catalyst /added to monomer), volume	Catalyst mixture amounts (mg/mg) (Cu(I)Cl/bipy)
1	*NS*-(PEGMA$_{Mn300}$)$_n$	50	15.5	88.4	5.01	MEK, 5 mL	37/109
2	*Bz*-(PEGMA$_{Mn300}$)$_n$	50	15.2	84.9	5.00	DMSO, 5 mL	33/109
3	*NS*-(PEGMA$_{Mn300}$)$_n$	16	5	274.6	5.00	DMSO, 5 mL	103/344
4	*NS*-(PEGMA$_{Mn1100}$)$_n$	5	5	240.1	5.00	DMSO, 10 mL	90/298

Table AB.2. ^{1}H-NMR and GPC summary data of preliminary synthesised polymers. Note, shaded in grey are purchased mPEG polymers which were further prepared to contain a carboxyl moiety. These polymers were included in the table as a comparison to those synthesised.

Polymer used	Target M_n / g mol^{-1}	Target Polymer DP_n	DP_n (^{1}HNMR)	GPC M_n / g mol^{-1}	DP_n (GPC)	Đ
NS-$(PEGMA_{Mn300})_{50}$	15,500	50	43	6,900	23	1.28
Bz-$(PEGMA_{Mn300})_{50}$	15,200	50	92	7,000	23	1.84
NS-$(PEGMA_{Mn300})_{16}$	5,000	16	98	3,000	10	1.55
NS-$(PEGMA_{Mn1100})_{5}$	5,000	5	99	5,500	5	1.22
$m(PEG)_{45}$-COOH	2,000	45			-	-
$m(PEG)_{112}$-COOH	4,600	112	-		-	-

Table AB.3. Summary of amidation coupling reactions of selected polymers with amino silane coated SPION and the colloidal stability results.

SPION core diameter (nm) (pXRD)	amino silane monolayers	Polymer used	Amount of polymer used	Av. Zeta potential (mV)	colloidally stable after dialysis into water? (y/n)	colloidally stable in PBS pH 7.4 @ 22 °C 24 h? (Y/N)	colloidally stable in PBS pH 7.4 @ 37 °C 24 h? (Y/N)
6.3	2.98	*NS*-$(PEGMA_{Mn300})_{50}$	0.75	+ 0.95	Y	N	
6.3	3.20	*Bz*-$(PEGMA_{Mn300})_{50}$	0.75	+ 10.24	N		
6.3	2.81	*NS*-$(PEGMA_{Mn300})_{16}$	0.24	+ 18.9	N		
6.3	2.81	*NS*-$(PEGMA_{Mn1100})_{5}$	0.28	+ 31.8	N		
6.3	2.81	$m(PEG)_{45}$-COOH	0.10	+ 9.48	Y	Y	N
6.3	2.81	$m(PEG)_{112}$-COOH	0.20	-2.42 ± 13.3	Y	Y	Y

References

1. E. K. Larsen, T. Nielsen, T. Wittenborn, *et al.*, *ACS Nano*, 2009, **3**, 1947-1951.
2. J. F. Lutz, S. Stiller, A. Hoth, *et al.*, *Biomacromolecules*, 2006, **7**, 3132-3138.
3. F. Hu, K. G. Neoh, L. Cen, *et al.*, *Biomacromolecules*, 2006, **7**, 809-816.
4. B. Parrish and T. Emrick, *Macromolecules*, 2004, **37**, 5863-5865.
5. C. F. Mora, E. Ranghini, S. Bruno, *et al.*, *Stem Cells Dev*, 2012, **21**, 296-307.